

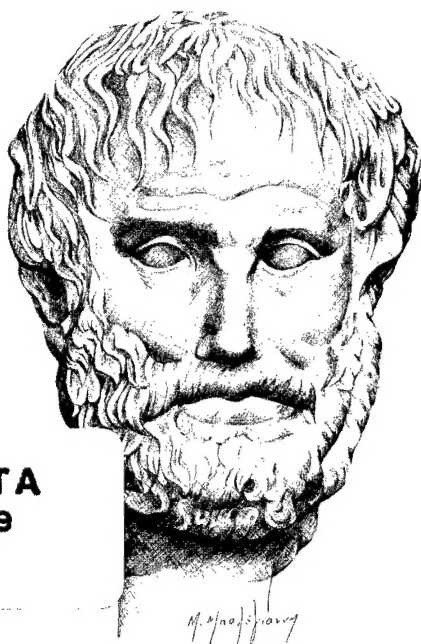
HELLENIC SOCIETY OF THEORETICAL
AND APPLIED MECHANICS (HSTAM)

ARISTOTLE UNIVERSITY
OF THESSALONIKI (AUTH)

6th NATIONAL CONGRESS OF MECHANICS

PROCEEDINGS VOLUME III

EDITORS
E.C.AIFANTIS
A.N.KOUNADIS



DISTRIBUTION STATEMENT A
Approved for Public Release
Distribution Unlimited

20020125 231

*Dedicated to the memory
of P.S.Theocaris*

THESSALONIKI,
JULY 19-21, 2001

6th National Congress of Mechanics

Thessaloniki, 19-21 July 2001

Hellenic Society of Theoretical and Applied Mechanics (HSTAM)

Aristotle University of Thessaloniki (AUT)

PROCEEDINGS

Volume III

Thursday 19 July 2001

Editors: *E. C. Aifantis* and *A. N. Kounadis*

Dedicated to the memory of
P. S. Theocaris

Thessaloniki 13 July 2001

Foreword

It was an honor that HSTAM (Hellenic Society of Theoretical and Applied Mechanics) assigned to the Laboratory of Mechanics of the General Department of AUT the responsibility of organizing the 6th National Congress of Mechanics in cooperation with the Department of Civil Engineering of AUT.

Special thanks to A. Kounadis and D. Beskos, president and secretary of HSTAM respectively, as well as to G. Manolis and D. Talaslidis who served as vice-chairmen of the organizing committee.

The Congress is dedicated to the memory of P. Theocaris whose influence on the Mechanics Community of Greece will remain for many years. My predecessor G. Lianis and A. Armenakas served as honorary chairmen of the Congress. My thanks go to them, as well as to the rest of the members of the organizing committees.

The Congress was organized during a very interesting period of substantial activity in the educational and scientific community in Greece. More than two months before the Congress, the University administration, at first, and the undergraduate student body as a whole, later, opposed certain educational proposals passed by the State, and daily university activities came to a standstill. This had a serious impact on the conference organization including the disruption of usual e-mail correspondence.

It was the determination of my graduate students G. Efremidis and P. Sapalidis, the help of F. Akintayo, K. Kosmidis, K. Kalaitzidou/S. Marras (currently at MTU/USA), the assistance of undergraduate students Th. Atmakidis and D. Dodou, as well as the encouragement of A. Kounadis, which helped me decide not to postpone the meeting. Special thanks go to George Efremidis who took upon himself the responsibility of completing the process of collecting the manuscripts, coordinating the e-mail correspondence, and other organizational details. My colleagues D. Beskos and G. Manolis were always available for consultation and advice. Many faculty of the General Department including its past and newly elected Chairman, as well as the Dean of Engineering were very supportive of this event.

The active participation of the travel agency Aethra, the publisher Giahoudi-Giapouli and the personal involvement of the owner of Philippon Hotel Helena Thoidou, who took the initiative to help with respective arrangements without requiring pre-payment, is worth mentioning. The financial support of the General Department, the College of Engineering, and the Research Committee of AUT, as well as of Democritus University of Thrace is

acknowledged. Also we acknowledge with thanks the financial support of the Ministry of Education, the Ministry of Culture and the Municipality of Thessaloniki. We also hope to have some financial support from the Ministry of Macedonia-Thrace and the Academy of Athens; but, at the time this foreword was composed, we had not yet received a definite decision from these governmental agencies, mainly due to difficulties in communication or decision-making during this unusual period of academic life.

Finally, sincere thanks go to all participants, especially those from abroad invited by HSTAM and myself or personally encouraged by me to attend. They all honored their commitment to participate despite the minimal information that could be distributed due to the aforementioned unforeseen circumstances. Many of the participants facilitated us greatly by pre-registering, thus enabling us to respond to initial financial obligations related to the Congress organization. It should be noted that as a result of the unusual circumstances mentioned above, it was not possible to activate a panel for a thorough review of the papers, which were accepted on the basis of their abstracts only.

Last, but not least, I would like to personally acknowledge the support and encouragement of the Minister of Yugoslavia, Professor Dragoslav Sumarac, for developing in Thessaloniki a Balkan Center of Mechanics with support from ERO and MTU with the participation of leading researchers of Mechanics and Materials of an international stature. In this respect, the sincere interest of Sam Sampath and the continuous help of my students I. Mastorakos, Avraam and Dimitris Konstantinidis in the organization of related research activities at AUT, as well as the scientific support of my student I. Tsagrakis, the research associate Mike Zaiser, and my physics colleague S. Logothetidis at AUT, are gratefully acknowledged.

*Elias C. Aifantis
Chairman*

6th NATIONAL CONGRESS OF MECHANICS

Thessaloniki. 19 – 21 July, 2001

Hellenic Society of Theoretical and Applied Mechanics (HSTAM)
Aristotle University of Thessaloniki (AUT)

ORGANIZING COMMITTEES

• *Chairmanship*

E. Aifantis,	Chairman, AUT
G. Lianis,	Honorary Chairman, Emeritus Professor, AUT
A. Armenakas,	Honorary Chairman, Emeritus Professor, NTUA
	Past President of HSTAM

• *HSTAM Council*

A. Kounadis,	Academy of Athens / NTUA, President
J. Katsikadelis,	NTUA, Vice-President
D. Beskos,	University of Patras, Secretary General
A. Vakakis,	NTUA, Treasurer
I. Vardoulakis,	NTUA
A. Mavraganis,	NTUA
D. Panayotounakos,	NTUA
H. Georgiadis,	NTUA
V. Koumoussis,	NTUA
G. Papadopoulos,	University of Athens
M. Papadrakakis,	NTUA

• *National Committee*

N. Alikakos,	University of Athens	A. Liolios,	DUTH
N. Aravas,	University of Thessaly	A. Mamalis,	NTUA
A. Bountis,	University of Patras	C. Massalas,	University of Ioannina
I. Dafalias,	NTUA	A. Payatakes,	University of Patras
G. Dassios,	University of Patras	P. Perdikaris,	University of Thessaly
V. Dougalis,	University of Athens	S. Pnevmatikos,	University of Patras
E. Economou,	University of Crete	D. Theodorou,	University of Patras
G. Fytas,	University of Crete	D. Tsahalidis,	University of Patras
E. Gdoutos,	DUTH	G. Tsamasphyros,	NTUA
A. Liakopoulos,	University of Thessaly	P. Varotsos,	University of Athens

• ***AUT Committees***

G. Manolis / D. Talaslidis: Vice-Chairmen

A. Anagnostopoulos	G. Kourouklis
J. Antonopoulos	P. Latinopoulos
P. Argyrakis	S. Logothetidis
G. Athanasiadis	G. Manos
Ch. Baniotopoulos	S. Natsiavas
S. Bantis	S. Nychas
K. Bouzakis	M. Pagitsas
N. Charalambakis	C. Panayiotou
A. Charalambopoulos	P. Papadopoulos
J. Ganoulis	G. Penelis
A. Goulas	K. Pitilakis
J. Hadjidemetriou	N. Platakis
S. Ichtiaroglou	G. Theodorou
G. Kanelis	A. Trochidis
A. Karabelas	G. Tsagas
Th. Karakostas	D. Tsipas
A. Kehagias	K. Tsouros
C. Kiparissides	C. Tzimopoulos

• ***Local Arrangements Committee***

Section of Mechanics: S. Ambatjidis, E. Douka, M. Matsikoudi, S. Papargyri

Graduate students: G. Efremidis, P. Sapalidis, F. Akintayo, I. Mastorakos, K. Kosmidis,
K. Kalaitzidou, S. Marras

Undergraduate students: Th. Atmakidis, D. Dodou

TABLE OF CONTENTS

VOLUME I

THERMOMECHANICS OF LOCAL STRUCTURAL REARRANGEMENTS <i>G. Maugin</i>	1
QUANTUM PLASTICITY <i>K. Valanis</i>	9
ON STRAIN GRADIENTS IN PLASTICITY <i>J. Kratochvil</i>	14
ENABLING NONLINEAR COMPUTATIONS THROUGH EFFICIENT TIME-STEPPING <i>E. Koronaki, C. Theodoropoulos, A. Boudouvis I. Kevrekidis</i>	21
RHEOLOGY OF DENSE LIGNITE-WATER SUSPENSIONS; TRANSITION STRESSES ON FLOW CURVES <i>T. Goudoulas, E. Kastrinakis, S. Nychas</i>	27
COMPUTER SIMULATION OF THE NONLINEAR EVOLUTION OF INCLINED FILM FLOWS <i>N. Malamataris, M. Vlachogiannis, V. Bontozoglou</i>	33
AN IMPROVED COASTAL CIRCULATION MODEL BASED ON THE CHARACTERISTIC-GALERKIN TECHNIQUE <i>H. Mpimpas, P. Anagnostopoulos</i>	39
ON THE EFFECT OF THE RELATIVE VISCOSITY OF TWO FLUIDS ON THE DYNAMICS OF AXISYMMETRIC CORE-ANNULAR FLOW IN A TUBE <i>C. Kouris, J. Tsamopoulos</i>	45
A COMPARISON OF THE ACCURACY OF VARIOUS INTERPOLATION TECHNIQUES FOR PROCESSING RANDOMLY SCATTERED BATHYMETRIC DATA <i>N. Volakos, R. Barber</i>	52
INTERRELATION BETWEEN STOKES AND PAPKOVICH - NEUBER EIGENMODES FOR SPHEROIDAL STOKES FLOW <i>M. Hadjinicolaou, P. Vafeas</i>	59
NUMERICAL STUDY OF OSCILLATORY FLOW PAST PAIRS OF CYLINDERS AT LOW REYNOLDS AND KEULEGAN-CARPENTER NUMBERS <i>P. Anagnostopoulos, A. Koutras, S. Seitanis</i>	66
INVERSE DESIGN OF AERODYNAMIC SHAPES USING ANT COLONY OPTIMIZATION <i>T. Zervogiannis, V. Assouti, K. Gagas, A. Kaounis, K. Giannakoglou</i>	72
STRATIFIED TWO -PHASE FLOW OF VAPOUR BOUNDARY LAYER- CONDENSATE FILM OVER A CYLINDER <i>D. Smyrniaios, N. Pelekasis, J. Tsamopoulos</i>	78
FLUID DISPLACEMENT BY AIR IN A CAPILLARY TUBE <i>Y. Dimakopoulos, J. Tsamopoulos</i>	84

FLOW BETWEEN TWO ROTATING HEATED SPHERES <i>V. Loukopoulos</i>	90
AN EXPERIMENTAL METHODOLOGY FOR ENHANCING 2-D FLOW CHARACTERISTICS IN A 3-D TURBULENT FLOW <i>G. Sideridis, E. Kastrinakis, S. Nychas</i>	96
FORCES FROM JET FLOWS ON INCLINED DISCS <i>J. Demetriou, D. Dimitriou</i>	102
FLOW IN OPEN CHANNELS LINED WITH DIFFERENT MATERIALS <i>J. Demetriou, C. Pourliotis, P. Sarantos</i>	108
AIRLIFT PUMP PERFORMANCE OPTIMISATION FOR DEEP-SEA MINING <i>D. Margaris</i>	114
BOUNDARY SHEAR IN COMPOUND NON-SYMMETRICAL CHANNELS <i>K. Nanou-Giannarou, J. Demetriou</i>	121
USE OF HEIGHT DENSITY FUNCTION FOR THE EVALUATION OF MEASUREMENTS WITH A LASER DOPPLER ANEMOMETER <i>Th. Panidis</i>	127
DAMAGE MODELS FOR VISCOELASTIC COMPOSITES <i>R. Schapery</i>	134
DAMAGE LOCALIZATION AND FRACTURE IN LAMINATE COMPOSITES <i>P. Ladeveze</i>	140
CYLINDRICAL SHELLS AND THEIR STABILITY (CHOICE OF THE DEFLECTION FUNCTION AND CRITICAL EXTERNAL RADIAL PRESSURE) <i>D. Ruzic, Lj. Markovic</i>	146
ESSENTIAL STRUCTURE OF DAMAGE MECHANICS MODELS <i>D. Krajcinovic</i>	155
FATIGUE OF MATERIALS AND STRUCTURES <i>J. Lemaitre</i>	163
LARGE DEFLECTION ANALYSIS OF BEAMS WITH VARIABLE STIFFNESS. AN ANALOG EQUATION SOLUTION <i>J. Katsikadelis, G. Tsiatas</i>	172
CRUSHING OF SHIP'S BOW STRUCTURE DURING COLLISION WITH BRIDGE PIERS <i>N. Hajdin, R. Mandic</i>	178
BEM SOLUTION OF VISCOPLASTIC PROBLEMS IN METALLIC STRUCTURES IN THE PRESENCE OF TEMPERATURE GRADIENTS <i>C. Providakis, S. Kourtakis</i>	184
ROCK DISCONTINUITIES IN TUNNEL DESIGN: NUMERICAL SIMULATION OF THE EFFECTS OF FILLED AND OPEN JOINTS <i>C. Stiakakis, Z. Gioutantis, G. Paschalis</i>	191
ON THE NUMERICAL PERFORMANCE OF A SIMPLIFIED METHOD OF ANALYSIS FOR CREEPING STRUCTURES LOADED CYCLICALLY <i>K. Spiliopoulos</i>	198

STATIC AND DYNAMIC ANALYSIS OF SHELL PANELS USING THE ANALOG EQUATION METHOD	
<i>J. Yiotis, J. Katsikadelis</i>	204
NUMERICAL STUDIES OF ANCHORS AND REBARS IN CONCRETE SPECIMENS BY DAMAGE MODELS	
<i>G. Hatzigeorgiou, M. Sfakianakis, D. Theodorakopoulos, D. Beskos</i>	210
ON THE FLEXURAL MODES OF THE BICKFORD BEAM THEORY	
<i>C. Sophocleous, K. Soldatos</i>	216
A REALISTIC ESTIMATION OF THE EFFECTIVE BREADTH OF RIBBED PLATES	
<i>J. Katsikadelis, E. Sapountzakis</i>	222
ON THE STUDY OF TIE PLATES IN PIN CONNECTIONS	
<i>I. Mademlis, S. Marnoutsidis, A. Avdelas</i>	228
THE EFFECT OF DECK ROUGHNESS IN CONJUNCTION WITH OTHER PARAMETERS ON THE DYNAMIC RESPONSE OF STEEL HIGHWAY BRIDGES UNDER VEHICULAR LOADING	
<i>G. Michaltsos, D. Sophianopoulos</i>	234
LQR AND H OPTIMAL STRUCTURAL CONTROL IN ASEISMIC DESIGN	
<i>E. Zacharenakis, K. Arvanitis, A. Soldatos, G. Stavroulakis</i>	240
RELIABILITY BASED OPTIMIZATION USING NEURAL NETWORKS	
<i>M. Papadrakakis, N. Lagaros</i>	246
A NUMERICAL ESTIMATION OF THE INTERRELATION BETWEEN ACCELERATION PARAMETERS AND DAMAGE INDICATORS IN EARTHQUAKE ENGINEERING	
<i>A. Elenas, A. Liolios, L. Vasiliadis, M. Sakellari, P. Koliopoulos</i>	254
ELASTOPLASTIC RESPONSE SPECTRA FOR THE DESIGN OF STRUCTURES SUBJECTED TO EXPONENTIAL BLAST LOADING	
<i>N. Pnevmatikos, C. Gantes</i>	261
ANALYTICAL ESTIMATION OF TOTAL DISPLACEMENT'S COMPONENTS OF R/C SHEAR WALLS WITH ASPECT RATIO 1.0-1.5 SUBJECTED TO SEISMIC LOADS	
<i>T. Salonikios</i>	267
COMPETITION AMONG GENETIC ALGORITHMS TO IMPROVE ROBUSTNESS IN OPTIMIZATION	
<i>C. Dimou, V. Koumousis</i>	275
YUGOSLAV INVESTIGATIONS CONCERNING THE PATCH LOADING ON GIRDERS	
<i>N. Hajdin, B. Coric, N. Markovic, D. Lucic</i>	282
SYNTHESIS OF NEW PHENOLIC POLYMERS VIA ENZYMATIC POLYMERIZATION AND THEIR PROPERTIES	
<i>S. Kobayashi</i>	290
ADAPTIVE FINITE ELEMENT ANALYSIS OF LIMIT-LOAD STATES IN DRY AND SATURATED SOILS	
<i>W. Wunderlich, R. Findei, H. Cramer</i>	298
MEASUREMENT OF THE MECHANICAL PROPERTIES OF MEMS MATERIALS	
<i>W. Sharpe Jr.</i>	306

BEHAVIOR OF PARTICLE REINFORCED COMPOSITES WITH SOFT MATRICES <i>C. Sciammarella, F. Sciammarella</i>	314
INDENTATION FAILURE OF SANDWICH PANELS <i>E. Gdoutos, I. Daniel, K.-A. Wang</i>	320
ESTIMATION OF THE CONCRETE CHARACTERISTICS USING PATTERN RECOGNITION METHODS <i>M. Titsias, D. Fotiadis, A. Likas</i>	327
DESTRUCTIVE AND ULTRASONIC NON-DESTRUCTIVE TESTING OF 28-DAY AND 28-YEAR OLD CONCRETE <i>I. Prassianakis, P. Giokas</i>	333
EXPERIMENTAL QUANTIFICATION OF CRACK TIP PARAMETERS FOR PARTICULATE METAL MATRIX COMPOSITES <i>S. Kourkoulis, V. Kytopoulos</i>	339
ON SELECTING A COMPATIBLE SUBSTITUTE FOR THE KENHCREAE POROS STONE USED IN THE EPIDAUREAN ASKLEPIEION <i>N. Ninis, S. Kourkoulis</i>	348
NON-LINEAR MECHANICS AND BUCKLING ANALYSIS OF COMPOSITE SHELLS WITH EMBEDDED PIEZOELECTRIC ACTUATORS AND SENSORS <i>D. Varelis, D. Saravanos</i>	357
A NEW DESIGN METHODOLOGY FOR HIGH TEMPERATURE STRUCTURAL COMPONENTS MADE OF CONTINUOUS FIBER CERAMIC COMPOSITES EXHIBITING THERMALLY INDUCED ANISOTROPIC DAMAGE <i>D. Vlachos, Y. Pappas, R. De Stefano, V. Kostopoulos</i>	365
EXPERIMENTAL AND THEORETICAL STRESS ANALYSIS OF INCOMPRESSIBLE BONDED ELASTOMERIC DISCS SUBJECTED TO COMPRESSION <i>P. Kakavas</i>	375
OPTICAL DEVICE FOR PROSTATE CANCER DETECTION <i>G. Anastassopoulos, J. Lytras, M. Sunaric, V. Moulitanitis, S. Panteliou, A. Bekos, N. Kalinderis, D. Hatzichristou</i>	381
EXPERIMENTAL VERIFICATION OF SHEAR WALL MODELING USING FINITE ELEMENT ANALYSIS <i>A. Papachristidis, G. Badaloukas, B. Badalouka</i>	388
FAILURE OF A COMPOSITE WITH A BROKEN FIBER <i>D. Zacharopoulos, E. Gdoutos, D. Karalekas</i>	394
MICROMECHANICS OF CARBON FIBRE MODEL COMPOSITES UNDER TENSILE, COMPRESSIVE AND FATIGUE LOADING CONDITIONS <i>C. Koimtzoglou, S. Goutianos, C. Galiotis</i>	401
DYNAMIC BEHAVIOR OF A HANGED CABLE FOR DEEP WATER APPLICATIONS <i>I. Chatjigeorgiou, S. Mavrakos</i>	408
EXPERIMENTS FOR THE ESTIMATION OF UNSATURATED HYDRAULIC CONDUCTIVITY <i>G. Arampatzis, Ch. Tzimopoulos</i>	416

VOLUME II

CONTINUUM THEORY OF SELF-HEALING INTERFACE CRACKS <i>M. Marder, E. Gerde</i>	1
MATERIAL DEGRADATION AND FRACTURE IN HYDRIDE FORMING METALS <i>A. Varias, A. Massih</i>	7
SOME PROBLEMS OF ELECTROMECHANICAL FRACTURE OF DIELECTRIC AND PIEZOELECTRIC BODIES <i>D. Bardzokas, A. Zobnin</i>	13
CONTROL OF DYNAMIC STRESS AND FRACTURE OF PIEZOELECTRIC BODIES WITH CRACKS <i>D. Bardzokas, M. Filshinsky</i>	22
OPTIMIZATION AND SOFT COMPUTING FOR INVERSE AND CRACK IDENTIFICATION <i>G. Stavroulakis, H. Antes</i>	28
MECHANICAL BEHAVIOR OF MULTILAYERED NANOCOMPOSITE FILMS <i>V. Singh, X. Nie, P. Gupta, E. Meletis</i>	33
A COMPARATIVE STUDY OF MECHANICAL PROPERTIES OF STATE-OF-THE-ART AMORPHOUS CARBON FILMS <i>C. Charitidis, S. Logothetidis</i>	40
THE ROLE OF POINT DEFECTS ON THE GROWTH AND BREAKDOWN OF METAL PASSIVE FILMS IN ELECTROLYTE SOLUTIONS <i>M. Pagitsas, A. Diamantopoulou, D. Sazou</i>	46
FAILURE RESISTANCE TO THERMAL SHOCK OF THERMAL BARRIER COATINGS USING THE FINITE ELEMENT METHOD <i>A. Kekatou, V. Sfakiotakis, D. Katsareas, N. Anifantis</i>	52
FINITE ELEMENT ANALYSIS OF THE ELASTIC MECHANICAL BEHAVIOUR OF LDPE FILM <i>D. Briassoulis, E. Schettini</i>	57
ADAPTIVE COMPOSITES INCORPORATING SHAPE MEMORY ALLOY WIRES; RECORDING THE INTERNAL STRESS BY LASER RAMAN SPECTROSCOPY <i>J. Parthenios, G. Psarras, D. Bollas, C. Galiotis</i>	63
A HEMIVARIATION ALINE QUALITY APPROACH TO THE RESISTANCE OF ALUMINIUM RIVETED CONNECTIONS <i>M. Zygomas, M. J. Kontoleon and C. C. Baniotopoulos</i>	70
ANALYSIS OF "CONVEX ENERGY" STRUCTURAL SYSTEMS UNDER STOCHASTIC LOADING <i>M. Kontoleon, C. Baniotopoulos, M. Betti, C. Borri</i>	78
FRICTION EVOLUTION IN FRACTAL INTERFACES <i>O. Panagouli, E. Mistakidis</i>	84

NUMERICAL STUDY OF THE F.E. MESH DEPENDENCY IN NONCONVEX-NONSMOOTH ENGINEERING PROBLEMS	
<i>E. Mistakidis, N. Politis</i>	90
FUZZY SETS IN ENGINEERING ANALYSIS AND DESIGN	
<i>E. Mistakidis, D. Georgiou</i>	96
BENDING AND WARPING IN FIBER REINFORCED RECTANGULAR BEAMS	
<i>C. Demakos</i>	102
ON THE POTENTIAL REPRESENTATIONS FOR POLYADICS AND ANISOTROPIC MEDIA	
<i>G. Dassios</i>	109
THE APPLICATION OF NOTHER'S THEOREM TO NON-LINEAR ANISOTROPIC ELASTIC MATERIALS	
<i>J. Jaric, K. Kishimoto, T. Wang, M. Omiya</i>	115
MICROMECHANICAL MODELING OF THE BEHAVIOR OF POROUS SHAPE MEMORY ALLOYS	
<i>D. Lagoudas, P. Entchev</i>	120
VARIATIONAL FORMULATION AND MATERIAL BALANCE LAWS OF DISSIPATIONLESS THERMOELASTICITY	
<i>V. Kalpakides, G. Maugin</i>	126
THE INFINITE ISOTROPIC WEDGE UNDER LINEARLY DISTRIBUTED LOADING	
<i>J. Stabouloulou, E. Theotokoglou</i>	133
SIZE EFFECT ON FAILURE LOAD OF MARBLE BEAMS UNDER THREE POINT BENDING	
<i>I. Vardoulakis, G. Exadaktylos, S. Kourkoulis</i>	140
FINITE ELEMENT TECHNIQUES FOR STRAIN-GRADIENT ELASTICITY PROBLEMS	
<i>E. Amanatidou, N. Aravas</i>	149
THE ELASTIC PUNCH PROBLEM REVISITED	
<i>G. Exadaktylos</i>	155
GRADIENT ELASTIC BERNOULLI-EULER BEAMS IN BENDING AND BUCKLING	
<i>S. Papargyri-Beskou, K. Tsepoura, D. Polyzos, D. Beskos</i>	163
DUAL MODE VIBRATION ISOLATION BASED ON NONLINEAR MODE LOCALIZATION	
<i>X. Jiang, A. Vakakis</i>	170
A FRACTIONAL BROWNIAN MOTION MODEL FOR TIMESERIES PRODUCED BY CONSTANT ENERGY MOLECULAR DYNAMICS SIMULATIONS	
<i>T. Karakasidis, I. Andreadis</i>	177
VIBRATIONAL PROPERTIES OF A $\Sigma 5(310)[001]$ NiO GRAIN BOUNDARY STUDIED BY MOLECULAR DYNAMICS SIMULATION	
<i>T. Karakasidis</i>	183
ANALYTICAL SOLUTION OF THE NONLINEAR DAMPED DUFFING OSCILLATOR	
<i>D. Panayotounakos, G. Exadaktylos, A. Vakakis</i>	189

NONLINEAR EFFECTS ON THE ELASTIC STABILITY OF A COLUMN-FOOTING SYSTEM ON ELASTIC BASE	
<i>Ch. Younis, D. Panayotounakos</i>	196
THE CONTINUOUS TIME HOMOGENEOUS MARKOV SYSTEM WITH FIXED SIZE AS A LINEAR ELASTIC CONTINUUM	
<i>G. Tsaklidis, K. Soldatos</i>	209
STUDY OF THE DYNAMIC CHARACTERISTICS DURING CALLUS FORMATION	
<i>G. Foutsitzi, A. Charalambopoulos, D. Fotiadis, C. Massalas</i>	216
ON THE ELECTROENCEPHALOGRAPHY (EEG) PROBLEM FOR THE ELLIPSOID ALBRAIN MODEL	
<i>G. Kamvyssas, F. Kariotou</i>	222
MATHEMATICAL MODELS FOR BIOMAGNETIC FLUID FLOW AND APPLICATIONS	
<i>E. Tzirtzilakis, N. Kafoussias</i>	227
LAMELLAR INHOMOGENEITIES IN PIEZOELECTRIC SOLIDS	
<i>C. Dascalu, D. Homentcovschi</i>	233
ON A NEW CRACK MODEL FOR PIEZOELECTRIC SOLIDS	
<i>C. Dascalu, D. Homentcovschi, V. Kalpakides, E. Hadjigeorgiou</i>	239
ON THE STOCHASTIC MICROMECHANICAL THEORY OF DISCRETE MATERIAL SYSTEMS	
<i>Y. Haddad</i>	245
A CONSTITUTIVE LAW FOR POWDER COMPACTION	
<i>S. Subramanian, P. Sofronis</i>	251
CONTINUUM MICROPOLAR MODELLING OF DISCONTINUOUS MASONRY-LIKE SYSTEMS	
<i>P. Trovalusci, R. Masiani</i>	257
SOME ASPECTS OF A MICROPOLAR PLASTICITY THEORY	
<i>P. Grammenoudis, Ch. Tsakmakis</i>	263
DESCRIPTION OF PLASTIC ANISOTROPY EFFECTS AT LARGE DEFORMATIONS	
<i>D. Schick, Ch. Tsakmakis</i>	269
"COLD" WORK AND STABILITY IN SOFTENED MATERIALS	
<i>N. Charalambakis</i>	276
SOME BASIC SOLUTIONS TO DYNAMIC PROBLEMS IN RANDOM MEDIA	
<i>C. Karakostas, G. Manolis</i>	280
ANALYSIS OF RAYLEIGH WAVES IN MICRO STRUCTURED SOLIDS BY DIPOLAR GRADIENT ELASTICITY	
<i>H. Georgiadis, I. Vardoulakis, E. Velgaki</i>	289
THE 3D THERMO-ELASTODYNAMIC PROBLEM OF MOVING LOADS IN A HALF - SPACE	
<i>G. Lykotrafitis, H. Georgiadis</i>	295
THE ATTITUDE MOTION OF A CARRIER-ROTOR SYSTEM WITH ALMOST SYMMETRIC INERTIA ELLIPSOID, UNDER BODY-FIXED TORQUES	
<i>K. Dimitrakopoulou, A. Mavraganis</i>	301

GRADIENT ANISOTROPIC DAMAGE IN MMCS FOR BRIDGING LENGTH SCALES BETWEEN MACROSCOPIC RESPONSE AND MICROSTRUCTURE	
<i>G. Voyiadjis, R. Dorgan</i>	309
TWO SCALE DAMAGE MODEL FOR FATIGUE REPRESENTATION OF GRADIENT EFFECTS	
<i>R. Desmorat</i>	318
GRADIENT ELASTIC BARS UNDER UNIAXIAL STATIC OR DYNAMIC LOAD	
<i>K. Tsepoura, S. Papargyri - Beskou, D. Polyzos, D. Beskos</i>	328
EVOLUTION OF PERSISTENT SLIP BANDS IN FATIGUED METALS	
<i>E. Douka, B. Polyzos, A. Trochidis</i>	335
CRACK IDENTIFICATION IN BEAM STRUCTURES	
<i>Y. Bamnios, E. Douka, A. Trochidis</i>	342
FRACTALS AND FRACTIONAL CALCULUS IN SOLID MECHANICS	
<i>A. Carpinteri, B. Chiaia, P. Cornetti</i>	349
CHARACTERIZATION OF MATERIALS WITH PORES AND INCLUSIONS AT DIVERSE SCALES	
<i>G. Frantziskonis</i>	359
SEMI-ANALYTICAL SOLUTION FOR A 1-D SIMPLIFIED THMPC MODELLING OF A NON-SATURATED SOIL	
<i>M - A. Abellan, J - M. Bergheau, J. M. Huyghe, R. de Borst</i>	365
COMPACT, HIGH-POWER, SYNTHETIC JET ACTUATORS FOR FLOW SEPARATION CONTROL	
<i>J. Gilarranz, O. Rediniotis</i>	371
LOCALIZED PERIODIC MOTIONS IN SYSTEMS OF COUPLED OSCILLATORS	
<i>V. Koukouloyannis, S. Ichtiaroglou</i>	379
EFFECT OF THE PARAMETERS ON THE DYNAMIC BEHAVIOR OF A SMALL PARTICLE IN AN ANNULAR DISTRIBUTION OF N BODIES	
<i>T. Kalvouridis, F. Psarros</i>	385
RESEARCH AND CHALLENGES OF ENGINEERING MECHANICS AND MATERIALS IN THE TWENTY FIRST CENTURY	
<i>K. Chong, D. Davis</i>	391
DAMAGE MECHANICS APPLICATION ON REPAIR OF DESTROYED STRUCTURES	
<i>D. Sumarac</i>	397

VOLUME III

COMPUTATIONAL ASPECTS OF MATERIAL INSTABILITIES <i>R. de Borst, H. Askes, M. Gutierrez, G. Wells</i>	1
EXPERIMENTAL STUDIES OF PLASTIC INSTABILITIES IN SOLID SOLUTIONS <i>H. Neuhaeuser, F. Klose, H. Dierke, A. Ziegenbein, A. Nortmann</i>	9
COMBINED MEASUREMENTS OF ACOUSTIC EMISSION AND LASER EXTENSOMETRY DURING PORTEVIN-LE CHATELIER DEFORMATION IN AN Al-Mg ALLOY <i>A. Ziegenbein¹, F. Chmelik, H. Neuhaeuser</i>	16
SERRATED YIELDING AND NONUNIFORM PLASTIC DEFORMATION OF PORTEVIN - LE CHATELIER EFFECT IN COMMERCIAL Al-Mg ALLOYS <i>K. Chihab, H. Ait-Amokhtar</i>	22
TIME SERIES ANALYSIS AND THE DETERMINISTIC STRUCTURE OF THE PLC EFFECT <i>D. Kugiumtzis, E. Aifantis</i>	29
SOME DYNAMICAL SYSTEM CONSIDERATIONS FOR DISLOCATIONS <i>G. Stagika, S. Ichtiaroglou, E. Aifantis, I. Groma</i>	35
THE DISLOCATION MODEL OF LOCAL BEND <i>N. Tokiy, T. Konstantinova, V. Varyukhin, A. Tokiy</i>	40
MULTISCALE PLASTICITY: LINKING DISCRETE AND CONTINUUM APPROACHES <i>L. Kubin, B. Devincere</i>	47
MACROSCOPIC MATERIAL BEHAVIOR FROM MICROSCOPIC SIMULATIONS <i>S. Luding, M. Laetzel</i>	53
MODELLING OF LAMINATED COMPOSITE STRUCTURES <i>A. Fernandes, J. Pouget</i>	61
INVARIANT RELATIONS IN A BOUSSINESQ TYPE EQUATION <i>E. Meletlidou, J. Pouget, G. Maugin, E. Aifantis</i>	67
KINK DYNAMICS IN A LONG-RANGE INTERACTION MODEL <i>T. Ioannidou, J. Pouget and E. Aifantis</i>	73
MAGNETIC SOLITONS <i>P. Sutcliffe</i>	79
THE PROPAGATION OF STRAIN WAVES IN MATERIALS WITH MICROSTRUCTURE <i>A. Potapov, V. Rodyushkin</i>	85
GOVERNING EQUATIONS AND BALANCE LAWS FOR MICROPOLAR CONTINUUM <i>S. Lisina, A. Potapov, G. Utkin</i>	90
SPLITTING UP OF MULTISTABLE SOLITONS IN SOLIDS <i>A. Potapov, V. Kazhaev, S. Gromov</i>	96

MODELING THE CRUSHING OF A CELLULAR MATERIAL	
<i>M. Zaiser, E. Aifantis</i>	102
APPENDIX WITH THE LATE PAPERS	111
AUTHOR INDEX	

6th National Congress on Mechanics

Session A

Volume III

COMPUTATIONAL ASPECTS OF MATERIAL INSTABILITIES

René de Borst, Harm Askes, Miguel A. Gutiérrez, Garth N. Wells
Koiter Institute Delft
Delft University of Technology, NL-2600 GB Delft, The Netherlands

1. SUMMARY

A concise overview is given of various numerical methods that can be used to analyze material instabilities and failure in engineering materials.

2. INTRODUCTION

Failure in most engineering materials is preceded by the emergence of narrow zones of intense straining. During this phase of so-called strain localisation, the deformation pattern in a body rather suddenly changes from relatively smooth into one in which thin zones of highly strained material dominate. In fact, these strain localisation zones act as a precursor to ultimate fracture and failure. Thus, in order to accurately analyse the failure behaviour of materials it is of pivotal importance that the strain localisation phase is modelled in a physically consistent and mathematically correct manner, and that the proper numerical tools are used.

Until the mid-1980s analyses of localisation phenomena in materials were commonly carried out using standard, rate-independent continuum models. This is reasonable when the principal aim is to determine the behaviour in the pre-localisation regime and some properties at incipient localisation. However, there is a major difficulty in the post-localisation regime, since localisation in standard, rate-independent solids is intimately related to a possible change in the character of the governing set of partial differential equations. In the static case, the elliptic character can be lost, while in dynamics, we typically observe a change of a hyperbolic set into an elliptic set. In both cases, the rate boundary value problem becomes ill-posed and numerical solutions suffer from spurious mesh sensitivity.

To remedy this problem, one must either introduce higher-order terms in the continuum representation that reflect the changes in the microstructure, or take into account the inherent viscosity of most engineering materials, or directly incorporate the discontinuity that arises as an outcome of the strain localisation process. The latter possibility is pursued with so-called cohesive-zone models. We will start by introducing them and discuss how they can be introduced in a numerical context. Among other matters, we will show that finite elements with "embedded" localisation zones do not rigorously incorporate discontinuities in finite element models. Conversely, finite element formulations that depart from the Partition-of-

Unity concept [1] can, and we will discuss this briefly. Indeed, this concept enables the gradual transition from a (higher-order) continuum description to a genuine discontinuum in a numerical context. Closely related to the Partition-of-Unity formulation are meshless discretisations, such as the element-free Galerkin method [2]. This concept has a tremendous advantage for models in which higher-order terms are incorporated, since it inherently provides for the required higher-order continuity. This is demonstrated for a simple example. Finally, we will indicate how the heterogeneous character of materials at a macroscopic scale can be incorporated in numerical analyses of inelastic solids. In particular, the effect of stochastically distributed imperfections on the failure load in inelastic solids will be quantified in the framework of the finite element reliability method.

3. COHESIVE-ZONE MODELS

An important issue when considering failure is the observation that most engineering materials are not perfectly brittle in the Griffith sense, but display some ductility after reaching the strength limit. In fact, there exists a small zone in front of the crack tip, in which small-scale yielding, micro-cracking or void growth and coalescence take place. If this *fracture process zone* is sufficiently small compared to the structural dimensions, linear-elastic fracture mechanics concepts apply. However, if this is not the case, the cohesive forces that exist in this fracture process zone must be taken into account, and *cohesive-zone models* must be utilised. In such models, the degrading mechanisms in front of the crack tip are lumped into a discrete line, and a stress-displacement ($\sigma - u$) relationship across this line represents the degrading mechanisms in the fracture process zone. Evidently, the shape of the stress-displacement relation is material dependent. The area under this curve represents the energy that is needed to create a unit area of fully developed crack. It is commonly named the fracture energy G_f and has the dimensions of J/m^2 . Formally, the definition of the fracture energy reads:

$$G_f = \int \sigma \, du \quad (1)$$

with σ and u the stress and the displacement across the fracture process zone. Cohesive-zone models were introduced by Dugdale [3] and Barenblatt [4] for elastic-plastic fracture in ductile metals, and for quasi-brittle materials Hillerborg [5] published his so-called Fictitious Crack Model, which ensured a discretisation-independent energy release upon crack propagation.

Adapting this concept to smeared formulations, Bažant and Oh [6] developed the Crack Band Model, in which the fracture energy G_f was smeared out over the width of the area in which the crack *localises*, so that

$$G_f = \int \sigma \, \varepsilon(s) \, ds \quad (2)$$

When we assume that the strains are constant over a band width w (an assumption commonly made in numerical analyses), we obtain

$$G_f = w g_f \quad (3)$$

with g_f the work dissipated per unit area of fully damaged material:

$$g_f = \int \sigma d\varepsilon \quad (4)$$

When we prescribe the fracture energy G_f as an additional material parameter, the global load-displacement diagram can become almost insensitive to the discretisation, even when smeared formulations are employed. Nevertheless, in two and three-dimensional finite element calculations a complete mesh insensitivity is normally not achieved. Apart from the normal grid sensitivity of numerical approximation methods, this is partly due to the fact that it is difficult to estimate the value of the band width w . Especially if a crack propagates obliquely to the mesh lines, a proper estimate for w can be difficult. Often, it is assumed that the width over which the fracture energy is distributed can be related to the area of an element A_{elem} , e.g. [7]:

$$w = \alpha \sqrt{A_{\text{elem}}} = \alpha \sqrt{\sum_{i=1}^{NINT} \gamma_i \det \mathbf{J}_i} \quad (5)$$

with γ_i the weight factors of the integration rule and $\det \mathbf{J}_i$ the Jacobian of the transformation between the local, isoparametric coordinates and the global coordinate system in integration point i . The factor α is a modification factor which depends on the element type and the integration scheme.

Recently, finite element models with embedded discontinuities have become popular. There are two versions of these models, namely the strong discontinuity approach [8-10] and the weak discontinuity approach [11-13]. We will depart from the latter approach and define an element in which a band is defined within the element where the strains are different in magnitude than the strains in the remainder of the element:

$$\varepsilon_{ij}^+ = \bar{\varepsilon}_{ij} + \frac{\alpha^+}{2} (n_i m_j + n_j m_i) \quad (6)$$

and

$$\varepsilon_{ij}^- = \bar{\varepsilon}_{ij} + \frac{\alpha^-}{2} (n_i m_j + n_j m_i) \quad (7)$$

with \mathbf{n} a vector normal to the band and \mathbf{m} related to the deformation mode, e.g., $\mathbf{m} = \mathbf{n}$ for mode-I behaviour and \mathbf{n} orthogonal to \mathbf{m} for mode-II behaviour. α^+ and α^- are scalars indicating the magnitude of the strain inside and outside of the band, respectively, measured relative to the average, continuous strain $\bar{\varepsilon}_{ij}$ in the element. The enhanced strain modes (second part of eqs (6)-(7)) are discontinuous across element boundaries. Consequently, they can be solved for at element level. The stress-strain relation in the band can be specified independently from that in the bulk of the element. Typically, a softening relation is prescribed which results in an energy dissipation per unit volume g_f (eq. (4)) upon complete loss of material coherence. For a band with a width w , which is incorporated in the finite element formulation, we thus retrieve the fracture energy

$$G_f = w \int \sigma d\varepsilon \quad (8)$$

that is dissipated for the creation of a unit area of fully developed crack.

A problem resides in the determination of the length of the crack band, l_{elem} in a specific element. Obviously, for a given length l_{elem} the total energy dissipation in an element reads

$$G_{f,\text{elem}} = l_{\text{elem}} G_f \quad (9)$$

If the crack length in an element is estimated incorrectly, the energy that is dissipated in each element is also wrong, and so will be the total load-displacement diagram [13]. Different possibilities exist, e.g. to relate l_{elem} to the area of the element A_{elem} in the spirit of eq. (5) [12]. Other possibilities are to assume that the enhanced mode passes through the element midpoint, and to calculate the band length accordingly, or to let the band connect at the element boundaries and to compute the band length in this fashion [10].

While the above considerations have been set up for the so-called weak discontinuity approach, in which the displacement is continuous, it is also possible to let the enhanced strain modes be unbounded. This so-called strong discontinuity approach can be conceived as a limiting case of the weak discontinuity approach for $w \rightarrow 0$ [14]. The strain then locally attains the form of a Dirac function and the displacement becomes discontinuous across a single discrete plane. Nevertheless, the integral over time of the product of the traction and the difference in velocities between both sides still equals the fracture energy.

The embedded discontinuity approaches enhance the deformational capabilities of the elements, so that the high local strain gradients inside localisation bands are better captured. However, a true discontinuity is not captured because the kinematics of eqs (6) and (7) are diffused over the element when the governing equations are cast in a weak format, either via a Bubnov-Galerkin or via a Petrov-Galerkin procedure.

A method in which a discontinuity in the displacement field is captured rigorously has been developed recently on the basis of the Partition-of-Unity concept [1]. A collection of functions ϕ_i , associated with node i , form a partition of unity if

$$\sum_{i=1}^n \phi_i(\mathbf{x}) = 1 \quad (10)$$

with n the number of discrete nodal points. For a set of functions ϕ_i that satisfy eq. (10), a field u can be interpolated as follows

$$u(\mathbf{x}) = \sum_{i=1}^n \phi_i(\mathbf{x}) (a_i + \sum_{j=1}^m \psi_j(\mathbf{x}) b_{ij}) \quad (11)$$

In eq. (11) a_i are the 'regular' nodal degrees-of-freedom, $\psi_j(\mathbf{x})$ are enhanced basis terms, and b_{ij} are the additional degrees-of-freedom at node i which represent the amplitude of the j th enhanced basis term $\psi_j(\mathbf{x})$.

A piecewise smooth displacement field \mathbf{u} which incorporates a discontinuity with a unit normal vector \mathbf{n} pointing in an arbitrary, but fixed direction can be described by:

$$\mathbf{u}(\mathbf{x}) = \bar{\mathbf{u}}(\mathbf{x}) + H_{\Gamma_d}(\mathbf{x}) \tilde{\mathbf{u}}(\mathbf{x}) \quad (12)$$

with $\bar{\mathbf{u}}$ the standard, continuous displacement field on which the discontinuity has been superimposed. The discontinuous field is represented by the smooth field $\bar{\mathbf{u}}$ and the Heaviside function H_{Γ_d} , centered at the discontinuity plane Γ_d . The displacement decomposition in eq. (12) has a structure similar to the interpolation of eq. (11). Accordingly, the Partition-of-Unity concept can be used in a straightforward fashion to incorporate discontinuities, and thus, cohesive-zone models in a manner that preserves the truly discontinuous character. Indeed, in conventional finite element notation, the displacement field of an element that contains a single discontinuity can be represented as:

$$\mathbf{u} = \bar{\mathbf{u}} + H_{\Gamma_d} \bar{\mathbf{u}} = \mathbf{N}\mathbf{a} + H_{\Gamma_d} \mathbf{N}\mathbf{b} = \mathbf{N}(\mathbf{a} + H_{\Gamma_d} \mathbf{b}) \quad (13)$$

where \mathbf{N} contains the standard shape functions, and \mathbf{a} and \mathbf{b} collect the conventional and the additional nodal degrees-of-freedom, respectively. Using a standard weak formulation, the governing finite element equations can be derived in a standard manner [15]. It is emphasised that in this concept, the additional degrees-of-freedom cannot be condensed at element level, because, at variance with the 'embedded' displacement discontinuity approach, it is node-oriented and not element-oriented. It is this property which makes it possible to represent a discontinuity in a rigorous manner.

The above approach enables the gradual and consistent transition from a continuum to a discontinuum description. While in [15] cohesive zones have been inserted in 'elastic' finite elements, the same numerical methodology has been utilised in [16] to insert tractionless discontinuities in a softening, viscoplastic medium. Accordingly, the viscous property of the continuum has been used to ensure a mesh-independent analysis prior to local failure. Then, i.e., when the local stress-carrying capacity has been exhausted, a traction-free discontinuity has been inserted using the above concept.

4. IMPROVED SPATIAL RESOLUTION

Apart from viscosity, nonlocal continuum models, either in an integral or in a gradient format, can be used to regularise continuum models that incorporate degradation of the strength properties. Among them, gradient-enhanced damage models [17] are conceptually simple and the most efficient from a computational point of view. However, when strain gradients are considered that are higher than the order two, C^1 -continuity is inevitably required. Here, it seems that meshless methods, which typically incorporate very smooth approximation functions, offer a clear advantage. In [18] the behaviour of one such method, namely the element-free Galerkin method has been applied to second and fourth-order gradient damage models.

In the element-free Galerkin method, approximants u are constructed as

$$u = \mathbf{p}^T(\mathbf{x}) \mathbf{a}(\mathbf{x}) \quad (14)$$

with \mathbf{p} a vector that contains monomials and \mathbf{a} a coefficient vector. The approximants are found by minimising the moving weighted least squares sum with respect to \mathbf{a} :

$$J = \sum_{i=1}^n w_i(\mathbf{x}) (\mathbf{p}^T(\mathbf{x}_i) \mathbf{a}(\mathbf{x}) - u_i) \quad (15)$$

with $p(\mathbf{x}_i)$ the value of p in node i , w_i the weight function attached to this node and u_i the nodal displacement. The weight functions should be smooth and should contain a certain minimum number of other nodes within its domain of influence.

To investigate the properties of the element-free Galerkin method when applied to a localisation analysis, the implicit gradient-enhanced continuum model of Peerlings *et al.* [17] has been adopted with the modification that the local equivalent strain $\tilde{\epsilon}$ has been coupled to the nonlocal equivalent strain $\bar{\epsilon}$ via a fourth-order averaging equation

$$\bar{\epsilon} - g_1 \nabla^2 \bar{\epsilon} - g_2 \nabla^4 \bar{\epsilon} = \tilde{\epsilon} \quad (16)$$

with g_1, g_2 the gradient coefficients. For $g_2 = 0$ the second-order gradient damage model of Peerlings *et al.* [17] is retrieved. A three-point bending beam has been analysed and it appeared that the results for both formulations are virtually identical [18].

The higher-order continuity that is incorporated in meshless methods makes them well suited for localisation analyses using higher-order continuum models. Moreover, the flexibility is also increased compared to conventional finite element methods, since there is no direct connectivity, which makes placing nodes in regions with high strain gradients particularly simple. This can also be achieved by finite element methods with spatial adaptivity [19,20].

5. STOCHASTICALLY DISTRIBUTED IMPERFECTIONS

So far, the discussion has concentrated on localisation and the ensuing failure in solids which have uniform strength and stiffness properties. In reality, strength and stiffness have a random distribution over any structure. The distribution and the size of imperfections may have a profound influence on the localisation pattern and, therefore, on the ultimate failure load, as was demonstrated more than half a century ago by Koiter in his landmark dissertation [21] on the influence of imperfections in *elastic* solids. We may expect that this observation holds a fortiori if material degradation plays a role.

Thus, for realistic analyses of localisation and failure, material parameters like Young's modulus, the tensile strength and the fracture energy should be considered as random fields, and the most probable realisation(s) should be sought which lead to failure or violate a certain serviceability criterion. Indeed, in such analyses, not only the scatter in material parameters, but also the uncertainty in the boundary conditions should be considered. The simplest, but also the most expensive method, would be to start a nonlinear analysis from different random distributions and to obtain the statistics of the response by carrying out a sufficient number of such Monte-Carlo simulations [22]. Evidently, this is very expensive and a more versatile approach is to utilise the finite element reliability method [23].

In the latter approach, the statistics of a certain measure for failure or loss of serviceability, say Q , are approximated as follows. First, the material parameters (or the boundary conditions) which are assumed to have a random distribution, are discretised and are assembled in a vector \mathbf{V} which is characterised by a joint probability density function f_v . Although the discretisation that is used to form \mathbf{V} can be different from the finite element discretisation that is used later, it simplifies the implementation if the random cells coincide with finite elements or patches of finite elements. To facilitate further computations, the vector \mathbf{V} of random variables is usually converted into a vector \mathbf{Y} which consists of

uncorrelated variables with a standard normal distribution. A crucial step is then the (nonlinear) mechanical transformation, which, given a random distribution of the material parameters and/or boundary conditions, computes a random response, assembled in \mathbf{Q} . If q_0 denotes the threshold value of the measure Q that is used to assess failure or serviceability, the realisation \mathbf{v} of \mathbf{V} is sought which furnishes a local maximum of its own probability density through a suitable optimisation algorithm. A weakness of the approach is that it generates a *local* maximum, which implies that to obtain a good global estimate of the likelihood of failure or loss of serviceability the algorithm must be started from different initial conditions.

As an example we take a double-edge notched specimen. For detailed information regarding the parameters that have been used and the way in which the analysis has been carried out, the reader is referred to [23]. Tensile tests on such specimens tend to be sensitive to the boundary conditions, in particular when the brittleness of the material increases. When an imperfection is not imposed in the material, nor an asymmetry in the boundary conditions, the deformations will remain symmetric throughout the entire loading path. However, if either of these occurs, asymmetric crack propagation evolves from one of the notches at a generic stage in the loading process. The probability that either of these failure modes occurs can be simulated via the approach discussed above where the tensile strength is randomised, while starting from a symmetric as well as from an asymmetric realisation. In particular, the influence of the boundary conditions can be quantified. For instance, taking the upper loading platen fixed of the double-notched specimen, the probability of failure was found to be $P_s = 5.84 \times 10^{-2}$, irrespective whether the algorithm was started from a symmetric or from an asymmetric realisation. Indeed, the failure mode was purely symmetric. However, when the upper loading platen is allowed to rotate freely, an asymmetric mode was found with a probability of failure that is significantly higher than that of the symmetric model, namely $P_a = 0.41$. Again, this result was obtained irrespective of the starting realisation, which, for the symmetric realisation, is probably attributable to numerical round-off errors. Next, the analysis was repeated for a longer specimen ($L = 250$ mm), while keeping the loading platens fixed. Not surprisingly, a symmetric failure mode was found with a probability of failure P_s which is almost the same as for the shorter specimen. However, an asymmetric failure mode now also emerged, with a probability of failure $P_a = 0.13$, which is purely a consequence of the increased rotational freedom of the longer specimen.

It is emphasised that the inclusion of randomness of the material parameters in the analysis does not resolve the issue of loss of ellipticity at the onset of localisation when standard, rate-independent continuum models are considered. Indeed, the above simulations were carried out using the implicit second-gradient continuum damage model of Peerlings *et al.* [17].

6. REFERENCES

- [1] Babuska, I. and Melenk, J.M., The partition of unity method, *Int. J. Num. Meth. Eng.*, 40, 727-758 (1997).
- [2] Belytschko, T., Lu, Y.Y. and Gu, L., Element-free Galerkin methods, *Int. J. Num. Meth. Eng.* 37, 229-256 (1994).
- [3] Dugdale, D.S., Yielding of steel sheets containing slits, *J. Mech. Phys. Solids* 8, 100-108 (1960).

-
- [4] Barenblatt, G.I., The mathematical theory of equilibrium cracks in brittle fracture, *Adv. Appl. Mech.* 7, 55-129 (1962).
 - [5] Hillerborg, A., Modeer, M. and Petersson, P.E., Analysis of crack formation and crack growth in concrete by means of fracture mechanics and finite elements, *Cement Concrete Res.* 6, 773-782 (1976).
 - [6] Bazant, Z.P. and Oh, B., Crack band theory for fracture of concrete, *RILEM Mat. Struct.* 16, 155-177 (1983).
 - [7] Feenstra, P.H. and de Borst, R., A plasticity model for mode-I cracking in concrete, *Int. J. Num. Meth. Eng.* 28, 2509-2529 (1995).
 - [8] Simo, J.C., Oliver, J. and Armero, F., An analysis of strong discontinuities induced by softening relations in rate-independent solids, *Comp. Mech.* 12, 277-296 (1993).
 - [9] Larsson, R., Runesson, K. and Ottosen, N.S., Discontinuous displacement approximation for capturing plastic localization, *Int. J. Num. Meth. Eng.* 36, 2087-2105 (1993).
 - [10] Lotfi, H.R. and Shing, P.B., Embedded representation of fracture in concrete with mixed elements, *Int. J. Num. Meth. Eng.* 38, 1307-1325 (1995).
 - [11] Ortiz, M., Leroy, Y. and Needleman, A., A finite element method for localized failure analysis, *Comp. Meth. Appl. Mech. Eng.* 61, 189-214 (1987).
 - [12] Belytschko, T., Fish, J. and Engelman, B.E., A finite element with embedded localization zones, *Comp. Meth. Appl. Mech. Eng.* 70, 59-89 (1988).
 - [13] Sluys, L.J. and Berends, A.H., Discontinuous failure analysis for mode-I and mode-II localization problems, *Int. J. Solids Struct.* 35, 4257-4274 (1998).
 - [14] de Borst, R., Wells, G.N. and Sluys, L.J., Some observations on embedded discontinuity models, *Eng. Comput.* in press.
 - [15] Wells, G.N. and Sluys, L.J., A new method for modeling cohesive cracks using finite elements, *Int. J. Num. Meth. Eng.* 50, 2667-2682 (2001).
 - [16] Wells, G.N., Sluys, L.J. and de Borst, R., Simulating the propagation of displacement discontinuities in a regularised strain-softening medium, *Int. J. Num. Meth. Eng.*, submitted for publication.
 - [17] Peerlings, R.H.J., de Borst, R., Brekelmans, W.A.M. and de Vree, H.P.J., Gradient-enhanced damage for quasi-brittle materials, *Int. J. Num. Meth. Eng.*, 39, 3391-3403 (1996).
 - [18] Askes, H., Pamin, J. and de Borst, R., Dispersion analysis and element-free Galerkin solutions of second-and fourth-order gradient-enhanced damage models, *Int. J. Num. Meth. Eng.* 49, 811-832 (2000).
 - [19] Askes, H. and Sluys, L.J., Remeshing strategies for adaptive ALE analysis of strain localisation, *Eur. J. Mechanics: A/Solids* 19, 447-467 (2000).
 - [20] Lackner, R. and Mang, H.A., Adaptivity in computational mechanics of concrete structures, *Int. J. Num. Anal. Meth. Geomech.*, in press.
 - [21] Koiter, W.T., *Over de Stabiliteit van het Elastisch Evenwicht*. Dissertation, Delft University of Technology, Delft (1945).
 - [22] Carmeliet, J. and de Borst, R., Stochastic approaches for damage evolution in standard and non-standard continua, *Int. J. Solids Struct.* 32, 1149-1160 (1995).
 - [23] Gutiérrez and de Borst, R., Stochastic aspects of localised failure: material and boundary imperfections, *Int. J. Solids Struct.* 37, 7145-7159 (2000).

EXPERIMENTAL STUDIES OF PLASTIC INSTABILITIES IN SOLID SOLUTIONS

H. Neuhäuser, F. Klose, H. Dierke, A. Ziegenbein¹, A. Nortmann²

Institute of Metal Physics and Nuclear Solid State Physics, Technical University of
Braunschweig, D-38106 Braunschweig, Germany

¹ now with: Volkswagenwerk, Wolfsburg, Germany

² now with: Goodyear, Luxembourg

1. SUMMARY

After a brief review of the classification of plastic instabilities, experimental results on two particular types are considered, (i) Lüders band propagation and (ii) Portevin-LeChatelier (PLC) effect, mainly with the example of Cu-15at%Al based solid solution. Observations of band propagation and slip line formation are compared for single and polycrystals on mesoscale and combined with macroscopic measurements of stress and of average as well as local strain employing a laser scanning technique. In particular the propagation rates of the different deformation bands is considered and discussed in terms of the controlling mechanisms.

2. INTRODUCTION

Instabilities during plastic deformation manifest themselves by rapid and localized shear events which produce deformation rates exceeding the imposed one. According to Estrin & Kubin [1] two important types of plastic instabilities can be classified into strain softening and strain rate softening instabilities depending on the underlying physical mechanisms.

In the *strain softening instabilities*, local softening of the obstacle structure by dislocations cutting through obstacles (e.g. [2]) exceeds work hardening produced by dislocation interaction in the heavily deformed small volume of the specimen. The unstable process is exhausting with increase of work hardening [3].

In the *strain rate softening instabilities*, a mechanism (like dynamic strain ageing, DSA, e.g. [4 –8]) occurs, which strengthens the original obstacles during the waiting time of dislocations and produces additional obstacles, such that with higher strain rate $\dot{\epsilon}$, i.e. shorter waiting times t_w , the additional obstacle strength or/and number decreases. This may occur by diffusive motion of solutes in the dislocation core region (formation of “Cottrell clouds” [4] around dislocations), or by pseudo-DSA effects as considered in [9]. The criteria for such plastic instabilities to occur have recently been reconsidered and cleared up by Hähner & Zaiser [10,11]. Their analysis shows clearly that only the combined action of both DSA and intensive dislocation interactions (correlations) can produce this type of instabilities.

However, these considerations do not explain and describe the often observed propagation of plastic fronts during both types of instabilities, Lüders bands (LB) in the strain softening, and

Portevin-LeChatelier (PLC) bands in the strain rate softening case. This requires the additional introduction of some length scale or an explicit propagation mechanism in order to specify the propagation rate. Early attempts in this direction were made by Aifantis [12,13] who formally introduced a second order stress gradient (cf. [14]). Recently Hähner [15] succeeded to show in a physically based DSA model by comparing estimates for different possible propagation mechanisms, that the interaction of dislocations on neighbouring slip planes itself provides an appropriate length scale and a second order stress gradient leading to the propagating modes of deformation bands of type A (continuously moving), type B (jerkily moving) and type C (non-propagating, randomly nucleating) [15], as have been observed during PLC effect in various alloys [16,17].

In the following, we review experimental studies on the development of local strain during instability events of both before-mentioned types of instabilities and on the propagation of the accompanying plastic fronts, i.e. LB (strain softening) and PLC bands (strain rate softening). For both cases we will compare experiments performed with single crystals and with polycrystals, where modifications of the propagation mechanisms are expected.

3. EXPERIMENTAL DETAILS

Cu-15at%Al was selected as a model solid solution which exhibits strong slip localization due to its tendency to short-range ordering [18] and enhanced by its low stacking-fault energy [19]. The single crystals are oriented for single glide to provide extended Lüders slip in the easy glide region; the polycrystals were annealed to produce grain sizes in the range of 50 to 500 μm [17]. Various specimen geometries were compared, including cylindrical shape (\varnothing 4 mm, length \approx 80 mm) and flat shape (thickness 0.2 to 2 mm, length 30 to 75 mm). Tensile deformation was performed in vacuum at elevated temperatures (300 to 930K) either at constant strain rates (in the range of 6.67×10^{-6} to $1.33 \times 10^{-3} \text{ s}^{-1}$), at constant stresses (creep test [20]), and at constant stress rates (10^{-3} to 10^2 MPa/s). Examples for the strain and stress controlled tests in Fig.1 show the stress drops in the first and the strain jumps in the second case.

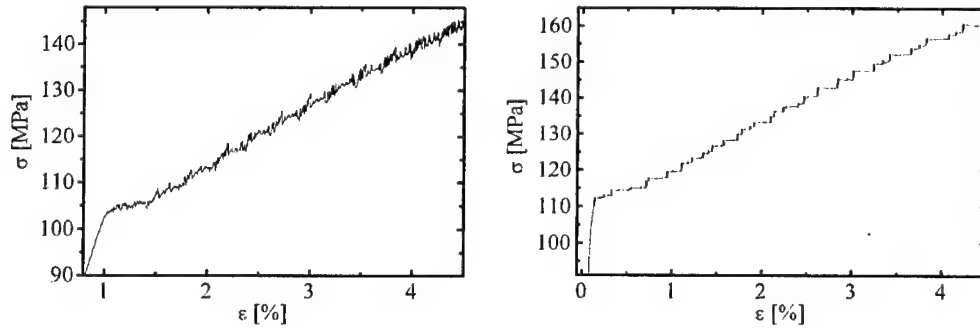


Figure 1: Examples for tensile tests on Cu-15at%Al polycrystals at 373 K (a) at constant strain rate $\dot{\epsilon} = 6.67 \times 10^{-6} \text{ s}^{-1}$, and (b) at constant stress rate $\dot{\sigma} = 5 \cdot 10^{-3} \text{ MPa/s}$.

Simultaneously to sensitive measurement and recording of load (stress) the local strains were measured in 20 neighbouring zones of 1 mm width along the center part of flat specimens by

means of a laser scanning extensometer [17]. In some other tests the local deformation was observed through an optical microscope and recorded by video following the development of slip bands in several neighbouring grains [21].

4. LÜDERS BAND PROPAGATION

At the onset of deformation of a virgin crystal and of an annealed polycrystal in most cases a narrow region of strain concentration develops (mostly near one of the grips) with an extension in the order of the smallest specimen dimension. This Lüders band propagates, at nearly constant external load, across the specimen length [22, 23]. If the specimen length has not yet been filled with sheared volumes (slip band clusters), another LB propagates at a slightly elevated stress until the whole volume has been fully covered by slip. Then the stress rises steeply entering the hardening region.

4.1. Single crystals

The formation of single slip bands and slip band clusters in Cu-15at%Al single crystals during propagation of the LB has been described in some detail [22-24], in particular the role of the bending moment, constriction of specimen diameter and of the stress fields of dislocation groups near crystal surface, which turns out to be the place of first source activation [25]. Because of the low probability for cross-slip in the Cu-15at%Al alloy of low stacking-fault energy, the mechanism for slip propagation in this case is provided by the long-range stresses of dislocation groups in the previously formed slip bands at the LB front.

The resulting stress concentration causes the very first part of each slip band to develop in an unstable manner because of a strain softening mechanism [24,26,27]: The first few dislocations of a freshly produced dislocation group destroy the short-range ordered obstacles so that the following dislocations of the group feel less resistance and push the former to very high speeds even at reduced stress (cf. [28,29]). The propagation rate for a LB in single crystals roughly obeys the relation $v_{LB} = (l_o \dot{\epsilon}) / \epsilon_F$ [23] where l_o is the specimen length and ϵ_F is the strain reached when the LB has traversed the specimen (about 20 % for Cu-15at%Al single crystals) which corresponds to the strain ϵ_{LB} carried by the LB.

4.2. Polycrystals

In polycrystals of Cu-15at%Al the slip bands are observed to develop in similar formation times [21] and in large grains ($> 500 \mu\text{m}$) proceed in a quite similar manner as in single crystals propagating in a deformation front. However, for compatibility reasons the complex stress pattern soon activates different slip systems in different parts of the grain and with increasing strain two or three slip band families nucleate in general in the grains [21]. No macroscopic LB as in 3.1. develops in polycrystals if the grain size exceeds about $100 \mu\text{m}$ [21,30]. For smaller grain sizes, however, LB deformation is observed over a small range of strain after the onset of plastic flow (cf. Fig.1 a). The effect of temperature at a fixed strain rate on the strains concentrated in LB (at low macroscopic strain) and in PLC bands (at higher macroscopic strain, see sect.4) is shown in Fig. 2 a), b) [17]. The LB strain $\epsilon_{LB} \approx \epsilon_F$ in the polycrystals is much less than that in single crystals and decreases rapidly with deformation from values of about 0.7 to 0.1 % at the onset of PLC (these ϵ values are referred to the total specimen length l_o). Accordingly the propagation rate $v_{LB} = l_o \dot{\epsilon} / \epsilon_{LB}$ is much higher in poly- than in single crystals. The mechanism of LB propagation most probably involves the incompatibility stresses between grains and the stress concentration due to the constriction of the specimen cross section by local plastic shear, as has been discussed in

detail by Hähner [31]. Miyazaki et al. [32] have shown that owing to the restriction of slip to few slip systems (because of slip localization in Cu-Al) the plastic relaxation for compatibility affects neighbouring grains up to an increasing order the smaller the grain size is. This explains the tendency to a propagating band for small but lacking propagation for large grains. We note that even in the latter case another LB propagation seems to occur at elevated temperatures and at high effective stresses immediately after leaving the PLC region at the onset of the viscous glide regime.

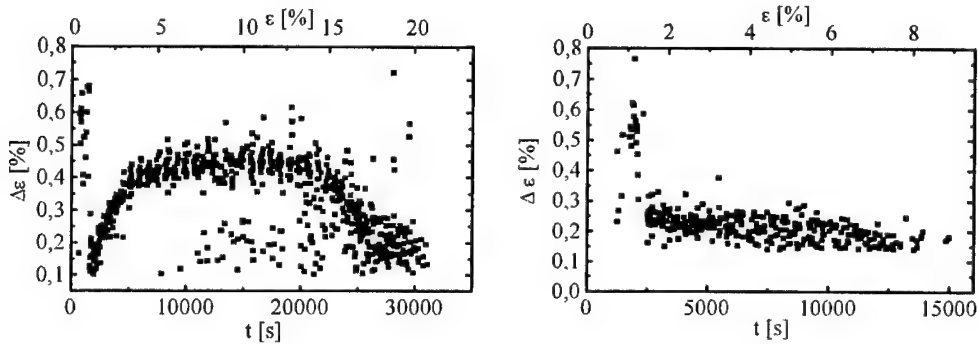


Figure 2: Local strains (referred to the total specimen length l_0) in LB and PLC bands measured by laser scanning extensometry during deformation of Cu-15at%Al polycrystals at $\dot{\epsilon} = 6.67 \times 10^{-6} \text{ s}^{-1}$, a) $T = 323$ K, b) $T = 383$ K.

5. PLC BAND PROPAGATION

If deformation temperature and solute concentration are high enough, no critical strain (cf. [16,17,33]) is necessary for the PLC effect to occur. It starts right from the onset of plasticity. For this condition the behaviour of single and polycrystals is compared in the following.

For Cu-15at%Al single crystals the transition from smooth to jerky glide with increasing temperature is gradual starting around 430 K with irregular slight fluctuations [34] until nearly periodic serrated flow occurs for $500 < T < 700$ K in the yield region. On the other hand, the transition from jerky to viscous glide at elevated temperature, when volume diffusion is rapid enough to prevent dislocation breakaway from their solutes [4], is very abrupt as well in single as in polycrystals [33,34,20] in this first stage of deformation.

For the Cu-15at% polycrystals serrations first start with type A at 330 K with zero critical strain. The existence of various types of PLC bands along the stress-strain curve and their transitions to viscous glide for various temperatures has been described earlier [33,17,20]; here the propagation behaviour will be discussed.

5.1 Single crystals

The rapid development of slip band clusters after breakaway of a first source dislocation from its cloud has been recorded by video microcinematography [34] in stage I of crystals oriented for single glide. The PLC band propagates in an intermittent fashion, with the next jump starting where it stopped previously, i.e. where DSA of dislocations is minimum [36,35]. The

propagation mechanism is supposed to involve, similar as in sect.3.1, the long-range stresses of dislocation groups in neighbouring active slip bands, here modified by DSA effects (cf. "precursors" as described in [36]). The strain concentrated in the PLC band on Cu-15at%Al at $T = 673$ K, for example, is $\varepsilon_{PLC} = 0.02$ %, referred again to the total specimen length l_0 as in 4.2. The jump (short time) propagation rate for this example reaches values of the order 0.1 to 1 mm/s, at an external strain rate of $\dot{\varepsilon} = 1.8 \times 10^{-5} \text{ s}^{-1}$ [34], while the mean propagation rate (averaged over repeated jumps) is about 0.02 mm/s.

5.2 Polycrystals

Polycrystals of Cu-Al (and Cu-Mn), which show a rather rich PLC behaviour for various strains (stresses) and temperatures, have been thoroughly studied by Schwink and coworkers [33, 6] with respect to DSA indicating various types of pipe diffusion. The various types of PLC deformation bands (type A continuous propagation, type B intermittent propagation, type C no propagation) have been identified unambiguously by means of laser scanning extensometry [17,15,30], which permits to establish "correlation diagrams" of time and location of local strain jumps, as shown for the examples in Fig. 3 a, b. Characteristics like strain concentration in the PLC band (Fig. 2 a,b), width of the bands, and their propagation rates (in case of A, averages in case of B) have been determined [17,15,30]. For example, the propagation rate of PLC bands of type A in a polycrystal is $v_{PLC}^A = 15$ mm/s at the *maximum* applied strain rate of $\dot{\varepsilon} = 1.3 \times 10^{-3} \text{ s}^{-1}$, at $T = 373$ K and in the plateau range of $\Delta\varepsilon$ (cf. Fig.2). For type B a typical average rate is $v_{PLC}^B = 0.1$ mm/s at the *minimum* external strain rate of $\dot{\varepsilon} = 6.67 \times 10^{-6} \text{ s}^{-1}$, at $T = 573$ K and at a low strain of $\varepsilon \approx 3$ %. The lacking dependence of the propagation rate on grain size in the studied regime of 50 to 500 μm suggests as the relevant length scale for propagation again the local interaction distance between neighbouring active slip bands (rather than cross-slip, incompatibility stresses, bending moment, or constriction of sample cross section) [15]. The width of the PLC bands appears to scale with the smallest specimen dimension [17,15] as expected from the nucleation and intensive correlation of dislocation groups.

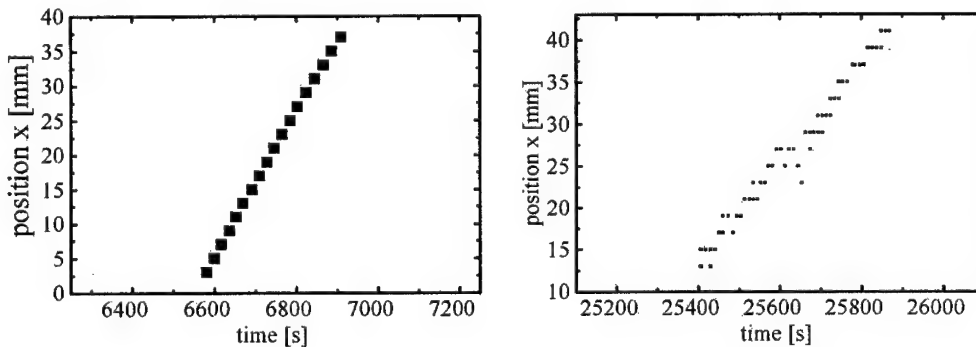


Figure 3: Correlation diagrams for time and location of local strain jumps during PLC deformation of types a) A (continuous propagation, $T = 323$ K, $\sigma \approx 155$ MPa), b) B (jerky propagation, $T = 473$ K, $\sigma \approx 210$ MPa). Cu-15at%Al, $\dot{\varepsilon} = 6.67 \times 10^{-6} \text{ s}^{-1}$.

Finally we note a few first results of experiments with imposed *constant stress rate* (cf. Fig. 1 b) on Cu-15at%Al polycrystals [37]. They show that the type A bands propagate at the lowest applied stress rate of $\dot{\sigma} = 5 \times 10^{-3}$ MPa/s with a similar velocity as in the strain rate controlled tests at the highest applied strain rate (see above). On the other hand, the type B behaviour disappears and the band runs continuously with higher rate than for type A (its rate corresponds to the propagation within each jump of type B). Similarly, in the type C region of strain controlled tests, in stress control single bands again propagate, now with an even higher rate than in the type B region. These observations indicate that the complex behaviour in strain-controlled tests results from the interaction of local high rate plasticity with the elastic machine producing stress drops which stop the propagating bands of types B and C. No differentiation seems to be necessary with respect to the basic DSA and dislocation interaction mechanisms.

Acknowledgements: The financial support of this work by the Deutsche Forschungsgemeinschaft and by the European Community in a TMR network is gratefully acknowledged. For numerous helpful discussions we thank Prof. Ch. Schwink and Priv.-Doz. Dr. P. Hähner.

6. REFERENCES

- [1] Y. Estrin, L.P. Kubin, Res Mechan. 23 (1998) 197-221.
- [2] A. Luft, Progr.Mater.Sci. 35 (1991) 91-204.
- [3] Y. Brechet, G. Canova, L.P. Kubin, Acta Metall.Mater. 44 (1996) 4261-4271.
- [4] A.H. Cottrell, Phil.Mag. 44 (1953) 829-832.
- [5] A. van den Beukel, U.F. Kocks, Acta Metall. 30 (1982) 1027-1034.
- [6] P.G. McCormick, C.P. Ling, Acta Metall. Mater. 43 (1995) 1969-1977.
- [7] F. Springer, A. Nortmann, Ch. Schwink, phys.stat.sol.(a) (1998) 63-81.
- [8] F. Balik, P. Lukac, Acta Metall.Mater. 41 (1993) 1447-1454.
- [9] Y. Brechet, Y. Estrin, Acta Metall.Mater. 43 (1995) 955-963.
- [10] P. Hähner, Acta Metall. Mater. 45 (1997) 3695-3707.
- [11] M. Zaiser, P. Hähner, phys.stat.sol.(b) 199 (1997) 267-330.
- [12] E.C. Aifantis, J.Mat.Eng.Techn. 106 (1984) 326-330; Int.J.Plast. 3 (1987) 211-247; Int.J.Eng.Sci.30 (1992) 1279-1299.
- [13] H.M. Zbib, E.C. Aifantis, Scripta Metall.Mater. 22 (1988) 1331-1336; Res.Mechan. 23 (1988) 293-305.
- [14] L.P. Kubin, in: Plasticity of Metals and Alloys (ed. P. Lukac), Key Engin.Mater. 97/98 (1995) 219-234.
- [15] P. Hähner, A. Ziegenbein, H. Neuhäuser, to be publ.; Phil.Mag.A (in press).
- [16] P.G. McCormick, Trans.Indian Inst.Metals 39 (1986) 98-106.
- [17] A. Ziegenbein, P. Hähner, H. Neuhäuser, Comput.Mater.Sci. 19 (2000) 27-34.
- [18] J. Plessing, Ch. Achmus, H. Neuhäuser, B. Schönfeld, G. Kostorz, Z.Metallk. 88 (1997) 630-635.
- [19] S.I. Hong, C. Laird, Acta Metall.Mater. 38 (1990) 1581-1595.
- [20] A. Nortmann, H. Neuhäuser, phys.stat.sol.(a) 168 (1998) 87-107.
- [21] M. Kügler, A. Hampel, H. Neuhäuser, phys.stat.ol.(a) 175 (1999) 513-526.
- [22] H. Neuhäuser, A. Hampel, Scripta Metall.Mater. 29 (1993) 1151-1157.
- [23] A. Ziegenbein, J. Plessing, H. Neuhäuser, Phys.Mesomech. 2 (1998) 5-18.
- [24] A. Hampel, Th. Kammler, H. Neuhäuser, phys.stat.so.(a) 135 (1993) 405-416.
- [25] J.W. Mitchell, phys.stat.sol.(a) 135 (1993) 455-466.
- [26] H. Godon, H.-H. Potthoff, H. Neuhäuser, Cryst.Res.Technol. 19 (1984) 373-385.

- [27] U. Hoffmann, A. Hampel, H. Neuhäuser, J. Microscopy (in press)
- [28] J. Olfe, H. Neuhäuser, phys.stat.sol.(a) 109 (1988) 149-160.
- [29] N. Clement, D. Caillard, J.-L. Martin, Acta Metall. 32 (1984) 961-975.
- [30] A. Ziegenbein, Dissertation, Techn. University of Braunschweig 2000, Cuvillier-Vlg. Göttingen ISBN 3-89712-917-5
- [31] P. Hähner, Appl. Phys. A 58 (1994) 41-48, 49-58.
- [31] S. Miyasaki, K. Shibata, H. Fujita, Acta Metall. 27 (1979) 855-862.
- [32] A. Nortmann, Ch. Schwink, Acta Metall. Mater. 45 (1997) 2043-2050, 2051-2058.
- [33] C. Engelke, J. Plessing, H. Neuhäuser, Mater. Sci. Eng. (A) 164 (1993) 235-239.
- [34] H. Neuhäuser, J. Plessing, M. Schülke, J. Mech. Behav. Mater. 2 (1990) 231-254.
- [35] R.B. Schwarz, in: Proc. ICSMA 7 (ed. H.J. McQueen), Vol. 1, Pergamon, Toronto 1985, p. 343-348.
- [36] H. Neuhäuser, Int. J. Plasticity 9 (1993) 421-435; Physica Scripta T49 (1993) 231-254.
- [37] F. Klose, P. Hähner, H. Neuhäuser, in preparation.

COMBINED MEASUREMENTS OF ACOUSTIC EMISSION AND LASER EXTENSOMETRY DURING PORTEVIN-LECHATelier DEFORMATION IN AN Al-Mg ALLOY

A. Ziegenbein¹, F. Chmelik², H. Neuhäuser¹

¹Institute of Metal Physics and Nuclear Solid State Physics, Technical University of
Braunschweig, D-38106 Braunschweig, Germany

²Department of Metal Physics, Charles University, Ke Karlovu 5, CZ-12116 Prague 2,
Czech Republic

1. SUMMARY

In addition to sensitive recording of load serrations during the Portevin-LeChatelier effect in tensile deformation of Al-1.5wt%Mg polycrystals at room temperature (strain rates 2.67×10^{-6} to $1.33 \times 10^{-4} \text{ s}^{-1}$), acoustic emission (AE) signals and local strains in 20 neighbouring zones of 2 mm width along the specimen length measured by a special laser scanning extensometry are recorded simultaneously. Strong AE bursts can be differentiated from the total AE signal, both showing characteristic dependencies along the stress-strain curve. By correlated evaluation of the measured quantities, the AE signals can be assigned to local deformation events of different kinds. AE events of long duration in the first stage of deformation are connected with a Lüders band propagating continuously along the gauge length, while short bursts of strong AE activity occur during nucleation of a PLC band. A strongly fluctuating AE rate connected with discontinuous propagation of type B Portevin-LeChatelier bands is superposed on the total activity decreasing with increasing strain due to the decrease of dislocation path length. The observations are discussed in terms of a superposition of both dislocation source activation events and collective breakaway with intensive dislocation multiplication.

2. INTRODUCTION

The Portevin-LeChatelier (PLC) effect, i.e. serrated flow in many solid solutions occurring in an appropriate regime of solute concentration, deformation temperature and strain rate, is one of the most prominent examples of plastic instabilities (cf. reviews [1, 2]). Recent theoretical research [3] has clarified that the dynamic strain ageing, i.e. solute mobility in the dislocation core region [4-6] resulting in a negative strain rate sensitivity, has to be combined with intensive dislocation interaction [7,8] in order to produce these plastic instabilities. They manifest themselves in repeated rapid load drops [1,2,4] during continuous external straining, which are due to the rapid nucleation and multiplication of shear bands [9] producing local strain rates which exceed the externally imposed one. These rapid plastic events are accompanied by acoustic emission (AE) (e.g. [10-13]) which in a variety of dislocation models has been correlated with nucleation and evolution of dislocation avalanches (e.g. [14-16]). Recently, by application of a multizone laser extensometric technique, the local strain

and its propagation in PLC deformation bands has been investigated for Cu-Al alloys [17, 18], permitting a clear distinction and evaluation of type A, B and C band propagation behaviour (cf. [2]).

In the following work, this technique has been combined with simultaneous recording of AE during straining to correlate the different types of AE (burst vs. continuum AE) with the modes of localized deformation (nucleation vs. propagation of deformation bands).

3. EXPERIMENTAL DETAILS

From a commercial Al-1.5at%Mg alloy (made by Alu Ranshofen, Austria) sheet tensile specimens (length 75 mm, width 4 mm, thickness 1.5 mm) were machined, annealed for 1 h at 400 °C (grain size about 100 μm) and quenched into water. Tensile deformation was performed at room temperature and with constant strain rates in the range of $\dot{\epsilon} = 2.67 \times 10^{-6}$ to $1.33 \times 10^{-4} \text{ s}^{-1}$. The load was recorded with high resolution ($\pm 0.01 \text{ N}$) and a data rate of 5 s^{-1} . The local strains in 20 neighbouring zones of 2 mm width along the sample length (produced by black and white varnishes) were detected and recorded by a special multizone laser scanning extensometer (Fa. Fiedler Optoelectronic, Lützen, Germany) which permits strain resolution of 0.05% in each zone and data rates up to 200 s^{-1} . From the variation of the local strains with time of these 20 zones, correlation diagrams of time and location of plastic bursts were constructed [17]. From these correlation diagrams, the propagation behaviour can be determined, i.e. for type A PLC bands continuous propagation, for type B bands intermittent propagation, and for type C bands no propagation but random nucleation of PLC bands along the sample [17, 18].

Simultaneously, AE has been recorded by a computer controlled AE monitoring system (XEDO-3, DAKEL, Prague), using a miniaturized MST8S transducer attached to the specimen surface. The sampling rate was 4 MHz [19]. Two threshold voltages of 730 and 1450 mV were set to discriminate the *total* AE count N_{c1} and the count rate \dot{N}_{c1} from *burst* AE count N_{c2} and the count rate \dot{N}_{c2} (not shown here as its behaviour turned out to be similar to that of \dot{N}_{c1}). The AE *event* is defined as a continuous AE activity between the start threshold of 1450 mV and the end threshold of 965 mV, until the signals are separated less than the dead time of the system (set to 1 ms), else the event is finished. The AE event duration Δt_{AE} includes also the dead time of the system. The event rate is called \dot{N}_{AE} . It will be shown below that large bursts with very high count rate \dot{N}_{c1} consisting of *short* events correspond to the initiation (nucleation) of a new PLC band(s) while the *short* events with moderate count rate correspond to repeated breakaway events during propagation of type B PLC bands. On the other hand, the nucleation and propagation of a Lüders band in the first stage of deformation is characterised by *long* (quasi-continuous) AE events and a high count rate.

4. EXPERIMENTAL RESULTS AND DISCUSSION

4.1. AE events during LB and PLC band nucleation and propagation: Dislocation source activation

The recorded AE event rate \dot{N}_{AE} varies along the stress strain curve as shown in Fig.1a, with high values at the onset (micro-yield) of plastic deformation (nucleation of a Lüders band LB) and after full propagation of the LB across the specimen (nucleation of first PLC bands).

The propagation of the LB is accompanied by a low rate of events (and by a high total count rate \dot{N}_{c1} , see Fig.3 and sect.3.2 below) during the near zero work hardening part of the stress strain curve. This and the steep rise of AE event activity at the end of LB propagation are also shown by the accumulated events ΣN_{AE} in Fig.1b. Simultaneously, the duration Δt_{AE} of AE events (shown in Fig.2 for averages over the last 10 s of deformation) is short during micro-yield and PLC. On the contrary, the events are long during propagation of the LB which indicates continuum character of AE, i.e. the signals are separated less than the dead time (1 ms) of the system. While in micro-yield deformation starts by activation of few favourably situated single sources which multiply locally and rapidly because of the long available free path lengths of the produced dislocations, propagation of the LB then occurs by quasi-continuous activation of neighbouring sources at the LB front in a region of some stress concentration.

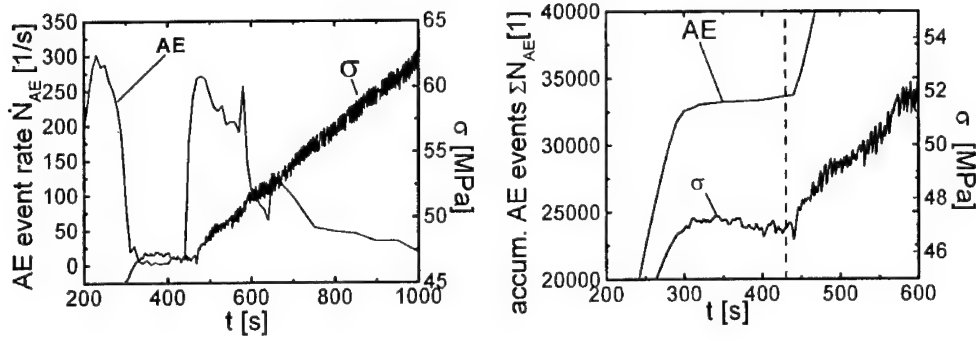


Figure1: a) AE event rate \dot{N}_{AE} , plotted versus deformation time t at constant strain rate $\dot{\epsilon} = 1.33 \times 10^{-5} \text{ s}^{-1}$ and compared with the recorded behaviour of stress σ .
b) Cumulated number of AE events ΣN_{AE} , compared with stress vs. time, conditions as in a).

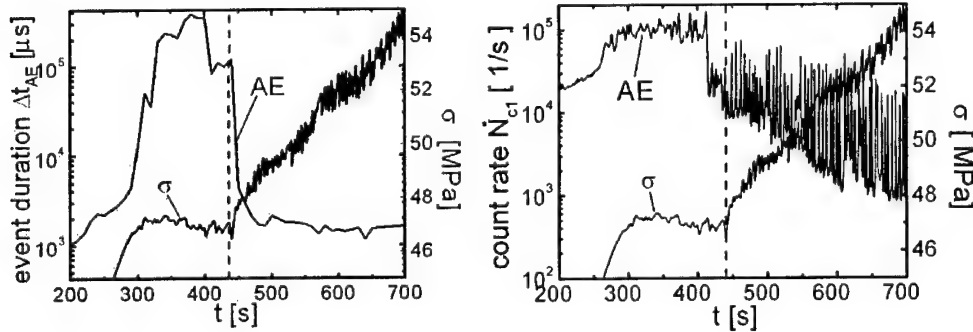


Figure 2: Average duration Δt_{AE} of AE events in correlation with the stress vs. time curve, for $\dot{\epsilon} = 1.33 \times 10^{-5} \text{ s}^{-1}$.

Figure 3: Total AE count rate \dot{N}_{c1} compared with the stress strain curve, for $\dot{\epsilon} = 1.55 \times 10^{-5} \text{ s}^{-1}$.

When the LB has covered the whole specimen length, the dislocation content is large enough to enhance dynamic strain ageing sufficiently (cf. critical strain for other deformation conditions [1, 2]) to start the genuine PLC effect. The initiation of PLC bands of type B is again accompanied by a high rate of short AE events (Fig.2), indicating triggering of big dislocation avalanches by breakaway of the first aged dislocation and rapid multiplication of nearly fresh dislocations under overstress. Nevertheless, the triggering event occurs on a much longer time scale than would be expected by excited shear sound waves: It appears to be caused rather by the stress fields built up by slip activity in the neighbouring region (cf. slip line cinematographic observations [9] and modelling [18]). The events are short (Fig.2) because of rapid local stress relaxation and recapture of the dislocations by diffusing solutes stopping local plasticity. As the path lengths of the activated dislocations are shorter than during LB propagation and still decrease with increasing deformation, the size of the bursts as well as the reloading period after stop of local plasticity decrease with increasing strain. As long as this time exceeds the dead time of the system, we record a high event rate \dot{N}_{AE} and short Δt_{AE} values, however, for larger strains only few large bursts will be resolved (see below), because the high threshold value will no longer be reached by most plastic avalanches.

4.2. AE activity during PLC band initiation and propagation: Collective dislocation breakaway

The AE count rate \dot{N}_{c1} is plotted in Fig.3 for a strain rate of $\dot{\epsilon} = 1.33 \times 10^{-5} \text{ s}^{-1}$ and in Fig.4a for $\dot{\epsilon} = 2.67 \times 10^{-6} \text{ s}^{-1}$ up to a larger total strain. There is a continuous increase of the count rate up to maximum values around the macroscopic yield stress with high values during LB propagation (Figs.3, 4a), then a decrease with increasing smooth deformation up to the critical strain (cf. Figs.4a,b) for the onset of PLC. The latter manifests itself by strong fluctuations of the AE count rate superposed on the further decreasing average total count rate. This overall decrease of \dot{N}_{c1} with strain is explained by the decrease of path length of dislocations after breakaway with increasing work hardening [19]. A stationary low level of

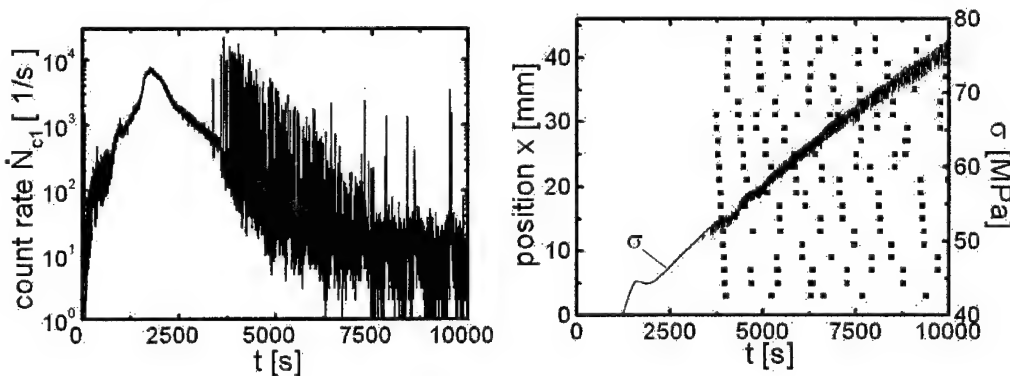


Figure 4: a) Total AE count rate \dot{N}_{c1} recorded during a long deformation experiment at low deformation rate of $\dot{\epsilon} = 2.67 \times 10^{-6} \text{ s}^{-1}$.
b) Space/time correlation of PLC band propagation, together with the stress vs. time curve, for the experiment shown in a) .

the rate \dot{N}_{cl} is reached for $\varepsilon > 8\%$ when with increasing ε (increasing mobile dislocation density) the work hardening rate ϑ is sufficiently low. The jerky type B propagation behaviour is clearly recognised in the space/time correlation diagram of Fig. 4b where each square represents a recorded jump in strain at time t occurring in the zone at location x . The slope of successive events in this plots yields the average band propagation rate which is in the order of 0.1 mm/s. For the effect of strain rate on propagation behaviour and AE see [19].

While the average count rate \bar{N}_{cl} appears to be determined by dislocation source activation and dislocation path length, the rapidly fluctuating superposed count rate is supposed to result from the collective breakaway of mobile dislocations (\dot{N}_{cl}^{PLC}) after pinning by dynamic strain ageing. The single very high peaks of the count rate can be assigned to the nucleation process of a new PLC band as will be shown below. Note that the total \dot{N}_{cl} here is the sum of the average \bar{N}_{cl} and \dot{N}_{cl}^{PLC} , contrary to [10] where only \dot{N}_{cl} was considered, and to [12] where only \dot{N}_{cl}^{PLC} was considered. Thus we suggest both source activation and collective breakaway processes to be important to describe and explain the total AE activity [19].

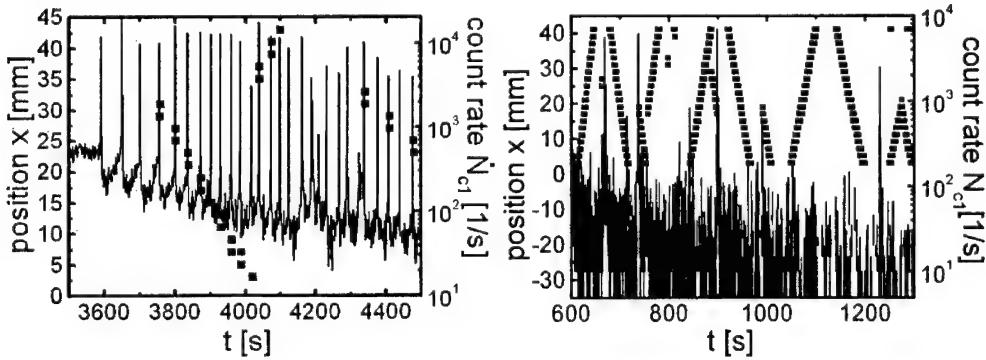


Figure 5: a) Count rate \dot{N}_{cl} and space/time correlation for an interval of low strain, taken at a low strain rate ($\dot{\varepsilon} = 2.67 \times 10^{-6} \text{ s}^{-1}$).
b) as a) for higher strains, taken at a higher strain rate ($\dot{\varepsilon} = 1.33 \times 10^{-4} \text{ s}^{-1}$).

We also note that the stress drop (occurring due to PLC breakaway and causing the AE event) is a consequence of strain localisation and not vice versa. The following plots (Fig.5) on an extended time scale show by direct comparison of the AE and the space/time correlation diagrams that each strong burst of AE count rate corresponds to a strong strain localisation. In Fig.5a (low strain rate, low strain of about 1%) the first 3 count rate peaks at the onset of the PLC effect correspond to jumps of the band occurring outside the specimen region covered by markings for the laser scanning extensometry. In the following peaks 2 simultaneous jumps occur in neighbouring zones, i.e. the width of the PLC band is in the order of 4 mm. Later, around 4030 s, the band propagates into the opposite direction. Preceding each strain jump there is a slightly increasing AE activity (probably connected with events like the precursors observed in [20]). This activity is followed by the catastrophic plastic relaxation event after breakaway of the front dislocation source, rapid multiplication and pushing by the stress fields of the newly produced dislocations to break away further aged mobile

dislocations. For higher strains (of about 13% in Fig.5b at higher strain rate) the total count rate has decreased to the low stationary value due to the short free path lengths of dislocations and smaller avalanches, many of them no longer reaching the AE threshold. Here the observed strong peaks of the AE count rate correspond to the nucleation event of a new PLC band in the most probable position, which is near the specimen head(s) where some stress concentration is present and hardening is lower due to the larger cross section. The following quasi-continuous propagation of the PLC bands between the grips in opposite directions is clearly seen in Fig.5b.

5. CONCLUSIONS

Combining simultaneous measurements of acoustic emission and local strain, the burst acoustic emission could be attributed to the nucleation of new Lüders and Portevin-LeChatelier bands, while a smaller AE count rate occurs during their propagation. The overall decrease of the measured AE count rate with strain along the stress-strain curve has been explained by the decrease of the mean free path lengths of dislocations with increasing strain, while the repeated breakaway processes cause strong fluctuations of AE activity.

Acknowledgements: The authors acknowledge gratefully the financial support by the Deutsche Forschungsgemeinschaft and by the European Commission in a TMR Network. F.C. is particularly grateful to the Alexander-von-Humboldt foundation for a fellowship in Germany and to the Grant Agency of the Czech Republic for the research grant Nr. 103/01/1058. Thanks are also due to P.Hähner for fruitful discussions and to F.Klose for his help with preparing the figures.

6. REFERENCES

- [1] Y. Estrin, L.P. Kubin, in: *Continuum Models for Materials with Microstructure* (Ed. H.B.Mühlhaus), Chapt.12, Wiley, New York 1995, p.395-453.
- [2] P.G. McCormick, *Trans.Indian Inst.Metals* 39 (1986) 98-106.
- [3] P. Hähner, *Acta Metall.Mater.* 45 (1997) 3695-3707.
- [4] A.H. Cottrell, *Phil.Mag.* 44 (1953) 829-832.
- [5] J. Friedel, *Dislocations*, Addison-Wesley, Oxford 1964.
- [6] F. Springer, A. Nortmann, Ch. Schwink, *phys.stat.sol.(a)* 170 (1998) 63-81.
- [7] P. Hähner, *Mater.Sci.Eng.A* 207 (1996) 208-215, 216-223.
- [8] M. Zaiser, P. Hähner, *phys.stat.sol.(b)* 199 (1997) 267-330.
- [9] H. Neuhäuser, J. Plessing, M. Schülke, *J.Mech.Behav.Mater.* 2 (1990) 231-254.
- [10] C.H. Cáceres, A.H. Rodriguez, *Acta Metall.* 35 (1987) 2851-2864.
- [11] F. Chmelik, Z. Trojanova, Z. Prevorsevsky, P. Lukac, *Mater.Sci.Eng.A* 164 (1993) 260-265.
- [12] R. Pascual, *Scripta Metall.* 8 (1974) 1461-1466.
- [13] F. Zeides, I. Roman, *Scripta Metall.Mater.* 24 (1990) 1919-1922.
- [14] C.B. Scruby, H.N.G. Wadley, J.E. Sinclair, *Phil.Mag.A* 44 (1981) 249-274.
- [15] C.H.Cáceres, A.H.Bertorello, *Scripta Metall.* 17 (1983) 1115-1120.
- [16] A. Pawelek, *Z.Metallk.* 80 (1989) 614-618.
- [17] A. Ziegenbein, P. Hähner, H. Neuhäuser, *Comput.Mater.Sci.* 19 (2000) 27-34; *Mater.Sci.Eng.A* (in press)
- [18] P. Hähner, A. Ziegenbein, H. Neuhäuser, *Phil.Mag.A* (in press)
- [19] F. Chmelik, A. Ziegenbein, H. Neuhäuser, P. Lukac, *Mater.Sci.Eng.A* (in press)
- [20] H. Neuhäuser, *Int.J.Plasticity* 9 (1993) 421-435.

SERRATED YIELDING AND NONUNIFORM PLASTIC DEFORMATION OF PORTEVIN - LE CHATELIER EFFECT IN COMMERCIAL Al-Mg ALLOYS

K. Chihab and H. Ait-Amokhtar

Plasticity and Microstructure of Metallic Materials Research Group
LTMGP - University of Bejaia, 06000 - Algeria

SUMMARY

The mechanical characteristics of plastic deformation of commercial Al-1Mg, Al-2Mg and Al-2.5Mg alloys whose the tensile curve presents serrated yielding of the Portevin - Le Chatelier effect (PLC) have been investigated in some detail. In this experimental work, tests at room temperature were conducted on a hard tensile machine and measurements of the most important parameters of serrated yielding show the influence of the difference in Mg content in these alloys. We also show that the Mg content is the responsible factor for a more or less heterogeneous plastic strain. The tendency towards serrated flow was characterized by the critical strain for the onset of PLC instabilities as well as by the magnitude of the stress drops. The strain rate dependence on the critical strain presents, in the domain of the explored strain rates, various types of behavior: "normal", "inverse then normal" and "inverse" for Al-1Mg, Al-2Mg and Al-2.5Mg, respectively. The evolution of type of instabilities vs. critical strain, the influence of the Mg content on the magnitude of the stress drop and their dependence on the strain and strain rate will be studied. The experimental results are compared and discussed with reference to a variety of Al-Mg alloys of the literature data.

Keywords: Plastic deformation; Serrated flow; Portevin - Le Chatelier effect; Aluminum - Magnesium alloys; Experimental study.

1. INTRODUCTION

Among the various plastic instabilities that a solid can undergo, the jerky flow, commonly referred to as the Portevin - Le Chatelier (PLC) effect, is the best understood one. Investigations on plastic flow reveal several distinct kinds of stress vs. time (or strain) behavior under constant rate of straining. To date the PLC effect has been recorded in several classes of dilute interstitial and substitutional alloys on Al, Cu, Ni, Fe, etc. basis (in polycrystalline form for the most part) around $0.3 T_m$, where T_m is the melting temperature. The occurrence of the PLC effect, within a certain range of temperatures and applied strain rates, appears to be systematically associated with negative strain rate sensitivity of the flow stress [1-6]. It is characterized by the formation and, in some cases, propagation of deformation bands. The experimental study of the phenomenon (characteristics of serrated yielding, spatial profile of localization and influence of the testing conditions) has been well documented [2,4,5,7-10]. Microscopically, PLC effect is associated with dynamic strain aging due to interactions between mobile dislocations temporarily arrested at forest obstacles and diffusing solute atoms [1-4,11]. Depending on the experimental conditions, the critical

value of uniform tensile strain at the onset of serrations involves a bifurcation from smooth to jerky flow. At a fixed temperature, the "normal" behavior of the critical strain at which serrated flow starts, i.e. the critical strain increasing with the strain rate, can be explained by dynamic strain aging models and is in concordance with experimental results in many dilute solid solutions [1-4]. However, the "inverse" behavior, i.e. the critical strain decreasing with the strain rate, was observed in many concentrated solid solutions or in alloys in which precipitation occurs [12-15].

Most of studies were carried out on Al-Mg alloys tend to show "inverse" behavior with strain rate for Mg concentrations larger than 4% [7,13,16] compared to the behavior observed in dilute solid solutions. Furthermore, for Al-1Mn-1Mg alloy, the experimental study [10] tends to show "normal" behavior in all the range of strain rates at room temperature. In the present study, various consequences of the PLC instabilities are discussed in connection with experimental data.

2. EXPERIMENTAL PROCEDURE

The materials used in this study were industrial aluminum-magnesium alloys. The chemical composition in weight percent is given in table 1.

	Mg	Fe	Cr	Si	Mn	Cu
Al-2.5Mg	2.606	0.199	0.210	0.125	0.028	0.070
Al-2Mg	1.998	0.270	0.194	0.098	0.079	0.020
Al-1Mg	1.097	0.327	0.023	0.170	0.644	0.070
As well as traces of Zn, Ti and Ni						

Table 1. Chemical composition of the Al-Mg alloys (in wt%).

These alloys were obtained in the form of a cold-rolled polycrystalline to 1.5 mm thick sheet. The grains were elongated in the rolling texture direction and fiber structures are observed for these alloys. Flat tensile specimens of 6 mm width and 42 mm gauge length were cut in the rolling direction and tested in the as - received condition. The tests were performed at room temperature (25°C) in tension on a hard Adamel tensile-testing machine. The effective elastic stiffness of the tensile system is 10^6 Nm^{-1} and the domain of PLC effect, where the serrations nature are B and A- types, was investigated as a function of the applied strain rate varying from 10^{-5} to 10^{-3} s^{-1} . In a previous paper [17], it is shown that, except for the case of the critical strain, these materials present a spatial isotropy with respect to the mechanical behaviour. Indeed, the structural anisotropy of the rolling texture of these materials doesn't have a substantial influence on the features of the nonuniform plastic flow and on the mechanical characteristics following different directions of tensile test with respect to the rolling direction. The values of the strain rate sensitivity stay unchanged as function of strain following three directions with respect to the tensile test, e.g. the value of the strain rate sensitivity measured between $3.96 \cdot 10^{-5} \text{ s}^{-1}$ and $2.38 \cdot 10^{-4} \text{ s}^{-1}$ seems to reach an average limit up to about -2.70 MPa around 15% of strain for the Al-2Mg and Al-2.5Mg alloys.

3. RESULTS

Onset strain of serrations vs. strain rate

Figure 1 shows an example of a stress - strain curve exhibiting a critical strain of the onset of the PLC serrated flow, the test was realized under applied strain rate at room temperature. As

shown in figure 2, the evolution of critical strain with the strain rate presents various behavior manners. For Al-1Mg alloy, the critical strain increases in the all range of strain rates (behavior called "normal"). For Al-2.5Mg alloy, in the domain of the strain rates less than $6 \cdot 10^{-4} \text{ s}^{-1}$, the critical strain starts at a lower strain rate with a maximum value and ends with zero at a higher strain rate (behavior called "inverse") in comparison to the Al-2Mg where the critical strain decreases and increases beyond $6 \cdot 10^{-4} \text{ s}^{-1}$, i.e. the "inverse" and "normal" behaviors in the range of the corresponding curve are separated by a minimum. In the case of "inverse" behavior, the mechanism by which the critical strain is affected is linked to precipitation before or during the deformation and can be approximated by a power law as $\dot{\epsilon} \propto \epsilon_c^{m+\beta}$ at a fixed temperature, where $\dot{\epsilon}$ is the strain rate, ϵ_c the critical strain and $m+\beta$ a constant which depends on the material [7,18]. In this study, $m+\beta$ is estimated to -2.6 for Al-2.5Mg alloy (fig 2). This result is in good agreement with the result one for Al-5Mg [7].

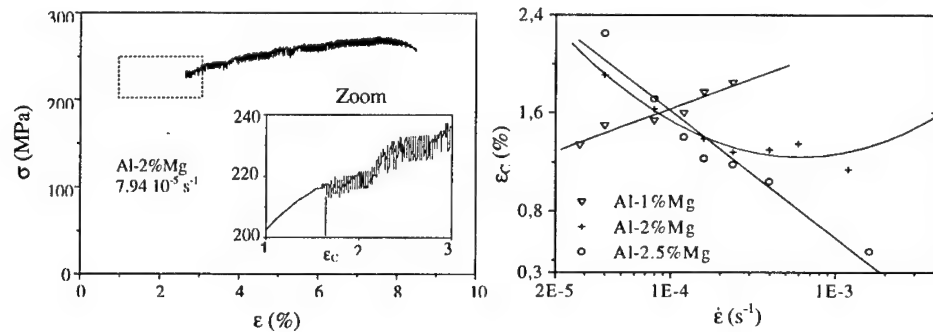


Figure 1: Example of stress vs. strain diagram exhibiting PLC serrations and the critical strain under constant strain rate at room temperature.

Figure 2: Logarithmic strain rate dependence of the critical strain.

Types of serrations vs. critical strain

At room temperature, no C-type serrations were recorded in the investigated strain rate range. For the Al-1Mg and Al-2.5Mg alloys, which behavior is "normal" and "inverse" in all the range of the strain rates, respectively, the first serrations to appear were of B-type at low test strain rates. During a discontinuity of plastic flow, B-type serrations vanish abruptly with increasing strain rate and A-type serrations will take place and finish with an irregular serrations at high strain rates. In Al-2Mg, where the behavior of the critical strain is "inverse then normal", we show a transition domain from B to A-type instabilities. The zone of transition which corresponds to a minimum of ϵ_c vs. strain rate represents a mixed A and B-type serrations, i.e. the B-type between the A-type serrations. The mixed A+B-type serrations were started at $6 \cdot 10^{-4} \text{ s}^{-1}$ (fig. 2) and are characterized by a well defined intermittence between irregular serrations and successive drop stress which develop after a certain amount of strain. A+B-type serrations result from fairly large heterogeneities which forbid the formation of a smooth strain gradient along specimen. Meanwhile, the feature corresponds to a kinetic of a transitory regime from the hopping bands (B-type) to the propagating bands (A-type).

Magnitude and frequency of the stress drops vs. strain

As shown in figure 3, for Al-2Mg and Al-2.5Mg alloys, the magnitude of stress drop increases with increasing strain. As predicted by some works in literature [7], the evolution of

the strain dependence of the magnitude of B- type instabilities can be approximated by a power law: $\Delta\sigma \propto \epsilon^\theta$, where $\Delta\sigma$ is the stress drop from its highest to its lowest point, ϵ is the tensile strain and θ is the strain exponent. The magnitude of the serrations seems to reach a maximal value of saturation up to about 15% of strain. As represented by figure 4, the values of the strain exponent, θ , calculated for various curves, were found to increase linearly with the applied strain rate. In the strain rates range, this variation is found to be in good agreement with the principle of negative strain rate sensitivity and the strain exponent will increase with increasing

Mg content in Al-2Mg and Al-2.5Mg alloys. Pink's data in Al-5Mg alloy [7], also reanalyzed for the comparison with the present results, are in a good agreement.

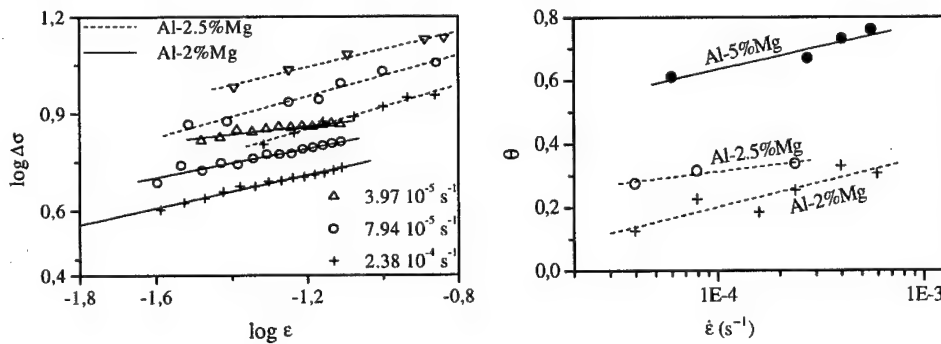


Figure 3: The strain dependence of $\Delta\sigma$ at various strain rates, showing the linear relation between $\log \Delta\sigma$ and $\log \epsilon$, in B-type serrated flow curves.

Figure 4: Logarithmic strain rate dependence of the strain exponent θ . The plot of Al-5%Mg is obtained from Pink's result [7].

For the Al-2.5Mg alloy in the range of B-type serrations, the local frequency per unit of strain stays unchanged following three directions of uniaxial tensile test with respect to the rolling direction and seems to reach an average limit value up to about 15% of strain (fig. 5). As shown in figure 6, the local frequency is plotted against the strain under three different strain rates. The experimental data show that the plots of $\log N$ vs. $\log \epsilon$ is also equally linear and the local frequency can be described with the tensile strain via: $N \propto \epsilon^\lambda$, where ϵ is the tensile strain and λ is a constant. As it has been shown in the figure 8, it is seen that the strain exponent is somewhat dependent on the strain rate and whose the measured values pass from -0.20 to -0.36 in the range 2 - 15% of strain. However, the measurements of Hong and Nam [19] for the Al-1Mg alloy suggested that the strain exponent is -0.5 up to about 12% of strain and this value is independent of the strain rate in this range.

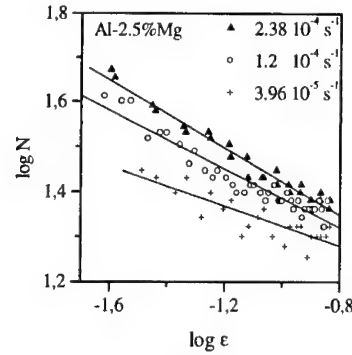
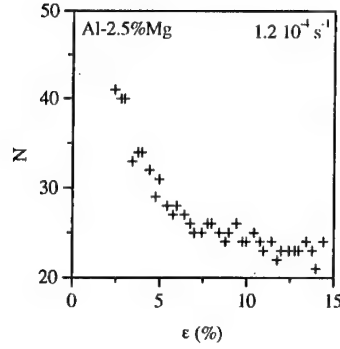


Figure 5: The strain dependence of the local frequency per unit of strain in B-type serrated flow curves.

Figure 6: The strain dependence of the local frequency per unit of strain at various strain rates, showing the linear relation between $\log N$ and $\log \epsilon$.

Magnitude of the stress drops vs. strain rate

As shown in figure 7, for Al-2Mg and Al-2.5Mg alloys, the magnitude of stress drop increases with decreasing strain rate. Similarly, the strain rate dependence of the magnitude of B-type serrations shows a linear dependence with a slope $-\alpha$ and can be written as power law via: $\Delta\sigma \propto \dot{\epsilon}^{-\alpha}$. Figure 8 shows the strain rate dependence of the exponent α for tests realized at different strain rates. From figure 8, it is seen that α , whose average value is measured to be about 1/3, is independent of the strain rate. This is in a good agreement with Pink's data for Al-5Mg alloy; Pink et al. [7] which show that the exponent α is about 0.3 consider the time as the one between two consecutive drops and have argued that the results with Al-5Mg did not agree with the relation $\Delta\sigma \propto \Delta t^{2/3}$. Here, a section at higher strain rates, i.e. A-type serrations, where the time falls to low values, is not taken into consideration. Furthermore, in the original Cottrell - Bilby model, the experimental results with the Al-2Mg and Al-2.5Mg alloys did not agree with α about 2/3. Plots of $\log \Delta\sigma$ vs. $\log \dot{\epsilon}$ must show a linear dependence with a slope $-2/3$ if the Cottrell-Bilby model and the assumptions of the previous models [1-4] are a valid description of serrated flow in all the range of the strain rates. However, as in our case, this is not true in the range of the type B instabilities at room temperature. Assuming the fact that the applied strain rate is inversely proportional to the waiting time according to: $\dot{\epsilon} = \Omega/t_w$, where Ω the elementary strain increment obtained when all the mobile dislocations simultaneously undergo a successful activation event, McCormick and Ling [11] indicate that the exponent 1/3 gives better agreement with experimental measurements. Springer and Schwink [20], Ling et al. [21] and McCormick and Ling [11] support an exponent of 1/3, instead of 2/3, in the above formula. The physical basis for such a difference is thought to be "pipe diffusion" along dislocation lines at the medium or higher waiting times (medium or lower strain rates). This result is qualitatively in a good agreement with the theoretical approach of Mesarovic [6].

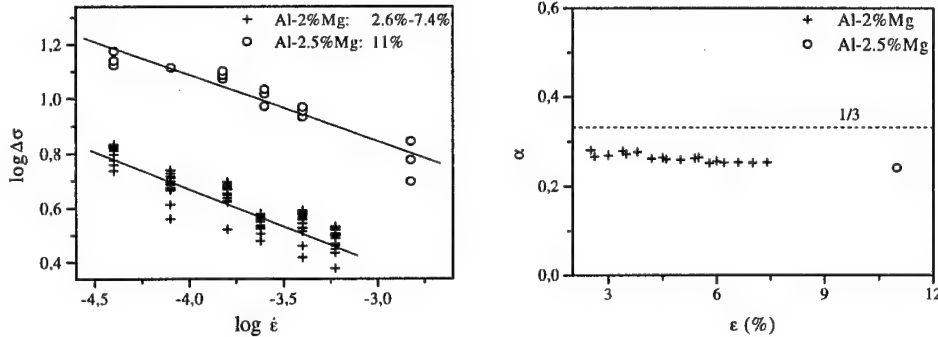


Figure 7: The strain rate dependence of $\Delta\sigma$ at various strain, showing the linear relation between $\log \Delta\sigma$ and $\log \dot{\epsilon}$, in B-type serrated flow curves.

Figure 8: The strain dependence of the exponent α .

4. DISCUSSION AND CONCLUSIONS

With increasing strain rate, the critical strain for the onset of PLC effect was "normal", "inverse then normal" and "inverse" with function of Mg content in the Al-1Mg, Al-2Mg, Al-2.5Mg alloys at room temperature, respectively. In agreement with this, on the basis of the comparison with the Al-3Mg [13], Al-4Mg [16] and Al-5Mg [7] alloys results which behavior is inverse at room temperature, we deduce that the Al-Mg alloys tend to show "inverse" behavior for Mg concentration larger than 2%Mg. The decrease of Mg content reduce the tendency to serrated flow and the critical strain values remain higher than those of Al-Mg alloys where Mg content is more than 2%. Furthermore, for the Al-2Mg alloy, where there exist "inverse then normal" behavior, the minimum of the critical strain at the onset of serrations corresponds to the change of the kinetic mode of the moving PLC bands, the transition of the critical strain from "inverse" to "normal" behavior manifest a mixed A+B serrations.

Starting from the logarithmic scale plots of the magnitude of the B-type stress drop with function of the tensile strain on one hand and with the strain rate on the other hand, it has been shown that the exponent θ will increase with increasing Mg content and the strain rate. However, the exponent α is independent of Mg content and the strain rate, and its average value, which is about $1/3$, is in agreement with a lot of works in literature. As suggested by several authors, the values of α show that the solute atoms move by core diffusion during the dynamic strain aging mechanism of the mobile dislocations temporarily arrested at obstacles. Also, the experimental measurements show that the exponent λ for the frequency is somewhat dependent on the strain rate and no observed change in all the range of the tensile strain.

Finally, it should be noted that the ductility of these alloys is connected to the tensile strain corresponding to the limit values of: saturation of the amplitude of serrated yielding, the strain rate sensitivity and the frequency of oscillations. With typical numerical values for Al-2.5Mg alloy, the limits of tensile strain corresponding to the above characteristics seemed to be about 15%, this value corresponds to the rupture strain of the material [17].

5. REFERENCES

- [1] A. Van den Beukel, *Phys. Stat. Sol. (a)* 30, 197 (1975)
- [2] A. Van den Beukel and U. F. Kocks, *Acta Metall.* 30, 1027 (1982)
- [3] L. P. Kubin, K. Chihab and Y. Estrin, *Acta Metall.* 36, 2707 (1988)
- [4] Y. Estrin and L. P. Kubin, *J. Mech. Behav. Metals.* 2, 255 (1990)
- [5] P. Penning, *Acta Metall.* 20, 1169 (1972)
- [6] S. Dj. Mesarovic, *J. Mech. Phys. Solids* 43, 671 (1995)
- [7] E. Pink and A. Grinberg, *Acta Metall.* 30, 2153 (1982)
- [8] K. Chihab, Y. Estrin, L. P. Kubin and J. Vergnol, *Scripta Metall.* 21, 203 (1987)
- [9] L. P. Kubin, K. Chihab, Y. Estrin, *NATO ASI Series E, App. Sci.*, 121, 220 (1987)
- [10] G. G. Saha, P. G. McCormick and P. Ramarao, *Mater. Sci. Eng.* 62, 187 and 197 (1984)
- [11] P. G. McCormick and C. P. Ling, *Acta Metall. Mater.* 43, 1969 (1995)
- [12] Y. Bréchet and Y. Estrin, *Acta Metall. Mater.* 43, 955 (1995)
- [13] J. Balík, P. Lukác and L. P. Kubin, *Scripta Metall. Mater.* 42, 465 (2000)
- [14] S. Kumar, *Scripta Metall. Mater.* 33, 81 (1995)
- [15] E. Pink, *Acta Metall.* 37, 1773 (1989)
- [16] J. Guillot and J. Grilhé, *Acta Metall.* 20, 291 (1972)
- [17] K. Chihab and K. Bouabdellah, *Ann. Chim. Sci. Mat.* 24, 47 (1999) and 25, 171 (2000)
- [18] P. G. McCormick, *Acta Metall.* 19, 463 (1971)
- [19] K. T. Hong and
- [20] F. Springer and Ch. Schwink, *Scripta Metall.* 25, 2739 (1991)
- [21] C. P. Ling, P. G. McCormick and Y. Estrin, *Acta Metall.* 41, 3323 (1993)

TIME SERIES ANALYSIS AND THE DETERMINISTIC STRUCTURE OF THE PLC EFFECT

D. Kugiumtzis

Department of Statistics
University of Glasgow, Glasgow G12 8QW, UK

E. C. Aifantis

Laboratory of Mechanics and Materials, Polytechnic School
Aristotle University of Thessaloniki, GR-54006, Thessaloniki, Greece

1. SUMMARY

The nature of the mechanism that produces the PLC effect is studied by analysing a single stress time series observed at a particular strain rate on Cu-10% Al. The time series is a stick-slip sequence, characterised by successive slow up and sharp down trends. We review critically recent analyses of these data suggesting nonlinear dynamics and chaos and we further investigate whether there is a deterministic mechanism that generates the successive up-down patterns by conducting a statistical test. The test uses surrogate data, suitably generated to represent the null hypothesis that the up-down trend sequence is random. Linear and nonlinear estimates are used as test statistics, such as autocorrelation, mutual information and Lyapunov exponents. The overall results do not give statistical evidence for a long term "memory" in the dynamical system underlying the PLC effect.

2. INTRODUCTION

The Portevin-Le Chatelier (PLC) effect or jerky flow is one of the best studied forms of plastic instability in many metallic alloys when tensile specimens are deformed in a certain range of strain rates and temperatures. In a number of experiments of occurrence of the PLC effect at single crystals of Cu-Al alloys^{1,2} and Al-Mg polycrystals,^{3,4} the application of methods of nonlinear time series analysis⁵ gave evidence for determinism, nonlinearity and chaos. The results were confirmed also by the surrogate data test for nonlinearity.^{6,7}

In the case of Cu-Al alloys, the stress time series is an erratic sequence of successive slow positive and fast negative linear trends. The so-called stick-slip nature of these data indicates some sort of nonlinear determinism in the generating system, and it is somehow expected that this type of time series passes the surrogate data test for nonlinearity. A more interesting question for this particular stress time series is whether the sequence of the stick-slip patterns is totally random or there exists a structure, which would then imply a long term "memory" of the underlying system for the material deformation at this particular range of strain rates and temperatures. In this paper, we attempt to answer this question by means of hypothesis testing, where the null hypothesis is that the stick-slip sequence is random.

3. REVIEW OF THE NONLINEAR ANALYSIS OF THE STRESS DATA

We focus on a single stress time series observed at the low strain rate of $3.3 \times 10^{-6} \text{ s}^{-1}$ on Cu-10% Al, sampled at 2Hz. The data were provided from the authors of Ref. 1. The stress time series and a segment of this is shown in Figure 1 (top panel). The special structure of successive stick-slip patterns for this stress range clearly indicates that the underlying system is deterministic in small time scales. It is therefore of no surprise that the estimates from nonlinear methods applied to this time series suggest nonlinear deterministic structure.

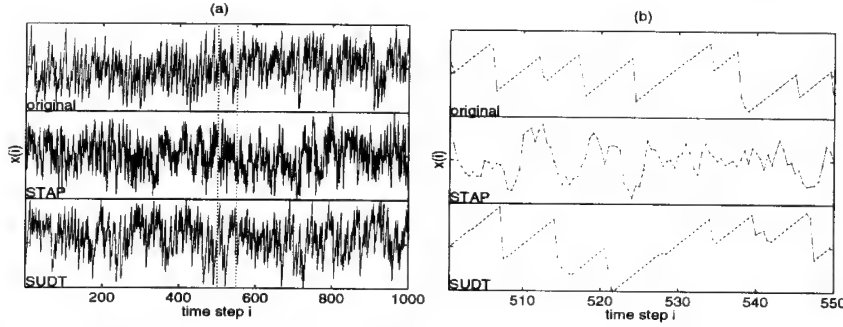


Figure 1: (a) The stress time series, a STAP surrogate and a SUDT surrogate, from top to bottom. The two gray vertical lines denote the data segments, which are enlarged in (b).

This result can also be established statistically, testing the null hypothesis H_0 that the stress time series is generated by a linear (Gaussian) process, perturbed by a static, possibly nonlinear, transform^{6,7}. The test involves the generation of an ensemble of surrogate data, i.e. time series that represent the null hypothesis, and the computation of a test statistic, here an estimate from a nonlinear method, on the original and surrogate data. If the estimate on the original data does not lie within the empirical distribution under H_0 , formed by the estimates on the surrogates, then H_0 is rejected and it is unlikely that the original time series is linear stochastic. However, solely by eyeball judgement one can exclude that the stress data are generated from the same process as the surrogate time series, as shown in Figure 1 (top and middle panel). The surrogate time series is generated using the STAP algorithm⁸. The surrogate data are designed to mimic the original time series in terms of marginal distribution and autocorrelation and are otherwise random. These two conditions do not constrain the surrogate data to have certain characteristic patterns the original data have, such as the stick-slip pattern of the stress data. So, the H_0 is easily rejected using nonlinear test statistics, such as the mutual information $I(\tau)$ (a measure of the general correlation, linear and nonlinear, for lags τ) and the largest Lyapunov exponent $\lambda_1(m)$ (a measure of the divergence in the evolution of nearby trajectories in a reconstructed state space of dimension m).

4. SURROGATE DATA TEST FOR INDEPENDENCE OF UP-DOWN TRENDS

The question we want to investigate here is whether there is evidence of determinism or correlation in the evolution of the stick-slip patterns of the stress time series. For this, we follow the same statistical approach of surrogate data testing as in Section 3, but for a different H_0 , i.e. the sequence of stick-slip patterns is random. The surrogate data for this H_0 should have the same stick-slip structure as the stress data, but in a random order.

4.1 The SUDT algorithm

We created an algorithm, called Stochastic Up-Down Trends (SUDT), to generate the appropriate surrogate data for this H_0 . The steps of the algorithm are as follows:

1. Scan the original time series, identify and store the up-down trend patterns, as well as the global minimum x_m , global maximum x_M , smallest end-point of the up-trend x_u and largest end point of the down-trend x_d .
2. The surrogate time series z starts at the same data point as the original, i.e. $z_1 = x_1$ (a random point could be chosen as well).
3. Using a uniform distribution, draw randomly an up-down trend from those stored in step 1, and displace it so that its starting point coincides with the currently last point of the time series z .
4. Check whether the end-point of the "up"-part of the candidate segment is within x_u and x_M , and the end-point of the "down"-part is within x_m and x_d . If the two end-points are within the given limits, accept the up-down trend and add it to z (the end-point of this segment is then the last data point of the z); if not, discard it and repeat the previous step.
5. Repeat the last two steps until the time series z is as long as the original time series (eventually truncating the last eligible trend).

Note that the algorithm assumes that the original time series starts with an upward trend as does the data set we study here. In the opposite case, one can simply reverse the values of the original data set (e.g. multiply by -1) before applying the algorithm. This algorithm implements bootstrapping on blocks of data (the up-down trends) from the original time series, allowing repetitions of the same data block in the surrogate time series. Simple shuffling of the original trends cannot be done because the end-points have to match. It was found necessary to constrain the random selection of the up-down trends using lower and upper limits for both the "up" and "down" end-points of each trend in order to keep the generated surrogate time series z within the bounds of the original data. Using only the global minimum and maximum (x_m and x_M) led to edge effect problems, so the additional limits of x_u and x_d had to be introduced to assure robust execution of the algorithm.

4.2 Examples with simulated data

The surrogate time series generated by the SUDT algorithm represent exactly the H_0 of independent up-down trends. Certainly, the original up-down trends may be correlated implying deterministic structure on longer time scales. Using simulated data, we show that the standard nonlinear methods have actually discriminative power for this test and can distinguish the original time series from its SUDT surrogates when this is the case. For the "deterministic" case, we used 2000 data of the log-transformed w variable of the Rössler hyperchaos system⁹, sampled at time $\tau_s=0.1$ sec, call it x^d . For the "random" case (original time series with random stick-slip states), we simply use a time series derived by the SUDT algorithm on x^d , call it x^s . Two segments of the two time series are shown in Figure 2a. Note that the time series x^d and x^s have the same structure and cannot be distinguished by eyeball judgement. The SUDT surrogate data for each of the two time series possess similar amplitude distribution and autocorrelation to the original ones, as shown in Figure 2b and Figure 2c, respectively. So, the SUDT surrogates preserve the original amplitude distribution and autocorrelation (as the surrogate data for the nonlinear test in Section 3), but in addition they preserve the stick-slip structure as well.

The results from two nonlinear methods, the mutual information $I(\tau)$ and the largest Lyapunov exponent $\lambda_1(m)$, on the x^d and x^s and their respective SUDT surrogates are shown in Figure 2d and Figure 2e, respectively. The chaotic deterministic data x^d are correctly distinguished from their respective SUDT surrogates with both the $\lambda_1(m)$ statistics (for the whole range of $m=1, \dots, 10$), and the $I(\tau)$ statistics (for $10 < \tau < 20$). Subsequently, the H_0 of independent stick-slip states is rejected at high confidence levels. On the other hand, the x^s data are correctly indistinguishable from their respective SUDT surrogates neither by $\lambda_1(m)$ or $I(\tau)$.

Very similar results were established for quasi-periodic deterministic systems that generate time series of stick-slip patterns, as well as when other nonlinear statistics were used. These findings show that even standard nonlinear statistics that are not tailored for this particular test can distinguish correctly correlated stick-slip states from non-correlated stick-slip states of similar shape. The $I(\tau)$ statistics for small τ do not seem to have discriminative power, possibly because for such small time lags the general correlation measured by $I(\tau)$ is affected only from the shape of the stick-slip states and not from their order.

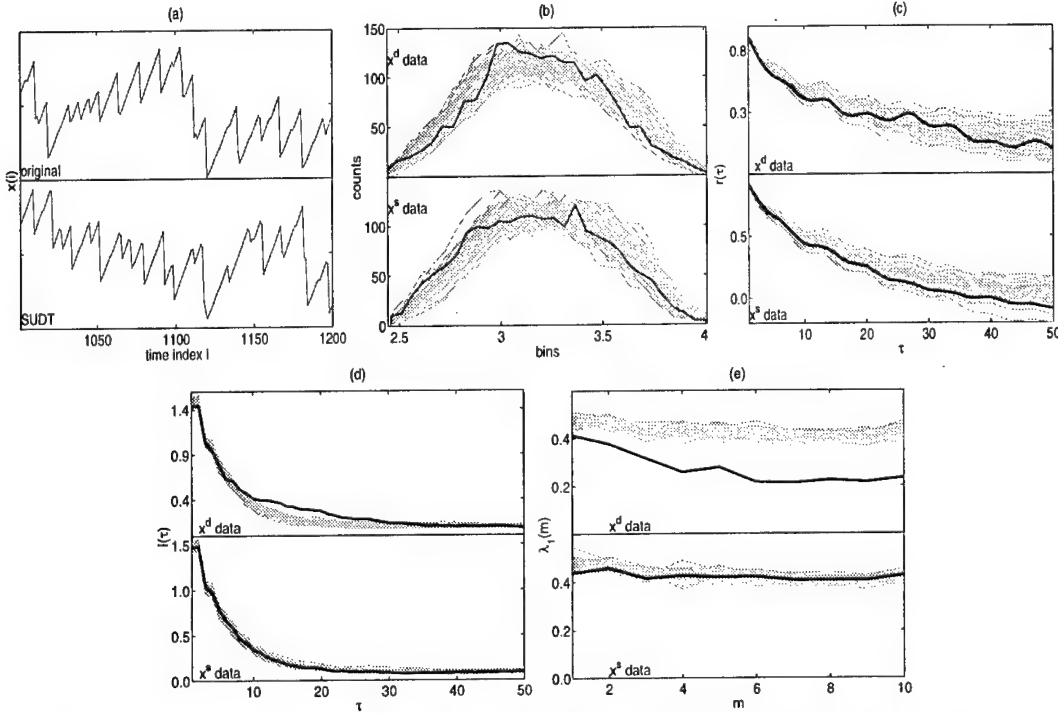


Figure 2: (a) A segment of the time series of the Rössler hyperchaos system x^d (upper panel) and a segment of a SUDT surrogate of it x^s (bottom panel). In (b) is the amplitude distribution (histogram), in (c) the autocorrelation $r(\tau)$, in (d) the mutual information $I(\tau)$, and in (e) the largest Lyapunov exponent $\lambda_1(m)$ of x^d and 40 SUDT surrogates (upper panel), and of x^s and 40 SUDT surrogates (lower panel). Black thick lines denote the original data and gray lines denote the surrogates.

5. APPLICATION OF THE TEST TO THE STRESS DATA

A SUDT surrogate time series of the stress data is shown together with the original data in Figure 1 (lower and upper panel, respectively). Obviously, this surrogate data preserves the stick-slip signature of the original data. The amplitude distribution of the surrogate data is similar to the original one, as shown in Figure 3a. The same yields for the distribution of the lengths and slopes of the up trends and down trends (not shown). However, the autocorrelation of the surrogate data deviates significantly from the original one, especially at lags around 10 (see Figure 3b). This feature was not met in the examples with simulated data and it is not clear whether it should be attributed to the existence of linear deterministic structure in the original stick-slip states, or to other factors not related with the dynamics of the stick-slip states (e.g. the shape of the up-down trends). Moreover, the $r(\tau)$ for τ around 10 of the original data is actually positive and smaller than for that of the surrogates suggesting the opposite to the alternative hypothesis we attempt to establish, i.e. the surrogate data involve more correlations than the original.

The results from the two nonlinear statistics, $I(\tau)$ and $\lambda_1(m)$, do not indicate clear discrimination of the original data from the surrogate data, as shown in Figure 3c and Figure 3d, respectively. The H_0 could be rejected marginally only for the statistics $\lambda_1(4)$ and $\lambda_1(7)$. These results suggest that there is not enough statistical evidence to establish that the stick-slip states of the stress time series are correlated and thus that there is a deterministic system at large time scales that controls the evolution of the stick-slip states.

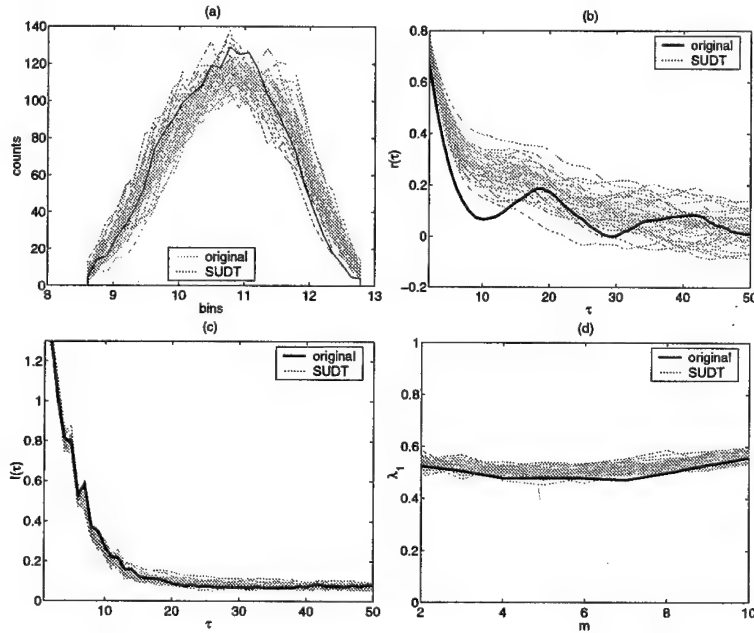


Figure 3: Stress time series and 40 SUDT surrogates: (a) amplitude distribution, (b) autocorrelation $r(\tau)$ vs the lag τ , (c) mutual information $I(\tau)$ vs τ , and (d) largest Lyapunov exponent $\lambda_1(m)$ vs the embedding dimension m .

6. DISCUSSION

It is plausible that the evolution of the stress of the PLC effect is rather deterministic at short time scales as the stress time series has a characteristic stick-slip structure. We employed statistical testing to investigate whether there is a deterministic mechanism that controls the stress at larger time scales that span over the duration of the stick-slip states. The standard surrogate data test for nonlinearity, used recently to establish determinism and nonlinearity of the PLC effect, is not suitable for the question of interest as the surrogate data do not preserve the stick-slip structure. We designed the SUDT algorithm to generate surrogate data of stick-slip structure and performed the surrogate data test for the null hypothesis of independent stick-slip states. Nonlinear statistics as the ones used for the test for nonlinearity turned out to perform appropriately when applied to simulated data. When we applied the test on the stress time series, the nonlinear statistics could not find significant differences between the original data and the SUDT surrogate data. Our results showed no statistical evidence for a long term "memory" of the underlying system of the PLC effect for the particular stress rate.

Actually, the SUDT surrogate data did not much well the autocorrelation of the stress data, as it was the case with the simulated data. An improvement of the SUDT algorithm would be to make the surrogates match also the original autocorrelation, but there does not seem to be an obvious way to do this. Also, the test may be improved by employing other test statistics that are tailored to capture the information relating the stick-slip states, such as the lengths of the successive up-down trends and the magnitudes of the successive turning points. A future work on the same hypothesis is to compress the information from each up-down trend of the stress time series in a single or few quantities (e.g. length and velocity of up and down trends) and make the test for independence on the derived univariate or multivariate time series.

7. REFERENCES

- ¹ Ananthakrishna, G., Noronha, S. J., Fresengeas, C. and Kubin, L. P., Crossover from Chaotic to Self-organized Critical Dynamics in Jerky Flow of Single Crystals, *Physical Review E*, Vol 60, No 5, 5455-5462 (1999).
- ² Lebyodkin, M. and Dunin-Barkowski, L. and Brechet, Spatio-Temporal Dynamics of the Portevin-Le Chatelier Effect: Experiment and Modelling, *Acta Materialia*, Vol 48, 2529-2541 (2000).
- ³ Ananthakrishna, G., Fresengeas, C. and Kubin, L. P., Chaos and the Jerky Flow in Al-Mg Polycrystals, *Materials Science and Engineering*, Vol A234-236, 314-337 (1997).
- ⁴ Noronha, S. J., Ananthakrishna, G., Quaoire, L., Fresengeas, C. and Kubin, L. P., Chaos in the Portevin-Le Chatelier effect, *Int. J. of Bifurcation and Chaos*, Vol 7, No 11, 2577-2586 (1997).
- ⁵ Kantz, H. and Schreiber, T., *Nonlinear Time Series Analysis*, Cambridge University Press, Cambridge (1997).
- ⁶ Schreiber, T. and Schmitz, A., Surrogate Time Series, *Physica D*, Vol 142, No 3-4, 346-382 (2000).
- ⁷ Kugiumtzis, D. Surrogate Data Test on Time Series, *Nonlinear Deterministic Modelling and Forecasting*, Soofi, A. and Cao, C. (Ed), Kwyer Academic Publishers (2001).
- ⁸ Kugiumtzis, D., Surrogate Data Test for Nonlinearity: A New Approach, Manuscript.
- ⁹ Rössler, O. E., An Equation for Hyperchaos, *Physics Letters A*, Vol 71, No 2-3, 155- 157 (1979).

SOME DYNAMICAL SYSTEM CONSIDERATIONS FOR DISLOCATIONS

G. Stagika and S. Ichtiaroglou

Department of Physics, Aristotle University of Thessaloniki,
54006 Thessaloniki, Greece
simosich@auth.gr

E. Aifantis

Laboratory of Mechanics and Materials, Polytechnic School
Aristotle University of Thessaloniki, GR-54006, Thessaloniki, Greece

I. Groma

Institute for General Physics
Eötvös University, H-1445, Budapest, Hungary

1. SUMMARY

We consider the dynamical interaction of two parallel edge dislocations under external periodic forcing and study the generation of stable fixed points of the associated Poincaré map and their basins of attraction with respect to the perturbation strength. This contribution is an extract of a more general article [1] under preparation.

2. INTRODUCTION

We consider the dynamical interaction of two parallel edge dislocations under external periodic forcing, described by the system of equations

$$\begin{aligned}\frac{dx_1}{dt} &= -F(x_1 - x_2, 2) + m \frac{\partial F}{\partial x}(x_1, 1) + \varepsilon G(t), \\ \frac{dx_2}{dt} &= F(x_1 - x_2, 2) - m \frac{\partial F}{\partial x}(x_2, 1) - \varepsilon G(t)\end{aligned}\tag{1}$$

where

$$F(x, y) = \frac{x(x^2 - y^2)}{(x^2 + y^2)^2}.$$

The parameter m defines the dipole strength and the term $\varepsilon G(t)$ is the external periodic forcing. In this study we have selected $m = 1$ and $G(t) = \sin t$. We present some preliminary results on the dynamical behavior of (1) as we increase ε . A complete presentation will appear in a forthcoming paper [1].

Equations (1) are invariant under the transformation

$$x_1 \rightarrow -x_2, \quad x_2 \rightarrow -x_1,$$

so that the straight line $x_1 + x_2 = 0$ is an invariant axis of symmetry. We define the 2π -Poincaré map and study the structure of the surface of section in a rectangle around the origin.

3. THE DEGENERATE SYSTEM

First we consider the degenerate case where both parameters m and ε equal zero. By transforming equations (1) to the new variables

$$\xi_1 = x_1 + x_2, \quad \xi_2 = x_1 - x_2$$

they become

$$\begin{aligned} \frac{d\xi_1}{dt} &= 0, \\ \frac{d\xi_2}{dt} &= -2F(\xi_2, 2). \end{aligned} \quad (2)$$

Equation (2a) implies that the straight lines $\xi_1 = x_1 + x_2 = \text{const.}$ are invariant, while the solution of equation (2b) in implicit form is

$$t = -\frac{1}{2} \int_{\xi_0}^{\xi} \frac{d\xi_2}{F(\xi_2, 2)}.$$

Equation (2b) possesses three equilibrium solutions, namely $\xi_2 = 0, \pm 2$. The linearized equation with respect to the small variation ζ around these equilibria are respectively

$$\frac{d\zeta}{dt} = \frac{1}{2}\zeta \quad \text{and} \quad \frac{d\zeta}{dt} = -\frac{1}{4}\zeta$$

so $\xi_2 = 0$ is unstable while $\xi_2 = \pm 2$ are asymptotically stable. The motion on each invariant line $x_1 + x_2 = \text{const.}$ is shown in Figure 1.



Figure 1: The flow on a line $\xi_1 = \text{const.}$

4. THE UNPERTURBED SYSTEM $\varepsilon=0$

The unperturbed system is an autonomous system of two first order differential equations and its phase space is the plane (x_1, x_2) . This system possesses in the domain $|x_i| \leq 10$ six asymptotically stable equilibria. The initial conditions and the corresponding characteristic exponents a_1, a_2 (the eigenvalues of the linearized system in their neighborhood) are given in Table 1.

Table 1: Initial conditions and characteristic exponents for the unperturbed system.

x_{10}	x_{20}	a_1	a_2
-0.4589184	0.4589184	-2.66669	-2.60489
1.7771629	-1.7771629	-0.35551	-0.30006
-5.1468123	-2.9238786	-0.23548	-0.01581
2.9238786	5.1468123	-0.23548	-0.01581

2.4142136	0.4142136	-3.04473	-0.20527
-0.4142136	-2.4142136	-3.04473	-0.20527

All these points are strong attracting nodes. The phase space (x_1, x_2) of the system is divided into eight domains, the six basins of attraction of these points and two domains of attraction of presumably $\pm\infty$, since all orbits starting from these domains show a continuous absolute increase of x_1, x_2 for a very long integration time. The stable equilibria and their basins of attraction are shown in Figure 2 where the symmetry line $x_1 + x_2 = 0$ is also shown. Two equilibrium points lie on the symmetry line.

5. THE PERTURBED SYSTEM

When ε is different from zero, the full system is non-autonomous. Its state space is the three-dimensional extended phase space (x_1, x_2, t) . In order to study the dynamical behavior of the system, we use the method of the Poincaré map (see e.g. [2], p. 22; [3], p. 64). Instead of following the phase orbit for all time in the three dimensional extended phase space, we consider only the sequence of the points (x_1, x_2) at $t = 2k\pi$, $k \in \mathbb{Z}$. In this way, every orbit is displayed as a sequence of discrete points on the so called surface of section, which is the

plane (x_1, x_2) the evolution of the system is represented by a discrete map from one point of the above sequence to the next, which is called the Poincaré map. Since the system (1) is invariant to time translations of the form $t \rightarrow t + 2k\pi$, every point of the map corresponds to a unique state of the system. A 2π -periodic orbit will be represented on the section by a fixed point of the map. Since the stable equilibria of the unperturbed system are hyperbolic, they are continued for $\varepsilon \neq 0$ to 2π -periodic orbits (e.g. [2], p. 186), which are fixed points of the Poincaré map.

In Figures 3 and 4 the asymptotically stable fixed points and their basins of attraction for $\varepsilon = 0.7$ and 0.8 are shown. The basin of the upper fixed point invades into the basin of

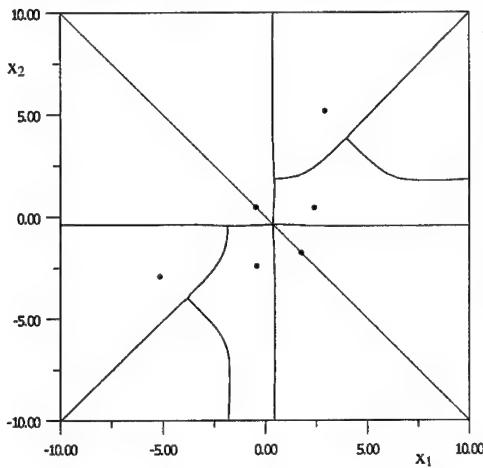
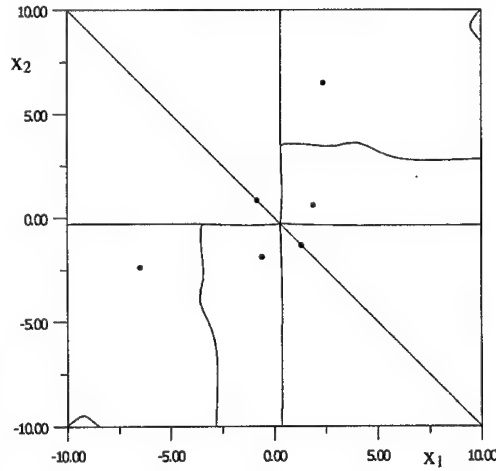
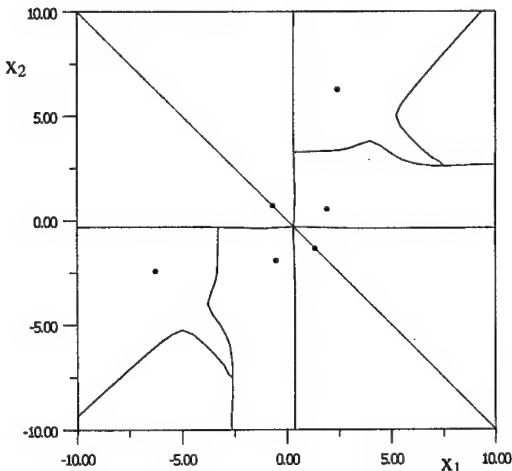


Figure 2: The stable equilibria and their basins of attraction for the unperturbed system $\varepsilon=0$.



infinity, which shrinks and for $\varepsilon = 1$ disappears from the domain, as is shown in Figure 5, i.e. as ε increases the domain of initial conditions that result in breaking ($x_i \rightarrow \pm\infty$) shrinks.

In Figures 6-8 the Poincaré map for $\varepsilon = 2, 3$ and 5 is shown. For $\varepsilon = 2$ a new stable fixed point on the symmetry line has appeared, while increasing the parameter ε further, new attracting fixed points appear. This means that there are many non-symmetric possible stable configurations for the periodic oscillation of the two dislocations. This system does not exhibit chaotic behavior. This can be attributed to the fact that all the stable fixed points are strongly attracting nodes, causing the asymptotic manifolds of the saddle points to bend and preventing them from intersecting.

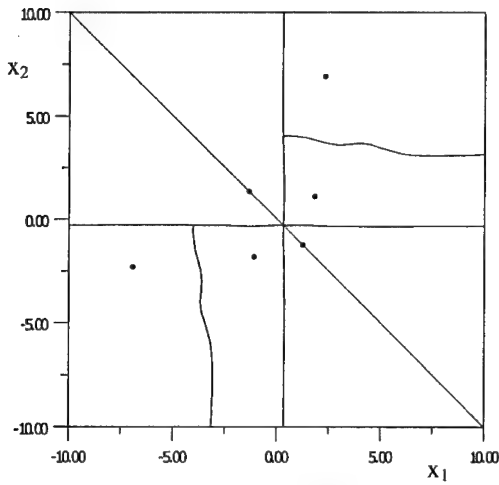


Figure 5: The Poincaré map for $\varepsilon=1$

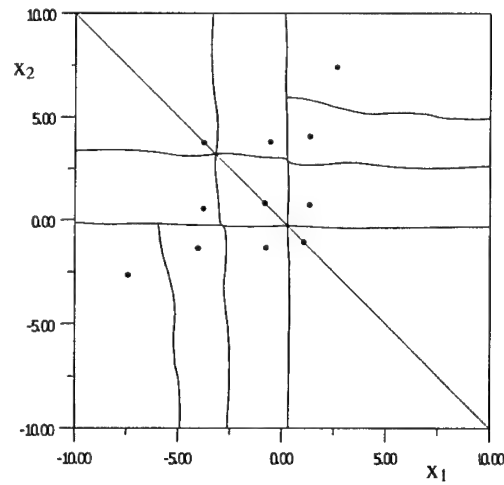


Figure 6: The Poincaré map for $\varepsilon=2$

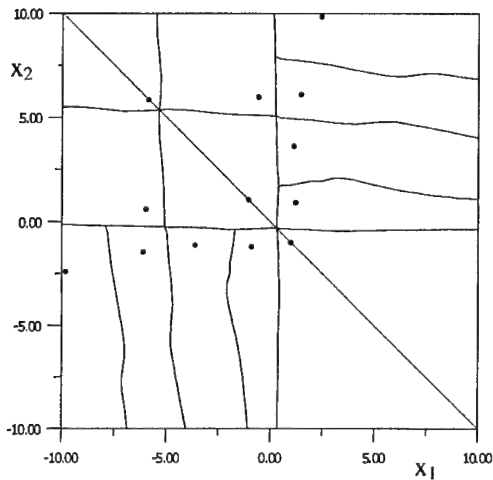


Figure 7: The Poincaré map for $\varepsilon=3$

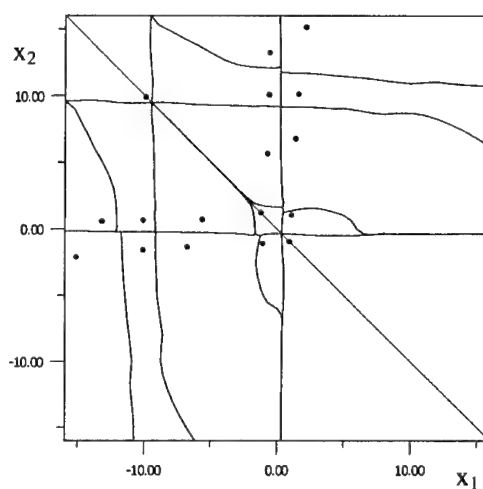


Figure 8: The Poincaré map for $\varepsilon=5$

Acknowledgements: This work has been supported by the scientific programme PENED-1999, "Gradient theory, stochasticity and self-organization", No 1958/100164, Greece. Support of a Greek-Hungarian cooperative research project which made possible I. Groma's visit in A.U.T. is also acknowledged.

6. REFERENCES

- [1] G. Stagika, S. Ichtiaroglou, I. Groma and E. Aifantis (2001) (in preparation).
- [2] J. Guckenheimer and P. Holmes, Nonlinear Oscillations, Dynamical Systems, and Bifurcations of Vector Fields, Springer-Verlag, New York, 1983.
- [3] S. Wiggins, Introduction to Applied Nonlinear Dynamical Systems and Chaos, Springer-Verlag, New York, 1990.

THE DISLOCATION MODEL OF LOCAL BEND

Natalya V.Tokiy, Tatjana Ye.Konstantinova, Victor N.Varyukhin, Alexander S.Tokiy

AA Galkin Donetsk Physical and Technical Institute NAS Ukraine
72, str. R. Luxemburg, Donetsk 83114, UKRAINE
Tel: (38) 0623379608, Fax: (38) 0622555121

1. SUMMARY

In our work on the basis of the mechanics of deformed solids and theory of dislocations, modeling of local bend is carried out. It is represented in the form of two rows of edge dislocations of opposite signs. The equation for local bend angle is found. The gradient of the angle change can be compared with parameters of twist – bend tensor determined by the electron microscopy. Parameters of the dislocation model of local bend are determined; stress fields generated by local bend within infinite crystal are estimated.

2. INTRODUCTION

The heterogeneity of plastic deformation is actual problem of mechanics [1,2]. The theory of electron microscopy contrasts of local bend of crystalline lattice which reflection is extinction contour was developed on the basis of the theory of diffraction of electrons [3,4]. This theory takes into account changes of transmission conditions for the electron beam as a function of

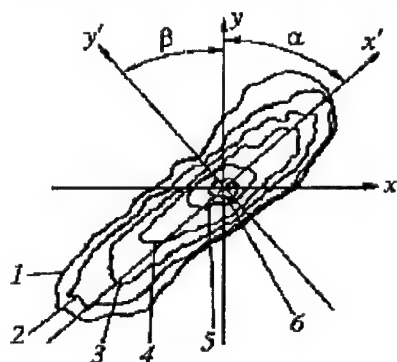


Figure 1. Scheme of the extinction contour in deformed alloy at different angles (1-6) of inclination [9]

foil inclination angle. A new method for calculation of twist-bend tensor components was developed. The experimental parameters of extinction contour [5, see Fig.1] for the different values of the foil inclination angle were used in it. Calculations of tensor components for local bend with symmetrical curvature dipole were carried out according to this method.

The substance of the work consists in the necessity of new models of defects and development of effective methods for their analysis taking into account the main peculiarities of real materials with mezostructure. Also it is determined by the wide perspectives of usage of these materials in different fields of science and technics.

The specific peculiarities of new materials limit the usefulness of traditional approaches for description of defects' behavior. The problem arises of creation of the models of defects and

their behavior which take into account these peculiarities and reliably describe the mechanisms of plastic deformation of the new materials becomes actual [6]

In the mechanics of deformed solids the movement of points is given by the field of translations u_i . The components of rotation vector ω_i in an infinite crystal are:

$$\omega_i = \frac{1}{2} e_{ikl} \left(\frac{\partial u_l}{\partial x_k} \right). \quad (1)$$

To describe the deformed state of solids twist-bend tensor is used, where rotation and bend are described by its diagonal and non-diagonal components, respectively [6]:

$$\kappa_{ij} = \frac{\partial \omega_j}{\partial x_i} \quad (2)$$

The trace of tensor is a scalar value κ_{ij} which represent an isotropic helicity state.

3. AN EDGE DISLOCATION IN A THIN PLATE

The main task is to find expression for local bend angle of a thin plate with edge dislocations, because its gradient can be compared with experimental measurements of twist-bend tensor [4] in contrast to Kroupa who found the expression for the total bend angle created by an edge dislocation in a plate [7].

It is said to be 'thin plate' when its thickness is much lower than sizes in other dimensions. Bend causes tensions in some places in a plate and compressions in the others. Tension takes place on the convex side of a plate. But in the depth of the plate the tension value decreases gradually, reaches zero, and increases gradually in the further layers. Thus, the neutral surface is into the plate where tension is absent and strain has opposite signs along two different sides of it. This surface is situated in the middle of the plate.

One can define the system of coordinates with the point of its origin in the neutral surface and axis y directed normally to it. Then plane xz coincides with the plane of the non-deformed plate. Let us denote the vertical displacements of points from the neutral surface, *i.e.* their y -coordinates by ζ . As to displacement components of these points in the plane xz , they are the values of the second infinitesimal order in relation to ζ and are assumed to be equal to zero. Thus the displacement vector of the points of neutral surface is as follows:

$$u_x^{(0)} = u_z^{(0)} = 0; \quad u_y^{(0)} = \zeta(x, z). \quad (3)$$

Because the displacement vector components u_x and u_y are negligible in the plate, the value of rotation component along axis z is determined by the average rotation of the deformed element (bend angle of the plate), which is defined by the following expression [5]

$$\omega_z = \varphi(x) = \frac{\partial u_y}{\partial x} \quad (4)$$

in contrast to expression (1) for an infinite crystal.

Let us consider the auxiliary problem concerned with determination of the stress field in a thin beam without dislocations. In its point x_m bend moment m (per unit length in direction z) is assumed to be applied. We denote the clockwise rotation direction as positive. Discussion of different calculations methods taking into account the boundary conditions on the surface of the plate, for example, by means of the method of image dislocation, was examined by Kroupa. In the work, calculation of the boundary conditions was carried out according to the simple technical theory [7]: stress σ_{xx} in section ($x = \text{const}$) is distributed linearly as a function of y . Other stress components are equal to zero that satisfies the boundary conditions

on the plate surface (*i.e.*, absence of normal stresses). Cross-sections remain flat, and the solution does not precisely satisfy the main equations of mathematical theory of elasticity. But these results well satisfy the conditions of a thin beam.

Resultant moment of all external moments from the left side of section x is equal to the following expression

$$M(x) = -m \frac{x}{l} + m \theta(x - x_m), \quad (5)$$

where $\theta(x)$ is Heaviside step-like function. Using this expression for $M(x)$ and the technical theory one can easily calculate the stresses:

$$\sigma_{xx}^m = -\frac{M(x)y}{I}, \quad (6)$$

where I is the moment of inertia of the section about the neutral axis. In the case of rectangular section (per unit length in direction z):

$$I = \frac{2}{3} h^3. \quad (7)$$

Local bend of the middle part of the foil surface created by dislocation can be calculated by means of Colonetti theorem. The plate is presumed to be bent under the influence of moment m , and after that dislocation is introduced in it. Due to this introduction the plate in point x_m will bend by angle φ and moment m will perform the work (per unit length in direction z):

$$R = m\varphi. \quad (8)$$

On the other hand according to Colonetti theorem the value of R is determined as follows [8]

$$R = \int dv \sigma_{ij}^m \varepsilon_{ij}^0, \quad (9)$$

where the stress field is defined by formula (6), *i.e.* after appearance of internal stresses the external forces fulfill the work for the own strains ε_{ij}^0 . In this case

$$\varepsilon_{ij}^0 = b \delta_{xi} \delta_{xj} \delta(\xi), \quad (10)$$

where δ_{xi}, δ_{xj} are Kronecker symbols, $\delta(\xi)$ is the delta-function, and axis x is directed along the axis of the plate, ξ is the coordinate calculated from the surface where the displacement vector undergoes a sudden change b_i . Therefore, volume integral (9) can be reduced to integration of σ_{xx}^m along the normal to the neutral line. Substituting (10) and (6) in formula (9) and equating to (8) one can obtain local bend angle for the foil with an edge dislocation:

$$\varphi(x, x_d, y_d, b) = \frac{3b}{4h} \left(1 - \frac{y_d^2}{h^2} \right) \left(\frac{1}{2} - \frac{x_d}{l} - \theta(x - x_d) \right), \quad (11)$$

where l is the foil size along axis x , x_d and y_d are coordinates of cross-sections of the dislocation line and plane xy , $2h$ is a foil thickness. The origin of coordinates is situated in the center of symmetry of the plate. Using (11) and the difference of local bend angles on the edges of foil with dislocation intersecting plane xy in point $(x_d; y_d)$ one can get the known result of Kroupa for the total bend:

$$\varphi_l = \varphi\left(\frac{l}{2}\right) - \varphi\left(-\frac{l}{2}\right) = -\frac{3b}{4h} \left(1 - \frac{y_d^2}{h^2} \right). \quad (12)$$

4. MODELLING OF LOCAL BEND A FOIL

The dislocation model of local bend for sufficiently small distances from the centre was created by us earlier [9]. The main aim of this work is to create the dislocation model describing local bend for large distances from the centre of bend.

Firstly, let us consider the simplest system of dislocation dipole of two edge dislocations with opposite signs divided by the distance $2d$ (arm of dipole). Using (11) one can easily get the following expression for local bend angle of plate with dislocation dipole:

$$\varphi(x, 2d) = \frac{3b}{4h} \left(1 - \frac{y_d^2}{h^2} \right) \left(2 \frac{d}{l} - \theta(x+d) + \theta(x-d) \right). \quad (13)$$

Using (13) and difference of local bend angles on the edges of foil with two edge dislocations intersecting plane xy in points $(-d; 0)$ and $(d, 0)$ one can make sure that the total bend angle is equal to zero. Using (13) one can easily obtain the following expression for local bend angle of plate with the dislocation dipole created by two rows of edge dislocations of opposite signs that are placed in the neutral surface of the foil:

$$\varphi(x, N, d) = \sum_{i=1}^N \frac{3b}{4h} \left[2 \frac{d_i}{l} - \theta(x+d_i) + \theta(x-d_i) \right], \quad (14)$$

where $(+d_i, 0)$ and $(-d_i, 0)$ are locations of dislocations of opposite signs in the foil.

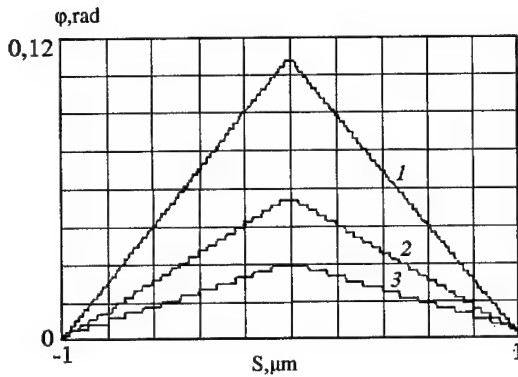


Figure 2. Simulation results for the dependence of local rotation angle on distance S to center of dipole formed by two flat rows of edge dislocations of opposite sign: 1 – $d=0.02 \mu\text{m}$, $N=50$; 2 – $d=0.04 \mu\text{m}$, $N=25$; 3 – $d=0.08 \mu\text{m}$, $N=13$

Simulation results for local bend angle created by two edge dislocations of opposite signs which are placed in the neutral surface of the foil are shown in Fig. 2. Taking into account discreteness of the crystalline structure one can smooth the step-like singularities in expression (14) and differentiating (14) by x one can obtain the xz -component of twist - bend tensor of the dipole created by two rows of edge dislocations of opposite signs

which, are placed in the neutral surface of the foil.

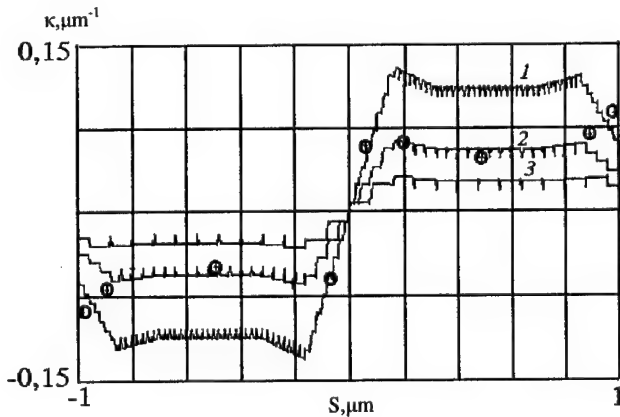


Figure 3. Dependence of twist-bend tensor components on distance S to dipole center: solid line – the results of simulation in thin plate for the dipole of flat rows: 1 – $d=0.02 \mu\text{m}$, $N=50$; 2 – $d=0.04 \mu\text{m}$, $N=25$; 3 – $d=0.08 \mu\text{m}$, $N=13$; dots – experimental results [4]: + - along direction of the largest linear dimension of the contour.

Simulation results for the xz -component of twist-bend tensor of the dipole created by two rows of edge dislocations of opposite signs which are placed in the neutral surface of the foil are shown in Fig. 3.

Comparison with experimental data [4] shows that the best compliance for the large distances from the dipole centre can be reached for the following parameters of dislocation model of local bend angle: the number of dislocation $N=25$, the distance between dislocations along x which is perpendicular to projection of the inclination angle, $d_x=0.04 \mu\text{m}$ (Fig. 3). Therefore, in the former direction the dipole arm is $D_x=Nd_x = 0.51 \mu\text{m}$.

Analysis of stability of such rows [6, 10] showed that the configurations described are not equilibrium, *i.e.* they are not stable and for explanation of then-stability one needs to take into consideration the availability of barriers impeding gliding and climbing dislocations. Cores of extended dislocations in immobile configuration can be such barriers [11]. However, additional information is needed for more detailed discussion of the barriers and mechanisms of their formation.

For comparison one can consider components of the bending-rotation tensor created by a more stable configuration, for example by partial disclinations of opposite sign. In the framework of dislocation theory these disclinations can be presented by tilt boundaries created by two vertical rows of edge dislocations of opposite signs. Using (13) one can obtain the following expression for local bend angle of plate with two rows of edge dislocations of opposite signs situated perpendicularly to the neutral surface, *i.e.* partial disclinations:

$$\varphi(x, N, D) = \sum_{i=1}^N \frac{3b}{4h} \left(1 - \frac{y_i^2}{h^2} \right) \left[2 \frac{D}{l} - \theta(x+D) + \theta(x-D) \right], \quad (14a)$$

where $(+D, y_i)$ and $(-D, y_i)$ are locations of dislocations of opposite signs in the foil. Simulation results for the xz -component of twist-bend tensor of dipole of partial disclinations are shown in Fig.4.

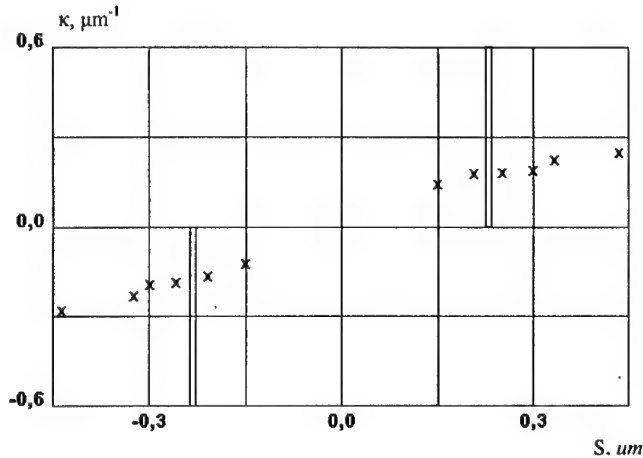


Figure 4. Components of twist-bend tensor as function of distance to a center of partial disclination dipole. Solid lines note the simulation results in thin plate for the dipole with the following parameters $D=0.225 \mu\text{m}$, $N=60$. Crosses (x) note the experimental results for the direction which is perpendicular to the projection of inclination angle [4]

Comparison of experimental data [4] and our simulation results for the plane rows shows that dependence of xz -component twist – bend tensor for the dipole created by two partial disclinations vs. The distance to the dipole center is qualitatively different both from the simulation

results for plane rows of dislocations and experimental data.

Knowing the parameters of the dislocation model of local bend in a thin foil one can easily calculate stresses and strains caused by local bend in an infinite crystal.

According to classic dislocation theory one can easily derive the expression for xz -component twist - bend tensor on plane $y = 0$ in an infinite crystal with the dipole created by two rows of edge dislocations of opposite signs which are placed in the neutral surface of the foil:

$$\langle \kappa_{xz}(x) \rangle = \sum_i \frac{b}{2\pi} \left[\frac{1}{h^2 + \left(x - d_i + \frac{d}{2} \right)^2} - \frac{1}{h^2 + \left(x + d_i - \frac{d}{2} \right)^2} \right] \quad (15)$$

Simulation results of xz -component of twist-bend tensor for the dipole created by two rows ($N = 25$) of edge dislocations of opposite signs on the distance between them $d_x = 0.04 \mu\text{m}$ are shown in Fig.5.

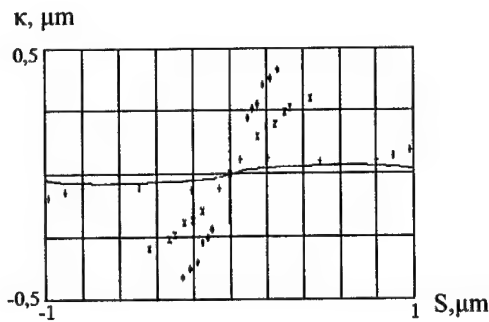


Figure 5. Dependence of twist-bend tensor components on distance S to dipole center: solid line – simulation in unlimited crystal ($d=0.04 \mu\text{m}$ and $N=25$); dots – experimental results.

Comparison with the experimental data [4] showed that (as it should be expected) dislocations cause lower bend in an infinite crystal.

Finally, by means of parameters of dislocation models of local bend we estimate the value of shear stresses σ in crystals with local bend. Then it will be equal to the following expression in the region of local bend

$$\sigma = \mu \frac{Nb}{d},$$

and beyond the region of local bend on the distance L from the center it will be as follows:

$$\sigma = \mu \frac{N^2 bd}{L^2},$$

where μ is shear modulus, N is the number of dislocations in the pile-up, d is a distance between them in the pile-up.

It should be noted that the parameters of dislocations in pile-ups and local density of dislocations can be understated, because we considered that the dipole plane is on the neutral surface of the foil.

5. CONCLUSIONS

Thus, simulation has been achieved of a defect of a complex kind such as local bend on the basis of notions of elementary defects, namely, dislocations. The mesodefekt is represented by two rows of dislocations of opposite signs. Simulation of the defect in such a way gives a close fit with experiment in both components of bending-rotation and dislocation density. According to calculations the aforementioned dislocation system causes smaller bend in an infinite crystal in contrast to a plate. By estimations the shear stress in crystals with local bend in local bend region is linearly proportional to the dislocation density in a pile-up (N/d), and they are proportional to (N^2/L^2) beyond local bend region, *i.e.* they quickly decrease at a distance L from the defect.

The model proposed is based on the combined notions of mechanics of continua and theory of dislocations. By means of this model one can explain the origination of structures with

continuously changing disorientation observed in deformed alloys Cr-45% Fe [13, 14], Nb with oxide particles [13, 14], multicomponent alloys on the basis of Fe— 17% Ni [3, 17, 18]. It not only supports the assumption about creation of local bend in the course of plastic deformation, but also give an opportunity of restoring a mesodefect in its main characteristics by investigations of diffraction contrasts on transmission electron microscopy images of the deformed material.

Acknowledgements: The authors express their sincere appreciation to S. O. Firstov and V. D. Natsik for useful discussion of the problems described in the work and their valuable comments.

6. REFERENCES

- [1] M. Avlonitis, A. Kehagias, E. C. Aifantis. Dislocation model of local bend. Multiscale phenomena in plasticity: from experiments to phenomenology, modelling and materials engineering. Ouranopolis, Greece, 1999.
- [2] A. Konstantinidis, D. Konstantinidis, E. C. Aifantis. Dislocation model of local bend. Multiscale phenomena in plasticity: from experiments to phenomenology, modelling and materials engineering. Ouranopolis, Greece, 1999.
- [3] V. V. Tokij, T. E. Konstantinova, V. B. Primisler, and A. A. Dobrikov, *Metallofiz. Noveishie Tekhnol.*, **16**, No. 3: 65 (1994) (in Russian).
- [4] T. E. Konstantinova, N. V. Tokij, V. B. Primisler, and A. A. Dobrikov, *Ehlektronnaya Mikroskopiya i Prochnost' Materialov* (Electron Microscopy and Strength of Materials) (Kyyiv: IPM NANU: 1994) p. 60.
- [5] M. Yu. Gutkin, *Modeli Defektov i Mekhaniyny Plasticheskoy Deformatsii v Neodnorodnykh Sredakh s Mezo- i Nanostrukturnoj* (Models of Defects and Mechanisms of Plastic Deformation in Heterogeneous Media with Mezo- and Nanostructure) (Thesis of Disser. for Doct. Phys.-Math. Sci.) (RAN: Inst. Problem Mashinovedeniya: St.-Petersburg: 1997) (in Russian).
- [6] F. R. N. Nabarro, *Theory of Crystal Dislocations*, (Oxford: Clarendon Press: 1967).
- [7] F. Kroupa, *Czechoslovak Physical Journal*, **9**, No. 3: 332 (1959).
- [8] V. L. Indenbom, *Tipy Defektov v Reshyotke. Teoriya Dislokatsij* (Types of Defects. Theory of Dislocations: Proc. of School on Theory of Defects in Crystals and Radiation Damage, Telavi GSSR, October 11-28, 1965) (Tbilisi: 1966), Vol. 1, p. 5 (in Russian).
- [9] V. Varyukhin, E. Konstantinova, and N. Tokij, *Met. Phys. Adv. Tech.*, 2000, Vol. 18, pp. 1303-1315. Printed in Singapore.
- [10] J. P. Hirth and J. Lothe, *Theory of Dislocations* (New York: John Wiley: 1982).
- [11] N. V. Tokij, V. I. Zajtsev, and M. A. Dulin, *Metallfizika*, **62**: 99 (1975) (in Russian).
- [12] W. T. Jr. Read, *Dislocations in Crystals* (New York: McGraw Hill: 1953).
- [13] G. F. Sarzhan, V. G. Tkachenko, V. I. Trefilov et al., *Izv. AN SSSR. Metally*, No. 2: 153 (1971) (in Russian).
- [14] Yu. E. Zubets, V. N. Manilov, G. F. Sarzhan et al., *Fiz. Met. Metalloved.*, **35**, No. 3: 609 (1973) (in Russian).
- [15] V. I. Gonchikov, A. N. Tyumentsev, A. D. Korotaev et al., *Fiz. Met. Metalloved.*, **63**, No. 3: 598 (1987) (in Russian).
- [16] V. I. Gonchikov, A. N. Vergazov, A. D. Korotaev et al., *Fiz. Met. Metalloved.*, **64**, No. 1: 170 (1987) (in Russian).
- [17] T. E. Konstantinova, V. B. Primisler, A. A. Dobrikov et al., *Metallfizika*, **13** No. 5: 62 (1991) (in Russian).
- [18] T. E. Konstantinova, V. B. Primisler, and A. A. Dobrikov, *Metallofiz. Noveishie Tekhnol.*, **18**, No. 10: 70 (1996) (in Russian).

6th National Congress on Mechanics

Session B

Volume III

MULTISCALE PLASTICITY: LINKING DISCRETE AND CONTINUUM APPROACHES

L.P. Kubin and B. Devincre
LEM, CNRS-ONERA

29, Av. de la Division Leclerc, BP 72, 92322 Châtillon Cedex, France

1. SUMMARY

The various frameworks used to establish a connection between the discrete and continuum approaches of plasticity necessarily make use of a homogenization procedure that introduces an arbitrary length scale. As exemplified by several examples, this length scale plays the role of a cut-off below which the spatial aspects of some dislocation mechanisms are averaged out.

2. INTRODUCTION

Due to the wide range of time and length scales involved from the atomic scale to that of the bulk material, a physically based model of plasticity still does not exist. Substantial progress has nevertheless been recorded in the past years, both from the numerical and theoretical sides. This progress was partly triggered by the present emphasis on the properties of nanostructured materials, in which size effects become easily observable. In a top-down approach, one tries to incorporate length scales and strain gradients within a continuum frame and to improve the physical content of the constitutive forms used to describe plastic behavior. The bottom-up approach, which is based on dislocation theory, attempts at providing some insight into the evolutionary laws for dislocation densities and is able to rationalize a certain number of size effects. The present discussion is focused on the critical area that involves establishing a connection between the discrete and continuum aspects of plasticity. Several frameworks are successively discussed, that make use of the concept of geometrically necessary dislocations (GNDs), of continuum models of dislocations and of numerical approaches. We focus on the treatment of some dislocation mechanisms governing size effects.

3. LENGTH SCALES AND SIZE EFFECTS

For a full discussion of length scales and size effects, the reader is referred to a recent review by Gil Sevillano [1]. Here, we discuss three different types of size effects that are classified according to their origin. Type I effects are due to the plastic relaxation of non-uniform stresses induced by external loading conditions. In this category, one typically finds size effects in bending or torsion [2] and the indentation size effect. Type II effects stem from the plastic relaxation of internal stresses produced by reasonably stable components of the microstructure, like second phase particles or grain boundaries. More complex are type III effects, which arise from the interaction of mobile dislocations with an evolving microstructure of stored dislocations.

It seems that the first mention of a hardening effect due to the plastic accommodation of elastic strain gradients by dislocations is found in the book by Friedel [3]. With reference to the bending of a specimen, as schematically depicted in Fig. 1, Friedel wrote "the *minimum* density ρ of dislocations with Burgers vector b giving an average curvature c to the lattice is evidently $\rho = c/b$... This density only .. introduces *short-range stresses* on a scale comparable with the average distance between dislocations. One expects therefore a parabolic [hardening] law $\sigma \approx \sigma_0 + (\mu/2\pi)(bc)^{1/2}$. Similar equations can be given for any type of macroscopic distortion".

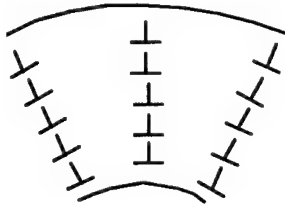


Figure 1 : Tilt walls of geometrically necessary dislocations accommodating an imposed bending.

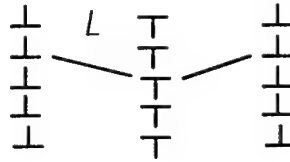


Figure 2 : A regular array of tilt walls with alternating misorientations.

These dislocations are of course geometrically necessary ones in the sense of Ashby [4]. All dislocations are, however, geometrically necessary by definition, since they ensure the accommodation between slipped and non-slipped areas in a crystal. As proposed by Needleman (oral communication) it would be more accurate to refer instead to the net excess density of Burgers vector. These dislocations are assumed to induce an additional short-range hardening by playing the role of "forest" obstacles to dislocations moving in other slip planes.

In the case of type I size effects, the minimum density of GNDs that relaxes the non-uniform elastic stresses can easily be deduced from the imposed loading. One may assume that the dislocations are generated in the bulk material (bending, torsion) or in the plastic zone under an indenter (microindentation). In some other situations, the need to generate dislocations that may, in addition, have a low mobility, can hinder a full relaxation of the elastic stresses. This occurs for example, under a nanoindenter as very small volumes of crystal are not likely to contain preexisting dislocations. Similar situations are also met with epitaxial layers, or around second phase precipitates (type II size effects). In all these cases, the concept of GNDs essentially describes an ideal equilibrium situation that is met only when there is no energy barrier opposed to the relaxation process.

We now consider a typical type III size effect, the hardening produced by dislocation subboundaries formed during plastic flow. Such microstructures are produced at large strains after room temperature deformation or at small strains after deformation by creep at medium and high temperature (cf. Fig. 2). These subgrains accommodate a misorientation $\delta\theta = L/c$ and the usual relation $\rho_{GND} = c/b$ establishes a local connection between the density of discrete GNDs and an equivalent continuous lattice curvature. Several remarks can be made at this step. In the case of Fig. 1, the density of GNDs is easily predictable as the curvature radius is imposed. The distance between the tilt walls is not predictable, however, within a continuum framework. Whether or not it can be predicted within a discrete dislocation framework is still a matter of debate. Microstructures like the one depicted in Fig. 2 occur spontaneously during plastic flow and evolve continuously. Although the misorientations seem to follow definite scaling laws [5], their evolutionary laws for these quantities can only be guessed or assumed. Further, the sign of the misorientations is often found to be spatially correlated with a tendency to alternate from one subgrain to the next. Thus, the net excess density of GNDs significantly depends upon the distance over which the lattice curvature is averaged. This averaging distance plays the role of a coarse-graining dimension for the

transition between discrete and continuum frameworks. As will be seen in the next part, the uncertainties related to its definition seem ubiquitous.

4. HOMOGENIZATION AND LENGTH SCALES

Continuum dislocation models

Several difficulties arise when formulating continuum models for the evolution of dislocation densities inside a crystal [6]. We first discuss the homogenization process that transforms a discrete dislocation density into a continuum one. Consider a set of equations describing the coupled evolution of dislocation populations in time (t) and space. Such models were initiated by Walgraef and Aifantis [7] and further developed in the past years in the context of dislocation patterning. A balance equation is written within a small homogenization volume of linear dimension ℓ . In scalar terms and for each population, we have :

$$\partial \rho / \partial t + \text{div}(\rho v) = \text{reactions} \quad (1)$$

where v is dislocation velocity and ρv a dislocation flux. The reaction side includes a number of dislocation mechanisms like multiplication, annihilation, blocking ... An example of annihilation mechanism is illustrated in Fig. 3, the annihilation by cross-slip of two screw dislocations of opposite sign. Under the effect of their mutual attraction, the two segments can move out of their slip plane and annihilate provided that the distance between the slip planes is smaller than a critical, stress-dependent value h_c . We see from Fig. 3 that if ℓ is taken smaller than h_c , cross-slip enters the transport term at the left-hand side of eq. (1), leading to a gradient form once the flux term is expanded. Conversely, if $h_c < \ell$, the annihilation process is a reaction term and its spatial aspects are averaged out. More generally, a length scale can be attached to each dislocation mechanism, which defines a hierarchy of length scales. The related mechanisms are for instance the annihilation of edge dipoles, the average distance between dislocations or between various obstacles along the dislocation lines, the typical wavelength of dislocation patterns and the grain size in a polycrystal. The values of the related length scales may, in addition, depend on stress when they stem from dislocation interactions. If ℓ increases, mechanisms are progressively shifted from the transport side to the reaction side of eq. (1), until ℓ becomes of the order of the specimen size. Then, the whole dislocation density has been spatially averaged. When ℓ decreases, more mechanisms appear on the transport side of eq. 1, until the homogenization volume contains either zero or one dislocation. At this point, the model becomes a discrete one.

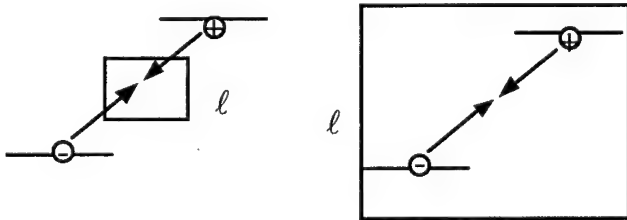


Figure 3: Homogenization of a dislocation process, here the annihilation of two screw dislocations of opposite sign, with different coarse-graining dimensions.

Actually, the dimension of the homogenization volume cannot be fixed by a physical argument. It is arbitrary and depends upon the nature of the mechanisms and length scales that one wishes to account for in a given model. Thus, there are many possible models and the homogenization length scale ℓ governs their spatial resolution, although it never appears explicitly in eq. 1. It seems that the occurrence of this spatial dividing line is the price to pay for integrating the inherently discrete character of dislocation mechanisms into a continuum description.

The discrete-continuum model

The same problem may arise at some point when the connection between discrete and continuum formulations is attempted by ways of numerical simulations. This is illustrated below by the case of one of such hybrid codes, the discrete-continuum model (DCM) [8, 9]. Schematically, in this model, a three-dimensional Dislocation Dynamics (DD) code [10, 11] computes the plastic strain given by dislocation motion under stress, whereas a Finite Element (FE) code is used in parallel to solve the boundary value problem (see [11] for more detail).

The motion of the dislocations, as given by the DD code, has to be converted into a plastic strain field taking specific values at the nodes of the FE code. The local shear strain produced by a dislocation (i) of Burgers vector b_i sweeping an area ΔS_s of a slip plane (s) is, by definition, $\gamma_i = \beta_i \Delta S_s / V$. The volume V is actually a homogenization volume and it can have several definitions. We consider the simplified situation depicted in Fig. 4-a, where a dislocation line has sheared the whole crystal. At the atomic scale, V is the volume of crystal bounded by the two slip planes sheared by the dislocation and the shear strain is a fraction of b/ℓ , where ℓ is now an interplanar spacing. Then, a computation of the resulting stress field by the discrete-continuum model exactly reproduces the result obtained from the elastic theory of dislocations. Within a fully homogenized frame, V is of the order of the specimen volume and ℓ is of the order of the specimen height (Fig. 4-b). The strain is uniform over the whole volume and all information about the localization of the shearing event is lost. The resulting stress field no longer resembles that of a dislocation.

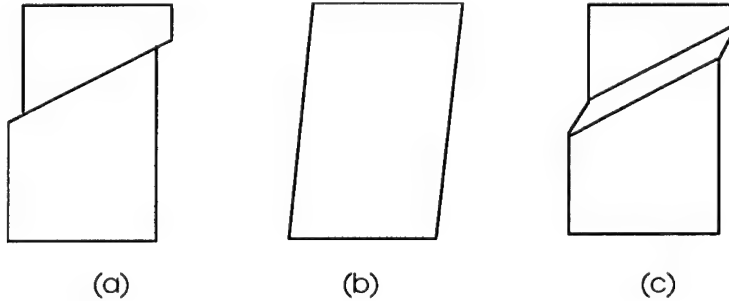


Figure 4: a) A crystal sheared by a dislocation. b) Plastic deformation of the sample within a fully homogenized frame. c) Homogenization within the discrete-continuum model.

Hence, just like in the previous example, the results obtained are sensitive to the choice of a homogenization volume whose value can be fixed in an arbitrary manner. In the DCM, the local shear is uniformized by smearing out the local displacement over a height ℓ that is set to a fraction of FE mesh length (Fig. 4-c). Then, the DCM can incorporate all dislocation length scales larger than the mesh length. By refining the latter, it is possible to obtain an accurate description of the dislocation fields down to atomic scale. A drawback is, however, that dislocation processes with length scales smaller than ℓ cannot be treated within such a frame since the dislocation fields cannot be computed accurately inside the homogenization volume. Finally, one ends up with a hybrid code that incorporates dislocation length scales, but yields results sensitive to the mesh dimension.

5. DISLOCATION SIZE EFFECTS

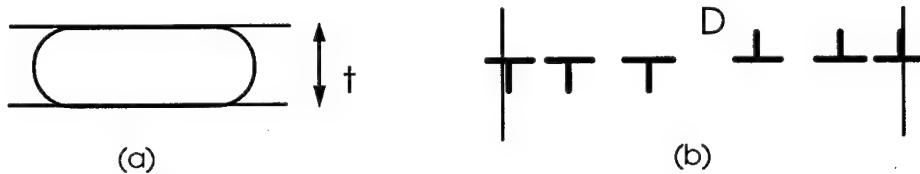


Figure 5. a) - Confinement of a dislocation between two interphases, leading to a line tension hardening proportional to $1/t$. b) - Double dislocation pile-up at a grain boundary.

Two important examples of situations where dislocation properties induce macroscopic size effects are illustrated by Fig. 5. When a dislocation line is blocked at obstacles under stress, it has to reach a critical bowed-out configuration beyond which it either breaks through the obstacles, circumvents them or, as depicted in Figure 5-a, trails interfacial segments. In every case, the applied stress has to overcome a resistance due to line tension effects that is inversely proportional to the inter-obstacle spacing. In lamellar materials, the confinement effect can induce a substantial hardening. A typical case is that of the γ/γ' superalloys, where the ductile γ phase is confined in channels of typical width $0.1 \mu\text{m}$ between cuboidal precipitates of the "hard" γ' phase (linear dimension $\approx 0.5 \mu\text{m}$) in large volume fraction. This composite material may seem to have paradoxical mechanical properties, since in a wide range of temperatures its yield stress is larger than the yield stress of the bulk hard phase. This is only true, however, if one fails to recognize that the yield stress of the confined ductile phase is much larger than the bulk value and may exceed that of the hard phase. The modeling of the yield and flow properties of superalloys typically requires a hybrid framework, as in addition to dislocation mechanisms, it is necessary to consider the complex internal stress states stemming from misfit stresses at the interfaces and the conditions of compatible deformation of the two phases during straining. An application of the DCM to this situation is presented in [11]. Finally, it is worth noticing that the continuum models for strain gradient plasticity seem to largely ignore these line tension effects.

Figure 5-b shows the traditional picture of a double dislocation pile-up at a grain boundary. The Hall-Petch scaling law (hardening proportional to $D^{-1/2}$) can be deduced from the consideration of such configurations. It is the stress concentration at the tip of the pile-up that induces slip activity in the neighboring grains when a critical value is reached [3]. This is a typically non-local mechanism and local continuum frameworks cannot capture it. This can be exemplified by the comparison of internal stress fields obtained from two different simulations of a 2-D composite material by van der Giessen et al. [12]. Within a discrete, non-local formulation, the internal stress shows much sharper contrasts than the local continuum one. Further, the values of these fields, when averaged over areas of different dimensions, are never found to coincide.

Within a different formulation of a Hall-Petch type of relationship [13], it is assumed that grain boundaries essentially affect the mean-free path of dislocations. This induces an additional contribution to the strain hardening rate, in contrast to the previous model that considered only grain behavior at yield. Dislocations are stored at the boundaries at random places and at a rate $dp/d\varepsilon = k/D$, where ε is the plastic strain. Assuming a parabolic hardening law of the form $\sigma = \sigma_0 + \alpha\mu b\rho^{1/2}$, one obtains directly a Hall-Petch scaling after integration. The dislocations piled-up at a grain boundary do not constitute short-range obstacles to other moving dislocations, however. They induce long-range stress fields, so that the parabolic hardening law is perhaps questionable. Finally, in the original formulation by Ashby [4], the GNDs stored at grain boundaries accommodate the compatibility stresses originating from the growing misorientations between deforming grains. Thus, we see that a unified picture of the Hall-Petch effect still does not exist. Further, very little is known from theory about where and in which conditions dislocations generation is initiated in one grain under the influence of the neighboring grains.

6. CONCLUSION

From this short discussion we draw the following conclusions. The concept of geometrically necessary dislocation applies well to idealized situations where the full plastic relaxation of non-uniform stresses induced by known boundary conditions is assumed. This concept is at present of little help as far as evolving dislocation microstructures are concerned, because of its purely static character. Whatever the type of framework used to perform a connection between discrete and continuum plasticity, a homogenization or coarse-graining dimension has to be defined. This leads to a spectrum of possible models depending on the relative value of this dimension with respect to dislocation length scales. Finally, it is emphasized that some important dislocation size effects are not sufficiently accounted for in continuum models or are not sufficiently well understood at the microscale.

7. REFERENCES

- [1] Gil Sevillano, J., Intrinsic and extrinsic size effects in plasticity by dislocation glide, *in Multiscale Materials Modeling*, L.P. Kubin, R. Selinger, J. Bassani and K.J. Cho (Eds.), Symposium Proceedings, MRS, Warrendale PA, (2001), in press.
- [2] Fleck, N. A., Muller, G. G. M., Ashby, M. F. and Hutchinson, J. W., Strain gradient plasticity: theory and experiment, *Acta metall. mater*, 42, 475-487 (1994).
- [3] Friedel, J., *Dislocations*, Pergamon Press Oxford, (1964).
- [4] Ashby, M. F., The deformation of plastically non-homogeneous materials, *Phil. Mag.* 21, 399-424 (1970).
- [5] Pantleon, W., Dislocation boundaries: formation orientation and implications, *in Deformation-Induced Microstructures: Analysis and Relation to Properties*, J.B. Bilde-Sørensen et al. (Eds.), Risø National Lab., Roskilde, Denmark (1999).
- [6] Kosevitch, A. M., Dynamical theory of dislocations, *Sov. Phys. Uspekhi* 7, 837-853 (1965).
- [7] Walgraef, D. and Aifantis, E. C., Dislocation patterning in fatigued metals as a result of dynamical instabilities, *J. Appl. Phys.* 58, 688 (1985).
- [8] Lemarchand, C., Devincre, B., Kubin, L.P. and Chaboche, J.L., Coupled meso-macro simulations of plasticity: validation tests, *MRS Symp Proc*, Vol. 538, V. Bulatov et al. (Eds.), Materials Research Society, Warrendale, PA, 63-68 (1999).
- [9] Lemarchand, C., Devincre, B. and Kubin, L.P., Homogenization method for a discrete-continuum simulation of dislocation dynamics, *J. Mech. Phys. Solids*, in press.
- [10] Devincre, B. and Kubin, L. P., Mesoscopic simulations of dislocations and plasticity, *Mat. Sci. Eng. A* 234-236, 8 (1997).
- [11] Devincre, B., Kubin, L., Lemarchand, C. and Madec, R., Mesoscopic simulations of plastic deformation, *Mat. Sci. Eng. A* (2001), in press.
- [12] Cleveringa, H.H.M., Van der Giessen, E. and Needleman, A., Comparison of discrete dislocations and continuum plasticity predictions for a composite material, *Acta mater.* 45, 3163-3179 (1997).
- [13] Estrin, Y., Dislocation-density-related constitutive modeling, *in Unified Constitutive Laws of Plastic Deformation*, A.S. Krausz and K. Krausz (Eds.), Academic Press, New-York, 69-105 (1996).

MACROSCOPIC MATERIAL BEHAVIOR FROM MICROSCOPIC SIMULATIONS

S. Luding

Institute for Computer Applications 1
University of Stuttgart, G-70569 Stuttgart, Germany

M. Lätzel

Institute for Computer Applications 1
University of Stuttgart, G-70569 Stuttgart, Germany

1. SUMMARY

A challenge of today's research is how to bridge the gap between a microscopic picture and some macroscopic description. The former involves contact forces and deformations, whereas the latter concerns tensorial, macroscopic quantities like the stress or the velocity gradient.

A two-dimensional shear-cell is filled with disks of different sizes, and then examined by means of a "microscopic" discrete element method (DEM). After a consistent averaging formalism is applied, scalar- and vector-fields are obtained and tensorial macroscopic quantities like fabric, stress or velocity gradient can be computed. In addition, micropolar quantities like curvature or couple-stress are discussed.

2. INTRODUCTION

Granular materials are ubiquitous, however, it is still an open issue to describe their rich phenomenology and interesting properties. The macroscopic balance equations for mass, momentum and energy can be used for the modeling of the behavior of granular media. However, they rely on constitutive relations between the physical quantities like stress and strain. The determination of both the physical quantities, important for the behavior of the system, and their inter-relations are subject of current research [2, 10, 24]. One possible way to obtain an observable like, for example, the stress is to perform discrete particle simulations [5, 10, 16] and to average over the "microscopic" forces and contact vectors in the simulation. A typical snapshot from a two-dimensional DEM simulation is displayed in Fig. 1. The aim of this paper is to review recent results for tensorial, averaged continuum quantities involving also micro-polar aspects [15, 25]. After the model system is briefly discussed in section 3, in section 4 our averaging method is introduced and applied to obtain some macroscopic fields in section 5. Section 6 contains the definitions and averaging strategies for fabric, stress, and elastic deformation gradient. The particle rotations are taken into account in section 7 and material parameters are discussed in section 8.

3. MICROSCOPIC APPROACH

The elementary units of granular materials are mesoscopic grains. With DEM [15, 16] the grains are treated as rigid particles but their local deformation at their contact points is realized as virtual overlaps. We relate the interaction forces to this overlap δ and to the tangential displacement of two particles during contact.

The Model System

In the simulations presented in this study, a two-dimensional Couette shear-cell is used. N disks are confined between an outer ring and an inner ring with radius R_o and R_i , respectively. The particles are of slightly different size $d_{\text{small}} = 7.42 \text{ mm}$ and $d_{\text{large}} = 8.99 \text{ mm}$, in order to reduce ordering effects. These

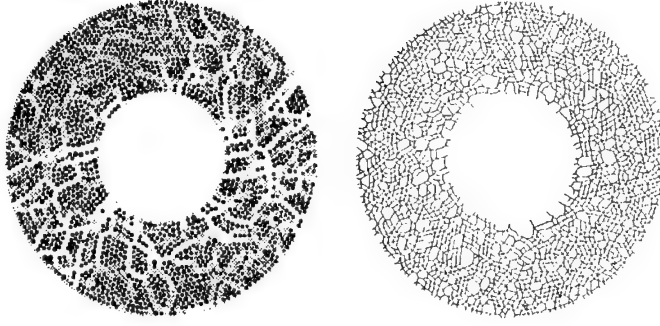


Figure 1: (Left) Representative snapshot of the model system. Light and dark grey indicate large and small values of the contact potential energy, respectively. (Right) Corresponding contact network.

boundary conditions are based on an experiment [11, 23]; for more details and other simulations, see [16, 19]. The outer wall is fixed and the inner wall rotates and thus introduces a slow shear deformation to the system. The simulations are started in a dilute state with an extended outer ring while the inner ring already rotates counter-clockwise with constant angular velocity $\Omega = 2\pi/T_i = 0.1 \text{ s}^{-1}$ and period $T_i = 62.83 \text{ s}$. The radius of the outer ring is reduced within about two seconds to reach its desired value R_o and thereafter it is kept fixed. Averages are performed after about three rotations at $t = 180 \text{ s}$ (to get rid of the arbitrary initial configuration), and during about one rotation, until $t = 239 \text{ s}$. In Fig. 1, a typical snapshot is displayed, where the potential energy of the particles is coded in greyscale so that the stress-chains become visible. Different global volume fractions \bar{v} were examined in the simulations. Here, we present data from three different simulations A, B, and C with $\bar{v} = 0.8084, 0.8149$ and 0.8194 , respectively. For the different simulations the number of large and small particles is N_{small} : 2511, 2545, 2555 and N_{large} : 400, 394, 399. For the calculation of the global volume fraction, the small particles glued to the wall are counted with half their volume only, and thus contribute with $\bar{v}_{\text{wall}} = 0.0047$ to \bar{v} . For more details and material parameters, see [16].

4. FROM MICRO- TO MACRO-DESCRIPTION

In a microscopic, discrete picture, the knowledge of the forces acting on each particle is sufficient to model the statics and the dynamics of the system. Tensorial quantities like the stress σ or the strain ε are not required for a discrete model. In order to establish a correspondence to continuum theories one has to compute tensorial fields as well as scalar material properties like, e. g., the bulk and shear moduli [4, 7, 13, 15–17, 19]. In the following, a consistent averaging strategy is introduced.

The mean value of some quantity Q is defined as

$$Q = \frac{1}{V} \sum_{p \in V} w_V^p V^p Q^p, \quad (1)$$

with the averaging volume V and the particle volume V^p . $Q^p = \sum_{c=1}^{C^p} Q^c$ is a quantity attributed to particle p , where the quantity Q^c is attributed to contact c of particle p with C^p contacts. The weight w_V^p accounts for the particle's contribution to the average, and corresponds to the fraction of the particle volume that is covered by the averaging volume. Since an exact calculation of the area of a circular particle that lies in an arbitrary volume is rather complicated, we assume that the boundaries of V are locally straight, i. e. we cut the particle in slices, see [16] for details.

5. MACROSCOPIC FIELDS

In the following, the averaging formalism in Eq. (1) is applied to obtain various macroscopic quantities. For example, the quantity Q^p can be chosen as ρ^p in order to obtain the density, as $\rho^p v^p$ in order to obtain the momentum density, or as $(1/2)\rho^p (v^p)^2$ for the kinetic energy density. In table 1, the macroscopic fields as well as particle-attributed quantities are collected.

Table 1: Macroscopic fields computed using the averaging formalism in Eq. (1) using particle properties

macroscopic quantity	Q^p
volume fraction ν	1
density ϱ	ϱ^p
flux density νv	v^p
momentum density ϱv	$\varrho^p v^p$

Volume Fraction

As a first example for an averaged scalar quantity, the local volume fraction ν , see Tab. 1, is directly related to the local density via $\varrho \approx \varrho^p \nu$. In Fig. 2, the volume fraction is plotted against the rescaled distance from the inner ring. Starting from an initially uniform volume fraction, a dilated shear-zone forms near the inner wheel as a consequence of the applied shear. This effect is less pronounced for higher initial global densities and, in the outer region of the shear-cell ($\tilde{r} > 10$), the structure of the packing remains frozen, i. e. not much reorganization takes place within the duration of the simulation.

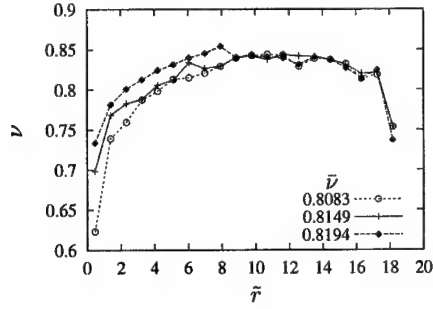


Figure 2: Volume fraction ν , plotted against the dimensionless distance from the origin $\tilde{r} = (r - R_i)/r_0$, with the typical length $r_0 = 8$ mm similar to the particle size, for different initial global densities $\bar{\nu}$

Flux Density

As a tensorial quantity of first order (vector), the velocity field v is obtained when dividing the flux density νv by the volume fraction ν . The momentum density is thus $\varrho v \approx \varrho^p \nu v$. In Fig. 3, the tangential velocity is plotted against the rescaled distance from the inner ring. The simulation data are fitted by a function $v_\phi(r)/\Omega R_i = v_0 \exp(-\tilde{r}/s)$ with v_0 : 0.670, 0.756, 0.788 and s : 1.662, 1.584, 1.191, thus showing an exponential profile corresponding to the shear band. The shear band, has a width of a few particle diameters, before the velocity v_ϕ reaches the noise level.

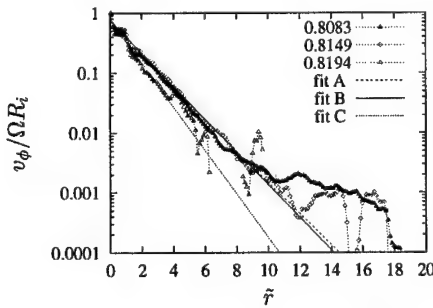


Figure 3: Tangential velocity v_ϕ normalized by the velocity of the inner wheel ΩR_i , plotted against \tilde{r} . The lines are the fits to the simulation data for $\tilde{r} = 0.25$ to 8.1 , using $v_\phi(r)/\Omega R_i = v_0 \exp(-\tilde{r}/s)$ with v_0 : 0.670, 0.756, 0.788 and s : 1.662, 1.584, 1.191, for increasing density, as given in the inset, respectively

Velocity Gradient

Given the velocity field, it is possible to compute the velocity gradient $\nabla \mathbf{v}$, a tensor of second order, by means of numerical differentiation. With $\nabla \mathbf{v}$ one has the components of the symmetric deformation rate

$$D_{r\phi} = \frac{1}{2} \left[\frac{\partial v_\phi}{\partial r} - \frac{v_\phi}{r} \right], \text{ and } W_{r\phi} = \frac{1}{2} \left[\frac{\partial v_\phi}{\partial r} + \frac{v_\phi}{r} \right], \quad (2)$$

the anti-symmetric continuum rotation rate, with the coordinates α and β , see [19] for details and [25] for a similar approach.

6. MACROSCOPIC TENSORIAL QUANTITIES

In this section, the averaged, macroscopic tensorial quantities in our model system are introduced. The fabric tensor describes the statistics of the contact directions, the stress tensor describes the stress distribution due to the contact forces, and the elastic deformation gradient is a measure for the elastic, reversible deformations due to the stress.

Table 2: Macroscopic tensorial quantities computed with Eq. (1) using contact-attributed properties pre-averaged over single particles. In this study, two tensors with no symbol in between mean a dyadic product, whereas ‘.’ is used for the scalar product, i. e. the order-reduction by one for each of the two tensors at left and right.

macroscopic quantity	Q^p
fabric tensor \mathbf{F}	$\sum_{c=1}^{C^p} \mathbf{n}^c \mathbf{n}^c$
static stress tensor $\boldsymbol{\sigma}$	$\frac{1}{V^p} \sum_{c=1}^{C^p} \mathbf{f}^c \mathbf{l}^{pc}$
deformation gradient $\boldsymbol{\epsilon}$	$\frac{\pi h}{V^p} \sum_{c=1}^{C^p} \Delta^{pc} \mathbf{l}^{pc} \cdot \mathbf{F}^{-1}$

Fabric Tensor

In assemblies of grains, the forces are transmitted from one particle to the next only at the contacts of the particles. Therefore, the local geometry and direction of each contact is important [16]. The fabric tensor, in our definition, involves the contact normal vector \mathbf{n}^c , related to the so-called branch vector via $\mathbf{l}^{pc} = a_p \mathbf{n}^c$, with particle radius a_p . For each contact the dyadic product $\mathbf{n}^c \mathbf{n}^c$ is used, i. e. a degenerate tensor of order two with non-zero eigenvalue in \mathbf{n}^c -direction only. In average over many contacts (and over many particles) one obtains the fabric tensor. The fabric tensor in table 2 is symmetric by definition and thus consists of up to three independent scalar quantities in two dimensions. The first of them, the trace (or volumetric part) $F_V = \text{tr}(\mathbf{F}) = (F_{\max} + F_{\min})$, is the contact number density, with the major and the minor eigenvalues F_{\max} and F_{\min} , respectively. With other words, one obtains the relation $\text{tr}(\mathbf{F}) = \nu C$ with reasonable accuracy for monodisperse particles, where C is the average number of contacts per particle. For polydisperse size distribution functions, a multiplicative correction factor was recently proposed [20], which depends on the first three moments of the size distribution function only. The trace of the fabric tensor is a measure for the contact number density, whereas the deviator of the fabric is a measure for the anisotropy of the contact network [15, 16]. In our situation, the contact number density is reduced in the shear zone and the anisotropy, i. e. the deviatoric fraction, is increased in the shear zone, but remains below 20 per-cent [15, 16].

Stress Tensor

The stress tensor $\boldsymbol{\sigma}$ is a measure for the force $\tilde{\mathbf{f}}^c = \boldsymbol{\sigma} \cdot \tilde{\mathbf{n}}^c$, acting on an imaginary surface with normal $\tilde{\mathbf{n}}^c$, per unit area. In order to account for both the stress and the distance of transfer to the center of mass, the static component of the stress tensor [13, 16, 21, 22] is defined as the dyadic product of the force \mathbf{f}^c acting at contact c with the corresponding branch vector, see table 2. Note that the formerly introduced surface quantity is here expressed as the sum over all particles in the averaging volume, with the respective weight factor in Eq. (1), for a detailed derivation see [16]. The diagonal elements of the

static stress tensor are almost constant, whereas the off-diagonal elements decay proportional to r^{-2} , in consistency with continuum theoretical equilibrium conditions [19]. The trace of the stress tensor, is almost constant over the whole shear-cell besides fluctuations. In contrast, the deviatoric fraction decays with increasing distance r from the inner ring, similar to the behavior of the deviatoric fraction of \mathbf{F} .

Elastic Deformation Gradient

In order to reach the final goal, i. e. to obtain the material properties of a granular ensemble, one is interested, e. g., in the stress-strain relationship of the material. The strain ϵ can be obtained by time integration of the velocity gradient, see subsection 5, and subsequent symmetrization and linearization. Here, an alternative quantity is introduced by application of "Voigt's hypothesis", i. e. assuming that the deformation is uniform and that every particle displacement conforms to the corresponding mean displacement field, but fluctuates about it [16, 17]. The deformation gradient in table 2 is calculated for the special case of two-dimensional disks with height h . This relates the actual deformations to a virtual, stress-free reference state where all contacts start to form, i. e. the particles are just touching, see [16] for a detailed derivation. The result is a non-symmetric tensor ϵ , which is *not* the strain. Instead, we refer to it as the elastic deformation gradient, since it accounts only for reversible (elastic) deformations.

Tensor Orientations

The orientations of the tensors \mathbf{F} , σ , and ϵ (data not shown here) are tilted from the radial outwards direction into shear direction [15, 16, 19]. Interestingly, the orientations of the three tensors are different, indicating an anisotropic material. All orientation angles show the same qualitative behavior, however, the fabric is tilted more than the stress which, in turn, is tilted more than the deformation gradient. Thus, the three tensorial quantities examined so far are *not* co-axial.

7. ROTATIONAL DEGREES OF FREEDOM

Due to the particles' surface roughness, forces are transmitted also tangentially and thus granular particles will rotate. Therefore, also micro-polar macroscopic quantities related to the rotational degrees of freedom are of interest [15, 25]. The particle rotation, the couple-stress and the curvature are discussed in this section.

Table 3: Tensorial quantities, connected to the rotational degrees of freedom, computed with Eq. (1)

macroscopic quantity	Q^p
spin density $\nu\omega$	ω^p
couple stress \mathbf{M}	$\frac{1}{V^p} \sum_{c=1}^{C^p} (l^{pc} \times f^c) l^{pc}$
elastic curvature κ	$\frac{\pi h}{V^p} \sum_{c=1}^{C^p} (l^{pc} \times \Delta^{pc}) l^{pc} \cdot \mathbf{F}^{-1}$

Particle Rotation

The mean angular velocity of the particles is obtained by using $Q^p = \omega^p$, see table 3. Note that ω also contains the continuum angular velocity $\omega_c = \mathbf{I} \times \mathbf{W}$, i. e. the vector product 'x' of the continuum rotation rate from Eq. (2) and the unit tensor \mathbf{I} . The excess rotation, or particle eigen rotation, with respect to the underlying mean motion, is thus $\omega^* = \omega - \omega_c$, i. e. the total mean spin minus the continuum spin. In Fig. 4 the (z -components of the) macroscopic particle rotations the continuum rotation and the particle excess-rotation are displayed. Both the particle- and the continuum-angular velocity decay exponentially with increasing \tilde{r} , paralleling the behavior of the velocity v_ϕ . The inset of Fig. 4 shows an oscillation of the excess-rotation near the inner wheel, from one disk layer to the next. This is due to the fact that the disks in adjacent layers are able to roll over each other in the shear zone.

Couple stress

In the framework of a Cosserat continuum [25] one has, in addition to the stress, also the couple stress \mathbf{M} . When an applied stress leads to a deformation, an applied couple-stress causes a rotational motion. It can thus be defined in analogy to the stress by replacing the force by the torque due to the tangential

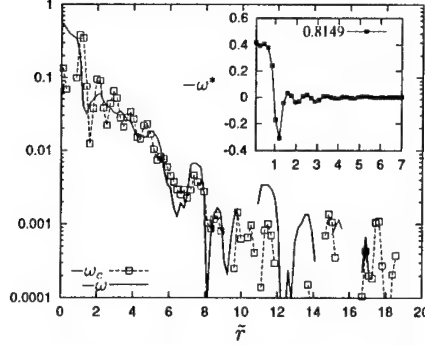


Figure 4: Angular velocities ω (solid line) and ω_c (symbols) of the particles and the continuum, plotted against the scaled radial distance (from simulation B). The dotted line is ω_c as obtained from the fit to v_ϕ , see subsection 5. In the inset, the excess-spin is displayed for the same simulation

component of the force, see table 3. In a two dimensional system with cylindrical symmetry, only the components M_{zr} and $M_{z\phi}$ of the tensor survive. Note that $\mathbf{M} = \mathbf{0}$, when the sum of the torques acting on spherical particles vanishes by definition in static equilibrium.

Elastic Curvature

In analogy to the elastic deformation gradient, we define the curvature κ by replacing the overlap with the respective axial vector, $\mathbf{l}^{pc} \times \Delta \mathbf{l}^{pc}$, see table 3. This leads to a measure for the reversible or “frozen in” rotations in the system. Consequently, in static equilibrium of spherical particles, one has $\kappa = \mathbf{0}$.

8. MATERIAL PARAMETERS

Bulk Stiffness

The material stiffness $\bar{E} = \text{tr}(\sigma)/\text{tr}(\epsilon)$ is here defined as the ratio of the volumetric parts of stress and elastic deformation gradient. In a mean field estimate it is found to be proportional to the “microscopic” contact stiffness k'_n and the trace of the fabric tensor: $\bar{E} \propto (k'_n/2\pi) \text{tr}(\mathbf{F})$. In Fig. 5 the rescaled stiffness of the granular material is plotted against the trace of the fabric. Note that all data collapse almost on a line, but the mean-field value underestimates the simulation data by some per-cent. The few data points which deviate most are close to the boundaries. The deviation from the mean field prediction (solid line in Fig. 5) seems to disappear in the absence of shear.

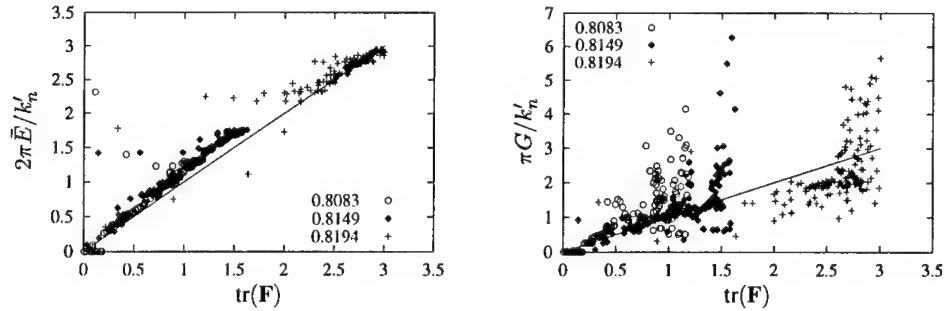


Figure 5: (Left) Scaled granular bulk stiffness $2\pi\bar{E}/k'_n$, plotted against $\text{tr}(\mathbf{F})$. Every point corresponds to one of 150 rings dividing the system. (Right)

Shear Stiffness

The typical shear stiffness of the material is defined as the ratio of the deviatoric parts of stress and elastic deformation gradient $G = \text{dev}(\sigma)/\text{dev}(\epsilon)$ and scales in a crude mean field approximation as

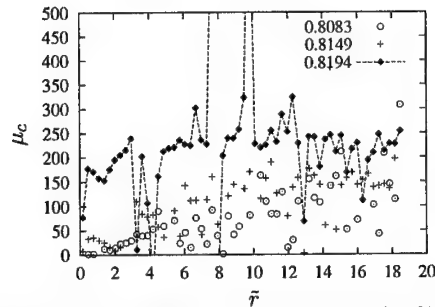


Figure 6: Torque resistance plotted against \bar{r} for 60 rings.

$G \propto (k'_n/\pi)\text{tr}(\mathbf{F})$. In Fig. 5 the ratio of the deviatoric parts of stress and strain is plotted against the trace of the fabric. Like the bulk stiffness, both quantities are proportional, at least for points near or within the dilute shear band. In the denser outer part of the shear-cell, the particles are strongly interlocked and thus resist much more against shear, so that G diverges. The critical contact number density grows with increasing global density, i. e. with increasing stress.

Torque Resistance

Since we are interested in the role the rotational degree of freedom plays for the constitutive equations, we define a new material parameter, the "torque resistance" μ_c , as the ratio of the magnitudes of the couple stress and the curvature components. This quantity describes how strongly the material resists against applied torques. In Fig. 6, μ_c is plotted against the scaled distance from the inner ring. In the dilute regions near to the shear zone, where the particles are able to rotate more easily, μ_c is smaller than in the denser regions, where the particles are interlocked and thus frustrated. This is consistent with the results for increasing global densities, i. e. the torque resistance increases with density. Note that the strongest fluctuations are due to the division by small values and have no physical relevance in our interpretation.

9. CONCLUSION

In brief, the transition from a microscopic to a macroscopic description of particulate materials was achieved. For this, a micro-macro averaging procedure was introduced and, for specific, cylindrical boundary conditions, a shear band is obtained, localized close to the inner, rotating cylindrical wall. Averaging was performed in time and space, leading to reasonably small statistical errors. The averaging strategy implies that the quantities are homogeneously smeared out over single particles which are cut in slices by the averaging volume.

With this averaging approach, the material density, the velocity field, the fabric tensor, the stress tensor and the elastic, (reversible) deformation gradient are obtained from DEM simulations. The tensors are not co-axial and thus indicate an anisotropic material. The system organizes itself such that more contacts are created to act against the shear and also the shear resistance increases with the contact density. From these tensorial quantities, some material properties like bulk and stress stiffness were determined.

In addition, the particles' angular velocity was averaged in analogy to the particle velocity. Subtraction of the continuum rotation from the particle rotation leads to the excess-eigen rotation of the particles, in the spirit of a micro-polar or Cosserat continuum theory. In analogy to the stress and the elastic deformation gradient, we define also the couple stress and the curvature. The quotient of the respective non-zero components gives a "torque-resistance" which increases with increasing local density and stress.

Future research concerns the application of the averaging formalism to other boundary conditions, the use of more realistic particle interaction models (static friction, cohesion), and the measurement of other

macroscopic quantities not discussed here. Also non-stationary situations and dynamic systems are of interest.

Acknowledgements: The authors thanks acknowledge financial support by the Deutsche Forschungsgemeinschaft (DFG).

10. REFERENCES

- [1] R. J. Bathurst and L. Rothenburg. Micromechanical aspects of isotropic granular assemblies with linear contact interactions. *J. Appl. Mech.*, 55:17–23, 1988.
- [2] R. P. Behringer and J. T. Jenkins, editors. *Powders & Grains 97*, Rotterdam, 1997. Balkema.
- [3] F. Calvetti, G. Combe, and J. Lanier. Experimental micromechanical analysis of a 2d granular material: relation between structure evolution and loading path. *Mech. Coh. Fric. Mat.*, 2:121–163, 1997.
- [4] B. Cambou, F. Dubujet, F. Emeriault, and F. Sidoroff. Homogenization for granular materials. *Eur. J. Mech. A/Solids*, 14(2):255–276, 1995.
- [5] P. A. Cundall and O. D. L. Strack. A discrete numerical model for granular assemblies. *Géotechnique*, 29(1):47–65, 1979.
- [6] F. Dedecker, M. Chaze, Ph. Dubujet, and B. Cambou. Specific features of strain in granular materials. *Mech. Coh.-Fric. Mat.*, 5(3):174–193, 2000.
- [7] F. Emeriault and C. S. Chang. Interparticle forces and displacements in granular materials. *Computers and Geotechnics*, 20(3/4):223–244, 1997.
- [8] E. Falcon, C. Laroche, S. Fauve, and C. Coste. Behavior of one inelastic ball bouncing repeatedly off the ground. *Eur. Phys. J. B*, 3:45–57, 1998.
- [9] S. F. Foerster, M. Y. Louge, H. Chang, and K. Allia. Measurements of the collision properties of small spheres. *Phys. Fluids*, 6(3):1108–1115, 1994.
- [10] H. J. Herrmann, J.-P. Hovi, and S. Luding, editors. *Physics of dry granular media - NATO ASI Series E 350*, Dordrecht, 1998. Kluwer Academic Publishers.
- [11] D. Howell and R. P. Behringer. Fluctuations in a 2d granular Couette experiment: A critical transition. *Phys. Rev. Lett.*, 82:5241, 1999.
- [12] D. W. Howell, R. P. Behringer, and C. T. Veje. Fluctuations in granular media. *Chaos*, 9(3):559–572, 1999.
- [13] N. P. Krut and L. Rothenburg. Micromechanical definition of strain tensor for granular materials. *ASME Journal of Applied Mechanics*, 118:706–711, 1996.
- [14] L. Labous, A. D. Rosato, and R. Dave. Measurements of collision properties of spheres using high-speed video analysis. *Phys. Rev. E*, 56:5715, 1997.
- [15] M. Lätzel, S. Luding, and H. J. Herrmann. From discontinuous models towards a continuum description. In P. A. Vermeer et al., editor, *Continuous and Discontinuous Modelling of Cohesive Frictional Materials*, pages 215–230, Berlin, 2000. Springer.
- [16] M. Lätzel, S. Luding, and H. J. Herrmann. Macroscopic material properties from quasi-static, microscopic simulations of a two-dimensional shear-cell. *Granular Matter*, 2(3):123–135, 2000. cond-mat/0003180.
- [17] C.-L. Liao, T.-P. Chang, D.-H. Young, and C. S. Chang. Stress-strain relationship for granular materials based on the hypothesis of best fit. *Int. J. Solids & Structures*, 34:4087–4100, 1997.
- [18] S. Luding. Collisions & contacts between two particles. In H. J. Herrmann, J.-P. Hovi, and S. Luding, editors, *Physics of dry granular media - NATO ASI Series E350*, page 285, Dordrecht, 1998. Kluwer Academic Publishers.
- [19] S. Luding, M. Lätzel, W. Volk, S. Diebels, and H. J. Herrmann. From discrete element simulations to a continuum model. *Comp. Meth. Appl. Mech. Engng.*, 2000. in press.
- [20] M. Madadi, O. Tsoungui, M. Lätzel, and S. Luding. On the fabric tensor of static, polydisperse granular materials. in preparation, 2001.
- [21] L. Rothenburg and A. P. S. Selvadurai. A micromechanical definition of the Cauchy stress tensor for particulate media. In A. P. S. Selvadurai, editor, *Mechanics of Structured Media*, pages 469–486. Elsevier, Amsterdam, 1981.
- [22] M. Satake and J. T. Jenkins. *Micromechanics of granular materials*. Elsevier, Amsterdam, 1988.
- [23] C. T. Veje, D. W. Howell, and R. P. Behringer. Kinematics of a 2D granular Couette experiment. *Phys. Rev. E*, 59:739, 1999.
- [24] P. A. Vermeer, S. Diebels, W. Ehlers, H. J. Herrmann, S. Luding, and E. Ramm, editors. *Continuous and Discontinuous Modelling of Cohesive Frictional Materials*, Berlin, 2001. Springer. Lecture Notes on Physics 568.
- [25] A. Zervos, I. Vardoulakis, M. Jean, and P. Lerat. Numerical investigation of granular interfaces kinematics. *Mech. Coh.-Fric. Mat.*, 5:305–324, 2000.

6th National Congress on Mechanics

Session C

Volume III

MODELLING OF LAMINATED COMPOSITE STRUCTURES WITH PIEZOELECTRIC LAYERS

Amâncio FERNANDES and Joël POUGET

Laboratoire de Modélisation en Mécanique (UMR 7607)

Université Pierre et Marie Curie, Paris, France

1. SUMMARY

A new approach to laminated piezoelectric plates based on an electric potential refinement in the plate thickness coordinate including layerwise modelling and shearing correction is presented. On using a variational formulation the fully electromechanically coupled plate equations are given. In order to account for the interface continuity conditions, Lagrangian multipliers are introduced. A number of benchmark tests is performed on the piezoelectric sandwich plate in cylindrical bending configuration undergoing two types of electromechanical loads (force density and electric potential). Comparisons to finite element simulations demonstrate that the present plate model gives excellent predictions for the global and local electromechanical responses of the piezoelectric composites.

2. INTRODUCTION

Applications of induced strain actuators are spreading widely in various fields of engineering such as precise positioning, adaptive devices for shape control or active damping of vibrations [1]. More precisely, the analysis of piezoelectric composites such as laminated plates requires theories with efficiently accurate approximation of both *sensor* and *actuator functions*. One of the most popular advantage of piezoelectric material is when an electric potential is applied to a piezoelectric element its dimensions change. Conversely, when is stressed mechanically by a force, it generates an electric charge. If the electrodes are not short-circuited a voltage associated with the electric charge can be measured. The most popular simple piezoelectric actuator consists usually of a slab of piezoelectric ceramics. When an electric field is placed across the thickness of the slab, the latter expands or contracts mainly in its length direction. However, the motion of a single slab is extremely small (on the order of one micrometer for one hundred volts). To overcome this limitation, *piezoelectric composites* using flexural-extensional deformation becomes necessary. One of the most practical multilayer piezoelectric composites commonly used is the *piezoelectric bimorph* or bender. The application of an electric field across the two layers of the bender causes one layer to expand while the other one contracts. The global result is a flexural deformation much greater than the length or thickness deformation of the individual layers (on the order of hundreds of microns for

100 volts). More sophisticated multilayer piezoelectric composites could be a sandwich structure made of an elastic center slab sandwiched with two piezoelectric layers. Very interesting technological applications have been proposed, ranging from aeronautical and automotive structures (shape control of large space antennas, active or passive control of vibration, etc.) to miniature positioning devices (mico-robot, medical apparatus, etc.) and many other engineering applications.

The purpose of the study attempts to develop consistent, yet comprehensive approach to piezoelectric plates made of a stack of piezoelectric or/and non-piezoelectric layers. Quite number of recent studies establishing correct and efficient piezoelectric plate model has been reported [2,3]. The various models for laminated piezoelectric structures are classified according to the kinematic assumptions and approximations of field variation through the plate thickness. Here, we propose a *combination of mixed through-the-thickness approximation* including *shear effects* for the elastic displacement and electric potential. More precisely, the present approach combines an *equivalent single-layer* theory for the mechanical displacements with a *layerwise-type approximation* for the electric potential. The modelling, examined here, includes the conservation law of the electric charge, therefore we do not consider any hypothesis on the electric induction. The derivation of the piezoelectric plate equation is based on a variational formulation which allows one to reduce the equations of the full 3D model to those of 2D. In addition, the variational formulation is then generalized to plate made of piezoelectric layers and accounts for the continuity conditions at the layer interfaces. A particular attention is devoted to piezoelectric sandwich plate subject to (i) a force density normal to the upper face and (ii) an electric potential applied to the bottom and top faces of the plate. Some comparisons to numerical results coming from the finite element method leads to excellent predictions of both global (deflexion, electric charge) and local (profiles) responses of the structure.

3. VARIATIONAL FORMULATION OF PIEZOELECTRICITY

Here, we briefly recall the basic ingredients about piezoelectricity and the related variational formulation based on the Hamiltonian principle. The advantage of this method is that it accounts for both the mechanical and electrical aspects simultaneously. The variational principle is stated as [2]

$$\delta \int_{t_1}^{t_2} \int_{\Omega} (K - H) dv dt + \int_{t_1}^{t_2} \int_{\Omega} \delta W dS dt = 0 \quad , \quad (1)$$

where $K = \frac{1}{2} \rho \dot{u}_i \dot{u}_i$ is the kinetic energy, $H = \frac{1}{2} C_{ijpq}^E S_{ij} S_{pq} - \frac{1}{2} \epsilon_{ij}^S E_i E_j - e_{ipq} E_i S_{pq}$ is the enthalpy density function and δW is the variation of the external work with $\delta W = T_i \delta u_i + q \delta \phi$. In addition, we have defined \mathbf{C}^E the fourth-order tensor of elasticity at zero electric field, \mathbf{e} the third-order tensor of piezoelectric coefficients and ϵ^S is the second-order tensor of dielectric constants at vanishing strain. The components of the strain tensor are $S_{ij} = \frac{1}{2} (u_{i,j} + u_{j,i})$ with \mathbf{u} the displacement vector, \mathbf{E} is the electric field which is derivable from an electric potential $E_i = -\phi_{,i}$.

On assuming there are no body forces the variational formulation yield the following governing equations

$$\begin{cases} \sigma_{ij,j} = \rho \ddot{u}_i \quad , \\ D_{k,k} = 0 \quad . \end{cases} \quad (2)$$

The first equation is the usual elasticity equation and the second one is the electric charge conservation or Gauss law. The coupled linear constitutive equations for piezoelectric materials are given by [2]

$$\begin{cases} \sigma_{ij} = \frac{\partial \Pi}{\partial S_{ij}} = C_{ijpq}^E S_{pq} - e_{kij} E_k, \\ D_i = -\frac{\partial \Pi}{\partial E_i} = e_{ipq} S_{pq} + \epsilon_{ij}^S E_j. \end{cases} \quad (3)$$

To the above equations we must add the boundary condition on $\partial\Omega$ where T_i is the surface traction and q is the applied electric charge per unit area.

4. DISPLACEMENT FIELD AND ELECTRIC POTENTIAL EXPANSIONS

Most plate theory consider an expansion of the displacement in power series of the thickness coordinate. In the present model, the displacement field and electric potential are assumed to be of the form

$$\begin{aligned} u_\alpha(x, y, z, t) &= U_\alpha(x, y, t) - zw_\alpha(x, y, t) + f(z)\gamma_\alpha(x, y, t), \quad \alpha \in \{1, 2\}, \\ u_3(x, y, z, t) &= w(x, y, t), \\ \phi^{(\ell)}(x, y, z, t) &= \phi_0^{(\ell)}(x, y, t) + z_\ell \phi_1^{(\ell)}(x, y, t) + P_\ell(z_\ell) \phi_2^{(\ell)}(x, y, t) + g(z) \phi_3^{(\ell)}(x, y, t). \end{aligned} \quad (4)$$

where ℓ is the index of the layer, $z_\ell \in [-\frac{h_\ell}{2}, \frac{h_\ell}{2}]$ (h_ℓ is the thickness of the ℓ th layer, see Fig.1). In the present approach, we consider the following function

$$P_\ell(z_\ell) = z_\ell^2 - \left(\frac{h_\ell}{2}\right)^2, \quad f(z) = \frac{h}{\pi} \sin\left(\frac{\pi z}{h}\right), \quad g(z) = \frac{h}{\pi} \cos\left(\frac{\pi z}{h}\right), \quad (5)$$

where h is the plate thickness which is supposed to be uniform. The case of purely elastic plates has been extensively examined by M. Touratier [4]. It is worthwhile noting that if $f(z) = 0$, we recover the classical Kirchhoff-Love thin plate theory.

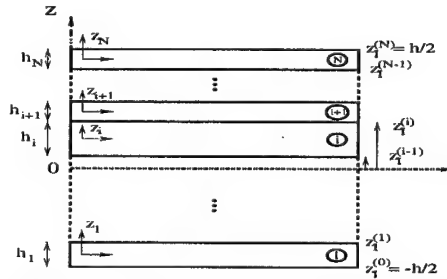


Figure 1 : piezoelectric multi-layered plate

5. PLATE EQUATIONS

In the case of multi-layered plate, we must check the *continuity conditions* for the *electric potential* and *normal components of the electric induction*. These conditions take on the following jump equations

$$\mathcal{A}_\ell = \llbracket \phi \rrbracket_{z=z_\ell^{(\ell)}} = 0 \quad \text{and} \quad \mathcal{B}_\ell = \llbracket D_3 \rrbracket_{z=z_\ell^{(\ell)}} = 0, \quad (6)$$

for the $(2N - 1)$ continuity conditions at the interfaces $z = z_I^{(\ell)}$ between the ℓ th and $(\ell+1)$ th layers ($\ell \in \{1, N-1\}$). In order to account for the condition (6) in the variational formulation we must introduce *Lagrange multipliers* λ_ℓ and μ_ℓ in the Hamilton principle. Then the virtual work due to the continuity conditions can be written as

$$\delta\Lambda = \sum_{\ell=1}^{N-1} \int_{t_1}^{t_2} dt \int_A \delta (\lambda_\ell A_\ell + \mu_\ell B_\ell) dS \quad . \quad (7)$$

Now on using the approximation defined by Eq.(4) in the variational principle Eq.(1) with Eq.(7), the dependency on the thickness variable is integrated out by introducing stress and electric charge resultants. Then, the plate equations (static case) are given by [2,5]

$$\begin{cases} \mathcal{N}_{\alpha\beta,\beta} + f_\alpha = 0 \quad , \\ \mathcal{M}_{\alpha\beta,\alpha\beta} - p = 0 \quad , \\ \hat{\mathcal{M}}_{\alpha\beta,\beta} - \hat{Q}_\alpha + \hat{m}_\alpha = 0 \quad , \\ D_{\alpha,\alpha}^{(m)(\ell)} - \mathcal{D}_3^{(m)(\ell)} + q_m^{(\ell)} = 0, \quad \ell \in \{1, \dots, N\}, \quad \text{and} \quad m \in \{0, 1, 2, 3\} \quad , \end{cases} \quad (8)$$

Moreover, the variation of the Lagrangian multipliers leads to the continuity conditions Eq.(6). Some comments are in order, in the set of Eq.(8) $\mathcal{N}_{\alpha\beta}$ is the stress resultant modified by the Lagrange multipliers, $\mathcal{M}_{\alpha\beta}$ is the stress momentum resultant altered by the Lagrange multipliers, $\hat{\mathcal{M}}_{\alpha\beta}$ is the stress momentum due to the shearing effect, \hat{Q}_α is the shear resultant. In the last Eq.(8) $D_\alpha^{(m)(\ell)}$ and $\mathcal{D}_3^{(m)(\ell)}$ are the electric charge resultants. In Eq.(8) f_α and p are density of force per unit of area and \hat{m}_α is a surface moment density. The associated boundary conditions on the edge \mathcal{C} of the plate can be added, but, we do not present them by sake of simplicity.

Now, we must consider the boundary conditions for the electric potential on the top and bottom faces of the plate, they are

$$\begin{cases} \phi^{(1)}(x, y, -h/2, t) = \phi_0^{(1)}(x, y, t) - \frac{h_1}{2} \phi_1^{(1)}(x, y, t) = -V(x, y, t) \quad , \\ \phi^{(N)}(x, y, +h/2, t) = \phi_0^{(N)}(x, y, t) + \frac{h_N}{2} \phi_1^{(N)}(x, y, t) = +V(x, y, t) \quad , \end{cases} \quad (9)$$

The boundary condition Eq.(9) reduce the number of unknown functions by 2. Then we have $4N + 5$ unknown functions and $2(N - 1)$ Lagrangian multipliers. On the other hand, $4N + 5$ equations with $2(N - 1)$ continuity conditions are available. Nevertheless, the condition of continuity Eq.(6) is replaced by a non-vanishing jump conditions on D_3 when an electric potential is applied to the interfaces, accordingly the Lagrangian multipliers do not apply in this case.

6. NUMERICAL RESULTS FOR A PIEZOELECTRIC SANDWICH PLATE

We consider a piezoelectric laminated plate *simply supported*. A *surface density of normal load* is imposed on the top face and *electric potential* is applied to the top and bottom faces. The shear traction is zero ($f_\alpha = 0$) and there is no moment density (\hat{m}_α). The simple support conditions for a rectangular plate of length L are simulated by $\sigma_{11}(0, z) = \sigma_{11}(L, z) = 0$, $\sigma_{13}(0, z) = \sigma_{13}(L, z) = 0$ and $u_3(0, z) = u_3(L, z) = 0$ (see Fig.2). Moreover, the electromechanical quantities do not depend on the y variable

and the displacement u_2 plays no role in the problem, so that we can set $U_2 = \gamma_2 = 0$. Next, the electromechanical load function can be expressed in the form of Fourier series as uniform surface density S_0 of force and electric potential V_0 . Consequently, a solution to the plate equations satisfying the boundary conditions of the cylindrical bending of a plate simply supported are also searched for in the form of Fourier series. At last, the Fourier coefficients are determined by solving a set of linear algebraic equations of the form $A_n X_n = B_n$ for each n (n being the Fourier coefficient number) where A_n is a symmetric matrix depending on the geometry and material parameters of the layers, X_n is a vector containing the unknown functions and B_n depends on the electromechanical loads.

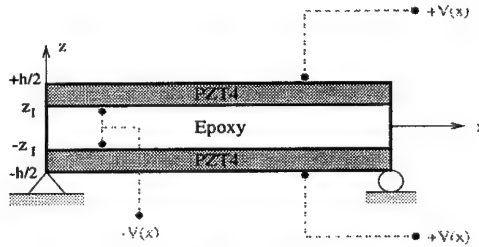


Figure 2 : Piezoelectric sandwich plate with electroded interfaces

In order to illustrate the capability of the present model, we consider a piezoelectric sandwich structure with a length $L = 25mm$, $\ell = L/2$ and $L/h = 10$. The piezoelectric layers are PZT4 ceramics with $h_1 = h_3 = 0.2h$. The results of the present approach are compared to those given by a simplified model (with $f(z) = g(z) = 0$, the Kirchhoff-Love theory) and to numerical simulations performed on the full 3D model by means of finite element method (ABAQUS code).

The numerical results are collected in Fig.3 in dimensionless variables. In this situation the plate is subject to a surface density of force normal to the top face. The flexural displacement at $x = L/2$ is presented in Fig.3.a, the straight line corresponds to the plate model. We note that the error in predicting the maximum values of the deflection, at the plate center, in comparison to the finite element results is excellent and it is less than 5 %. The discrepancy increases for the simplified model and it is about 16 %. Figure 3.b provides the through-the-thickness distribution of the induced electric potential at $x = L/2$, the profile is very close to the 3D computation. Once more, the error goes to the advantage of the present approach.

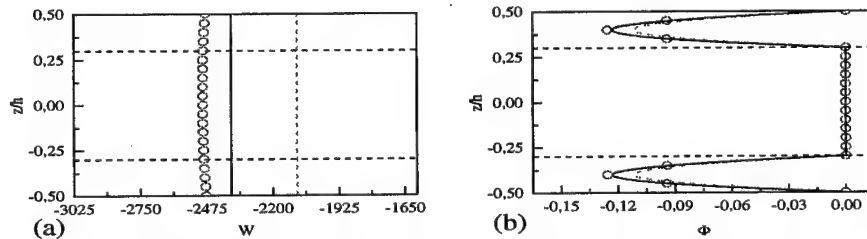


Figure 3 : Piezoelectric sandwich plate - surface density of force

The through-the-thickness profiles of the electromechanical variables produced by an applied electric potential are shown in Fig.4. The straight line in Fig.4.a corresponds to the

deflexion given by present plate model. We note that the result provided by the simplified model is less accurate. The variation of the electric induction is plotted in Fig.4.b, it exhibits very clearly the jump of D_3 at the layer interfaces. This means that surface electric charges are produced on the interfaces and the top and bottom faces, as well. We observe that the discrepancy between the present model and finite element simulation is satisfactory, less than 2 %. Although the simplified model provides rather correct results, it is worse than the refined model.

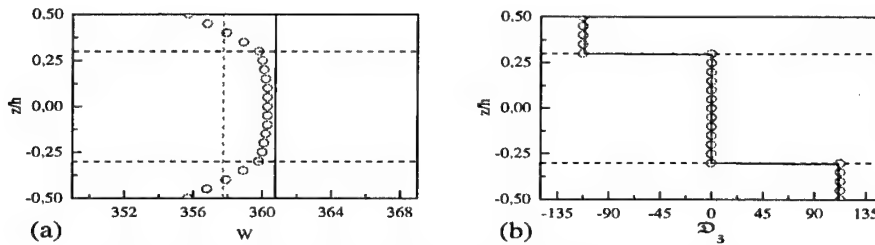


Figure 4 : Piezoelectric sandwich plate - applied electric potential

6. CONCLUSIONS

In the present research work, an efficient and accurate approach to laminated piezoelectric plates has been proposed. The model is based on the combination of an *equivalent single-layered approach* for the *elastic displacements* with a *layerwise-type modelling* for the electric potential. Furthermore, the approach accounts for the shearing correction, which plays an important role in the accuracy of the response prediction. The model thus presented, here, has been tested for two kinds of electromechanical loads (force density and electric potential) applied on the plate faces. In order to ascertain the validity of the present laminated plate approach, we have performed some numerics for a plate made of an elastic layer sandwiched by two piezoelectric slabs. The results indicate that the present model provides some interesting comparison to the results obtained with the finite element method for the full 3D model. The through-the-thickness distribution for mechanical and electric quantities are given with excellent predictions (less than 2 %). Moreover, the refined approach improves the results given by a simplified model.

References.

- [1] Rao S.S. and Sunar M., Piezoelectricity and its use in disturbance sensing and control of flexible structures. A survey, *ASME Appl. Mech. Rev.* **47**, 113-123 (1994).
- [2] Fernandes A. and Pouget J., Two-dimensional modelling of laminated piezoelectric composites. Analysis and numerical results, *J. Thin-Walled Struct.* (to be appeared 2001).
- [3] Saravanan D.A. and Heyliger P.R., Mechanics and computational models for laminated piezoelectric beams, plates and shells, *ASME Appl. Mech. Rev.* **52**, 305-320 (1999).
- [4] Touratier M., An efficient standard plate theory, *Int. J. Engng. Sci.* **29**, 901-916 (1991).
- [5] Fernandes A. and Pouget J., An accurate modelling of piezoelectric plates - Single-layered plate, *Arch. Applied Mech.* (to be appeared 2001).

INVARIANT RELATIONS IN A BOUSSINESQ TYPE EQUATION

Efi Meletlidou

Department of Physics
University of Thessaloniki, 54006 Thessaloniki, Greece
email: efthymia@auth.gr

J. Pouget, G.A.Maugin

Laboratoire de Modélisation en Mécanique, UMR 7607 CNRS,
Université Pierre et Marie Curie, Case 162
4 place Jussieu, 75252 Paris cedex 05, France

E. C. Aifantis

Laboratory of Mechanics and Materials, Polytechnic School
Aristotle University of Thessaloniki, GR-54006, Thessaloniki, Greece

1. SUMMARY

A wide class of partial differential equations have at least three conservation laws that remain invariant for certain solutions of them and especially for solitary wave solutions. These conservation laws can be considered as the energy, the pseudomomentum and the mass integrals of these solutions. We are investigating the invariant relation between the energy and the pseudomomentum for solitary waves in a Boussinesq type equation that comes from the theory of elasticity. It is proven to be neither a classical relation nor a classical field theory one. This contribution is an extract of a more general article [1] under preparation.

2. INTRODUCTION

Hydrodynamics, physics of elastic or plastic media and other fields of physics use models that after some manipulation lead to a certain class of fourth order partial differential equations that are called Boussinesq type equations [2].

At the microscopic level in elastic media one considers the lattice. A model for the displacement of the atoms after deformation depends on the interaction of first and second order neighbours. The resulting differential difference equation is not manageable. Therefore, one uses the continuous approximation and arrives at a Boussinesq type equation [3-8].

At the macroscopic level in elasticity one uses the constitutive equation for the relationship between the stress and the strain tensors. This depends on the model used, is inserted in the equation for the conservation of momentum and models the displacement. In this case also one arrives at a Boussinesq type equation, if one considers that the constitutive equation depends not only on the strain, but also on the second gradient of the strain. This is analogous to the second neighbours interaction for the models at the microscopic level.

The Boussinesq type equations have two important features. They are a nonlinear equation and fourth order with respect to the variables. This is due to the second neighbours interaction and to the second gradient of the strain respectively. In these and various other equations the dispersion (due to the fourth order derivatives) is compensated by the non linearity and solitary waves appear. Another important aspect of partial differential equations are the conservation laws. These are quantities that for certain solutions of the equations (that have some derivatives with respect to the spatial variables that tend to zero as the variables tend to infinity) remain invariant with respect to time. There is also widely known certain partial differential equations that have an infinity of conservation laws and are completely integrable. These equations may have soliton solutions [9-12]. However, a partial differential equation may in general have a finite set of conservation laws. We are going to investigate the elastic-crystal Boussinesq equation (see e.g. [13]), which is probably non-integrable in the above sense. On the other hand, a wide class of partial differential equations are invariant under the Lie groups of time, space and function translations, i.e. they do not change their form under the action of the groups $t \rightarrow t + \varepsilon$, $x \rightarrow x + \varepsilon$ and $u \rightarrow u + \varepsilon$. We have restricted our attention to one-dimensional equations with one spatial and one temporal variable. The

evolutionary infinitesimal representatives of these groups are $u_t \frac{\partial}{\partial u}$, $u_x \frac{\partial}{\partial u}$, and $\frac{\partial}{\partial u}$ respectively. There is also a wide class of partial differential equations that are derived from a variational principle on a Lagrangian density. If the symmetries of an equation possessing a Lagrangian representation are also variational symmetries, then Noether's theorem guarantees that each one of them produces a conservation law. As we will see in the main part of this work, for the pertinent equation the specific symmetries mentioned above, through Noether's theory, produce the conservation laws of the energy, the pseudomomentum and the mass.

We are going to find the invariant relation between the energy and the pseudomomentum of the above mentioned equation following the theory developed by Maugin [13].

3. BOUSSINESQ EQUATION AND CONSERVATION LAWS

The Boussinesq type equation we are going to investigate is

$$\Delta = u_{tt} - du_{xx} + 2au_x u_{xx} + bu_{xxx} = 0 \quad (1)$$

with a, b different from zero. The above equation (1) can be derived from the equation for the conservation of momentum $T_x = u_{tt}$, where T is the stress tensor and u is the displacement. The constitutive equation is $T = f(s_x) + s_{xx}$, where $s = u_x$ is the strain. By expanding $f(s_x)$ in power series up to second order with respect to s_x and substituting it to the conservation of momentum, we find (1).

It is obvious that, since (1) does not depend on x, t, u it is invariant under the Lie group action $t \rightarrow t + \varepsilon_1$, $x \rightarrow x + \varepsilon_2$ and $u \rightarrow u + \varepsilon_3$ respectively. On the other hand, equation (1) is the Euler-Lagrange equation obtained from a variational principle with the Lagrangian

$$L = \frac{1}{2}u_t^2 + \frac{d}{2}u_x^2 + \frac{a}{3}u_x^3 - \frac{b}{2}u_{xx}^2 \quad (2)$$

where the subscripts denote partial differentiation. A Lie group is also a variational symmetry of the system if $\int L dx dt$ remains invariant under the transformation induced by the Lie group. Since also the Lagrangian (2) that produces (1) does not depend explicitly on x, t, u , the above mentioned Lie groups are also variational symmetries.

A conservation law for a differential equation is of the form $\text{div} F = 0$. In our case, since we have a (1+1)D system, it takes the form $(F_1)_t + (F_2)_x = 0$ where $F = (F_1, F_2)$. The conserved quantity that remains invariant with respect to time is

$$\int_{-\infty}^{\infty} F_1 dx. \quad (3)$$

F_1 is called the density of the conservation law. The above conserved quantity remains invariant for those solutions of the equation, for which $F_2|_{-\infty}^{\infty} = 0$. The solitary waves of the equation (1) that we are going to investigate have the property that u_x, u_t and the higher derivatives that appear in F_2 tend to zero as $x \rightarrow \pm\infty$.

Now, Noether's theorem guarantees that, if a Lie group is a variational symmetry of the partial differential equation, it also produces a conservation law. If $u = Q \frac{\partial}{\partial u}$ is the evolutionary infinitesimal representative of a variational symmetry, then

$$Q \cdot \Delta = \text{div} F, \quad (4)$$

i.e. the inner product of Q with the equation itself gives the divergence of F . For the above theory see e.g. [14].

4. DERIVATION OF ENERGY, PSEUDOMOMENTUM AND MASS

We first calculate (3) for the vector field of the energy $Q = u_t$ which, since it corresponds to the homogeneity of time, i.e. to the invariance of Δ with respect to the Lie group $t \rightarrow t + \varepsilon_1$, it corresponds to the conservation of energy. We arrive at the relation

$$\mathcal{E}_t = \left(\frac{1}{2} u_t^2 + \frac{d}{2} u_x^2 - \frac{a}{3} u_x^3 + \frac{b}{2} u_{xx}^2 \right)_t = \left(du_x u_t - a u_x^2 u_t - b u_{xxx} u_t + b u_{xx} u_{xt} \right)_x = \bar{\mathcal{E}}_x \quad (5)$$

where \mathcal{E} is the conserved density of the energy. The conserved quantity E is given by (3) with $F_1 = \mathcal{E}$. By multiplying by $Q = u_x$ equation (1), as shown in equation (4), we find the density of the pseudomomentum, since it corresponds to space translations, in other words to the homogeneity of space.

$$\mathcal{P}_t = (-u_x u_t)_t = \left(-\frac{1}{2} u_t^2 - \frac{d}{2} u_x^2 + \frac{2a}{3} u_x^3 + b u_x u_{xxx} - \frac{b}{2} u_{xx}^2 \right)_x \quad (6)$$

where \mathcal{P} is the density of the pseudomomentum. The conserved pseudomomentum P is given by (3) with $F_1 = \mathcal{P}$. Last we calculate the conservation law for the mass

$$M_t = (u_t)_t = \left(du_x - a u_x^2 - b u_{xxx} \right)_x \quad (7)$$

The conserved quantity \bar{M} is given by (3) with $F_1 = M$.

It is known that equation (1) possesses solitary wave solutions of the form

$$u_\xi = \frac{3(d-c^2)}{2a \cosh^2 \left(\frac{\sqrt{D}}{2} (\xi - \xi_0) \right)} \quad (8)$$

where $D = (d-c^2)/b > 0$ and where $\xi = x \pm ct$. Our solitary wave u_ξ is a kink solitary wave. The above solution is easily found by considering a wave solution of (1) $u(\xi) = u(x \pm ct)$. We replace such a solution in (1), integrate it once and arrive at an ordinary differential equation whose homoclinic solution to the equilibrium (0,0) is (8).

5. THE INVARIANT RELATION BETWEEN E AND P

For the solitary wave solution $u(x-ct)$ we substitute in (1) $u_x = u_\xi$ and $u_t = -cu_\xi$. The conservation law for the energy becomes

$$E = \frac{c^2 + d}{2} \int_{-\infty}^{\infty} u_\xi^2 d\xi - \frac{a}{3} \int_{-\infty}^{\infty} u_\xi^3 d\xi + \frac{b}{2} \int_{-\infty}^{\infty} u_{\xi\xi}^2 d\xi. \quad (9)$$

There are two identities that the derivatives of u with respect to ξ have to satisfy in order for u to be a solution of (1). First of all we present the integrations by parts that will be used for finding these identities. They are

$$\int_{-\infty}^{\infty} u_\xi^2 d\xi = - \int_{-\infty}^{\infty} uu_{\xi\xi} d\xi, \quad \int_{-\infty}^{\infty} u_\xi^3 d\xi = -2 \int_{-\infty}^{\infty} uu_\xi u_{\xi\xi} d\xi, \quad \int_{-\infty}^{\infty} u_{\xi\xi}^2 d\xi = \int_{-\infty}^{\infty} uu_{\xi\xi\xi\xi} d\xi.$$

For solution (8), the partial differential equation (1) can be expressed as an ordinary differential equation with respect to ξ . By multiplying it by u , integrating with respect to ξ from $-\infty$ to ∞ and using the above relations, we discover the first identity we are going to use for the derivation of E and P , which is

$$(d - c^2) \int_{-\infty}^{\infty} u_\xi^2 d\xi - a \int_{-\infty}^{\infty} u_\xi^3 d\xi + b \int_{-\infty}^{\infty} u_{\xi\xi}^2 d\xi = 0. \quad (10)$$

The second identity is derived from (5) for the energy conservation law. For a solitary wave solution we have

$$\begin{aligned} -cE_\xi = \bar{E}_\xi &\Rightarrow -c \int_{-\infty}^{\xi} E_\xi d\xi = \int_{-\infty}^{\xi} \bar{E}_\xi d\xi \Rightarrow -cE(\xi) = \bar{E}(\xi) \Rightarrow \\ -c \int_{-\infty}^{\infty} E(\xi) d\xi &= \int_{-\infty}^{\infty} \bar{E}(\xi) d\xi. \end{aligned} \quad (11)$$

If we replace in (11) the form of E and the form of \bar{E} , the second identity becomes

$$\frac{(c^2 - d)}{2} \int_{-\infty}^{\infty} u_\xi^2 d\xi + \frac{a}{3} \int_{-\infty}^{\infty} u_\xi^3 d\xi + \frac{b}{2} \int_{-\infty}^{\infty} u_{\xi\xi}^2 d\xi = 0. \quad (12)$$

By solving equations (10) and (12), we can find $\int_{-\infty}^{\infty} u_\xi^3 d\xi$ and $\int_{-\infty}^{\infty} u_{\xi\xi}^2 d\xi$ as functions of $\int_{-\infty}^{\infty} u_\xi^2 d\xi$. By replacing them into the expression for the energy (9), we find E as a function of $\int_{-\infty}^{\infty} u_\xi^2 d\xi$,

$$E = \frac{4c^2 + d}{5} \int_{-\infty}^{\infty} u_\xi^2 d\xi. \quad (13)$$

The pseudomomentum $P = - \int_{-\infty}^{\infty} u_x u_t dx$ is easily seen to be

$$P = c \int_{-\infty}^{\infty} u_\xi^2 d\xi. \quad (14)$$

The mass is defined to be $M = \int_{-\infty}^{\infty} u_\xi d\xi = -\bar{M}/c$ and is a conserved quantity, since (7) holds. It is easily computed that

$$M = u|_{-\infty}^{\infty} = \frac{6}{a} \sqrt{b(d - c^2)} \quad (15)$$

The rest mass is obtained for $c = 0$ and is $M_0 = 6\sqrt{db}/a$.

By a procedure analogous to that which resulted in equation (11), for the conservation of mass (7) we can relate $\int_{-\infty}^{\infty} u_{\xi}^2 d\xi$ and $\int_{-\infty}^{\infty} u_{\xi} d\xi$ as

$$a \int_{-\infty}^{\infty} u_{\xi}^2 d\xi = (d - c^2) \int_{-\infty}^{\infty} u_{\xi} d\xi. \quad (16)$$

With the help of (15) and (16), we can express E, P from equations (13) and (14) as functions of c ,

$$E = \frac{6(4c^2 + d)\sqrt{b}}{5a^2} (d - c^2)^{3/2}, \quad (17)$$

$$P = \frac{6c\sqrt{b}}{a^2} (d - c^2)^{3/2}. \quad (18)$$

If we replace in the expression for the energy (13) the integral $\int_{-\infty}^{\infty} u_{\xi}^2 d\xi$ from (14), we find

$$E = \frac{4c^2 + d}{5c} P. \quad (19)$$

We solve relation (19) with respect to c and denote the two roots of this second degree polynomial by c_+ and c_- . They are expressed as functions of E, P as

$$c_{\pm} = \frac{5E \pm \sqrt{25E^2 - 16dP^2}}{8P}. \quad (20)$$

Therefore, if we substitute in the value of P given in (18) either c_+ or c_- , we find the invariant relation between E, P i.e.

$$P - \frac{6\sqrt{b}c_+}{a^2} (d - c_+^2)^{3/2} = 0 \quad (21)$$

or

$$P - \frac{6\sqrt{b}c_-}{a^2} (d - c_-^2)^{3/2} = 0. \quad (22)$$

In order to have the invariant relation as a rational function of E, P it is preferable to take the square of (21) and (22) and multiply them together, since either one or the other is valid. Thus we arrive at an invariant relation between E, P , where we have also replaced the rest mass $M_0 = 6\sqrt{db}/a$,

$$P^4 - \frac{5^3 M_0^2}{4^8 a^2 d P^8} (19 \cdot 4^4 d^3 P^6 E^2 - 7 \cdot 4^3 5^2 d^2 E^4 P^4 + 5^4 4^2 d E^6 P^2 - 5^5 E^8 - 2 \cdot 4^4 d^4 P^8) + \frac{5^6 d^3 M_0^4}{4^8 a^4} \left(d - \frac{E^2}{P^2} \right)^3 = 0 \quad (23)$$

The relations for the solitary wave $u(x + ct)$ are easily derived from the previous relations by the transformation $c \rightarrow -c$. The invariant relation (23) obviously remains the same as it should.

6. CONCLUSIONS

We have been able to find the relation between the energy, the pseudomomentum and the mass, without actually computing the integrals involved. If we consider the solitary wave as a

fictitious "particle" then equation (23) reveals the invariant relation of the energy and the pseudomomentum of the "particle". One can see that it is not either a classical theory relation or a classical field theory one.

Acknowledgements: This work has been supported by the scientific programme PENED-1999, "Gradient theory, stochasticity and self-organization", No 1958/100164, Greece and by the TMR Programme "Spatiotemporal instabilities in deformation and fracture mechanics, materials science and nonlinear physics aspects".

7. REFERENCES

- [1] Meletlidou E., Pouget J., Maugin G. and Aifantis E. (2001) (in preparation).
- [2] Boussinesq J.V. (1872) *J. Math. Pures Appl.* **17**, 55-108.
- [3] Peyrard M., Pnevmatikos S. and Flytzanis N. (1986) *Physica* **19D**, 268-281.
- [4] Flytzanis N., Pnevmatikos S. and Remoissenet M. (1987) *Physica* **26D**, 311-320.
- [5] Pouget J. (1991) *Phys. Rev.* **43B**, No 4, 3575-3581.
- [6] Pouget J. (1991) *Phys. Rev.* **43B**, No 4, 3582-3592.
- [7] Pouget J. (1992) *Phys. Rev.* **46B**, No 17, 10554-10562.
- [8] Pouget J. (1993) *Phys. Rev.* **48B**, No 2, 864-874.
- [9] Gardner C.S., Greene J.M., Kruskal M.D. and Miura R.M. (1967) *Phys. Rev. Let.* **19**, 1095-1097.
- [10] Zakharov V.E. (1974) *Sov. Phys. JETP* **38**, 108-110.
- [11] Axel D. and Aubry S. (1967) *J. Phys. C* **14**, 5433.
- [12] Christov C.I. and Velarde M.G. (1994) *Int. J. Bifurcation & Chaos* **4**, 1095-1112.
- [13] Maugin G.A. and Christov C.I. (1999) in "Non-linear wave Phenomena", Birkhäuser, Boston.
- [14] Olver P.J. (1986) "Applications of Lie Groups to Differential Equations", Springer-Verlag, New York.

Kink Dynamics in a Long-Range Interaction Model*

T. Ioannidou^{1†}, J. Pouget¹ and E. Aifantis^{2‡}

¹*Laboratoire de Modélisation en Mécanique (associé au CNRS),
Université Pierre et Marie Curie, Tour 66, 4 place Jussieu,
75252 Paris Cédex 05, France*

²*Laboratory of Mechanics and Materials, Polytechnic School,
Aristotle University of Thessaloniki, 54006, Thessaloniki, Greece*

Abstract

This paper proposes a one-dimensional lattice model with long-range interactions which, in the continuum, keeps its nonlocal behaviour. In fact, the long-time evolution of the localized waves is governed by an asymptotic equation of the Benjamin-Ono type and allows the explicit construction of moving kinks on the lattice. The long-range particle interaction coefficients on the lattice are determined by the Benjamin-Ono equation.

1 Introduction

This paper is concerned with the effects of long range interactions in the behaviour of solitons (kinks) in a lattice system. In particular, we show that the introduced lattice model asymptotically leads to a nonlocal continuum equation.

The lattice model we study, possesses an inherent nonlocal behaviour, *ie* the motion of a particle at node n depends on the motion of its neighbours (for more details see [1]). More precisely, we show how to keep the nonlocal behaviour of the lattice model at the continuum level, or in other words, how to describe the nonlocality at the continuum level. This transition from the continuum to the discrete system with long-range interactions and vice-versa, is straightforward due to the quasicontinuum approximation. The idea of preserving the nonlocality at the continuum limit occurs in condensed-matter physics to describe phase transition in crystals, nonlinear waves in crystals and biological molecules.

*Talk given by T. Ioannidou

†Permanent Address: Institute of Mathematics, University of Kent, Canterbury CT2 7NF, UK

‡Center for Mechanics of Materials and Instabilities, Michigan Technological University, Houghton, MI 49931, USA

2 The Lattice Model

We consider a one-dimensional lattice with mass M , lattice spacing b and long-range interactions. The Lagrangian of the system is

$$\mathcal{L} = \sum_n \frac{1}{2} M \dot{u}_n^2 - \sum_{nn'} \frac{1}{4} \Psi(n-n') (u_n - u_{n'})^2 - \sum_n \frac{1}{3} k_3 (u_{n+1} - u_n)^3. \quad (2.1)$$

The equations of motion obtained from the variation of (2.1) are

$$M \ddot{u}_n = \sum_{m=1}^{\mathcal{M}} \Psi(m) (u_{n+m} + u_{n-m} - 2u_n) + k_3 [(u_{n+1} - u_n)^2 - (u_n - u_{n-1})^2], \quad (2.2)$$

where k_3 is a positive constant ($k_3 < 1$). $\Psi(n)$ are the interaction coefficients of the particles, related to the force constants $\Phi(n)$ (see equation (2.4)) which determine the effective characteristics of the elastic bonds between the particles.

Here, we consider the chain to be homogeneous and so, the unique definition of $\Phi(n)$ leads to the identity $\Phi(n) = \Phi(-n)$. If $\Phi(n)$ differs from zero for $|n| \leq \mathcal{M}$, then every particle interacts with \mathcal{M} neighbours to the right and to the left.

The distances between the particles do not change and therefore the forces acting on them are equal to zero [2]. This leads to the following condition for the force constants

$$\Phi(0) = - \sum_n' \Phi(n), \quad (2.3)$$

where \sum_n' means summation over all $n \neq 0$. This equation is deduced from the lattice energy invariance; *ie* the invariance by translation of the chain as a whole.

Assume now, that the particles interact nonlocally with measure $\Psi(n)$. Then it can be shown that [2]

$$\Phi(n) = -\Psi(n), \quad n \neq 0; \quad \Phi(0) = \sum_n' \Psi(n). \quad (2.4)$$

Note that for real mechanical systems all $\Psi(n) > 0$ and hence $\Phi(0) > 0$, $\Phi(n) < 0$ ($n \neq 0$). However, a system may be constructed, for which some particles would have negative interaction coefficients; which is the case of our model described below.

3 The Continuum Approximation

By assuming that the displacements are slowly varying over the lattice spacing, the continuum approximation may be derived as follows:

3.1 The Nonlocal Model

The Lagrangian (2.1) in the form which is invariant with respect to n and x representations, can be written as

$$\mathcal{L} = \frac{1}{2} \langle \rho \dot{u}, \dot{u} \rangle + \frac{1}{2} \langle u, \Phi u \rangle - \frac{1}{3} \langle \Delta u, k_3 \Delta u^2 \rangle, \quad (3.5)$$

where ρ is the mass density, while $u = u_n(t)$, $\Delta u = b^{-1}(u_{n+1} - u_n)$ and $u = u(x, t)$, $\Delta u = u_x$ in the discrete and continuum space.

The equation of motion of the medium in the (x, t) representation is

$$\rho \ddot{u}(x, t) = - \int_R \Phi(x - x') u(x', t) dx' + k_3 (u_x^2)_x. \quad (3.6)$$

In the x representation the force constant can be expressed as [2]: $\Phi(x - x') = \frac{\partial^2}{\partial x \partial x'} c(x - x')$, where $c(x - x')$ is the so-called kernel operator of elastic moduli.

Then, equation (3.6) after integration by parts becomes

$$\rho \ddot{u}(x, t) = \frac{\partial}{\partial x} \int_R c(x - x') \frac{\partial u(x')}{\partial x'} dx' + k_3 (u_x^2)_x. \quad (3.7)$$

By letting $c = c_0^2 \delta(x - x') + c_1(x - x')$, where c corresponds to the local response with c_0^2 denoting the local elastic modulus and c_1 describing the nonlocal behaviour of the model, equation (3.7) simplifies to

$$\rho \ddot{u}(x, t) = c_0^2 u_{xx} + \frac{\partial}{\partial x} \int_R c_1(x - x') \frac{\partial u(x')}{\partial x'} dx' + k_3 (u_x^2)_x, \quad (3.8)$$

which is further examined below.

3.2 The Long-Time Evolution of the Localized Wave

By assuming that the contribution of the nonlinear term is significant throughout we rescale the nonlinear and the dispersive term by introducing a small parameter $\varepsilon < 1$, as follows: $2k_3 = \gamma \varepsilon$ and $c_1 = \varepsilon g$. Here, γ is the rescaled nonlinearity coefficient and g is the rescaled elastic kernel. Then, for large times, the asymptotic expansion for the displacement field can be expressed as $u(x, t) = u_0(\xi, \tau) + \varepsilon u_1(x, t) + O(\varepsilon^2)$, where $\xi = x - vt$ is a shifted coordinate and $\tau = \varepsilon t$ is the slow time variable.

Using the above conditions and keeping terms of order ε only, equation (3.8) becomes

$$2\rho v u_{0\xi\tau} + \frac{\partial}{\partial \xi} \int_R g(\xi - \xi') u_{0\xi'} d\xi' + \gamma u_{0\xi} u_{0\xi\xi} = -c_0^2 u_{1xx} + \rho u_{1tt}, \quad (3.9)$$

where $c_0^2 = \rho v^2$.

Then, the secularity condition [3] implies that both the left and right-hand sides of (3.9) are zero. Thus, the right-hand side leads to the standard linear wave equation for u_1 ; while the left-hand side gives the long-time behaviour of u_0 , ie

$$2\rho v u_{0\xi\tau} + \frac{\partial}{\partial \xi} \int_R g(\xi - \xi') u_{0\xi'} d\xi' + \gamma u_{0\xi} u_{0\xi\xi} = 0. \quad (3.10)$$

Finally, by letting $u_{0\xi} = \mathcal{F}$ and $g(z) = \frac{\partial}{\partial z} G(z)$, where $z = \xi - \xi'$ and $y = \xi - z$, equation (3.10) becomes

$$2\rho v \mathcal{F}_\tau + \gamma \mathcal{F} \mathcal{F}_\xi + \int_R G(\xi - y) \frac{\partial^2}{\partial^2 y} \mathcal{F}(y, \tau) dy = 0, \quad (3.11)$$

which transforms to the Benjamin-Ono equation for

$$\tau = \frac{1}{2\rho\nu}T, \quad \mathcal{F} = \frac{1}{\gamma}U, \quad G(\xi - y) = -\frac{\alpha}{\pi} \frac{1}{\xi - y}. \quad (3.12)$$

3.3 The Benjamin-Ono Equation

The Benjamin-Ono evolution equation

$$U_T + UU_\xi + \alpha H(U_{\xi\xi}) = 0, \quad (3.13)$$

with α being a positive parameter, was originally derived in [4, 5, 6] for interval-wave propagation in a two-layer system: one shallow and the other infinitely deep. The operator H designates the one-dimensional Hilbert transform, *ie* $\alpha H(U_{\xi\xi}) = \frac{\alpha}{\pi} \int_R \frac{1}{y-\xi} U_{yy} dy$, which implies that (3.13) is an integro-differential weakly nonlinear evolution equation.

Equation (3.13) has a simple solitary wave solution in the form of a Lorentzian (*algebraic*) shape [3, 7], *ie*

$$U(\xi, T) = \frac{4\nu}{\left(\frac{\xi}{\alpha}\right)^2 (\xi - \nu T)^2 + 1}, \quad (3.14)$$

where 4ν is the amplitude of the wave and $\frac{\alpha}{\nu}$ measures the wavelength. The velocity of the soliton is amplitude-dependent and equals to ν .

4 Numerical Simulations

We propose a numerical scheme by directly considering the lattice equations (2.2), employing a Runge-Kutta method of fourth order and imposing pseudo-periodic boundary conditions, *ie*

$$u(N+i) = u(i) + u_0, \quad i \in [-\mathcal{M}, \mathcal{M}], \quad (4.15)$$

where N is the number of particles in the lattice, \mathcal{M} is the range of particle interactions considered and u_0 is the amplitude of the initial kink.

The initial conditions for the displacements and the velocities of each lattice particle are given by the analytic expression

$$u(x, t) = \frac{2\varepsilon\alpha}{k_3} \arctan\left[\frac{\nu}{\alpha} \left(x - x_0 - c_0 \left(1 + \frac{\varepsilon\nu}{2c_0^2}\right) t\right)\right], \quad (4.16)$$

and its time derivative, respectively. Here x_0 denotes the soliton position and we have set the mass density equal to one ($\rho = 1$).

From Figure 4, one can observe that the initial soliton solution of the Benjamin-Ono equation is also a solution of the lattice model with long-range interactions given by (2.2). In fact, the initial lattice kink relaxes and propagates in the lattice space with small oscillations. It can be observed from Figures 4(a), 4(e) and 4(f) that as the kink thickness increases (*ie* ν decreases) the lattice radiation is eliminated. Numerical simulations of the

discrete nonlocal model for kink widths equal to three or six lattice spacings have been presented in Figures 4(b)-4(d): at this level the kink changes slightly and loses energy by radiation of small amplitudes waves. In all cases where the kink contains at least 20 particles, it is remarkable stable and emits (almost) no radiation.

5 Conclusion

The present work is concerned with the dynamics of lattice models with long-range and nonlinear interactions. The main objective is the description of the dynamics of the lattice model, at the continuum level, by keeping the nonlocal nature of the discrete system. It has been observed from numerics that the initial soliton (kink) solution propagates almost without perturbation and it is very stable. Moreover, wide kinks propagate in the lattice without any loss due to discreteness radiations.

Acknowledgements

This work has been performed in the framework of the TMR European Contract **FMRX-CT-960062**: *Spatio-temporal instabilities in deformation and fracture mechanics, material science and nonlinear physics aspects*. TI acknowledges the Nuffield Foundation for a newly appointed lecturer award.

References

- [1] Ioannidou T., Pouget J. and Aifantis E.: Kink Dynamics in a Lattice Model with Long-Range Interactions, *J. Phys. A: Math Gen*, **In press** (2001), nlin.si/0104053
- [2] Kunin I.A.: *Elastic Media with Microstructure I: One Dimensional Models*, Springer Series in Solid-State Sciences Vol. **26** (Springer - Verlag, Berlin, 1982).
- [3] Nayfeh A.: *Perturbation Methods*, (John Wiley & Sons, New York, 1973).
- [4] Benjamin T.B.: Internal waves of permanent form in fluid of great depths, *J. Fluid. Mech.* **29**, 559-592 (1967).
- [5] Davis R.E. and Acrivos A.: Solitary internal waves in deep water, *J. Fluid. Mech.* **29**, 593-607 (1967).
- [6] Ono H.: Algebraic solitary waves in stratified fluids, *J. Phys. Soc. Japan* **39**, 1082-1091 (1975).
- [7] Abdelouhab L., Bona J.L., Felland M. and Saut J.C.: Nonlocal models for nonlinear dispersive waves, *Physica D* **40**, 360-392 (1989).

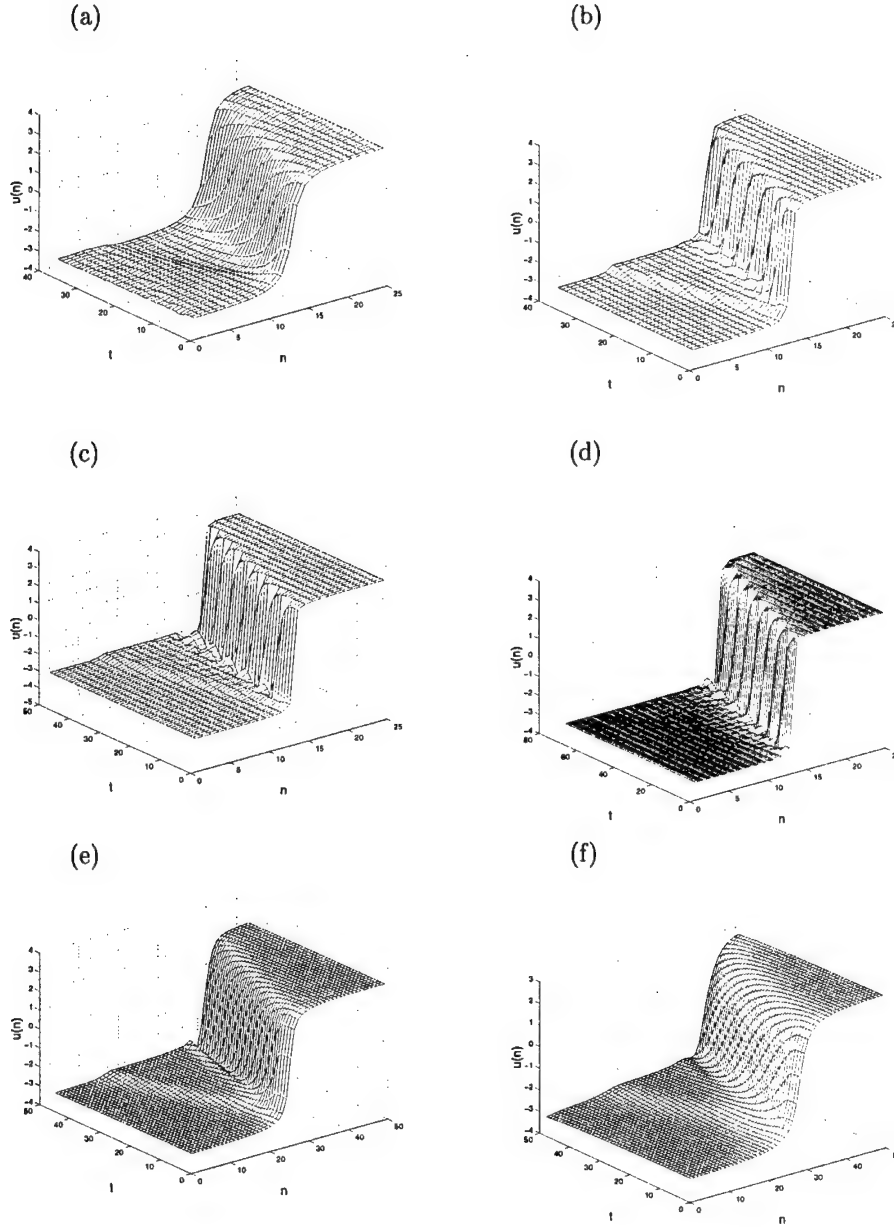


Figure 1: Kink plane for (a) one-range interaction, $\nu = 1/8$, $c_0 = 0.7$ (b) two-range interaction, $\nu = 1/2$, $c_0 = 0.54$ (c) four-range interaction, $\nu = 1$, $c_0 = 0.6$ (d) seven-range interaction, $\nu = 1$, $c_0 = 0.7$ (e) ten-range interaction, $\nu = 1/4$, $c_0 = 0.6$ (f) twenty-range interaction, $\nu = 1/8$, $c_0 = 0.6$.

MAGNETIC SOLITONS

Paul M. Sutcliffe

Institute of Mathematics, University of Kent at Canterbury,
Canterbury, CT2 7NF, U.K.

1 SUMMARY

We study the dynamics of solitons in a Landau-Lifshitz equation describing the magnetization of a three-dimensional ferromagnet with an easy axis anisotropy. We numerically compute the energy dispersion relation and the structure of moving solitons, using a constrained minimization algorithm. We compare the results with those obtained using an approximate form for the moving soliton, valid in the small momentum limit. We also study the interaction and scattering of two solitons, through a numerical simulation of the (3+1)-dimensional equations of motion. We find that the force between two solitons can be either attractive or repulsive depending on their relative internal phase and that in a collision two solitons can form an unstable oscillating loop of magnons.

2 INTRODUCTION

In the continuum approximation the state of a ferromagnet is described by a three component unit vector, $\phi(\mathbf{x}, t)$, which gives the local orientation of the magnetization. The dynamics of the ferromagnet, in the absence of dissipation, is governed by the Landau-Lifshitz equation

$$\frac{\partial \phi}{\partial t} = -\phi \times \frac{\delta E}{\delta \phi} \quad (1)$$

where E is the magnetic crystal energy of the ferromagnet. We have chosen units in which the spin stiffness and magnetic moment density of the ferromagnet are set to one. The case we study in this paper is that of a three-dimensional ferromagnet with isotropic exchange interactions and an easy-axis anisotropy, in which case the energy is given by

$$E = \frac{1}{2} \int (\partial_i \phi \cdot \partial_i \phi + A(1 - \phi_3^2)) d^3 \mathbf{x} \quad (2)$$

where $A > 0$ is the anisotropy parameter and we choose the ground state to be $\phi = (\phi_1, \phi_2, \phi_3) = (0, 0, 1) = \mathbf{e}_3$. In this case the Landau-Lifshitz equation becomes

$$\frac{\partial \phi}{\partial t} = \phi \times (\partial_i \partial_i \phi + A \phi_3 \mathbf{e}_3). \quad (3)$$

This equation has finite energy, stable, exponentially localized solutions known as magnetic solitons [2].

3 STATIONARY SOLITONS

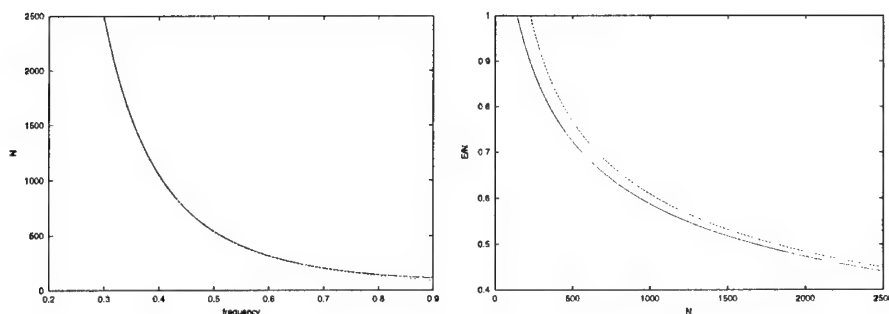


Figure 1: (a) The number of spin reversals, N , as a function of the precession frequency ω . (b) The energy per spin reversal, E/N , as a function of the spin reversal N . The solid curves are the numerical results and the dashed curves are the approximate formulae (6).

In addition to the energy (2), the Landau-Lifshitz equation (3) has two other conserved quantities. These are the number of spin reversals, N , and the momentum \mathbf{P} , given by [3]

$$N = \int (1 - \phi_3) d^3 \mathbf{x}, \quad P_i = \frac{1}{4} \epsilon_{ijk} \int x_j \epsilon_{klm} \phi \cdot \partial_l \phi \times \partial_m \phi d^3 \mathbf{x}. \quad (4)$$

In the quantum description, N counts the number of quasi-particles in the magnet, that is, it may be interpreted as the magnon number. There are no static solitons, but stationary solitons (ie $\mathbf{P} = 0$) have a time dependence which resides only in the constant motion of an internal phase. Explicitly, the stationary soliton has the form

$$\phi = \frac{1}{1 + f^2} (2f \cos(\omega t), -2f \sin(\omega t), 1 - f^2) \quad (5)$$

where ω is the frequency and $f(r)$ is a real profile function. A soliton solution exists only for $0 < \omega < A$, so an anisotropy term is vital for the existence of these

stationary solitons. From now on we set $A = 1$. There is a one-parameter family of stationary solitons parameterized by either the frequency ω or the number of spin reversals N . In figure 1a (solid curve) we plot the relation between these two quantities and in figure 1b we display (solid curve) the energy per spin reversal of the soliton, E/N as a function of N . In the limit of small ω the following asymptotic formula may be derived, which are valid for large N

$$N = \frac{64\pi}{3\omega^3}, \quad E = \frac{32\pi}{\omega^2} = (72\pi N^2)^{1/3}. \quad (6)$$

The dashed curves in figures 1a and 1b are obtained from these asymptotic formulae and fit the numerical results well.

4 MOVING SOLITONS

To compute moving solitons is a more difficult task than in the stationary case and can not be reduced to simply solving an ordinary differential equation, though it can be formulated as a minimization problem. Let $\hat{E}(\mathbf{P}, N)$ be the minimal value of E for fixed values of the momentum \mathbf{P} and number of spin reversals N . Then the solution of this constrained minimization problem produces a soliton solution which moves at constant velocity \mathbf{v} and rotates in internal space with frequency ω , where

$$\omega = \left. \frac{\partial \hat{E}}{\partial N} \right|_{\mathbf{P}}, \quad v_i = \left. \frac{\partial \hat{E}}{\partial P_i} \right|_N. \quad (7)$$

A moving soliton has an axial symmetry in the plane perpendicular to its momentum \mathbf{P} , which, without loss of generality, we choose to be $\mathbf{P} = (0, 0, P)$.

In figure 2 we plot (crosses) the energy dispersion relation, $\hat{E}(P, N)$ obtained from these computations for the three values $N = 204, 317, 542$ (corresponding to $\omega = 0.7, 0.6, 0.5$ for $P = 0$). The energy increases with N so the data need not be labelled individually. The soliton velocity, if required, can be read-off from this data by making use of formula (7).

There is an approximate initial condition for the field ϕ given by

$$\phi = \frac{1}{1+f^2} (2f \cos(Px_3/N), 2f \sin(Px_3/N), 1-f^2) \quad (8)$$

where $f(r)$ is the stationary soliton profile function with N spin reversals, which we have already introduced earlier. One can easily verify that this configuration has N spin reversals and momentum P . The dispersion relation obtained from this approximation is also displayed in figure 2 (solid curves) for comparison with the full numerical results. This reveals that this ansatz is not a good approximation if $P \gg N^{2/3}$.

The explanation for this failure can be found by examining how the spin reversal density changes with increasing momentum. In figure 3 we plot, in the

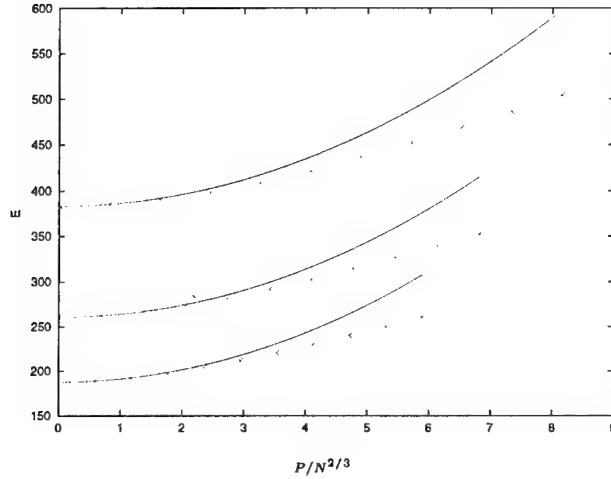


Figure 2: The energy, E , as a function of the scaled momentum, $P/N^{2/3}$, for the three values $N = 204, 317, 542$. The crosses represent the numerical data and the curves are obtained from the small momentum approximation.

$x_2 = 0$ plane, the spin reversal density, $1 - \phi_3$, for the soliton with $N = 317$ and four different values of the scaled momentum, $P/N^{2/3} = 0, 6.8, 13.6, 68.2$. We see that the spherical assumption in the ansatz is substantially violated for $P \sim N^{2/3}$, with the true soliton being stretched in the plane orthogonal to its motion. For very large momenta, $P \gg N^{2/3}$, there is a transition from a single lump of magnons into a magnon loop, in which the spin reversal density is now localized around a circle in a plane perpendicular to its motion.

5 MULTI-SOLITON INTERACTIONS

In this section we discuss the results of a numerical evolution of the full time-dependent Landau-Lifshitz equation (3) in order to investigate the interaction and scattering of two solitons. As an initial condition we take two solitons, each corresponding to a stationary soliton with $N = 317$, placed on the x_3 -axis at the positions $x_3 = \pm 7$, with the internal phase of the second soliton rotated by an angle α relative to that of the first. Figure 4 displays the subsequent evolution of their relative separation for the cases when there is no relative phase, that is $\alpha = 0$, (bottom curve) and when the two solitons are exactly out of phase, that is $\alpha = \pi$, (top curve).

From figure 4 we see that when there is no relative phase the two solitons

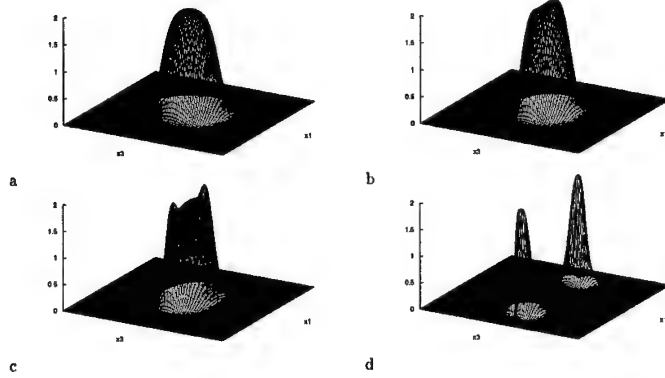


Figure 3: The spin reversal density, $1 - \phi_3$, in the $x_2 = 0$ plane, for the soliton with $N = 317$, and four values of the scaled momentum, $P/N^{2/3} = 0, 6.8, 13.6, 68.2$

attract and form a single larger soliton, but when the solitons are out of phase they repel and quickly settle to a state in which the two solitons are moving away from each other at a constant speed. Thus we have demonstrated that the force between two solitons can be attractive or repulsive depending on their relative phase.

Next we consider initial conditions in which two solitons (with zero relative phase) are sent towards each other with a momentum $P = \mp 158$. In figure 5 we display a fully three-dimensional isosurface plot corresponding to the surface where $1 - \phi_3 = 1.5$, at six different times $t = 0, 20, 30, 65, 80, 115$. We see that the two solitons collide and form a single lump which then expands to form an axially symmetric loop of magnons, which initially expands and then contracts to produce two solitons which move apart along the initial line of approach. The solitons then attract once more, repeating the above pattern until eventually the configuration settles to a single large soliton with no momentum. Clearly this complicated process requires further study and hopefully a more analytical understanding will emerge.

6 CONCLUSION

We have used several different numerical techniques to study the dynamics and interaction of magnetic solitons in a three-dimensional ferromagnet with easy-axis anisotropy. We have computed moving solitons and demonstrated a transition from lump-like solitons to ring-like solitons. We have found that the interaction between two solitons has a strong dependence on their relative phase and that the collision of solitons can be highly non-trivial and lead to the formation of unstable magnon loops.

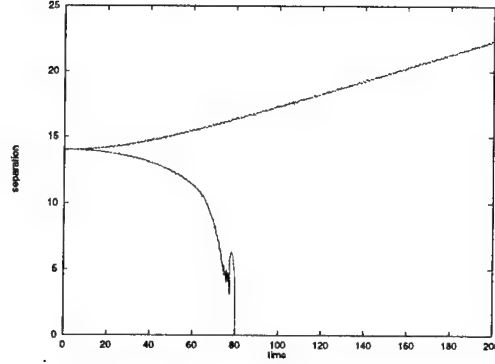


Figure 4: The time evolution of the separation between two initially stationary solitons. The relative internal phase, α , is set to 0 (bottom curve) and π (top curve).

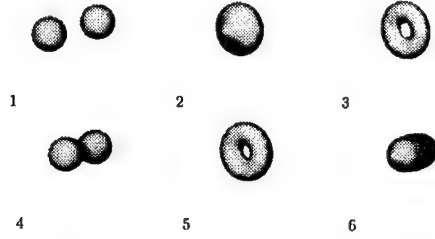


Figure 5: Isosurface plots of $1 - \phi_3 = 1.5$ at times $t = 0, 20, 30, 65, 80, 115$ during the collision of two solitons.

Acknowledgements: The work reported here was done in collaboration with Theodora Ioannidou and more details can be found in [1].

References

- [1] T. Ioannidou and P.M. Sutcliffe, *Physica D* 150, 120 (2001).
- [2] A.M. Kosevich, B.A. Ivanov and A.S. Kovalev, *Phys. Rep.* 194, 117 (1990).
- [3] N. Papanicolaou and T.N. Tomaras, *Nucl. Phys. B* 360, 425 (1991).

THE PROPAGATION OF STRAIN WAVES IN MATERIALS WITH MICROSTRUCTURE

A.I. Potapov and V.M. Rodyushkin

Mechanical Engineering Institute of the Russian Academy of Sciences
603024 Nizhny Novgorod, Russia

1. ABSTRACT

Transmission of an impulse with a velocity different from the velocity of longitudinal waves in a material with microstructure was observed in experiment. The internal structure of such a medium is shown to impart to its wave properties features that cannot be described within the framework of the classical theory of elasticity.

2. INTRODUCTION

Exhaustive investigation of dynamical behaviour of materials with microinhomogeneities is impossible within the framework of classical models of continua that ignore the structure of the material. Such complex media include numerous materials existing in the nature whose properties are determined by mesostructure: dislocations, grains, residual internal stresses and microcracks [1-3], as well as granular and reinforced materials [4]. In spite of diverse molecular structure, the inner space of nearly all optically non-transparent constructive materials is accessible for waves of mechanical origin. Therefore, internal structure and physico-mechanical properties of real media are investigated by the methods of acoustic probing that differ by the type of action on material [5, 6, 8, 10].

3. EXPERIMENTS

In the present research strain waves in materials with microstructure were investigated employing pulsed action and subsequent observation of material response. Dynamical tests were carried out by the Kolsky technique using the Hopkinson split rod. The medium under consideration in the form of a cylindrical sample 20 mm in diameter was placed between two steel cylinders. A striker (a steel cylinder 50 to 150 mm long) was brought up to the speed of 10-20 m/s by means of a gas gun and struck the edge of the steel rod thus exciting in it a one-dimensional strain wave. A pair of transducers arranged on the rods symmetrically relative to the sample recorded the wave incident on the sample as well as after it traversed the sample and was reflected at it. Signals from the transducers were recorded by a digital oscillograph. The discretization time was 500 ns, and the total duration of the recordable dynamical process amounted to 500 mcs (or 1024 points). The experimental technique was described in detail in [7].

In interpreting experimental oscillograms it is important to take into account that the compression (or tension) pulse changes its polarity depending on the medium from which it

arrives and to which it gets. Since the impedance of the sample is always less than that of the steel rods, the reflection coefficient at the front edge of the sample (i.e., at the soft boundary) is negative and the reflected impulse changes polarity. When the wave is reflected at the back edge (hard boundary), the reflection coefficient is positive and polarity of the reflected impulse remains unchanged. Apparently, the curve for the response of the transducer placed on the rod in front of the sample (point x_1) is a sum of oscillograms of the incident signal $\xi_1(x_1, t)$, of the signal reflected at the front edge of the sample $\xi_2(x_1, t)$, of the signal reflected at the back edge $\xi_3(x_1, t)$, and so on while re-reflections go on. For a sample of small length, the delay ($\tau_0 = l_{\text{samp}}/C_{\text{samp}}$) of the time of arrival of the signal $\xi_3(x_1, t)$ from the time of arrival of the signal $\xi_2(x_1, t)$ is less than the impulse duration τ , and the summed parts $\xi_n(x_1, t)$ overlap. The sophisticated structure of the response makes the obtained oscillograms hard to interpret and demands modelling of the shape of response by calculating several first re-reflections of the signal. For example seven re-reflections were calculated in [8, 9].

The impulse velocity C_{rod} in a steel rod can be found in experiments by the time that elapsed between the maxima of the signal that passed a calibrated distance. This method is invalid for a sample of small length. The velocity C_{samp} of such a sample is usually determined indirectly, by known or measured parameters of the materials, such as Young's modulus E and density ρ . For direct determination of C_{samp} in experiments one needs to use samples in which the delay time is longer than the impulse duration ($\tau_0 > \tau$). This condition contradicts the requirements of the Kolsky method. The classical variant of this method implies the use of short samples (with the length less than the diameter) in which a homogeneous stress-strain state is realized. In our experiments we used both short and long samples in which a stress-strain state is not homogeneous, instead it is a superposition of travelling strain waves.

The tested materials were aluminium alloy taken as a reference medium without microstructure and tungsten-epoxy composite fabricated from epoxy resin and round tungsten granules 0.002-0.2 mm in diameter. The density of the composite was about 2000 kg/m³. The velocity of longitudinal waves was measured acoustically to an accuracy of 50 m/s employing the pulsed technique [5, 6] according to which the time during which the ultrasound wave impulse travels a known distance is measured. The velocity in the composite at the frequencies of 1-5 MHz was measured to be $c_l \approx 1950$ m/s. The damping at those frequencies was 4.5-5 dB/cm. The dynamical elasticity modulus measured by the Kolsky technique in the sample 20 mm thick for deformations up to 0.02 was 4502 MPa. Results of independent tests for the sample of the same material were well reproducible. Typical oscillograms of the sample response to dynamical action are shown in figs.1-3. Experiments were carried out for two samples, 10 mm and 75 mm long, made so as to meet the requirement $\tau_0 < \tau$ in the first case and $\tau_0 > \tau$ in the second case. The results obtained were compared with the reference sample of aluminium alloy. The upper oscillogram in the figures corresponds to the signal from the transducer placed on the support rod at a distance of 50 cm behind the sample, the lower oscillogram to the signal from the transducer placed on the measuring rod 50 cm in front of the sample. The ordinate axis is given in arbitrary units proportional to sample deformation, and the abscissa axis is the time scale in microseconds.

The measured time delay between the maxima of the incident and reflected impulses at a distance of 100 cm was used to find the impulse velocity in the rod $C_{\text{rod}} = l_{\text{rod}} / T = 5000$ m/s that agrees well with the calculated velocity $C_{\text{rod}} = (E/\rho)^{1/2}$ for the rod material. Noises caused by the interaction of the rod and sample surfaces (misalignment, roughness, nonflatness, and so on) were observed in the measured signal. It is clear from fig. 1 that the dynamical response of the samples of the tested materials (aluminium alloy, epoxy compound) are well predictable

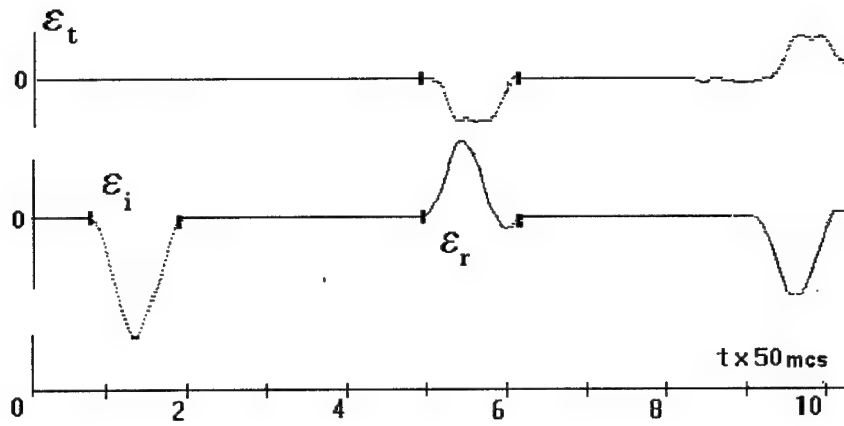


Figure1: Response of the reference aluminium alloy sample

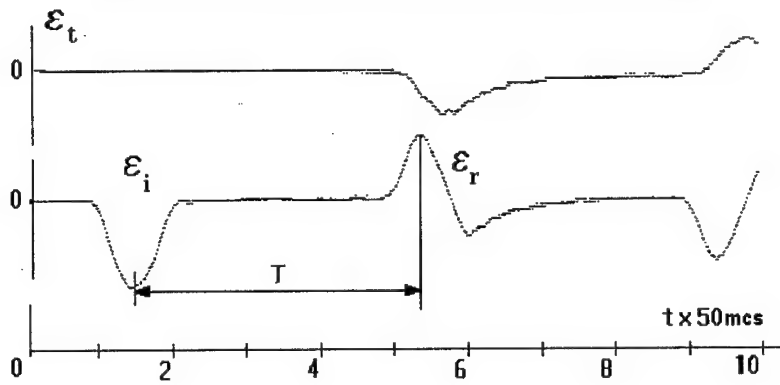


Figure2: Response of a 10 mm long sample of material with microstructure

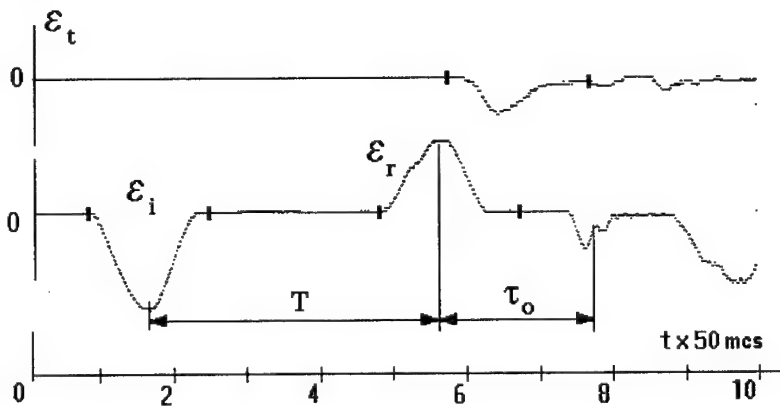


Figure3: Response of a 75 mm long sample of material with microstructure

Small differences are due to weakening of the signal caused by dissipation in the medium. The difference between predicted and experimental response becomes more pronounced in samples of tungsten-epoxy composite, when the signal weakens and time discrepancy appears (figs. 2,3). Such effects were observed only in samples of tungsten-epoxy composite and were not revealed in aluminium alloy samples.

4. DISCUSSION

The samples had identical design and conditions of dynamical loading. Consequently, it is natural to conjecture that the observed differences in responses are caused by the distinctive features of the internal structure of the tested materials. The responses differ not only in signal absorption due to different energy dissipation of oscillations in materials but also in appearance in the oscillogram of new, additional oscillations, which agrees with results of the experiments described in [8-10]. This effect is due to the existence in the medium with internal structure of new types of oscillations predicted by the theory. As a result of dynamical excitation these oscillations are excited in the sample and propagate in it transferring the excitation energy with velocities other than longitudinal waves. To unambiguously show the presence of new types of oscillations in a medium with internal structure it is necessary to investigate the appearing "distortions" of the impulse in samples of different lengths. Because the excitation energy is transferred in the sample with smaller velocity than the primary impulse, the latter "spreads" (see the short sample in fig. 2). On passing a sufficiently long path, part of the impulse attributed to oscillations of the new type will separate from the primary impulse and exist independently, which is accompanied by disappearance of the distortions earlier observed in the primary impulse.

The method described above allows one to determine the velocity of strain pulse in a material with microstructure. From fig. 3 it follows that $C_{\text{SAMP}} = 2 l_{\text{SAMP}} / \tau_0$ can amount to 1200-1300 m/s. The spread is due to ambiguity in determining the reference point when measuring the time of impulse propagation and to the influence of the impulse delay in the transition sample-rod layer.

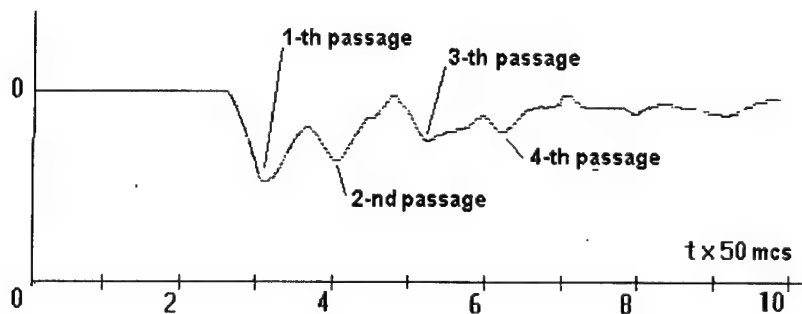


Figure4: Response of a sample made of material with microstructure. The signal is obtained from transducer placed in the longitudinal direction directly on the sample

Analysis of dynamics of an impulse in a sample enabled us to decrease the influence of the above mentioned causes on results of measurements. Oscillograms of the signals from the transducers placed directly on the sample (fig. 4) were used to calculate the impulse velocity by $4l_{\text{SAMP}}$ (with multiple reflections taken into account) to an error of 50 m/s.

The recorded value of velocity was 1300 m/s, which obviously does not correspond to the velocity of longitudinal waves in this material. Two components are pronounced in the

impulse, which indicates that the impulse is transmitted by two types of oscillations having different velocities. The difference in velocities is comparable with the measurement error. The origin of this effect and its detailed qualitative estimation will be investigated in our further experiments.

Acknowledgements: The research was partially supported by INTAS (project 961-2370) and RFBR (projects 00-02-16582 and 01-01-00386).

REFERENCES

- [1] T.D. Shermergor. The Theory of Elasticity of Microinhomogeneous Media, Nauka, Moscow, 1977.
- [2] V. N. Nikolaevsky. Geomechanics and Fluid Dynamics, Nedra, Moscow, 1996.
- [3] L. D. Gyk. Anomalous effects of seismic wave propagation in porous and cracked media, *Physical Mesomechanics*, 1998, 1, № 2, p.101-106.
- [4] C. S. Chang and J. Gao. Wave propagation in granular rod using high-gradient theory, *J. of Engn. Mech.-ASCE.*, 1997, №1, p.52-59.
- [5] V. I. Erofeev and V. M. Rodushkin. Observation of elastic wave dispersion in a granular composite and mathematical model for its description, *Acoust. J.*, 1992, 38, № 6, p.1116-1117.
- [6] V. M. Rodyushkin. The experimental estimation of the microstructure of granular composite material, *Mecanique Industrielle et Materiaux*, 1995, 48, №5, p.208-209.
- [7] A. M. Bragov, A. K. Lomunov, and E. E. Rusin. A method for investigating dynamical properties of materials using composite Hopkinson rods, Applied Problems of Strength and Elasticity, in: All-Union University Collected Papers, Gorky University Press, 1980, issue16, p.138-144.
- [8] R. D. Gauthier. Experimental investigations on micropolar media, in: Mechanics of Micropolar Media, World Scientific, Singapore, 1982, p.395-463.
- [9] R. D. Gauthier and W. E. Jashman. A quest for micropolar elastic constants, *Arch. Mechanics*, 1981, 33, №5, p.717-737.
- [10] R. Lakes. Experimental methods for study of Cosserat elastic solids and other generalized elastic continua, in: Continuum Models for Materials with Microstructure, Eds. H.-B. Mulhaus, John Willey and Sons Inc., 1995, p.1-20.

GOVERNING EQUATIONS AND BALANCE LAWS FOR MICROPOLAR CONTINUUM

S.A. Lisina, A.I. Potapov and G.A. Utkin

Mechanical Engineering Institute of the Russian Academy of Sciences
Nizhny Novgorod, Russia

1. SUMMARY

It has been shown that the appropriate choice of dynamic variables in the variational approach allows one to construct effectively the nonlinear mathematical models describing dynamics of micropolar media in terms of both Lagrange's and Euler's variables. Equivalence of the variational equations and local balance laws of the energy, momentum and angular momentum in terms of Euler's variables has been proved using an example of liquid crystal.

2. INTRODUCTION

The classical mechanics of continuum proceeds from the idea that a medium consists of material points having three translational degrees of freedom. The orientational effects which cannot be described by equations of the classic theory of continuum mechanics occur in composites, polymers, liquid crystals and so on [1,2]. In the structural-phenomenological description of such media it is supposed that the representative volume is a solid having three translational and three orientational degrees of freedom. The kinematics of oriented medium can be described by two vector fields: a field of particles displacements and by a field of their microrotations.

The initial formulation of variational principles in the mechanics is connected with variations of the motion law of particles in terms of Lagrange's variables. Such a formulation is usually convenient for problems of the mechanics of a solid. As a rule, it is more preferable to state and investigate problems of hydromechanics in terms of Euler's variables. Therefore in hydromechanics the variational principles with unknown field functions of Euler's variables have the main importance for practical applications.

3. HAMILTON'S PRINCIPLE IN TERMS OF LAGRANGE'S VARIABLE

For nonlinear elastic media, the most simple way to obtain equations of motion is to derive them from the variational Hamilton's principle, using Lagrange's variables. In case of continuous medium the mathematical formulation of this principle has the form [3]:

$$\delta J = \delta \int_{t_0}^{t_1} \left(\iiint_{V_0} L dV \right) dt = 0. \quad (1)$$

The integrals are taken over the volume occupied by the medium at moment t_0 . Here L is a volume density of the Lagrange's function. The co-ordinates of all the points of the system

are set at the time moments t_0 and t_1 , i.e. the configuration of the system is fixed at these moments.

In rectangular co-ordinates Lagrangian L is written as a difference between density of the kinetic energy T and density of the free energy of a medium which characterises an interaction of particles in a medium. In this case Lagrangian takes the form:

$$L = \frac{1}{2} \rho_0 u_\alpha^2 + \frac{1}{2} \rho_0 J_{\alpha\beta} \phi_\alpha \phi_\beta - \rho_0 F(\phi_{\alpha\beta}, u_{\alpha\beta}), \quad (2)$$

where the fields of displacements $u_\alpha(X, t)$ and microturns $\phi_\alpha(X, t)$ are considered as functions of Lagrange's variables and time. In case of isotropic central-symmetric micropolar medium, the expression for free energy is a power expansion:

$$\begin{aligned} \rho_0 U = & \frac{\mu + \alpha}{2} \varepsilon_{ji} \varepsilon_{ji} + \frac{\mu - \alpha}{2} \varepsilon_{ji} \varepsilon_{ij} + \frac{\lambda}{2} (\varepsilon_{kk})^2 + \frac{\gamma + \varepsilon}{2} \gamma_{ji} \gamma_{ji} + \frac{\gamma - \varepsilon}{2} \gamma_{ji} \gamma_{ij} + \frac{\beta}{2} (\gamma_{kk})^2 + \\ & + \frac{\nu_1}{2} (\varepsilon_{kk})^3 + \frac{\nu_2 + \delta_1}{2} \varepsilon_{ji} \varepsilon_{ji} \varepsilon_{kk} + \frac{\nu_2 - \delta_1}{2} \varepsilon_{ij} \varepsilon_{ji} \varepsilon_{kk} + \frac{2\nu_3 + \delta_2}{3} \varepsilon_{ij} \varepsilon_{jk} \varepsilon_{ki} + \frac{2\nu_3 - \delta_2}{3} \varepsilon_{ij} \varepsilon_{jk} \varepsilon_{ik} + \\ & + \sigma_1 \gamma_{nm}^2 \varepsilon_{kk} + \sigma_2 \gamma_{ij} \gamma_{ji} \varepsilon_{kk} + \sigma_3 \gamma_{ij} \gamma_{ij} \varepsilon_{kk} \end{aligned}$$

where $\varepsilon_{kl} = u_{l,k} - \varepsilon_{klm} \phi_m$, is macrostrain tensor $\gamma_{mn} = \phi_{n,m}$, is microstrain tensor, λ, μ are the elastic Lamé constants, and $\alpha, \gamma, \varepsilon$ are the linear microelastic constants $\nu_1 + \nu_3, \delta_1 + \delta_3$ and $\sigma_1 + \sigma_3$ are the nonlinear constants. The other representations of free energy with account of the nonlinear factors are in ref. [1, 5]. The Euler-Lagrange equations for variational principle (1) give us the governing equations for micropolar media:

$$\rho_0 \ddot{u}_\alpha = \frac{\partial}{\partial X_\beta} \left(\frac{\partial \rho_0 F}{\partial u_{\alpha,\beta}} \right), \quad \rho_0 J_{\alpha\beta} \ddot{\phi}_\beta = \frac{\partial}{\partial X_\beta} \left(\frac{\partial \rho_0 F}{\partial \phi_{\alpha,\beta}} \right). \quad (3)$$

The first eq. of (3) describes macromotions, i.e. motions of mass centres of the particles. The second eq. of (3) describes micromotions of a medium, namely, rotational movements of microelements. The expression $\sigma_{\alpha\beta} = \partial / \partial X_\beta [\partial (\rho_0 F) / \partial u_{\alpha,\beta}]$ is a macrostress tensor in terms of Lagrange co-ordinates and $m_{\alpha\beta} = \partial / \partial X_\beta [\partial (\rho_0 F) / \partial \phi_{\alpha,\beta}]$ is the tensor of microstresses in a micropolar medium. For unipolar media, when, eqs. (3) are transformed into equations of the classical theory of elasticity.

4. HAMILTON'S PRINCIPLE IN TERMS OF EULER'S VARIABLES

In this case, the field variables and in L are not independent. They are connected by mass conservation law and the condition of Lagrange's variables conservation for each material particle.

There are two equivalent approaches for variational derivation of governing equation in terms of Euler's variables. The variational problem (1) about conditional extreme for action functional is considered using the method of Lagrange's multipliers [3], or the variational problem about unconditional extreme is investigated for action functional in which the field variables and etc. are expressed in terms of Lagrange's variables [4, 5].

The first approach is interesting because it allows to receive equations of motion in the hydrodynamic form. To use it, it is necessary to know additional restraints imposed on field variables. Such restraints, in particular, are known for some problems of hydrodynamics of an ideal liquid. However, media with inner structure the necessary quantity of these restraints

is not known beforehand. The complexity of the second approach consists in necessity to express all field variables in terms of independent Lagrange's variables: variables and angular variables.

Below we use the second approach to derive nonlinear governing equations of nematic liquid crystal (NLC). Free energy of NLC has the form [6]:

$$\rho F = \rho F_0(\rho) + \frac{K_1}{2} (\text{div} \mathbf{n})^2 + \frac{K_2}{2} (\mathbf{n} \cdot \text{rot} \mathbf{n})^2 + \frac{K_3}{2} (\mathbf{n} \times \text{rot} \mathbf{n})^2 - \frac{\chi_m}{2} (\mathbf{n} \cdot \mathbf{H}_0)^2. \quad (4)$$

where K_i are Frank's elastic constants, χ_m is the diamagnetic anisotropy, \mathbf{n} is the director, and ρF_0 is the hydrodynamic part of free energy of NLC. In this case, the expression of kinetic energy contains Euler's field of velocities, a medium density and the field of angular velocities of microparticles, which should be considered as functions of Euler's variables and time. In order to employ the variational principle (1) having a direct physical sense only for material "volume" consisting of the same particles of a medium, it is necessary to express \mathbf{v} , and in terms of Lagrange's variables and their derivatives. Field of linear velocities \mathbf{v} can be expressed in terms of Lagrange's variables due to condition of conservation of Lagrange's variables of a particle (i.e.) from which it follows that the linear velocity v_i is equal to

$$v_j = -\frac{\partial x_j}{\partial X_\alpha} \frac{\partial X_\alpha}{\partial t}, \quad \rho(\mathbf{x}, t) = \rho_0(X) \det \left\| \frac{\partial X_\alpha}{\partial x_i} \right\|, \quad \Omega_i = \dot{\phi}_i = \epsilon_{\alpha\beta i} n_\alpha \dot{n}_\beta, \quad (5)$$

where $\rho_0(X)$ is the density of a medium at the initial time moment $t=0$, $\dot{n}_\beta = n_{\beta,t} + v_m n_{\beta,m}$ is the complete (material) derivative with respect to time. Their substitution into (2) and (4) give a Lagrangian as a function of independent variables X_α, n_β and their derivatives. Thus, the variational Hamilton's principle in terms of Euler's variables can be formulated as [4]:

$$\delta J[X_\alpha(\mathbf{x}, t), n_\beta(\mathbf{x}, t)] = \delta \int_{t_0}^{t_1} \int_{V(t)} (L(X_{\alpha,t}, X_{\alpha,j}, n_\beta, n_{\beta,t}, n_{\beta,j})) dV dt = 0 \quad (7)$$

Note that here, in contrast to (1), we integrate over the time-varying volume occupied by the same particles of the medium. Variation of functional (5) over independent variables and leads to variational equations:

$$\begin{aligned} \frac{\partial}{\partial t} \frac{\partial L}{\partial X_{\alpha,t}} + \frac{\partial}{\partial x_j} \frac{\partial L}{\partial X_{\alpha,j}} &= 0, \\ \frac{\partial L}{\partial n_\beta} - \frac{\partial}{\partial t} \frac{\partial L}{\partial n_{\beta,t}} - \frac{\partial}{\partial x_j} \frac{\partial L}{\partial n_{\beta,j}} &= 0. \end{aligned} \quad (8)$$

The obtained equations have not yet a physical sense of governing equations and represent formal mathematical expressions, as they contain both Greek indexes relating to Lagrange's reference system and Latin indexes relating to Euler's reference system. They receive a physical sense after return in (6) to field variables. These problems are discussed below.

5. INTEGRALS OF MOTION

If not to pay attention to Greek and Latin indexes in variational eqs. (13), these equations coincide by the form with equations of the classical field theory. Therefore, it is possible to obtain integrals of motion using Lagrange's formalism. In accordance with Neter's theorem, the balance laws of energy, momentum and moment of a momentum (angular momentum) follow from a condition of invariance of Lagrangian L with respect to time-variation, space displacement, and space turn accordingly. In this paper we used a simpler way of derivation of integrals of motion directly from eq.(6).

5.1. Integral of energy.

Convolutions of the first eq. (6) with and of the second eq. (6) with and summing up of these equations lead to integral of energy.

$$\frac{\partial}{\partial t} \left(\frac{\partial L}{\partial X_{\alpha,i}} X_{\alpha,i} + \frac{\partial L}{\partial n_{\beta,i}} n_{\beta,i} - L \right) + \frac{\partial}{\partial x_j} \left(\frac{\partial L}{\partial X_{\alpha,j}} X_{\alpha,i} + \frac{\partial L}{\partial n_{\beta,j}} n_{\beta,i} \right) = 0 \quad (9)$$

The energy density w and its flux s_j are introduced as:

$$W = \frac{\partial L}{\partial X_{\alpha,i}} X_{\alpha,i} + \frac{\partial L}{\partial n_{\beta,i}} n_{\beta,i} - L, \quad S_j = \frac{\partial L}{\partial X_{\alpha,j}} X_{\alpha,i} + \frac{\partial L}{\partial n_{\beta,j}} n_{\beta,i} \quad (10)$$

The terms in right-hand side of (7) characterise time-varying parameters of a medium and show, that the energy does not conserve in a nonstationary medium.

5.2. Integral of a linear momentum.

If to convolute the first eq. (6) with and the second eq. (6) with , after similar transformations one can obtain an integral of motion:

$$\frac{\partial}{\partial t} \left(\frac{\partial L}{\partial X_{\alpha,i}} X_{\alpha,i} + \frac{\partial L}{\partial n_{\beta,i}} n_{\beta,i} \right) + \frac{\partial}{\partial x_j} \left(\frac{\partial L}{\partial X_{\alpha,j}} X_{\alpha,i} + \frac{\partial L}{\partial n_{\beta,j}} n_{\beta,i} - L \delta_{ij} \right) = 0 \quad (11)$$

$$P_i = \frac{\partial L}{\partial X_{\alpha,i}} X_{\alpha,i} + \frac{\partial L}{\partial n_{\beta,i}} n_{\beta,i} \quad \Pi_{ij} = \frac{\partial L}{\partial X_{\alpha,j}} X_{\alpha,i} + \frac{\partial L}{\partial n_{\beta,j}} n_{\beta,i} - L \delta_{ij}$$

Here p_i represents the momentum of the field, and represents the density tensor of a momentum flux. Derivative in the right-hand side of (9) characterises inhomogeneity of the medium and shows, that in the inhomogeneous medium the field momentum does not conserve.

5.3. Integral of a kinetic moment.

Convolute the first eq. (6) with and the second eq. (6) with (that is equivalent to vector multiplication). After addition of these equations we shall received

$$\frac{\partial}{\partial t} \left(\epsilon_{kll} x_l \left(\frac{\partial L}{\partial X_{\alpha,i}} X_{\alpha,i} + \frac{\partial L}{\partial n_{\beta,i}} n_{\beta,i} \right) \right) + \frac{\partial}{\partial x_j} \left(\epsilon_{kll} x_l \left(\frac{\partial L}{\partial X_{\alpha,j}} X_{\alpha,i} + \frac{\partial L}{\partial n_{\beta,j}} n_{\beta,i} - L \delta_{ij} \right) \right) = 0 \quad (12)$$

Complete kinetic moment of the micropolar medium equals:

$$g_i^{(macro)} = \epsilon_{kll} x_l \left(\frac{\partial L}{\partial X_{\alpha,i}} X_{\alpha,i} + \frac{\partial L}{\partial n_{\beta,i}} n_{\beta,i} \right) \quad (13)$$

Here the first term characterises the kinetic moment of macromovements, while the second one stands for the kinetic moment of micromovements.

The expression under spatial derivative, represents tensor of density of the kinetic moment flux:

$$\mathcal{Q}_{kj}^{(macro)} = \epsilon_{kij} x_l \left(\frac{\partial L}{\partial X_{\alpha,j}} X_{\alpha,i} + \frac{\partial L}{\partial n_{\beta,j}} n_{\beta,i} - L \delta_{ij} \right) \quad (14)$$

The right-hand side of (11) characterises processes leading to change of the kinetic moment of the medium during the motion.

6. EQUIVALENCE OF INTEGRALS OF MOTION TO THE LOCAL BALANCE LAWS

Passing in (9) to the hydrodynamic variables, leads to the balance law of momentum:

$$\frac{\partial}{\partial t} (\rho v_i) + \frac{\partial}{\partial x_j} \left(\rho v_i v_j + p \delta_{ij} + \frac{\partial \rho F}{\partial n_{k,j}} n_{k,i} \right) = 0 \quad (15)$$

where p is the hydrodynamic pressure and Ericksen's stress tensor is introduced by formula:

$$\sigma_{ij}^e = p \delta_{ij} + \frac{\partial \rho F}{\partial n_{k,j}} n_{k,i} \quad (16)$$

Equation (11) reduces to the differential form of the translation equation of spin of the micropolar medium:

$$\frac{\partial}{\partial t} (J \rho \omega_i) + \frac{\partial}{\partial x_j} (J \rho \omega_i v_j) = \epsilon_{isk} n_s h_k \quad (17)$$

where ω_i is the angular velocity of director rotation for derivation of (16), the kinetic moment of macromovements of a liquid was supposed to be constant, as a liquid is assumed to be ideal. The quantity in the right-hand side of (16)

$$\begin{aligned} \frac{\partial v_i}{\partial t} + v_j \frac{\partial v_i}{\partial x_j} &= -\frac{1}{\rho} \frac{\partial \sigma_{ij}^e}{\partial x_j}, \\ \frac{\partial \rho}{\partial t} + \frac{\partial v_i}{\partial x_j} (\rho v_j) &= 0, \\ \rho J \left(\frac{\partial \Omega_i}{\partial t} + v_j \frac{\partial \Omega_i}{\partial x_j} \right) &= \epsilon_{skl} n_s h_k. \end{aligned} \quad (18)$$

is called a molecular field. It characterises availability of moments of internal forces and exert an orienting effect on molecules of liquid crystals. From the local balance laws of linear momentum and angular momentum it is easy to pass to equations of motion of NLC [].

7. CONCLUSIONS

The potential energy density was supposed to depend only on the first-order derivatives and this assumption a priori does not follow from anywhere. It is possible to suppose that the free energy of the medium depends, in general case, also on higher-order derivatives and etc.

To take into account the effect of material microstructure, it is formally possible to include various derivatives from and into expression for free energy density. There are two difficulties interfering with the construction of multipolar theory of microstructured media. The first one consists in finding the complete system of basic invariants of tensors without which the invariant density of Lagrangian cannot be constructed. Secondly, it is necessary to give a physical interpretation for vectors that are used for definition of material microstructure.

Acknowledgements: The research described in this publication was made possible in part by RFBR (grant N 00-02-16582 and 01-01-00386).

8. REFERENCES

- [1] *G.A.Magin, J.Pouget.*, Nonlinear dynamics of oriented elastic solids, I. Basic equations, *J. Elas.*, 1989, **22**, 135-155.
- [2] *A.I.Potapov, I.S.Pavlov, S.A.Potapova*, Vibro-acoustic analysis of physical properties of nonlinear oriented media. In: *New Advances in Modal Synthesis of Large Structures*, L.Jezequel (ed.) / A.A.Balkema, Rotterdam, 1997, pp.399-410.
- [3] *P.L.Seliger, G.B.Whitham*, Variational principles in continuum mechanics, *Proc. Roy Soc., Ser A*, 1968, **305**, 1-25,
- [4] *S.A. Potapova, G.A.Utkin*, The variational principle for micropolar continuum. 3rd EUROMECH Solid Mechanics Conference, Stockholm, Sweden, 1997, p.84.
- [5] *V.B.Lisin, A.I.Potapov*, Variational principle in mechanics of liquid crystals, *Int. J. Non-Linear Mech.*, 1997, **32**, № 1, pp. 55-62
- [6] *P.G. de Gennes*, *The Physics of Liquid Crystals*, Clarendon Press, Oxford, (1974)
- [7] *A.C.Eringen*, Balance laws of micromorphic mechanics, *Int. J. Engn. Sci.*, 1970, **8**, № 10, 819-828.
- [8] *A.E.Green, R.S.Rivlin*, Multipolar continuum mechanics, *Arch. Rat. Mech. Anal.*, 1964, **17**, 113-147.
- [9] *Muhlhaus HB; Aifantis EC*, A variational principle for gradient plasticity. *Int. J. Solids and Structures*, 1991, V28(N7):845-857.

SPLITTING UP OF MULTISTABLE SOLITONS IN SOLIDS

A. I. Potapov, V. V. Kazhaev and S. V. Gromov

Mechanical Engineering Institute of the Russian Academy of Sciences
603024 Nizhny Novgorod, Russia

1. SUMMARY

Strongly nonlinear particle-like waves described by a wave equation with cubic nonlinearity and anomalous dispersion are investigated. Such waves possess some properties which distinguish them from the classical solitons. Their amplitude cannot be smaller than a certain critical value and the energy has a minimum. Besides, there exists still another threshold value of the amplitude above which the colliding heteropolar waves split up, generating secondary particle-like waves and quasi-linear wave trains

2. INTRODUCTION

The interaction between nonlinear localized waves under rear-end and head-on collisions has been actively investigated for many years but it is still one of the least understood problems. Using a number of examples and employing analytical and numerical methods the authors of [1,2] showed that localized waves (solitons) in integrable systems behave like particles, i.e., on collision, they preserve their individual character and acquire only phase shifts ("elastic" interaction). This was supported by experiments with nonlinear waves in plasma, in fluids with gas bubbles, and with electromagnetic waves. In nonintegrable systems, nonlinear particle-like waves interact in a different manner. On rear-end collisions, they emit part of their energy in the form of quasi-linear wave trains ("inelastic" interaction) [3-5]. Moreover, numerical modeling revealed that they split up on head-on collisions [6,7]. The first experimental evidence of this effect was reported in [8].

It is worthy of noting that processes of interaction on rear-end collisions, strictly speaking, cannot be described by equations of one-wave approximation (KdV equations and others). Therefore, complete equations of nonlinear dynamics which allow for the waves travelling in both directions must be employed [3,5,7]. Such equations are usually nonintegrable and their solutions describe solitary waves that are not solitons in the rigorous, mathematical sense [1].

In this paper we study particle-like waves described by an equation with cubic nonlinearity and two types of dispersion. Results of numerical modeling demonstrating the effect of the splitting up of such waves on head-on collisions are given.

3. THEORY

A one-parameter family of nonintegrable equations with cubic nonlinearity of "rigid" type [7] is considered

$$\frac{\partial^2 u}{\partial t^2} - \left(1 + \left(\frac{\partial u}{\partial x}\right)^2\right) \frac{\partial^2 u}{\partial x^2} - \frac{\partial^2}{\partial x^2} \left(\frac{\partial^2 u}{\partial t^2} - C^2 \frac{\partial^2 u}{\partial x^2} \right) = 0 \quad (1)$$

It is the generalization of the Boussinesq equation used in various fields of mechanics and physics [3]. In particular, such models are employed in investigations of nonlinear-elastic waves in laminated crystals and in granular materials [9,10], when rotational degrees of freedom of the particles are taken into account, as well as in the study of elastically plastic waves in solids with allowance for the effects of nonlocality [11,12]. For $C > 1$, the equation has anomalous (positive) dispersion, which results in the appearance of new nonlinear effects. For stationary waves, when $C > 1$, there exist two regions of bounded solutions with a qualitatively different wave behavior. Region I corresponds to weakly nonlinear periodic waves that degenerate into linear perturbations at small amplitudes. Region II corresponds to the waves whose amplitude cannot be below the critical value. Such strongly nonlinear waves have no linear degeneration. Let us analyze in more detail localized particle-like waves realized in region II. These waves are described by

$$u(x, t) = \pm A \Delta \arctan \left[\sinh \left(\frac{x \pm Vt}{\Delta} \right) \right], \quad \frac{\partial u}{\partial x} = \pm A \cosh^{-1} \left(\frac{x \pm Vt}{\Delta} \right), \quad (2)$$

where the variable $u(x, t)$ has the meaning of displacement in mechanics, $\partial u / \partial x$ are the deformations [4]. The amplitude A , the velocity V , and the wave width Δ are related by (Fig. 1)

$$A = \sqrt{6(V^2 - 1)}, \quad \Delta = \sqrt{\frac{V^2 - C^2}{V^2 - 1}}. \quad (3)$$

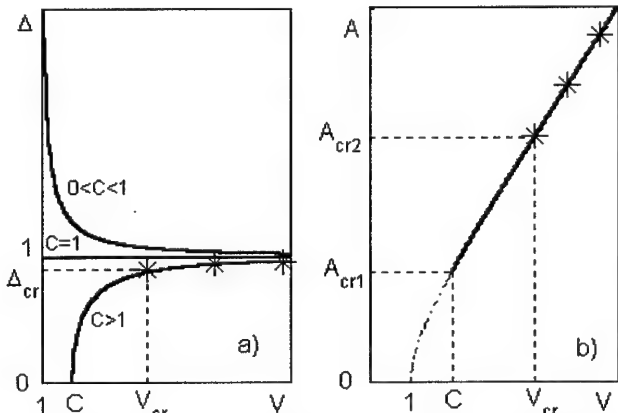


Fig. 1: The width (a) and amplitude (b) of a particle-like wave plotted versus its velocity

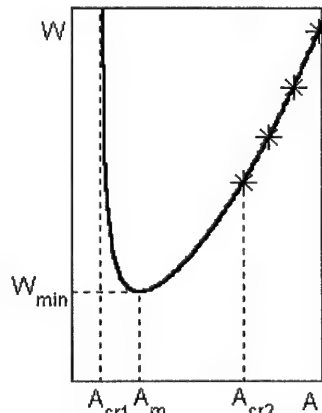


Fig. 2: The energy of a particle-like wave plotted versus its amplitude

As is evident from the figures, the amplitude is always above the critical value $A_{cr1} = \sqrt{6(C^2 - 1)}$, and the width varies from 0 to 1. It is also interesting to note that the energy of such waves is not a monotonic function of the amplitude:

$$W = \left[(V^2 + 1)\Delta + \frac{V^2 + C^2}{3\Delta} \right] A^2 + \frac{1}{9} \Delta^2 A^2 \quad (4)$$

The wave energy decreases in the amplitude interval $A_{cr1} < A < A_m$, while for $A > A_m$ it increases so that the energy is proportional to A^4 (Fig. 2) for large amplitudes.

It is worthy of noting that the particle-like waves under consideration, similarly to the classical solitons, have a similarity parameter

$$\sigma = \frac{A\Delta}{\sqrt{6(V^2 - C^2)}}, \quad (5)$$

that can be used for their identification in numerical modeling.

4. RESULTS OF NUMERICAL MODELING

The initial conditions were set in accordance with the solutions of eq.(2), and the boundary conditions were imposed by introducing fictitious nodes which provide the same approximation accuracy as the difference scheme. Results of numerical calculations of the interaction

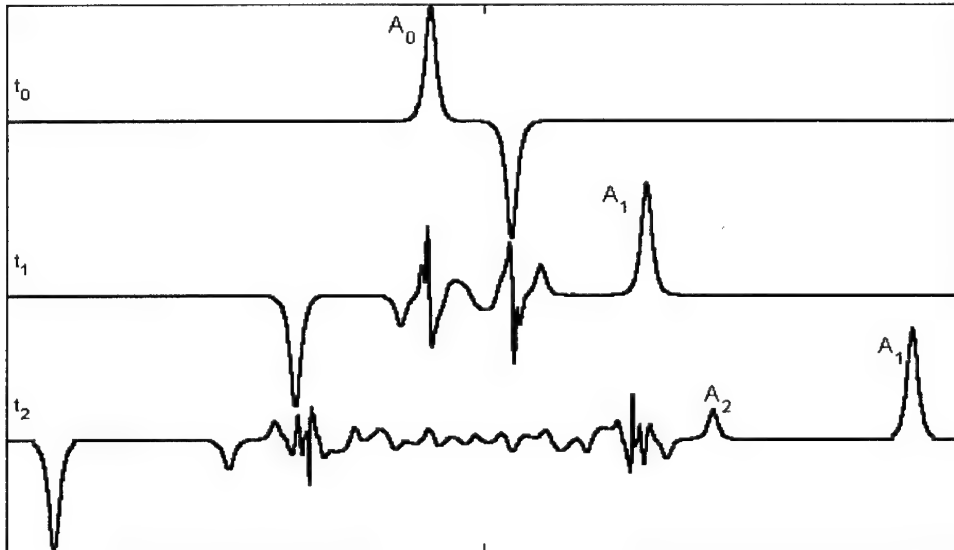


Fig. 3: Splitting up of heteropolar particle-like waves under head-on collision:
 A_0 – primary wave amplitude; A_1 and A_2 – amplitudes of secondary waves

between heteropolar solitary waves under head-on collisions are given in Fig. 3 for different moments of time ($C = 8/5$, $V = 8$). Analysis of result of the numerical modeling shows that the localized waves (2) frequently behave like solitons. Similarly to solitons, they propagate at a constant, amplitude-dependent velocity and are stable with respect to small perturbations. The main feature of solitons is that they preserve their individual properties in the interactions [1-4]. Whereas the particle-like waves of interest to us possess features which distinguish them from the classical solitons. In particular, if the wave amplitudes are above a certain threshold $A > A_{cr2}$, the waves will split up on head-on collisions, giving rise to secondary particle-like waves and a quasi-linear wave train. The relationship between the amplitude of primary (curve A_1) and secondary (curve A_2) solitary waves is plotted in Fig. 4. For the primary waves, the A_1 curve is almost linear, while it is distinct from a straight line for the secondary waves. The obtained curves are in a good agreement with the theoretical formula (3) from which it follows that the A - V curve tends asymptotically to a straight line for large wave velocities.

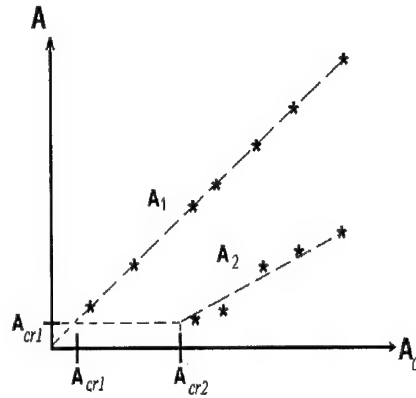


Fig. 4: Secondary wave amplitudes plotted versus primary wave amplitude

The calculations demonstrate, in particular, that, when waves having equal initial amplitudes $A_0 = 18.4$, secondary waves with amplitudes $A_1 = 17.6$ and $A_2 = 3.5$ are formed on splitting up, and the remaining energy is radiated in the form of a quasi-harmonic wave train.

5. EXPERIMENTAL RESULTS

Below we present results of experimental research on nonlinear wave processes in a mechanical apparatus [8]. The apparatus consisted of a rubber belt fixed vertically. A fluoroplastic slider being a mobile boundary was moved along the belt near its lower end. A narrow slot was cut out in the slider so as to allow it to slide along the belt without friction and bringing about no changes in the belt tension, i.e., the slider was "transparent" for longitudinal waves. Whereas transverse waves reflected from the moving boundary almost completely. The source of transverse waves in such a system is the moving boundary (slider). We investigated the interaction of nonlinear localized waves for different ratios of amplitudes and different polarities. The transverse displacement waves travelling along the belt were recorded with the help of a high-speed movie camera capable of making up to 2000 frames per second.

Two qualitatively different types of interaction of solitary waves were observed in experiment. Those were weakly nonlinear interactions, when $V_{\max} < 1$, i.e., the maximal velocity of boundary motion was less than the propagation velocity of the transverse wave, and strongly nonlinear interactions of solitary waves, when $V_{\max} > 1$. Most interesting effects were observed under head-on collisions of strongly nonlinear waves when the slider moving with "supersonic" velocity excited displacement waves $u(x, t)$ with a steep front ($\varphi \approx 45-60^\circ$)

and the difference with the amplitude of the weakly nonlinear displacement wave was a factor of 5-6 (Fig. 5). Such waves can evidently be considered as an analog of shock waves in a gas, but unlike in gas dynamics, the transverse waves in a belt may show an ambiguous S-shaped profile (Fig. 5, frames 15,...,25). In the course of propagation "shock" displacement waves transformed, due to dispersion, into soliton-like waves (Fig. 5, frames 1,...,5). One can visualize in the cinegram (Fig. 3) the process of propagation and interaction among three nonlinear localized waves A_i, B_i, C_i ($i=0,1,\dots$). On collision of heteropolar waves A_1 and B_0 (Fig. 5, frames 6,...,10), the primary "quasi-soliton" B_0 split up into two secondary "quasi-solitons" B_1' and B_1'' .

Note that on splitting up of the "quasi-soliton" B_0 , the superposition principle is not fulfilled: the sum of the secondary wave amplitudes is more than the primary wave amplitude before splitting up, and the sum of their energies ($W_{B_1'} = 3.09, W_{B_1''} = 3.61$) is much less than the primary wave energy ($W_{B_0} = 10.1$). Hence, splitting up of the strongly nonlinear wave B_0 into two secondary localized waves B_1' and B_1'' is accompanied by radiation of a quasi-linear wave train taking away part of the energy stored in the primary wave.

Splitting up of "quasi-solitons" has a threshold nature. For example, interaction between the localized waves C_0 and A_2 (Fig. 5, frames 10,...,13) did not result in their splitting up. They remained similar to themselves after collision.

Another nonlinear effect of interaction of localized waves was manifested in their phase shifts after collision, with the sign of the phase shift depending on the polarity of the interacting waves. The heteropolar waves A_1, B_0 and A_2, C_0 were slowed down on collision and acquired negative phase increments (Fig. 5, frames 7,...,9,11,...,13), while unipolar waves B_2, C_1 , on the contrary, were accelerated on collision and acquired positive increments (Fig. 5, frames 16,...,18). A similar effect was observed in numerical modeling of head-on collisions of solitary waves described by the modified Boussinesq equation [5].

The phase shifts of localized waves resulted in chaotic behavior in a nonlinear dynamic system. The closest analogy in this case seems to be that of the random motion of a material particle between two rigid walls one of which is vibrating by a periodic law. Whereas in the case of weakly nonlinear waves, the process is periodic.

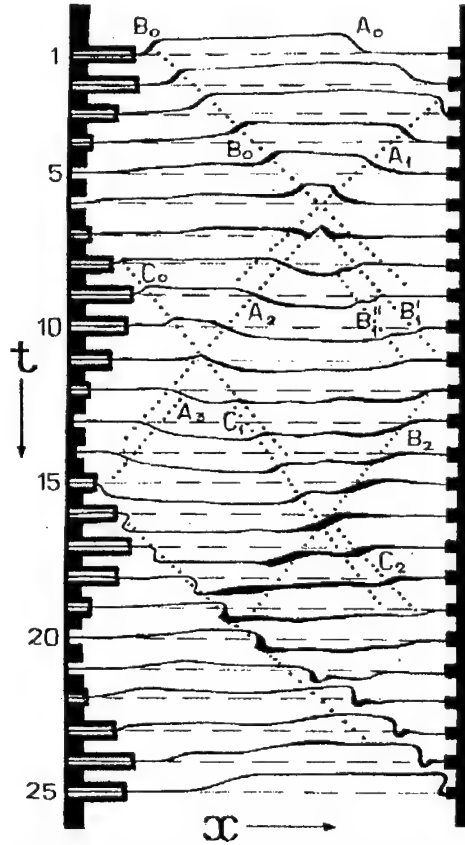


Fig. 5. Cinegram of interaction of strongly nonlinear waves in a rubber belt.

6. CONCLUSION

The results presented are indicative of the appearance in the considered system with anomalous dispersion of two types of localized waves – weakly nonlinear and strongly nonlinear ones. The strongly nonlinear waves represent a new type of metastable formation and possess a set of properties that distinguish them from weakly nonlinear waves (classical solitons). Namely, they can split up under head-on collisions, giving rise to new localized waves (quasi-solitons) if their amplitudes exceed a certain critical value. In this case, part of the energy stored in the primary wave is radiated in the form of a quasi-linear wave train.

Acknowledgement: The research was partially supported by the RFBR (grants 00-02-16582 and 01-01-00386).

7. REFERENCES

- [1] *Solitons*, R.K.Bullough and P.J.Caudrey (eds.), Springer-Verlag, Berlin (1980).
- [2] *Solitons in Actions*, K. Lonngren and A. Scott (eds.), Academic Press, New York (1978).
- [3] Ostrovsky L.A. and Potapov A.I., *Modulated Waves. Theory and Applications*, John Hopkins Univ. Press, Baltimor and London (1999)
- [4] Yan C.T., Elastic and inelastic collisions-A microstructural analysis for solitary waves. *Chaos Solitons & Fractals*, v. 4(n 11), 2103-2109 (1994).
- [5] Soerensen M.P., Christiansen P., and Lomdahle P.S., Solitary waves on nonlinear elastic rods I, *J. Acoust. Soc. Amer.*, v.76, 871-879 (1984).
- [6] Santarelli A.R., Numerical analysis of the regularized long wave equation: inelastic collision of solitary waves, *Nuovo Cimento*, v.46B (n 1), 179-188 (1978).
- [7] Kazhaev V.V., Potapov A.I. and Semerikova N.P., Splitting-up of particle-like waves under head-on collision, *Radiophysics and Quantum Electronics*, v.38 (n 1-2), 67-70 (1995).
- [8] Potapov A.I. and Vesnitsky A.I., Interaction of solitary waves under head-on collision. Experimental investigation, *Wave Motion*, v.19, 29-35 (1994).
- [9] Potapov A.I., Pavlov I.S., and Maugin G.A., Nonlinear wave interactions in 1D crystals with complex lattice. *Wave Motion*, v.29, 297-312 (1999).
- [10] Potapov A.I., Lisina S.A., and Nesterenko V.F., Mathematical modelling of nonlinear waves in granular media. In 4th EUROMECH Solid Mechanics Conference, Metz, France, 2000, Book of Abstracts II, p. 722.
- [11] Muhlhaus H.B. and Aifantis E.C., The influence of microstructure-induced gradients on the localization of deformation in viscoplastic materials, *Acta Mechanica*, v.89 (n 1-4), 217-231 (1991).
- [12] Popov V.L. and Tschertova N.V., Gauge theory of "plastically incompressible" medium -II. Dispersion relations with dissipation, *Int. J. Engng. Sci.*, v.30 (n 3), 335-340 (1992).

MODELING THE CRUSHING OF A CELLULAR MATERIAL

M. Zaiser

Max-Planck Institut für Metallforschung
Heisenbergstr. 1, D-70569 Stuttgart, Germany

E. C. Aifantis

Aristotle University of Thessaloniki, Polytechnic School,
54006 Thessaloniki, Greece

1. SUMMARY

Deformation of cellular materials is characterized by a strain softening regime where cells collapse. This is modeled in terms of a local constitutive relation with a strain softening part. Interactions between adjacent cells during cell collapse are taken into account, and it is shown that on macroscopic scale such interactions can be approximated by a second-order gradient term in the constitutive equation. Structural randomness of the cellular material is modeled in terms of a random distribution of the local crushing thresholds. The interplay between local softening, gradient coupling and structural randomness is studied. For small randomness, the stress-strain curves are characterized by a yield point followed by a plateau. In the spatio-temporal domain this behaviour is associated with the nucleation and propagation of a localized 'crushing band'. At larger values of the randomness, one finds a monotonically increasing stress-strain relationship associated with a diffuse crushing mode.

2. INTRODUCTION

Compression of cellular materials usually proceeds in three stages [1,2]. Initially, deformation occurs by elastic bending of the cell walls. As the load exceeds a certain threshold, cells begin to collapse. Cell collapse involves in general a combination of elastic buckling, shear and rotation, depending on the local configuration of cells [3]. Irrespective of the details of the collapse mode, a cell which has started to collapse will in most cases continue to do so even if the load is decreased. Hence, deformation in the stage of cell collapse must be envisaged as a *strain softening* phenomenon which proceeds until a characteristic 'crushing strain' $\varepsilon_{\text{crush}}$ is accomplished. Once all cells have collapsed, one enters a third stage ('compaction') where the stress increases rapidly.

Deformation in the stage of cell collapse is characterized by various strain localization phenomena. Often, deformation proceeds by the nucleation and propagation of a *crushing band* (see Figure 1): Once cells have started to collapse, the collapse spreads to adjacent cells by first propagating transversally across a row of cells and then to adjacent rows [4]. The propagation velocity of the resulting deformation band depends on the imposed compression rate and on the crushing strain. The overall behaviour is very reminiscent of strain

localization and propagation phenomena in metals such as Lüders bands (for an overview, see [5]).

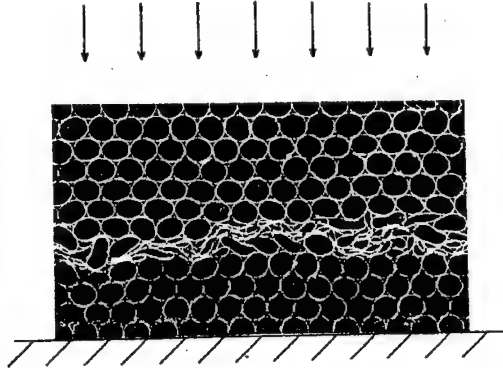


Figure 1: Crushing band in a bed of drinking straws under compression, after Weaire and Fortes [2].

Several models of cell crushing have been proposed in the literature. In the studies by Shim et. al. [6] and Fatima Vaz et. al. [4], a phenomenological constitutive equation with a strain softening part is used to study the propagation of crushing along a one-dimensional chain. In these models, which consider a chain of masses connected by non-linear springs, inertia is crucial for propagating the crushing from one cell to another. Accordingly, a propagating crushing band is found under dynamic (impact) loading, while under quasi-static loading (low-velocity deformation) no band propagation is found [4].

Under quasi-static loading conditions, another band propagation mechanism prevails: Collapse of a cell leads to damage of the adjacent cells and is therefore likely to decrease their crushing threshold. In the following we demonstrate that this leads to band propagation even in the quasistatic limit. We then investigate the influence of structural randomness on the crushing behaviour.

3. CONSTITUTIVE MODEL

We assume quasistatic compression and consider a phenomenological constitutive relation between the compressive stress σ and strain ϵ in a cell which is given by (cf. [6])

$$\begin{aligned} \sigma &= M\epsilon, \quad \epsilon < \epsilon_c = \frac{\sigma_c}{M}, \\ \sigma &= M\epsilon_c \left[\exp\left(\frac{\epsilon_{\text{COMP}}(\epsilon - \epsilon_c)}{\epsilon_{\text{COMP}} - \epsilon}\right) - \epsilon_0(\epsilon - \epsilon) \right], \quad \epsilon < \epsilon_c. \end{aligned} \quad (1)$$

Here, M is the initial elastic slope, σ_c is the crushing threshold, and the parameter ϵ_0 determines the extension of the strain-softening regime. This parameter is given by

$$\epsilon_0 = \frac{1}{\epsilon_{\text{CRUSH}}} \left[\exp\left(\frac{\epsilon_{\text{COMP}}\epsilon_{\text{CRUSH}}}{\epsilon_{\text{COMP}} - \epsilon_{\text{CRUSH}} - \epsilon_c}\right) - 1 \right]. \quad (2)$$

For definition of the 'crushing strain' ϵ_{CRUSH} see Figure 2.

When a cell starts to collapse, this influences also the adjacent cells. We model this effect by an 'interaction stress' between two cells i and j which is proportional to the difference in compression strain between both cells when the cells are adjacent to each other,

$$\sigma_{ij} = D_{ij}(\varepsilon_i - \varepsilon_j) \quad , \quad D_{ij} = \beta_{ij} \frac{\sigma_c}{\varepsilon_{\text{CRUSH}}} \quad (3)$$

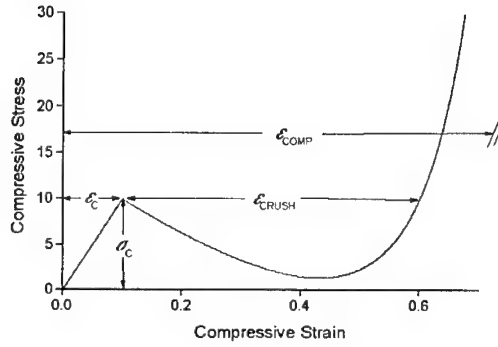


Figure 2: $\sigma(\varepsilon)$ characteristics, Eq. (1), for the parameters $\sigma_c = 10$, $M = 100$, $\varepsilon_{\text{CRUSH}} = 0.5$, $\varepsilon_{\text{COMP}} = 1$.

The non-dimensional coupling constants β_{ij} are zero for non-adjacent cells. For adjacent cells, they depend in general on the orientation with respect to the direction of compression: Along a row of cells normal to the compression direction, the coupling is strong since collapse of a cell implies that the load is shed on the walls of the adjacent cells. Between two rows above or below each other in the compression direction, on the other hand, the coupling is much weaker and arises from the fact that collapse of a cell slightly distorts the cells above or below. In the following we consider a two-dimensional model with two coupling constants, $\beta_N \approx 1$ in the direction normal to the compression axis and $\beta_P < 1$ in the compression direction. The quasistatic stress balance for the i th cell is given by

$$\sigma_{\text{EXT}} - \sigma(\varepsilon_i) - \sum_j D_{ij}(\varepsilon_i - \varepsilon_j) = 0 \quad (5)$$

In a material frame of reference, we may label a cell i by the coordinates \mathbf{r}_i of its 'point of gravity'. Henceforth, we choose the coordinate system such that compression is done along the x axis. Coarse graining Eq. (5) over a volume large as compared to the cell size d , we obtain

$$\sigma_{\text{EXT}} - \sigma(\varepsilon(\mathbf{r})) + \nabla[D\nabla\varepsilon(\mathbf{r})] = 0 \quad , \quad D = \sigma_c \frac{d^2}{\varepsilon_c} \begin{bmatrix} \beta_P & 0 \\ 0 & \beta_N \end{bmatrix} \quad (6)$$

This is a gradient-dependent constitutive equation similar to those proposed by Aifantis and co-workers for shear banding and strain localization in unidirectional [7] and cyclic [8] deformation. The gradient term implies that there is an internal length scale in the material; here this is simply the cell size.

4. BAND PROPAGATION IN A REGULAR ARRAY OF CELLS

We first consider the case of an ideal cellular solid where all cells have equal crushing thresholds and coupling constants. Since the coupling between cells within a row is strong, we may reduce the problem to one dimension by assuming that all cells within a row

perpendicular to the direction of compression collapse simultaneously. With this simplification, Eq. (6) reduces to

$$D_N \frac{\partial^2 \varepsilon}{\partial x^2} = -\frac{\partial f(\varepsilon)}{\partial \varepsilon} \quad , \quad f(\varepsilon) = \sigma_{\text{EXT}} \varepsilon - \int \sigma(\varepsilon) d\varepsilon \quad , \quad D_N = \beta_N \sigma_c \frac{d^2}{\varepsilon_c} \quad . \quad (7)$$

This is a simple case of a problem studied extensively by Aifantis and Serrin [9]. In the external stress range where three branches of the $\sigma(\varepsilon)$ characteristics coexist, Eq. (7) exhibits 'reversal'-type solutions which correspond to localized deformation bands. In an infinite medium, these solutions describe a compressive strain profile which starts at $x = -\infty$ at a value ε_0 which is on the left stable branch of the $\sigma(\varepsilon)$ characteristics increases towards a maximum strain ε_1 and decays for $x = +\infty$ again to ε_0 . The solution which fulfils these boundary conditions can be found easily using the 'particle in a potential' analogy which is evident from Eq. (7); it is given by

$$\tilde{x} = \int_{\varepsilon_1}^{\varepsilon} \frac{d\varepsilon'}{\sqrt{2(f(\varepsilon_0) - f(\varepsilon'))}} \quad , \quad \tilde{x} = \frac{x}{\sqrt{D_N}} \quad , \quad f(\varepsilon_1) = f(\varepsilon_0) \quad , \quad \sigma(\varepsilon_0) = \sigma_{\text{EXT}} \quad . \quad (8)$$

As indicated in Figure 3, the solution corresponding to a given external stress fulfils the condition that the area enclosed from ε_0 to ε_1 between the curves $\sigma = \sigma_{\text{EXT}}$ and $\sigma = \sigma(\varepsilon)$ is zero.

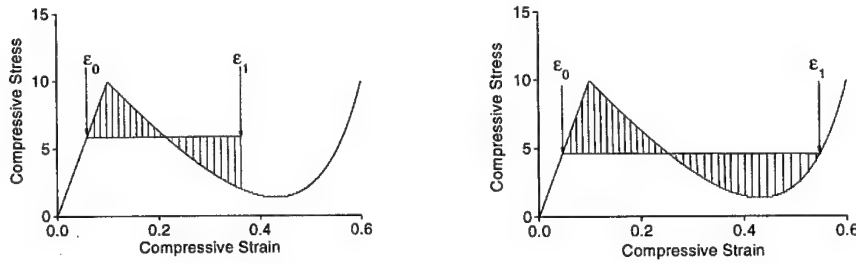


Figure 3: Equal-area condition, left: 'reversal'-type solution corresponding to the nucleus of a crushing band; right: 'transition'-type solution corresponding to a fully developed crushing front in an infinite medium.

When the external stress reaches the critical stress σ_c , a localized band develops and the strain profile evolves through the sequence shown in Figure 4. The behaviour is similar to the evolution of a shear band discussed by Zbib and Aifantis [7], with two differences: a) the system finally ends up on the right stable branch of the $\sigma(\varepsilon)$ graph while in the case of a shear band the peak strain may grow indefinitely. This implies that the strain profile ultimately approaches a transition-type solution which connects the two stable branches. This solution describes a front which propagates at constant stress across the sample; the propagation stress follows from the Maxwell construction shown in Figure 3, left, and the propagation speed is proportional to the imposed rate of compression. b) the strain on the left stable branch is *elastic* and may therefore decrease during the stress decrease which goes along with the formation of the crushing band.

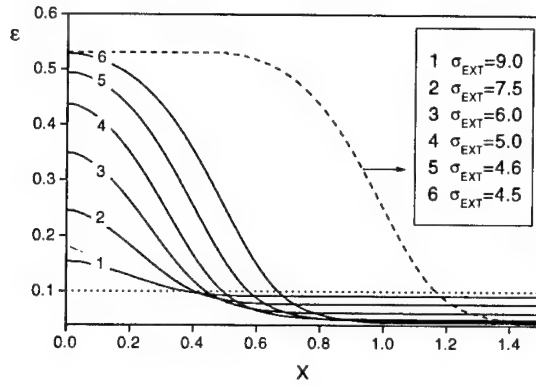


Figure 4: Strain profile for different stresses during the formation of a crushing band; parameters as in Figure 2; dotted line: Initial strain profile for $\sigma_C = 10$.

5. INFLUENCE OF DISORDER

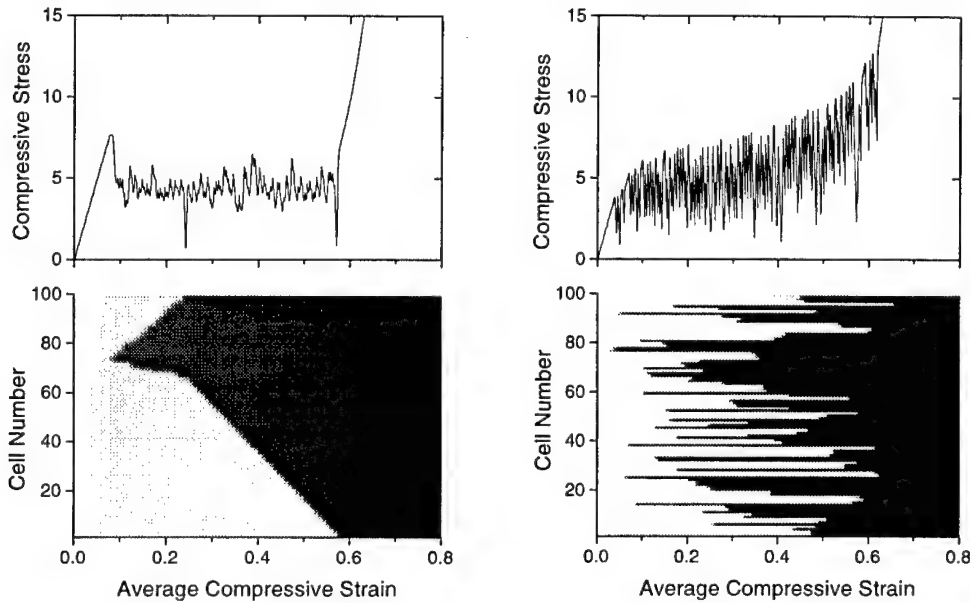


Figure 5: Simulations of crushing of a linear chain with 100 elements; top: stress-strain curves, bottom: greyscale maps (white: local strain zero, black: local strain 0.8) of the evolution of strain distribution with average strain; left: parameters $\sigma_C \geq 10$, $\delta\sigma_C=1$, $\beta_N=1$; right: parameters $\sigma_C \geq 10$, $\delta\sigma_C=10$, $\beta_N=0.2$; other parameters as in Figure 2.

Real cellular materials are non-periodical and characterized by a large degree of structural disorder. Their properties are strongly influenced by local heterogeneities, which may lead to a substantial reduction in strength in comparison with periodical cell arrangements [10]. We take into account disorder in terms of random variations of the crushing thresholds. In the

following we assume that the thresholds σ_c are independent random variables which have a log-normal distribution with average $\langle \sigma_c \rangle$ and variance $\delta\sigma_c$. Simulations of the constitutive equation (5) with random thresholds have been performed for the one-dimensional case using a cellular automaton model. Results are shown in Figure 5 for two extreme cases.

For small randomness and strong spatial couplings (Figure 2, left), the behaviour is as in the deterministic limit. As soon as the stress comes close to the crushing threshold, a localized deformation band nucleates where cells are weakest. Band nucleation goes along with a yield point followed by a stress plateau. In the plateau regime, the band spreads across the sample. In Figure 5, left, one observes two 'crushing fronts' which move from the nucleation point first to the top, then to the bottom. The direction of propagation is governed by the random variations in crushing strength which also lead to irregular stress oscillations throughout the plateau regime.

For large randomness and weak spatial couplings (Figure 2, right), band propagation is strongly hindered by the fluctuations in crushing strength. Crushing starts already at low stresses when the weakest cells fail. This does, however, not lead to the formation of a propagating band. Rather, bands continue to nucleate at random sites. As soon as their propagation is hindered by strong regions, a new band is nucleated at another 'weak spot' within the sample. The stress-strain curve oscillates strongly in the crushing regime, each stress drop corresponds to the crushing of one or a few cells. The upper envelope of these oscillations increases with average strain in a manner which directly monitors the distribution of the crushing thresholds.

6. CONCLUSIONS

We have formulated a phenomenological model of cell crushing which relates the formation and propagation of a crushing band to (i) strain softening during cell crushing and (ii) the spatial coupling that arises from the fact that collapse of a cell leads to damage of the adjacent cells. The formation of the crushing band is accompanied by a yield point and stress plateau in the macroscopic stress-strain curve. It has been shown that structural randomness may impede band propagation, suppress the yield point and give rise to a macroscopic stress-strain curve which (in spite of large fluctuations) increases with strain. This leads to the slightly paradoxical conclusion that random structural *heterogeneity* in a strain softening cellular material leads to a more *homogeneous* distribution of strain on macroscopic scale (Figure 5) and, in a certain sense, to a suppression of the strain softening instability.

The present model may be further improved. It has been implicitly assumed that crushing proceeds in a reversible manner, i.e., the original shape is recovered after unloading. While this is approximately true for some cellular materials (e.g. American toast bread), in general one has to distinguish plastic (irreversible) and elastic (reversible) strain. To generalize the model to 2D, both crushing and shear modes of deformation must be envisaged, and one must account for the anisotropy of the material which results from the crushing of cells.

Acknowledgements: The authors acknowledge support by the Commission of the European Communities under contract No. ERB FMRX-CT96-0062.

7. REFERENCES

- [1] Gibson, L.J. and Ashby, M.F., *Cellular Solids: Structure and Properties*, Pergamon, Oxford (1988).
- [2] Weaire, D. and Fortes, M.A., Stress and strain in liquid and solid foams, *Advances in Physics* 43, 685-738 (1994)

-
- [3] Bastawros, A.F., Bart-Smith, H., and Evans, A.G., Experimental analysis of deformation mechanisms in a closed-cell aluminum alloy foam, *Journal of the Mechanics and Physics of Solids* 48, 301-322 (2000).
 - [4] Fatima Vaz, M., Faria, L., and Fortes, M.A., Initiation and propagation of cell collapse in dynamic compression of cellular materials, *International Journal of Impact Engineering* 16, 253-271 (1995).
 - [5] Kubin, L.P., Estrin, Y., and Aifantis, E.C., Introductory remarks to the viewpoint set on propagative plastic instabilities, *Scripta Metallurgica et Materialia* 29, 1147-1150 (1993).
 - [6] Shim, V.P.W., Tay, B.Y., and Stronge, W.J., Dynamic crushing of strain-softening cellular structures- a one-dimensional analysis, *ASME Journal of Engineering Materials and Technology* 112, 398-405 (1992).
 - [7] Zbib, H. M. and Aifantis, E. C. (1988) On the Localization and Postlocalization Behaviour of Plastic Deformation I-III, *Res Mechanica* 23, 261-305 (1988).
 - [8] Zaiser, M., Avlonitis, M., and Aifantis, E.C., Stochastic and Deterministic Aspects of Strain Localization During Cyclic Plastic Deformation, *Acta Materialia* 46, 4143-4151 (1998).
 - [9] Aifantis, E. C. and Serrin, J. B., The mechanical theory of fluid interfaces and Maxwell's rule, *Journal of Colloid and Interface Science* 96, 517-529 (1983).
 - [10] Chen, C., Lu, T.J., and Fleck, N.A., Effect of imperfections on the yielding of two-dimensional foams, *Journal of the Mechanics and Physics of Solids* 47, 2235-2272 (1999).

6th National Congress on Mechanics

Appendix Late Papers*

Volume III

** Several late papers arrived just a few days before the proceedings were sent to the printer. They were received much after the deadline but an effort was made to include them in the Proceedings. In this category belong the five papers collected in this Appendix. Two additional papers by I. Groma and X. Markenscoff were not included because it was impossible for them to be reformatted according to the guidelines and print requirements of the Publisher. We apologize to these authors.*

MICROSTRUCTURES AND DEFECTS AT MECHANICALLY STRESSED COMPOUND SEMICONDUCTOR INTERFACES

Aris Christou

Materials Science and Engineering, University of Maryland, College Park, MD 20742 USA
email: christou@eng.umd.edu

A. Cornet

Department of Electronics, University of Barcelona, Barcelona, Spain

1. Introduction

Pseudomorphic growth of III-V heterostructures on non-(001) InP substrates have been investigated comprehensively since 1994 as shown by the initial publications [1-4] reporting phase decomposition and growth related defects including anti-phase domains. We may summarize these results for the (110), (111) and (112) InP substrates as follows:

(110) InP results in a polarization anisotropy [1,2,5,6],

(111) InP shows a strong piezoelectric effect along the growth direction [7], and

(112) InP also shows a strong polarization anisotropy for modulators and polarizers [8].

Reported polarization control of vertical channel surface emitting lasers (VCSELs) through use of an anisotropic gain distribution in (110) oriented strained quantum well structures has indicated the renewed importance of non (100) substrates for optics applications [9,10]. Anisotropy in the gain distribution was observed for the first time as well as second-order nonlinear polarization and harmonic generation in (112) InP based VCSELs.

In the present investigation we report the epitaxial growth by MBE of InAlAs on InGaAs on InP Substrates oriented as – (100), (110)A, (110)B, (111)A, (111)B, (112)A, (112)B. The objective of these investigations was to determine the influence of substrate orientation on possible alloy decomposition and ordering. Table 1 shows the double layer structure on InP. For comparison, we also grew a series of InAlAs with Al mole fraction of 0.478. Table 2 shows a comprehensive list of samples grown as a function of growth temperature and arsenic pressure.

Specimen analysis on all samples were carried out using transmission electron microscopy, either as plane view microscopy denoted as (PVTEM) or as cross-sectional microscopy denoted as (XTEM). Additionally, high resolution transmission electron microscopy (HRTEM) was utilized to identify ordering whenever necessary. Photoreflectance optical measurements were carried out on two (110), and (100) samples in order to identify optical anisotropies present in off (100) oriented samples. Atomic force microscopy (AFM) was also applied in order to identify and measure surface roughness on all samples. Through correlation of these techniques we now have a clear understanding of the reasons for surface roughness and for the origin of interfacial defects.

2. Experimental Results

The results of the present comparative investigation show that growth on (100) and (110)B index substrates resulted in smooth surfaces, without roughness, and hence without growth generated defects. However, growth on (110)A InP substrates resulted in pronounced roughness oriented along the $[220]$. These observations of surface roughness are general in nature and were detected on all samples grown on (110)B substrates shown in Table 2. They are not affected by arsenic over-pressure indicating that the growth conditions on non - (100) InP were optimal. Growth temperature also did not affect surface morphology but probably only affected factors related to surface diffusion. From AFM, the distance between hillocks was determined to be 90-95 nm. In addition, using XTEM techniques, we observed contrast stripes in the InAlAs inclined 8-12 degrees with respect to the horizontal. These contrast stripes are due to anti-phase domain boundaries (APBs) that separate the ordered microdomains that exist in these layers. These APBs create the surface roughness when they propagate to the sample surface. We concluded that sample roughness was related to contrast inhomogeneities due to composition modulation as reported by Guyer (9). The transmission electron diffraction (TED) patterns show two diffuse intensity maximum between 220 and 440 indicating CuAu I-type ordering on (110) planes. From such TED analysis we confirmed that the contrast stripes were APBs breaking the ordered microdomains. The presence of two maxima dividing the (220) vector in three equal pieces indicates that the ordered structures have a periodicity of three atomic planes, with every third plane being aluminum atoms. Neither stacking faults nor threading defects are observed in these samples.

On the other hand, growth on (111)B InP resulted in a high density of inverted pyramid defects and a faint roughness in the $[20\bar{2}]$ direction. The growth on (112)B InP showed a high density of the same crater defects (inverted triangular faceted pyramid). Lateral phase decomposition was also evident. The comparison of the above samples indicates no dependence on the mole fraction of aluminum. Table 4 summarizes the defects present on InAlAs surfaces grown on both (111)B and (112)B. These pyramid structures present faceted faces, forming inverted pyramids (Fig.1). The XTEM analysis allowed us to approximate the orientation of each facet. From other XTEM images, it is apparent that these inverted pyramids originated at the InGaAs/InP interface, and grew to the sample surface crossing both (InGaAs and InAlAs) layers. The origin of these faceted defects was due to the growth inhibition of the InGaAs layer over the InP substrate. These samples also presented an important lateral contrast modulation, which was deduced from the XTEM observation. This contrast modulation was also initiated at the InGaAs/InP interface and then extended to the remainder of the layer, continuing to the InAlAs upper layer. The lateral contrast modulation can be due to lateral decomposition or to a pure strain contrast. There is slight evidence of an ordered structure of CuPt-type. Due to the weakness of diffraction pattern maxima one cannot entirely conclude that the contrast is due to ordering. The XTEM data shows a quasi-periodic structure of contrast stripes perpendicular to growth axis of the InAlAs and InGaAs layers. These images are summarized by the schematic of Fig. 1.

Samples on (112)B InP substrate: In general, these surfaces are covered by faceted crater defects with inverted pyramid shape (Fig. 1). These defects are formed in the InGaAs layer which was initially grown on the InP substrate. The presence of the defects does not depend on arsenic pressure, nor on growth temperature.

The smooth surfaces, characteristic of the layers grown on (110)B is shown in the AFM images of Fig. 2. The morphology of Fig. 2 is characteristic of all samples grown on (110)B

and does not depend on aluminum mole fraction or growth temperature. In addition, arsenic overpressure, does not appear to be the primary reason for smooth surface formation. Typical surface roughness indicating periodic hillocks on (110)A surfaces is shown in Fig. 3. Such hillock formation extended over the entire lateral surface, and probably originated from the roughness of the APBs shown in Fig. 3. The TEM images show the inclined APBs in the InAlAs layer and the lateral APBs in the InGaAs layer (Fig. 4). The TED patterns of Fig. 5 again confirmed the type of order present in the heterostructures grown on (110)A InP. In contrast to (110)A and (110)B InP, the structures grown on (111)B and (112)B InP resulted in a different morphology. Fig. 6 shows typical triangular pyramid defects on heterostructures grown on (112)B InP. The origin of the triangular defects is the surface of the InP substrate at locations of local compositional perturbations or surface steps of undetermined origin. InAlAs grown on (111)A and (112)A did not show the presence of triangular defects and hence the B orientation is critical to the formation of such defects. The smooth surfaces on "B" type (110) substrates are presented first in the AFM images which follow. These surfaces were observed on all (110)B samples and were independent of arsenic pressure and growth temperature.

Two diffuse diffraction spots between the 220 and 440 reflections for (110)A is shown in Fig. 5. The division of the 220 vector into three parts indicates that every third atomic plane is a mono-atomic platelet. This also indicates that the distance between the matrix and the diffuse spots is slightly larger than $(1/3) g_{220}$. In direct space, this corresponds to a smaller interplanar (110) distance between the platelets. Since aluminum atoms have a smaller radius than In or Ga, then every third plane is occupied by aluminum atoms. The contrast modulation must then be due to compositional modulation because of the presence of aluminum in the InAlAs compound. The compound InAlAs is therefore more susceptible to contrast modulation than the InGaAs compound.

Fig. 6 shows the faceted craters for growth on (112)B InP which were similar to growths on (111)B InP. The facet formation may be explained by the different growth velocities on the inclined planes. Growth inhibition therefore created these faceted structures, and their extent does depend on surface diffusivity differences.

Photoreflectance spectrum on InAlAs and InGaAs grown on (110)B substrates shows a shift in the main reflectance transition depending on the direction of beam propagation. Such shifts in photoreflectance are indicative of an optical anisotropy or a polarization anisotropy. Similar studies carried out on (100) InP substrates showed an overlap of spectra independent of the direction of propagation. Photoreflectance of samples on (100) InP are shown in Fig. 7, while Fig. 8 shows the spectrum of samples grown on (110)B InP. It is interesting to note that the same anisotropy was found on samples grown on InP (110)A surfaces. Hence, the polarization anisotropy may not be explained by phase decomposition or contrast modulation and may be due to strain effects resulting in valence band mixing, or even from lateral modulation.

3. Conclusions

We have reported the effect of the InP substrate orientation on the surface morphology of InAlAs deposited by molecular beam epitaxy on InGaAs buffer layers. The phosphorus termination of the InP substrate and the defects generated at the buffer layer – substrate interface, rather than the growth parameters, determines the surface morphology of InAlAs grown on non – (100) InP. These defects ranged from anti-phase domain boundaries (APBs) to triangular pyramid defects to surface hillocks. Surface structure indicative of APB

formation and phase decomposition was indicative of InAlAs grown on (110)A InP. Such morphologies were not significantly affected by growth temperature nor arsenic overpressure. In contrast, InAlAs/InGaAs layers grown on (110)B InP substrates were smooth without noticeable unique surface morphologies. It has also been shown by the present investigation that on (110)A substrates regions of InAlAs layers had CuAuI type ordering and composition modulation. These morphologies were caused by the presence of aluminum and hence was weakly affected by the growth temperature. The pyramid faceted craters likewise were observed in InAlAs/InGaAs layers grown on (111)B and (112)B indexed InP substrates. In addition, evidence of lateral contrast modulation was also present. A preliminary investigation of optical anisotropy in InAlAs on non – (100) InP substrates showed evidence of in-plane optical anisotropy on (110)A and (110)B InP substrates. The optical anisotropy was not observed in InAlAs grown on (100) InP.

Acknowledgements: The authors thank Prof. Salamanca-Riba for assistance in the analysis of some of the InAlAs/InGaAs/InP samples. The authors acknowledge the assistance of R. Leavitt of the Army Research Laboratory for the MBE growth of some of the samples. The investigations were supported by the ARL-UMD cooperative research agreement in microelectronics.

4. References

- [1] X. Chen, C. H. Malloy, D. J. Someford, J. Sharma, J. Appl. Phys. Lett. **67**, 1393 (1995).
- [2] Y. Okuno, T. Tsuchiya and M. Okai, Appl. Phys. Lett. **71**, 1918 (1997).
- [3] E. Bhat, M. A. Koza, D. M. Hwang, M. Brasil, R. E. Nahory, J. Crystal Growth **124**, 311 (1992).
- [4] G. J. Rees, J. Microelec. **28**, 957 (1997).
- [5] M. Mitsuhashi, M. Okamoto, R. Iga, T. Yamada, J. Crystal Growth **136**, 195 (1994).
- [6] N. D. Zakharov, Z. Liliental-Weber, W. Swider, J. Wasburn, A. S. Brown and R. Metzger, J. Elec. Mat. **22**, 1495 (1993).
- [7] J. E. Guyer and P. Voorhees, J. Crystal Growth **187**, 150 (1998).
- [8] J. Mawst, A. Bhattacharya, J. Lopez, D. Botez, D. Z. Garbuzov, L. DeMarco, J. C. Connolly, M. Jansen, F. Fang and R. F. Nabiev, Appl. Phys. Lett. **69**, 1532 (1996).
- [9] N. D. Whitbread and P. N. Robson, IEEE J. Quantum Electron. **30**, 139 (1994).
- [10] J. A. Armstrong, N. Bloembergen, J. Ducuing and P. S. Pershan, Phys. Rev. **127**, 1918 (1962).

Materials Grown	X, Mole Fraction
50nm $\text{In}_{1-x}\text{Al}_x\text{As}$	0.478 – 0.518
50 nm $\text{In}_{0.53}\text{Ga}_{0.47}\text{As}$	0.53
InP Substrate	
Orientation: (100), (110)A, (110)B, (111)A, (111)B, (112)A, (112)B	

Table 1. Layers grown on InP of various orientations, and on one 50 nm $\text{In}_{0.53}\text{Ga}_{0.47}\text{As}$ buffer layer.

Sample No.	Substrate Orientation	Al Mole Friction	Growth Temperature (°C)	As Pressure, 1×10^{-5} Torr
695	(100)	0.478	544 °C	1.10
	(110)A, (110)B	0.478	544 °C	1.10
	(111)A, (111)B	0.478	544 °C	1.10
	(112)A, (112)B	0.478	544 °C	1.10
697	(100)	0.518	544 °C	1.64
	(110)A, (110)B	0.518	544 °C	1.64
	(111)A, (111)B	0.518	544 °C	1.64
	(112)A, (112)B	0.518	544 °C	1.64
698	(100)	0.518	562 °C	1.64
	(110)A, (110)B	0.518	562 °C	1.64
	(111)A, (111)B	0.518	562 °C	1.64
	(112)A, (112)B	0.518	562 °C	1.64
699	(100)	0.518	544 °C	0.65
	(110)A, (110)B	0.518	544 °C	0.65
	(111)A, (111)B	0.518	544 °C	0.65
	(112)A, (112)B	0.518	544 °C	0.65
705	(110)A, (110)B	0.478	567 °C	1.73
	(111)A, (111)B	0.478	567 °C	1.73
	(112)A, (112)B	0.478	567 °C	1.73
706	(110)A, (110)B	0.478	522 °C	1.10
	(111)A, (111)B	0.478	522 °C	1.10
	(112)A, (112)B	0.478	522 °C	1.10

Table 2. Summary of the samples grown for the present investigation. The set of samples 697 and 705 were grown under excess arsenic conditions in order to compare the degree of surface roughness under these conditions.

Sample No.	Orientation	Al Mole Fraction	Distance Between Hillocks, (nm)
695	(110)A	0.478	103
	(111)A	0.478	110
697	(110)A	0.518	95
	(111)A	0.518	102
698	(110)A	0.518	91
	(111)A	0.518	95
706	(110)A	0.478	78
	(111)A	0.478	85

Table 3. Hillocks separation distance measured for the series of (110)A and (111)A samples. Growth on (110)A resulted in a shorter separation distance in comparison to growth (111)A surfaces.

Sample No.	Orientation of Substrate	Hillocks Separation Distance(nm)	Density of Oval Defects 10^7 cm^{-2}
697	(111)B	142	10
	(112)B	135	10
698	(111)B	106	10
	(112)B	100	8 - 9
699	(111)B	72	2
	(112)B	65	7 - 8

Table 4. Comparison of Hillock Separation Distance and Density of Oval Defects for Samples Grown on (111)B and (112)B.

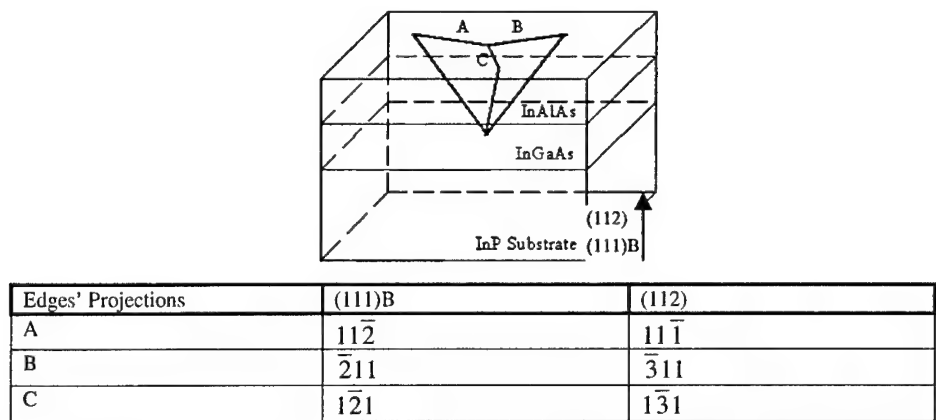


Fig. 1. Scheme of inverted pyramid structures in samples (111)B and (112)B. Letters A, B and C label the three edge projections on sample surface.

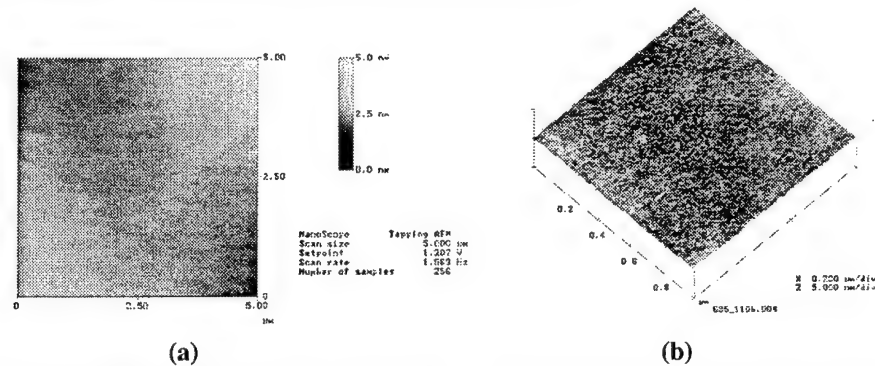


Fig. 2a) AFM image of sample 695 (110)B. The surface is completely smooth and lacking any indication of roughness. Similar smoothness was evident on all (110)B surfaces.**Fig. 2b)** 3D AFM image of sample 695 (110)B again indicates smoothness. Similar morphologies was observed for samples 697, 698, 699, 705 and 706.

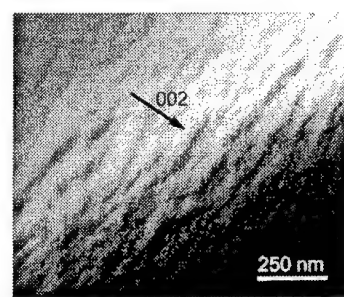


Fig. 3. AFM image of a typical InAlAs/InGaAs heterostructure grown on the (110)A surface of sample 697. Periodic surface roughness shown is indicative of all samples grown on “A” type surfaces



Fig. 4. Cross-sectional TEM of InAlAs/InGaAs grown on (110)A showing the inclined APBs. These APBs resulted in a surface roughness consisting of wave like hillocks separated by distances listed in Table 3.

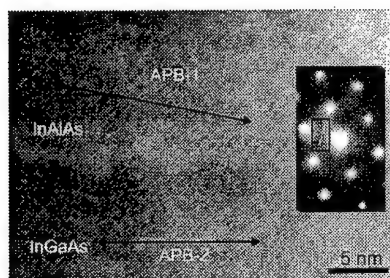
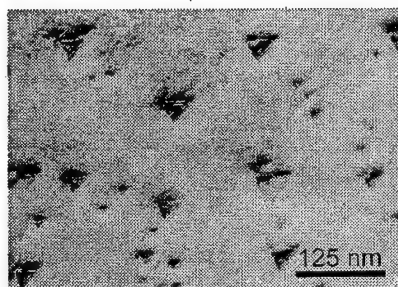
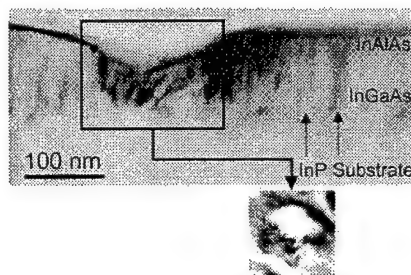


Fig. 5. TED pattern of samples grown on (110)A showing ordering present in the InAlAs layer.



(a)



(b)

Fig. 6a) PVTEM micrograph of sample 695 (112)B. The triangle faceted defects are homogeneously distributed on the sample surface. **Fig. 6b)** Cross-sectional TEM image of sample 695 (112) InP. The triangle defects have a faceted structure.

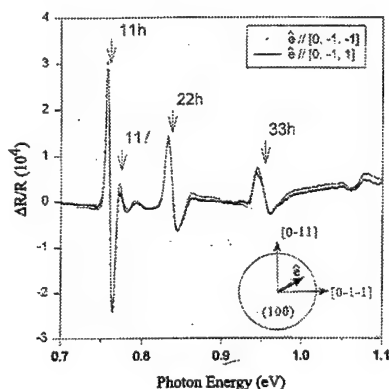


Fig. 7. Photoreflectance spectrum of InAlAs/InGaAs heterostructures grown on (100) InP showing no change in polarization direction. The spectra overlap for two polarization directions $[0, -1, -1]$ and $[0, -1, 1]$ is shown.

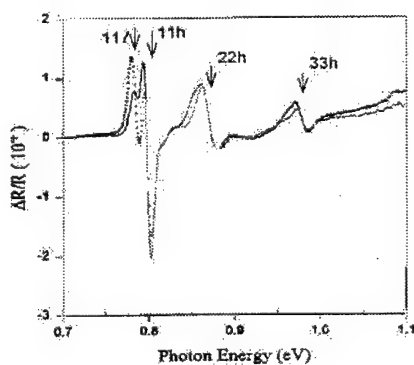


Fig. 8. Photoreflectance spectrum of heterostructures grown on (110)B InP. The dotted line is plane wave parallel to $[0, \bar{1}, 0]$, while solid line is parallel to $[0, 1, 0]$.

MECHANICAL PROPERTIES OF CEMENT - CLAY MORTARS CONTAINING METHYL - METHACRYLATE POLYMER

C.A. Anagnostopoulos and J.N. Grammatikopoulos

Department of Civil Engineering
Aristotle University of Thessaloniki, GR - 54006, Greece

S. Hadjispyrou

Department of Chemical Engineering
Aristotle University of Thessaloniki, GR - 54006, Greece

1. SUMMARY

The parameters, which should be taken into account, during the restoration of ancient masonries, are the retaining of a constructional aesthetic, using mortars made of materials compatible with the existing ones and the strengthening of the construction.

Taking all the above into consideration, in this work we studied the mechanical and physical properties of mortars, with various mixing proportions.

These mortars were made of materials, which usually are employed for the restoration of ancient masonries, in combination with polymeric latex, a new technology product.

2. INTRODUCTION

The prediction of mortars content, which should be used in the restoration of ancient masonries, as a coating or as joining material, has been the subject of many workers until now [1, 2, 3].

A particular subject of research is the adhesion of the new mortar onto the old brick and the cooperation developed between them under several mechanical stresses or under specific environment conditions (e.g. excess humidity).

The use of mortars with high cement and pozzolane content, is incompatible with the existing fabric from aesthetics point of view. Beside that, this use is problematic, due to enhanced humidity on the interface between old and new material, a fact that results usually in several damages [4, 5].

On the contrary, repairing mortars with low cement and high silt content, which is compatible with the materials of the ancient masonries, from the one hand maintain the traditional shape of the construction, but from the other hand they exhibit low mechanical strength and high erodibility in environment conditions [6, 7, 8].

Taking all the above factors into consideration, our work was focused on the study of mortars with proper composition, in order to be compatible with the existing masonry and acceptable

Fig. 2: Sieve analysis of the sand

Methyl - Methacrylate (MMA, latex)

It was prepared in the laboratory of Chemical Engineering dpt. of Thessaloniki as a 30% (w/w) solution.

4. LABORATORY PROCEDURE

Mixing proportions of the mortars used for the preparation of the specimens, are given in Table 2. Also the properties of a mortar, usually applied in the restoration of ancient masonries have been studied and compared with the corresponding properties of polymer mortars. The composition and the mechanical parameters of the common mortar were the following: Lime: Pozzolane: Cement: Sand: Water = 1:0,2:0,6:6:1,5

Compressive strength was $1,64 \text{ N/mm}^2$, flexural strength was $0,33 \text{ N/mm}^2$ and the interface strength was $0,206 \text{ N/mm}^2$.

Compressive, flexural and interface strengths of polymer mortars were measured at 28 days according to the specifications of A.S.T.M. C 109-92 and C 78-84 correspondingly. Specimens for compressive strength were cubic with 2in edge and specimens for flexural strength had size $4 \times 4 \times 14 \text{ cm}$. Determination of interface strength was done by using bricks made of clay with dimensions $4 \times 5,3 \times 21 \text{ cm}$. Bi - material bending specimens were made with two bricks connected with each other at their $40 \times 53 \text{ cm}$ surface by mortar of 1 cm thickness. This system was placed between two support blocks and tested with the third - point loading method (fig. 3). The results of the above tests are shown in Table 3 and the stress - strain state is provided in fig. 4.

For the determination of mortars porosity, specimens with size $4 \times 4 \times 14 \text{ cm}$ were prepared and cured in laboratory air until the development of satisfactory strength. Afterwards, their weight was determined and they were submerged in water. After a week, the specimens were taken out of the water and their weight was recorded again. From the weight change, the porosity of the specimens was easily calculated.

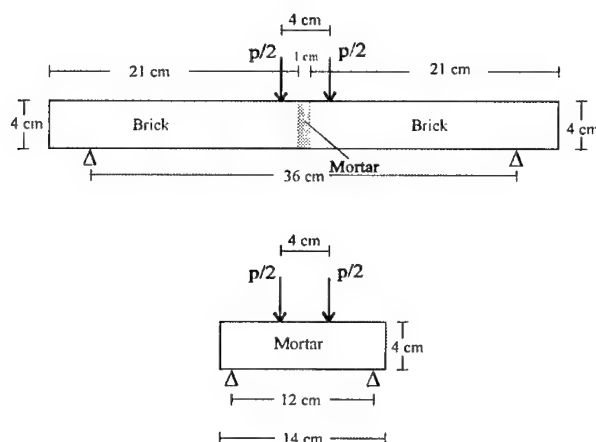


Fig. 3: Flexural test of mortar and bi - material specimens by third - point loading method

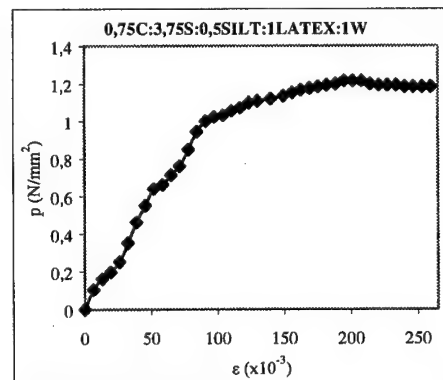
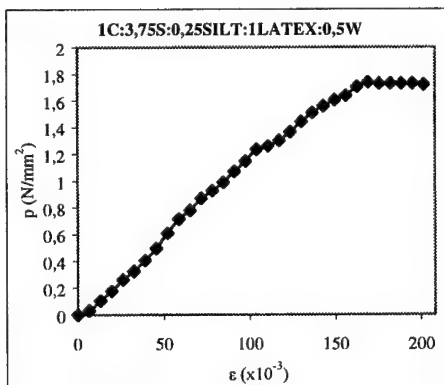
Table 2: Mixing proportions of mortars (by weight)

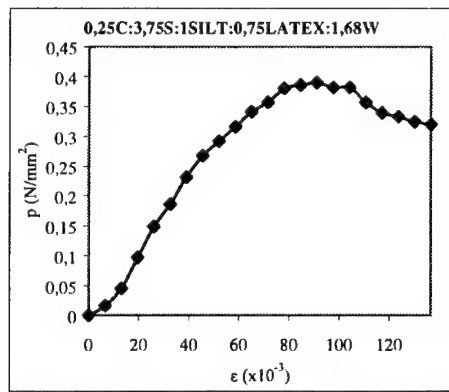
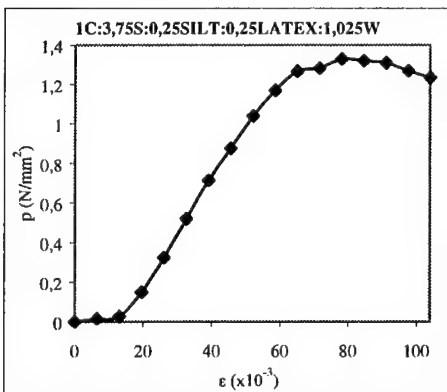
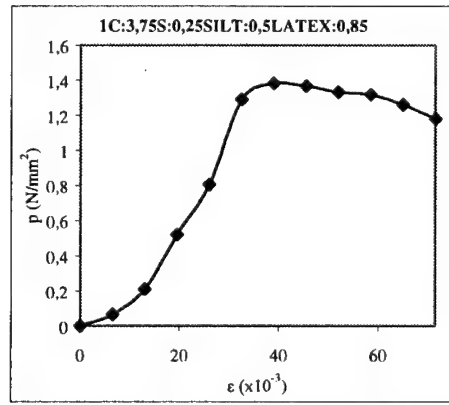
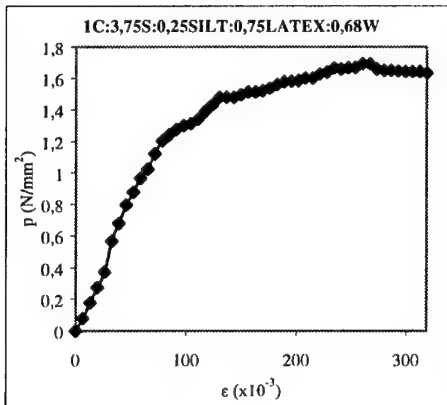
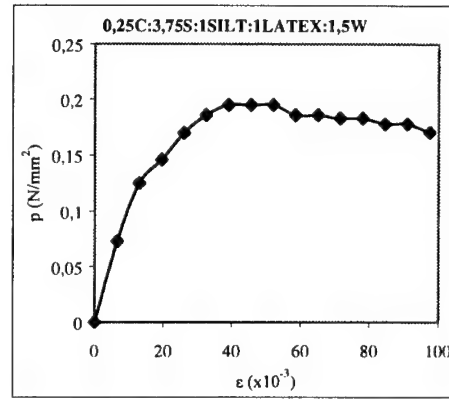
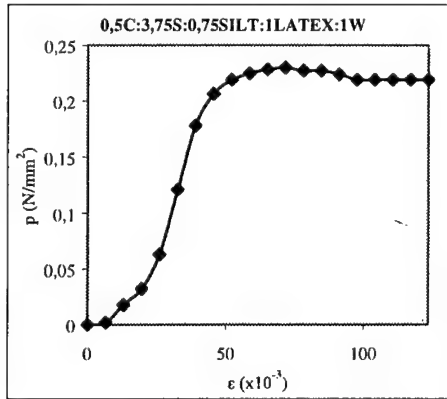
Mortar	Cement	Sand maxd=6mm	Silt	Latex	Water
M ₁	1	3,75	0,25	1	0,5
M ₂	0,75	3,75	0,5	1	1
M ₃	0,5	3,75	0,75	1	1
M ₄	0,25	3,75	1	1	1,5
M ₅	1	3,75	0,25	0,75	0,68
M ₆	1	3,75	0,25	0,5	0,85
M ₇	1	3,75	0,25	0,25	1,025
M ₈	0,25	3,75	1	0,75	1,68
M ₉	0,25	3,75	1	0,5	1,85
M ₁₀	0,25	3,75	1	0,25	2

Table 3: Test results (28 and 90 days) of mortars of Table 2

Mortar	Compressive Strength (N/mm ²)		Flexural Strength (N/mm ²)		Interface Strength (N/mm ²)		Porosity (%)
	28 days	90 days	28 days	90 days	28 days	90 days	
M ₁	1,74	*	0,571	0,75	0,98	1,56	9
M ₂	1,24	*	0,421	0,436	0,82	1,277	9,4
M ₃	0,235	*	0,105	0,24	0,618	1,03	37,7
M ₄	0,195	0,2	0,075	0,08	0,239	0,33	53,1
M ₅	1,7	*	0,526	0,65	1,21	1,45	24,6
M ₆	1,38	*	0,4	0,54	0,83	1,22	29,4
M ₇	1,33	*	0,36	0,466	0,65	0,84	27,1
M ₈	0,394	0,41	0,045	0,05	0,123	0,135	44
M ₉	0,552	0,55	0,087	0,09	0,247	0,32	36,7
M ₁₀	0,243	0,26	0,037	0,042	0,208	0,3	48,4

* Extended plastic zone





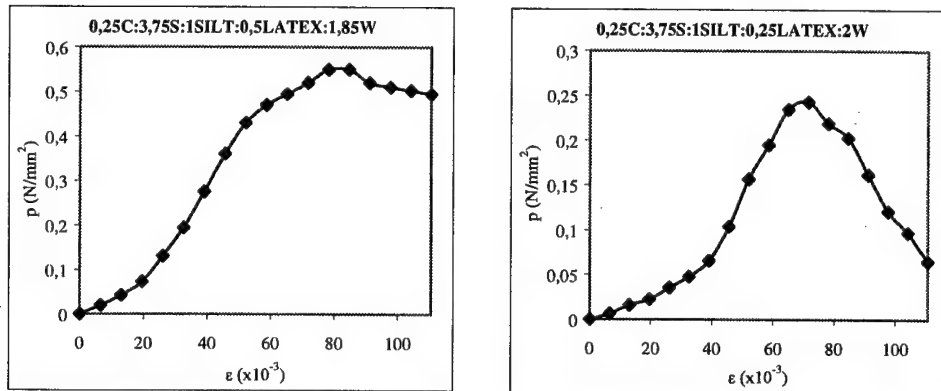


Fig. 4: Stress - strain state of mortars aged 28 days

5. RESULTS AND DISCUSSION

In 28 days tests, mortars with high cement and latex content, exhibited slightly higher compressive strength than the conventional mortar. Especially high difference was observed in flexural and interface strength which were much more higher than the corresponding of cement mortar usually employed. From the diagrams of stress - strain state for compressive pressure, it is obvious that these mortars were subjected to significant deformations without breaking, whereas the plastic zone was especially extended.

It should be pointed out here, that interface strength is higher than the flexural strength, for all mortars studied in this work.

Lowering of the cement content with concomitant increase of the silt, resulted in the decrease of compressive, flexural and interface strength, whereas the plastic zone remained very extended. Nevertheless, interface strength was higher than the mortar's flexural strength, which is an indication of the important contribution in the development of mortar adhesion on the brick, triggered by latex. Increase of the silt content, resulted in high porosity values.

When the latex content of the mortar was decreased, this had as an implication the concomitant significant reduction of compressive, flexural and interface strength. The specimen's deformation was reduced and the plastic zone was narrowed thoroughly.

6. CONCLUSIONS

1. Mortars with high latex content, have higher flexural and interface strength than the cement mortars usually employed. Also, they exhibit enhanced deformation and extended plastic zone.
2. Reduction of latex content, results in the lowering of strength and especially the interface strength. Reduction of the cement content, has an impact on the mechanical properties, as a whole.
3. Mortars with high clay content exhibit very low strength, whereas the porosity is high. This factor should be taken into account, in cases of masonries restoration, which are surrounded by very humid environment.

7. REFERENCES

- [1] Atkinson, R.H., Amadei, B.P., Saeb, S. and Sture, S., (1989), Response of Masonry Bed Joints in Direct Shear, Proc. ASCE, Vol. 115, SE 9, pp. 2276-2296.
- [2] Augustijns, R., (1997), Development of a lime - pozzolane - cement grout with an ultrasonic mixing procedure for the repair and strengthening of historical masonry, Thesis, De Nayer Inst. - K.U. Leuven.
- [3] Chandra, S., Van Rickstal F. and Van Gemert D., (1993), Evaluation of cement grouts for consolidation injection of ancient masonry, Proc. Nordic, Concrete Research Meeting, Goeteborg, pp. 353-355.
- [4] Collepardi, M., (1990), Degradation and restoration of masonry walls of historical buildings, J. Materials and Structures, Vol. 23, pp. 81-102.
- [5] Justnes, H., Ardoullie, B., Hendrix, E., Sellevold, E.J. and Van Gemert, D., (1998), The chemical shrinkage of Pozzolanic Reaction Products, SP 179-11, Int. Conf. on fly ash, Silica fume, Slag and Natural Pozzolans in Concrete, 6th CANMET/ACI/JCI, Bangkok, Vol. 1, pp. 191-205.
- [6] Mann W. And Muller H., (1982), Failure of Shear - Stressed Masonry. An enlarged Theory, Tests and Application to Shear Walls, Proc. of the British Ceramic Society, No 30, Load Bearing Brickwork (7), pp. 223-235.
- [7] Rosvall, J. and Aleby, S., (1988), Air Pollution in Conservation, Ed. Elsevier.
- [8] Toumbakari, E.E. and Van Gemert, D., (1997), Lime - pozzolana - cement injection grouts for the repair and strengthening of masonry structures, Proc. IVth Int. Conf. on the Conservation of Monuments in the Mediterranean Basin, Rhodes, Vol. 3, p.p. 385-394.

THE POTENTIAL OF THE MULTIPLE POROSITY MODEL

Konstadinos N. Moutsopoulos

Laboratory of Mechanics and Materials, Laboratory of Engineering Geology,
Engineering School, Aristotle University, 54006 Thessaloniki, GREECE

1. SUMMARY

The hydraulic behavior and the contaminant transport in fractured aquifers are complex processes. A large number of models are proposed in the literature for their modelization. In this paper we will focus our interest on the multiple porosity model. Original equations using this concept are presented, concerning the hydraulic behavior of karst aquifers and the description of chemical reactions taking place in fractured aquifers. Methods for the determination of phenomenological coefficients are also presented.

2. INTRODUCTION

The flow behavior of fractured aquifers, in many cases cannot be simulated using the conventional approach of groundwater hydraulics.

It is largely recognized that more sophisticated approaches have to be introduced: the discrete fracture model [1], the network fracture model [2], the double porosity model [3].

In this paper we will focus our interest on the multiple porosity model developed by Aifantis, [4,5,6]. It is adequate to simulate the flow behavior of aquifers which contain one or more families of fractures in addition to the porous matrix. The justification for the introduction of more than one families of fractures was provided by Bai *et al.* [7] and Moutsopoulos *et al.* [8].

The conditions that should be satisfied for the above mentioned theoretical framework to be valid are:

- (a) Each group of pores (fractures or porous matrix) can be treated as a fictitious equivalent continuum.
- (b) At every point of the pore space the Stokes equation holds.

3. SIMULATION OF THE FLOW BEHAVIOR OF MULTIPLE POROSITY AQUIFERS

The macroscopic equations

The expression for the flow transport in 2D was developed by Moutsopoulos *et al.* [8]

$$S_i \frac{\partial h_i}{\partial t} - \nabla \cdot [\mathbf{T}_i \cdot \nabla h_i] = \sum_{j=1, n_f} \kappa_{i,j} (h_j - h_i); \quad i = 1, \dots, n_f \quad (1)$$

where the subscripts i, j denote families of fractures, S the storage coefficient, \mathbf{T} the transmissivity tensor, ∇ the 2D Nabla operator, $\kappa_{i,j}$ is an adequate exchange coefficient and h is the piezometric head.

An important feature of the multiple porosity model is its flexibility. To illustrate this fact we will present extensions of the macroscopic equations and extensions of relations for the phenomenological coefficients.

We consider a karst aquifer in which a fracturization process took place. We further assume that in the microscopic scale the flow process is described by the Stokes equation in the pore-space was created by mechanical means (so that the use of the Darcy-equation is justified in the REV scale), while the inertial terms cannot be neglected in conduits created by chemical erosion, so that the Forchheimer equation [9] is the adequate modelization approach for this continuum.

The Forchheimer equation reads:

$$-\frac{\partial h_k}{\partial x} = W_x q_x + b_x q_x^2, \quad -\frac{\partial h_k}{\partial y} = W_y q_y + b_y q_y^2 \quad (2a,b)$$

The subscript k denotes the karst area, q the flux, h the piezometric head, while W and b are phenomenological coefficients.

By expressing the mass balance of each continuum in a control box and assuming that

$$\left| \frac{b_x \frac{\partial h_k}{\partial x}}{W_x^2} \right| \ll 1, \quad \left| \frac{b_y \frac{\partial h_k}{\partial y}}{W_y^2} \right| \ll 1, \quad (3)$$

the mathematical expression for the piezometric heads is given by the following system of equations:

$$S_k \frac{\partial h_k}{\partial t} - \frac{\partial}{\partial x} \left[\frac{B}{W_x} \frac{\partial h_k}{\partial x} \right] - \frac{\partial}{\partial x} \left[\frac{B b_x}{(W_x)^3} \left(\frac{\partial h_k}{\partial x} \right)^2 \right] - \frac{\partial}{\partial y} \left[\frac{B}{W_y} \frac{\partial h_k}{\partial y} \right] - \frac{\partial}{\partial y} \left[\frac{B b_y}{(W_y)^3} \left(\frac{\partial h_k}{\partial y} \right)^2 \right] = \sum_{i=1, n_f} R_{k,i} \quad (4a)$$

$$S_i \frac{\partial h_i}{\partial t} - \nabla \cdot [\mathbf{T}_i \cdot \nabla h_i] = \sum_{j=1, n_f} \kappa_{i,j} (h_j - h_i) + R_{k,i}; \quad i = 1, \dots, n_f \quad (4b)$$

where $R_{k,j}$ is a sink-source term. For practical purposes we suggest the use of the equation

$$R_{k,j} = \kappa_{k,j}(h_j - h_k)$$

On the estimation of the exchange coefficients

For the calculation of the coefficients T_i and S_i one can use the classical relations proposed in the literature, developed for single porosity aquifers [9,10,11].

In order to estimate the exchange coefficients one can use a schematization of the fracture geometry[8]. The exchange coefficient $\kappa_{i,j}$ is solely influenced by the geometrical properties of "type-2" fractures connecting media i and j .

Its mathematical expression reads:

$$\kappa_{i,j} = n_{i,j} \frac{\pi r_{i,j}^4 B g}{8 l_{i,j} \nu} \quad (\text{circular cross-section of the type-2 fractures}), \quad (5a)$$

$$\kappa_{i,j} = n_{i,j} \frac{d_{i,j} w_{i,j}^3 B g}{12 l_{i,j} \nu} \quad (\text{rectangular cross-section of the type-2 fractures}) \quad (5b)$$

where ν is the cinematic viscosity of the fluid, $n_{i,j}$ denotes the number density of type-2 fractures connecting media i and j , $r_{i,j}$ denotes radius of a circular cross-section, $w_{i,j}$ denotes fracture height and $d_{i,j}$ denotes fracture width ($d_{i,j} \gg w_{i,j}$) of a rectangular cross-section. The symbol $l_{i,j}$ denotes the length of the type-2 fractures connecting families i and j , while g is the gravity constant. For the case of a double porosity medium, the subscripts can be omitted.

If the geometric properties of the type -2 fractures inside a control box are not constant, we propose the use of the following expression:

$$\kappa_{i,j} = \sum_{g=1, n_g} n_{i,j}^g \frac{\pi (r_{i,j}^g)^4 B g}{8 l_{i,j}^g \nu} \quad (6)$$

where the superscript g denotes a group of fractures and n_g the total number of groups. One can get a similar expression for fractures having a rectangular cross-section.

Measurements of the fractures characteristics can take place in field by various techniques which are both time consuming and expensive.

We propose alternatively or complementary an other procedure.

The creation of a discrete fracture network by numerical means, and the calculation of its hydraulic characteristics is described by Long & Billaux, [12] and Billaux, [13]. The creation of a fracture network is technically an easier task than the simulation of its hydraulic behavior.

We propose therefore, that the geometrical network properties of the network should be used to compute phenomenological coefficients describing its macroscopic behavior (by using for example eqns (5) presented in this issue). The simulation of the various procedures taking place in the aquifer can be undertaken by using a continuum approach.

It is worth mentioning that use of discrete network models have been useful in problems of near-field simulation over length scales of 50 to 100 m. The use of the discrete network approach in problems involving non-linear hydraulic behavior or chemical reactions might be an even more extraordinary task.

4. CONTAMINANT TRANSPORT AND CHEMICAL REACTIONS

We think that a case for which the advantages of the introduction of more than one continuum in a aquifer is spectacular, is the occurrence of chemical/biochemical reactions : the correct simulation of the reaction processes depends on the detailed description of the concentration field.

This fact was demonstrated by Sun *et al.* [14], albeit for a special case: only two continua were considered, in one of them no flow was taking place.

The equations for the contaminant transport in a multiple porosity medium, for the case of horizontal flow and conservative species were developed by Moutsopoulos *et al.* [8].

We propose a generalized version of the above system by considering the presence of n_s species in each medium.

$$\frac{\partial c_i^s}{\partial t} + \nabla \cdot [\mathbf{v}_i^s c_i^s] - \nabla \cdot [\mathbf{D}_i^s \cdot \nabla c_i^s] = (r_d)_i^s + (r_c)_i^s + X_i^s; \quad s = 1, \dots, n_s; \quad i = 1, \dots, n_f \quad (7)$$

where

$$(r_c)_i^s = \sum_{j=1, n_f}^{i \neq j} (r_c)_{i,j}^s, \quad (r_d)_i^s = \sum_{j=1, n_f}^{i \neq j} (r_d)_{i,j}^s,$$

c denotes the concentration, the subscript i the medium, the superscript the specie s , \mathbf{v} is the front velocity, \mathbf{D} is the dispersion tensor, $(r_c)_i^s$ and $(r_d)_i^s$ the advection and diffusion driven sink-source terms respectively. (If both i and j are fracture families one can use the expression referred in [8], otherwise one can use those referred by Dykhuizen [15]). Finally X represents the chemical reaction sink-source terms [16,17,18].

5. CONCLUSIONS

The multiple porosity model is a powerful and flexible tool for the simulation of processes taking place in aquifers.

This fact was partially demonstrated in this paper: Some extensions concerning the hydraulic behavior of karst aquifers and the description of chemical reactions in multiple porosity aquifers were presented, the estimation of the estimation of some phenomenological

coefficients was also discussed. Another important issue is the compactness of the model: One can use the same concept to simulate the processes discussed above, but also the transport of chemical inert species (Moutsopoulos *et al.*, [8]), and the consolidation of aquifers, as it was demonstrated by Wilson & Aifantis [19] and Aifantis [20].

Acknowledgements: The support of GSRT under PENED 1958 and several discussions with Professor Aifantis are gratefully acknowledged.

6. REFERENCES

- [1] Zielke W.:1991, Grundwasserstroemungen und Schadstofftransport *Finite Elemente Anwendungen in der Baupraxis* 5.-6. September Karlsruhe Germany).
- [2] Andersson J. and Dverstop B.: 1987 Conditional simulation in three dimensional networks of discrete fractures. *Water Res., Res.* vol 23 (10), p. 1876-1886.
- [3] Barenblatt G. I., Zheltov I.P. and Kochina N.:1960, 'Basic concepts in the theory of seepage of homogeneous liquids in fissured rocks, *Prikl. Math. Mekh.*, vol. 24, (5), p. 852.
- [4] Aifantis E.C.:1977,Introducing a multi-porous medium, *Developments in Mechanics*, vol. 8, p.209-211.
- [5] Aifantis E.C.:1979, A new interpetation of diffusion in high diffusivity paths- A continuum approach, *Acta Metallurgica*, vol. 27, p. 638-69.
- [6] Aifantis E. C. and Hill J. M.:1979, On the theory of diffusion in media with double diffusivity I-Basic mathematical results, *Quarterly Journal of Mechanics and Applied Mathematics*, **33**, 1-21.
- [7] Bai M., Elsworth D. and Roegiers J. C.: 1993, Multiporosity /Multipermeability Approach to the Simulation of Naturally Fractured Reservoirs, *Water Res. Res.*, **29**, no 6, 1621-1633.
- [8] Moutsopoulos K.N., Konstantinidis A.A., Meladiotis I.D., Tzimopoulos C. D., and Aifantis E.C.:2001, Hydraulic behavior and contaminant transport in multiple porosity media, *Transport in porous Media*, vol 42, p.265-292.
- [9] Bear, J.:1979, *Hydraulic of Groundwater*, McGraw-Hill, New York, 560 pp.
- [10] Louis, C.:1967, Groundwater flow in rock masses and its influence on stability. *Rock. Mech. Res. Rep.* 10, Imperial college, London.
- [11] Spyrides A. S. and Tzimopoulos C.D.: 1997, Sensitivity analysis of the storativity coefficient and its estimation with the aid of hydrodynamic parameters, *7th Congress of the Greek Hydrotechnical Society*, Patra, Greece (in greek).
- [12] Long, J.C.S. and Billaux, D.: 1987, From field data to fracture network modelling: An example incorporating spatial structure, *Water Resour. Res.*, vol. 23(7), p.1201,1216.
- [13] Billaux, D.:1990, Hydrogeologie des milieux fractures. Geometrie, connectivite et comportement hydraulique, Ph. D. thesis, Ecole des Mines, Paris, 277p
- [14] Sun Y., J. N. Petersen, J. Bear, T.P. Clement and Hooker B.S.:1999, Modeling Microbial Transport and Biodegradation in a Dual-Porosity System. *Transport in Porous Media*, vol 35, p. 49-65
- [15] Dykhuizen, R.C.:1990, A new coupling term for dual porosity models, *Water Resour. Res.* Vol. 26 (20), p. 351-356.
- [16] Molz, F.J., Widdowson, and Benefield. L.D.:1986, Simulation of microbial growth dynamics coupled to nutrient oxygen transport in porous media, *Water Resources Research*, vol22 (8), p. 1207-1216.

- [17] Rifai S. H. and Bedient P.B.:1990, Comparison of biodegradation kinetics with an instantaneous reaction model for groundwater, *Water Resources Research*, vol. 26 (4) p.637-645.
- [18] Clement T.P., Peyton , B.M., Skeen, R.S., Jennings, D.A., Petersen, J. N.:1997, Microbial growth and transport in porous media under denitrification conditions: Experiment and simulations, *Journal of Contaminant Hydrology*, p. 245-282
- [19] Wilson R. K. and Aifantis E. C.:1982, On the theory of consolidation with double porosity, *Int. J. Eng. Sci.*, vol. 20, 1009-1035.
- [20] Aifantis E.C.:1984, Compressibility phenomena in subsidence. *Proceedings of the Engineering Foundation International Conference on Compressibility Phenomena in Subsidence*. Henniker New Hampshire.

GRADIENT PLASTICITY THEORY AND SIZE EFFECTS IN DEFORMATION AND FAILURE OF THICK-WALLED TUBES

G. Efremidis, I. Tsagrakis and E. C. Aifantis

Laboratory of Mechanics and Materials, Polytechnic Faculty
Aristotle University of Thessaloniki, GR – 540 06, Thessaloniki, HELLAS
e-mail: efremidi@mom.gen.auth.gr

1. SUMMARY

In recent years, the role of higher-order strain gradients in the localization of deformation and fracture has been extensively studied [1-3]. This paper illustrates the influence of specimen size on the plastic deformation and failure behaviour of a thick-walled tube subjected to high internal stress without change of axial length. A simple form of the gradient modification of the deformation plasticity theory is used, which involves one extra term proportional to the Laplacian $\nabla^2(\cdot)$ of the equivalent plastic strain ε in the yield condition [2, 3].

The well-known size effect relates to the question of the transferability of mechanical test results of a geometrically similar scaled-down structural model to the full-scale structure using similitude laws [2-4]. It also concerns the validity of small-scale laboratory type test results and their use as a basis for the computational modeling of large-scale components. The obtained analytical solution in combination with a maximum strain failure criterion is used to interpret: a) the influence of the gradient term, and b) the observed size effect.

2. INTRODUCTION

The mathematical theories of classical plasticity can be divided, generally, into two types: a) deformation theories (the relations between stress and strain tensor), and b) flow theories (the relations between stress and strain rate) [5-9]. In deformation theories, an averaging process over the entire deformation history is utilized and the total plastic strain is related to the current stress. Flow theories consider a succession of infinitesimal increments of distortion in which the instantaneous stress is related to the strain increment. In general, flow theories are more convenient to describe plastic deformation phenomena involving loading and unloading. On the other hand, deformation theories are mathematically simpler for proportional loading and suitable for providing insight on the usefulness of various constitutive models.

The simplest form of the gradient deformation plasticity theory reads [2, 3]

$$\sigma = \kappa(\varepsilon) - c\nabla^2 \varepsilon, \quad (1)$$

where the equivalent stress σ and the equivalent plastic strain ε are defined by

$$\sigma = \sqrt{\frac{3}{2} S_{ij} S_{ij}} \text{ (Von Mises stress),} \quad \varepsilon = \sqrt{\frac{2}{3} \varepsilon'_{ij} \varepsilon'_{ij}}, \quad (2)$$

with $\kappa(\varepsilon)$ denoting the usual homogeneous flow stress, $c = c(\varepsilon)$ being the gradient coefficient, S_{ij} meaning the deviatoric stress tensor and ε'_{ij} denoting the deviatoric strain tensor which for incompressible plastic deformation ($\varepsilon_{kk} = 0$) equals the strain tensor ε_{ij} .

3. THICK-WALLED TUBE UNDER INTERNAL PRESSURE

In this paper, a gradient deformation plasticity theory is used in order to investigate the stress state of a thick-walled tube, and to interpret the related size effect. We consider a thick-walled tube, subjected to high internal pressure (Fig. 1). The stresses reach the plastic limit in the entire tube [5-7]. The material has a well-defined limit of plasticity and it has not been strained much above a unit elongation of a few percent. We consider a thick-walled cylinder stressed symmetrically with respect to its axis (the z axis) and uniformly along its length. Hence, the directions of principal stresses are the z direction (σ_z), the radial (σ_r) and tangential (σ_θ) directions. Since everything is symmetrical with respect to the axis of the tube, all three stress components $\sigma_r, \sigma_\theta, \sigma_z$ depend only on one independent variable, the radial distance r .

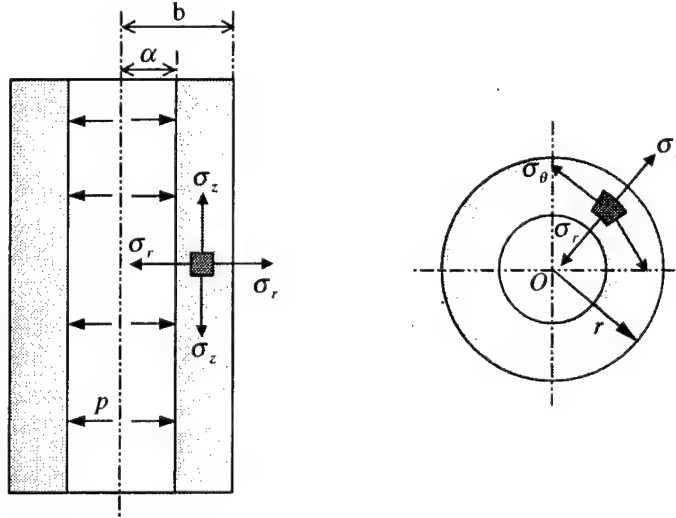


Figure 1: Thick-walled tube under internal pressure p .

In the case of plane strain, the cross sections of the cylinder remain plane, the unit extension of the tube parallel to its axis ε_z is therefore constant along the tube and independent of r . For a long tube $\varepsilon_z = 0$. During plastic flow the material will be stretched. The amount of unit elongation in the radial and circumferential directions will be denoted by ε_r and ε_θ ,

$$\varepsilon_r = \frac{\partial u}{\partial r}; \quad \varepsilon_\theta = \frac{u}{r}; \quad \varepsilon_z = 0. \quad (3)$$

Since plastic deformation is volume conserving, we have

$$\varepsilon_r + \varepsilon_\theta + \varepsilon_z = 0. \quad (4)$$

Remembering that $\varepsilon_z = 0$, the last condition (4), determines completely the radial displacement u which follows from the differential equation,

$$\frac{\partial u}{\partial r} + \frac{u}{r} = 0 \quad \Rightarrow \quad u = \frac{D}{r}, \quad (5)$$

where D is an integration constant. If one introduces the radial displacement $u = r\varepsilon_\theta = D/r$ and the constant D by $D = u_\alpha \alpha$ with u_α denoting the displacement at the inner surface $r = \alpha$ of the cylinder in which the pressure p is transmitted, then the non-zero strain components are

$$\varepsilon_r = -\frac{D}{r^2}, \quad \varepsilon_\theta = \frac{D}{r^2}. \quad (6)$$

The equivalent strain can then be found as,

$$\varepsilon_{eq} = \sqrt{\frac{2}{3} \varepsilon_{ij} \varepsilon_{ij}} = \sqrt{\frac{2}{3} (\varepsilon_r^2 + \varepsilon_\theta^2)} = \frac{2}{\sqrt{3}} \frac{D}{r^2}. \quad (7)$$

The modified yield condition in gradient plasticity connects the radial and the tangential stress components (σ_r, σ_θ) with the yield stress (σ_0) and the equivalent strain (ε_{eq}) [2, 3],

$$\sigma_\theta - \sigma_r = \frac{2}{\sqrt{3}} (\sigma_0 + k\varepsilon_{eq}^N + c\nabla^2 \varepsilon_{eq}), \quad (8)$$

where c is the gradient coefficient, k is the hardening modulus, and N is the hardening exponent, $0 < N \leq 1$. By combining (7) and (8) we obtain,

$$\sigma_\theta - \sigma_r = \frac{2\sigma_0}{\sqrt{3}} + \left(\frac{2}{\sqrt{3}}\right)^{N+1} \frac{kD^N}{r^{2N}} + \left(\frac{2}{\sqrt{3}}\right)^2 \frac{4cD}{r^4}. \quad (9)$$

The axial stress σ_z is at every point of the tube equal to the average value of the radial and the tangential stresses [5],

$$\sigma_z = \frac{\sigma_r + \sigma_\theta}{2}. \quad (10)$$

A second equation for calculating the unknown stresses (σ_r, σ_θ) is given by the condition of equilibrium,

$$\frac{\partial \sigma_r}{\partial r} + \frac{\sigma_r - \sigma_\theta}{r} = 0. \quad (11)$$

Substitution of (9) into (11) leads to the differential equation

$$r \frac{\partial \sigma_r}{\partial r} - \left(\frac{2}{\sqrt{3}}\right)^2 \frac{4cD}{r^4} - \left(\frac{2}{\sqrt{3}}\right)^{N+1} \frac{kD^N}{r^{2N}} - \frac{2\sigma_0}{\sqrt{3}} = 0. \quad (12)$$

The solution of this differential equation is given by,

$$\sigma_r = C_1 + \frac{2\sigma_0}{\sqrt{3}} \ln r - \left(\frac{2}{\sqrt{3}}\right)^{N+1} \frac{1}{2N} \frac{kD^N}{r^{2N}} - \left(\frac{2}{\sqrt{3}}\right)^2 \frac{cD}{r^4}, \quad (13)$$

where C_1 is an integration constant. The tangential stress component σ_θ is given by

$$\sigma_\theta = C_1 + \frac{2\sigma_0}{\sqrt{3}} (1 + \ln r) + \left(\frac{2}{\sqrt{3}}\right)^{N+1} \left(1 - \frac{1}{2N}\right) \frac{kD^N}{r^{2N}} + \left(\frac{2}{\sqrt{3}}\right)^2 \frac{3cD}{r^4}. \quad (14)$$

In a tube with inner radius α and outer radius b , the radial stress σ_r satisfies the boundary conditions [5-7],

$$\sigma_r = -p \text{ at } r = \alpha, \quad \sigma_r = 0 \text{ at } r = b, \quad (15)$$

if the tube is subjected to internal pressure p . In this case, by using (13) and (15) we can determine the integration constant C_1 as

$$C_1 = \frac{-2\sigma_0}{\sqrt{3}} \ln b + \left(\frac{2}{\sqrt{3}}\right)^{N+1} \frac{1}{2N} \frac{kD^N}{b^{2N}} + \left(\frac{2}{\sqrt{3}}\right)^2 \frac{cD}{b^4}. \quad (16)$$

Hence, the radial and tangential stress components $(\sigma_r, \sigma_\theta)$, after transformation in dimensionless form, are given by

$$\frac{\sigma_r}{\sigma_0} = \frac{-2}{\sqrt{3}} \ln \left(\frac{w}{\xi}\right) - \left(\frac{2}{\sqrt{3}}\right)^{N+1} \frac{1}{2N} \frac{\bar{k}}{w^{2N}} \left(\frac{D}{\alpha^2}\right)^N \left(\frac{w^{2N}}{\xi^{2N}} - 1\right) - \left(\frac{2}{\sqrt{3}}\right)^2 \frac{\lambda^2}{w^4} \left(\frac{D}{\alpha^2}\right) \left(\frac{w^4}{\xi^4} - 1\right), \quad (17)$$

$$\begin{aligned} \frac{\sigma_\theta}{\sigma_0} = & \frac{2}{\sqrt{3}} \left[1 - \ln \left(\frac{w}{\xi}\right) \right] + \left(\frac{2}{\sqrt{3}}\right)^{N+1} \frac{1}{2N} \frac{\bar{k}}{w^{2N}} \left(\frac{D}{\alpha^2}\right)^N \left[\frac{(2N-1)w^{2N}}{\xi^{2N}} + 1 \right] \\ & + \left(\frac{2}{\sqrt{3}}\right)^2 \frac{\lambda^2}{w^4} \left(\frac{D}{\alpha^2}\right) \left[\frac{3w^4}{\xi^4} + 1 \right]. \end{aligned} \quad (18)$$

The dimensionless quantities in the above expressions are defined as follows:

$$w = \frac{b}{\alpha} \left(\frac{\text{outer radius}}{\text{inner radius}} \right); \quad w > 1, \quad \ell^2 = \frac{c}{\sigma_0} \left(\frac{\text{gradient coefficient}}{\text{yield stress}} \right); \quad \ell: \text{internal length} \quad (19)$$

$$\lambda = \frac{\ell}{\alpha} \left(\frac{\text{internal length}}{\text{inner radius}} \right); \quad 0 < \lambda < 1, \quad \bar{k} = \frac{k}{\sigma_0} \left(\frac{\text{hardening modulus}}{\text{yield stress}} \right); \quad (20)$$

$$\xi = \frac{r}{\alpha} \left(\frac{\text{radial distance}}{\text{inner radius}} \right); \quad 1 < \xi < w, \quad \varepsilon_\theta|_{r=\alpha} = \frac{D}{\alpha^2}: \text{maximum tangential strain.} \quad (21)$$

From (17), one can determine the dimensionless yield stress $\bar{p} = p / \sigma_0$ under which yielding in the tube is maintained. By using the first boundary condition (15)_a, one finds that the dimensionless yield stress \bar{p} is

$$\bar{p} = \frac{p}{\sigma_0} = \frac{2}{\sqrt{3}} \ln w + \left(\frac{2}{\sqrt{3}}\right)^{N+1} \frac{\bar{k}}{2N} \left(\frac{u_\alpha}{\alpha}\right)^N \left(1 - \frac{1}{w^{2N}}\right) + \left(\frac{2}{\sqrt{3}}\right)^2 \lambda^2 \left(\frac{u_\alpha}{\alpha}\right) \left(1 - \frac{1}{w^4}\right). \quad (22)$$

The variation of \bar{p} versus maximum tangential strain $\varepsilon_\theta|_{r=\alpha}$ for different values of the dimensionless length λ and for constant w, \bar{k}, N is depicted in Fig. 2. In classical plasticity ($\lambda = 0$), the dimensionless yield stress is not affected by the internal length ℓ of the material. On the other hand, in gradient plasticity, the dimensionless yield stress is strongly dependent on ℓ . This leads to results which differ for different materials. This deviation between classical and gradient plasticity becomes negligible for low values of the ratio u_α / α . In fact, for negligible tangential strain in the inner surface of the tube, gradient plasticity predicts the same mechanical response as classical plasticity.

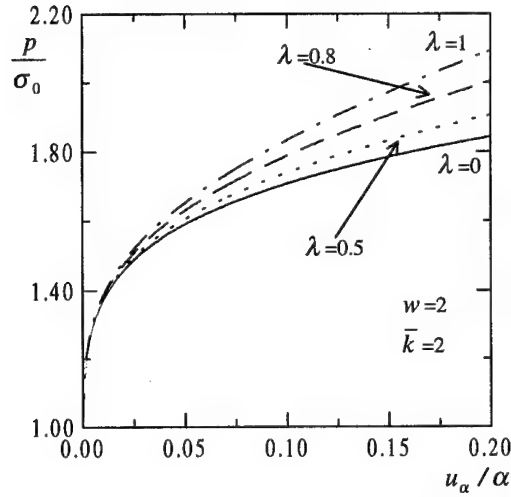


Figure 2: Distribution of the dimensionless quantity \bar{p} in a thick-walled tube versus the dimensionless ratio u_α/α (maximum radial displacement / inner radius) for $w=2$, $\bar{k}=2$ and $N=0.2$.

4. SIZE EFFECTS IN A THICK-WALLED TUBE

On the basis of the previous results, one may show that gradient plasticity theory predicts the occurrence of size effects which cannot be described by classical plasticity. We consider the following maximum strain fracture criterion:

$$(\varepsilon_{eq})_{max} = \varepsilon_c \quad \Rightarrow \quad \frac{2}{\sqrt{3}} \frac{D}{\alpha^2} = \varepsilon_c, \quad (23)$$

where ε_c is a material constant. This assumes that the material fails when the maximum equivalent strain $(\varepsilon_{eq})_{max}$ is equal to the critical value ε_c . By combining equations (22) and (23) we have the following expression for the dimensionless failure stress $(\bar{p})_c$ of the thick-walled tube:

$$(\bar{p}_0)_c = \frac{2}{\sqrt{3}} \ln w + \left(\frac{2}{\sqrt{3}} \right) \frac{\bar{k} \varepsilon_c^N}{2N} \left(1 - \frac{1}{w^{2N}} \right) + \left(\frac{2}{\sqrt{3}} \right) \frac{\varepsilon_c}{(\alpha/\ell)^2} \left(1 - \frac{1}{w^4} \right). \quad (24)$$

Fig. 3 illustrates the distribution of the dimensionless failure stress $(\bar{p})_c$ versus the dimensionless ratio α/ℓ (inner radius / internal length). As seen from Fig. 3, for low values of the ratio α/ℓ the tube fails at higher stresses. On the contrary, classical plasticity is not able to interpret the size dependence of the failure behavior of the tube.

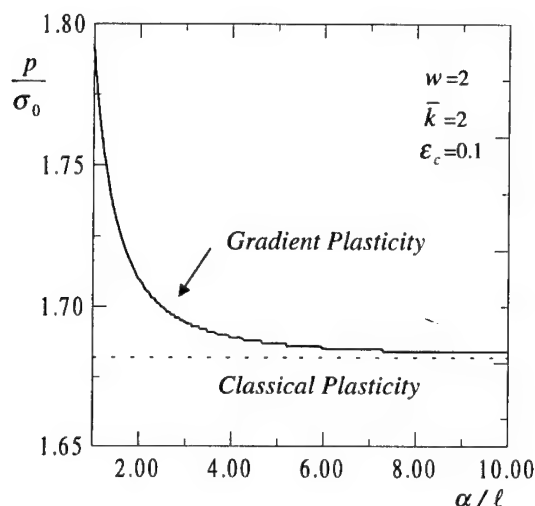


Figure 3: Distribution of the dimensionless failure stress $(\bar{p})_c$ in a thick-walled tube versus the dimensionless ratio α/ℓ (inner radius / internal length) for $w = 2$, $\bar{k} = 2$, $\varepsilon_c = 0.1$ and $N = 2$.

Acknowledgements: The financial support of the European Commission under the TMR Project grant No. FMRXCT960062 and the LISSAC Project No. FIKS-CT1999-00012 and of GSRT under PENED 1958 is gratefully acknowledged. A preliminary study for the expansion of a cylindrical cavity using the present gradient deformation plasticity model was described in [10]. Some of the basic results obtained in that paper are the same as those described in the present one. The authors are grateful for the availability of [10] in a preprint form.

5. REFERENCES

- [1] Aifantis E.C., On the role of gradients in the localization of deformation and fracture, *Int.J. Engng.Sci.* 30, 1279-1299 (1992).
- [2] Aifantis E.C., Higher order gradients and size effects, in *Size-Scale Effects in the Failure Mechanisms of Materials and Structures*, A. Carpinteri, (ed.), E & FN Spon, London 231-241 (1996).
- [3] Malmberg T., Tsagrakis I., Eleftheriadis E. and E.C. Aifantis, On the Gradient Plasticity Approach to Size Effects, Part I: Reviews, Scientific Report FZKA 6321, Reactor Vessel Integrity in Severe Accidents (REVISA) (1999).
- [4] Huang Y., Gao H., Nix W. D. and J. W. Hutchinson, Mechanism-based strain gradient plasticity – II. Analysis, *Journal of the Mechanics and Physics of Solids* 48, 99-128 (2000).
- [5] Nadai A., *PLASTICITY: A Mechanics of the Plastic State of Matter*, Revised and Enlarged from the first German Edition, McGraw-Hill Book Company, Inc., New York and London (1931).
- [6] Kachanov L. M., *Fundamentals of the Theory of Plasticity*, English Translation, Mir Publishers, Moscow (1974).

-
- [7] Ugural A. C. and S. K. Fenster, *Advanced Strength and Applied Elasticity*, PTR Prentice Hall, Englewood Cliffs, New Jersey (1995).
 - [8] Calladine C. R., *Engineering Plasticity*, Pergamon Press Ltd., London (1969).
 - [9] Johnson W. and P. B. Mellor, *Engineering Plasticity*, Van Nostrand Reinhold Company Ltd., London (1973).
 - [10] Gänser, H.-P., Konstantinidis D. and Aifantis E. C., Approximate yield surface for a gradient plastic material containing spherical voids, (preprint).

SOLUTION OF SPHERICAL LAME PROBLEM WITHIN THE FRAMEWORK OF GRADIENT ELASTICITY

K. Kosmidis, F. Akintayo and E. C. Aifantis

Laboratory of Mechanics and Materials, Polytechnic Faculty
Aristotle University of Thessaloniki, GR – 540 06, Thessaloniki, HELLAS

1. SUMMARY

A solution of the spherical Lamé problem using the model of Gradient elasticity is presented. Stress, strain, displacement and strain energy are computed and compared with the classical elasticity solution. A general method for solving similar problems in curvilinear coordinates is illustrated. The results are very preliminary, they were obtained during progress for a Master (K. Kosmidis) and Doctoral (F. Akintayo) thesis supervised by E. C. Aifantis and they should be re-examined before proper journal publication.

2. INTRODUCTION

In classical elasticity the strain energy is a quadratic function of the strain tensor. This strain energy expression leads to the well known constitutive equation, i.e. Hooke's law

$$\sigma = \lambda (\text{tr } \epsilon) \mathbf{I} + 2 \mu \epsilon. \quad (1)$$

The idea of taking into account higher gradients of the displacement field in the expression for the strain energy can be traced back to Bernoulli and Euler. It was further elaborated upon by Mindlin [1], [2]. More recently, Aifantis and co workers[3]-[4] have proposed a higher strain order gradient model where the strain energy density function is given by

$$w = \frac{1}{2} \lambda \epsilon_{ii} \epsilon_{jj} + \mu \epsilon_{ij} \epsilon_{ij} + c \left(\frac{1}{2} \lambda \epsilon_{ii,k} \epsilon_{jj,k} + \mu \epsilon_{ij,k} \epsilon_{ij,k} \right), \quad (2)$$

where c denotes a newly introduced strain gradient parameter which is the only non-standard coefficient of the theory.

It was shown by Aifantis and Ru [3] that the above expression leads to the following constitutive equation

$$\sigma = \lambda (\text{tr } \epsilon) \mathbf{I} + 2 \mu \epsilon - c \nabla^2 (\lambda (\text{tr } \epsilon) \mathbf{I} + 2 \mu \epsilon), \quad (3)$$

where ∇^2 denotes the Laplacian operator.

Note that the quantity $\lambda (\text{tr } \epsilon) \mathbf{I} + 2 \mu \epsilon$ is a tensor of Rank 2. The Laplacian of a rank 2 tensor has a simple expression in Cartesian coordinates but it turns out to have a quite complicated form in curvilinear coordinates. We will not give the exact expression in this paper but simply note that when using curvilinear coordinates, the Cartesian tensor notation is no longer valid and instead of the normal spatial derivative one has to use the "covariant" derivative as it is known from differential geometry [5]. The same is true also for equation (2) where for example $\epsilon_{ij,k}$ in curvilinear coordinates has to be interpreted as the covariant derivative of ϵ_{ij} with respect to $q(k)$. The details will be given in a forthcoming paper, as well as in [6].

In order to illustrate the problem we will determine stresses and displacements in a closed spherical shell loaded internally ($r=a$) and externally ($r=b$) by uniformly distributed pressures (p_i and p_o).

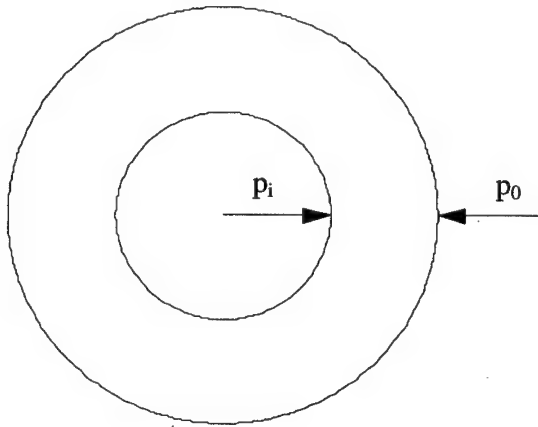


Fig 1: Spherical shell under internal and external pressure.

Classical Solution

The problem has spherical symmetry. So we deal with it in spherical coordinates. The Navier equations are

$$\mu \nabla^2 \vec{u} + (\lambda + \mu) \nabla (\nabla \cdot \vec{u}) = 0, \quad (4)$$

and the Classical solution is $u = \{u_r[r], 0, 0\}$ where

$$u_r = C_1 r + C_2 / r^2.$$

The strain matrix is

$$\epsilon = \begin{pmatrix} C_1 - \frac{2C_2}{r^3} & 0 & 0 \\ 0 & C_1 + \frac{C_2}{r^3} & 0 \\ 0 & 0 & C_1 + \frac{C_2}{r^3} \end{pmatrix}$$

and the stress matrix is

$$\sigma = \begin{pmatrix} 3\lambda C_1 + 2\mu(C_1 - \frac{2C_2}{r^3}) & 0 & 0 \\ 0 & 3\lambda C_1 + 2\mu(C_1 + \frac{C_2}{r^3}) & 0 \\ 0 & 0 & 3\lambda C_1 + 2\mu(C_1 + \frac{C_2}{r^3}) \end{pmatrix}.$$

Obviously, the following boundary conditions should be satisfied:

$$\sigma_{rr} = -p_i \quad \text{at} \quad r = a,$$

$$\sigma_{rr} = -p_o \quad \text{at} \quad r = b,$$

and thus

$$C_1 = \frac{-a^3 p_i + b^3 p_o}{(a^3 - b^3)(3\lambda + 2\mu)}, \quad C_2 = -\frac{a^3 b^3 (p_i - p_o)}{4(a^3 \mu - b^3 \mu)}.$$

We will examine two cases: one when $p_o > p_i$ and the second when $p_i < p_o$.

a. Case 1 : $p_o > p_i$

We present graphic representations of strain energy and displacement. In order to produce the following diagrams we have used the arithmetic values $a=1, b=2, \lambda=1, \mu=0.4, p_i=1, p_o=2$. This choice of values is somehow artificial in the sense that Lamé coefficients are small and the strain gradient parameter will be rather large in order to reveal some qualitative difference of the relevant diagrams; e.g. curvature, which otherwise would be quite difficult to comprehend. Of course this choice does not affect the generality of our results or the method that we have used in order to derive them.

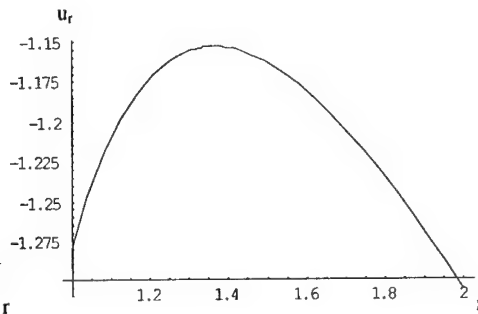
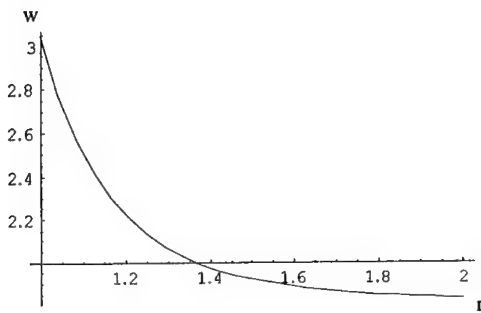


Fig. 2: Classical strain energy density ($p_o > p_i$) Fig. 3: Classical radial displacement ($p_o > p_i$)

b. Case 2 : $p_o < p_i$

We once again present graphic representations of strain energy and displacement. In order to produce the following diagrams we have used the arithmetic values $a=1$, $b=2$, $\lambda=1$, $\mu=0.4$, $p_i=2$, $p_o=1$.

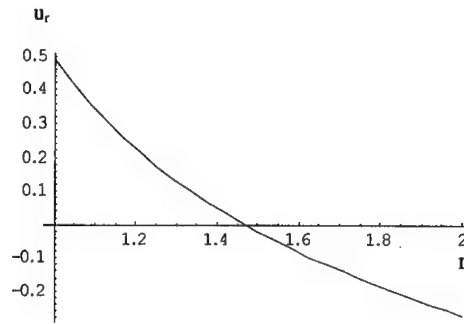
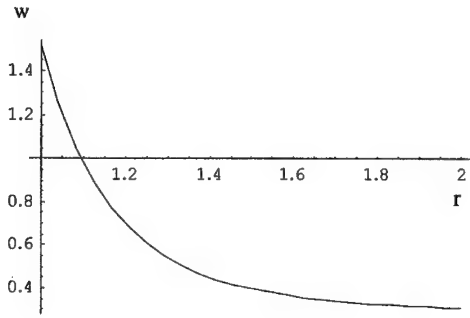


Fig. 4: Classical strain energy density ($p_o < p_i$) Fig. 5: Classical radial displacement ($p_o < p_i$)

There is no qualitative difference between the strain energy distribution in the two cases. Most of the energy is stored near $r = a$.

GRADIENT SOLUTION

The equilibrium equations are

$$\text{div } \sigma = 0 \quad (5)$$

where σ is given by (3). In this case we seek solutions where the displacement has the form $u = (u_r[r], 0, 0)$. This leads to the following forth-order ordinary differential equation for the displacement

$$\frac{c r (r u_r^{(4)} + 4 u_r^{(3)}) - (4c + r^2) u_r'' - 2r u_r' + 2u_r}{r^2} = 0. \quad (6)$$

Instead of attempting to solve the above equation directly, it is better to follow the approach of Ru and Aifantis [2]. In [2] it is shown that if the classical solution is known, then the solution of the gradient elasticity problem can be derived by solving the following second order problem:

$$(1 - c \nabla^2) u = u^0, \quad (7)$$

where u^0 stands for the classical solution. It turns out that the general solution of (6) is

$$u_r = C_1 r + C_2 / r^2 + C_3 \left(\left(\frac{\sqrt{c}}{r^2} \cosh\left(\frac{r}{\sqrt{c}}\right) - \frac{1}{r} \sinh\left(\frac{r}{\sqrt{c}}\right) \right) \right) + C_4 \left(\frac{\sqrt{c}}{r^2} \sinh\left(\frac{r}{\sqrt{c}}\right) - \frac{1}{r} \cosh\left(\frac{r}{\sqrt{c}}\right) \right). \quad (8)$$

Furthermore, Ru and Aifantis in [2] have shown that we can choose C_1 and C_2 to be the same as in the classical case and by doing so the traction boundary conditions will be fulfilled also in the gradient case. Thus, we have again

$$C_1 = \frac{-a^3 p_i + b^3 p_o}{(a^3 - b^3)(3\lambda + 2\mu)}, \quad C_2 = -\frac{a^3 b^3 (p_i - p_o)}{4(a^3 \mu - b^3 \mu)}.$$

It remains to determine the other two constants C_3 and C_4 . In order to do so two extra boundary conditions are needed. The usual choices in the literature are that at the boundary one can choose either $d^2 u_r / dr^2 = 0$ at $r = a, b$ or $du_r / dr = 0$ at $r = a, b$. However these two boundary conditions are suitable when we have "displacement" problems, while this is not always the case when we have a traction boundary problem as the present one. They are however a very good approximation for small tractions. A complete discussion of the extra boundary conditions is postponed for a forthcoming article.

It turns out that in the case of the Lamé problem there is an explicit analytic solution and one does not have to resort to numerical methods. The resulting form of C_3 and C_4 however is not very simple and we will not explicitly give it here.

In the particular case we have chosen as an example it turns out that

$$C_3 = -C_4 = 37.43 C_1 - 29.68 C_2.$$

The fact $C_3 = -C_4$ is not generally true. It is a coincidence due to the numbers chosen for the example.

We present the graphic representations of strain energy density and displacement for the same two subclasses as in the classical case. We choose $c=0.04$ and all other parameters are the same as in the analysis of the classical case.

a. Case 1 : $p_o > p_i$

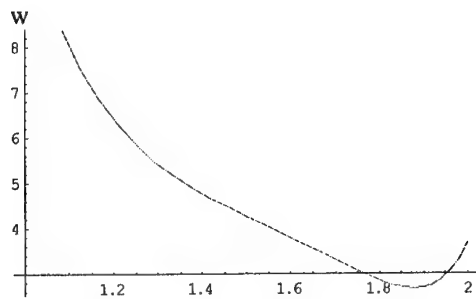


Fig. 6 : Gradient strain energy density ($p_o > p_i$)

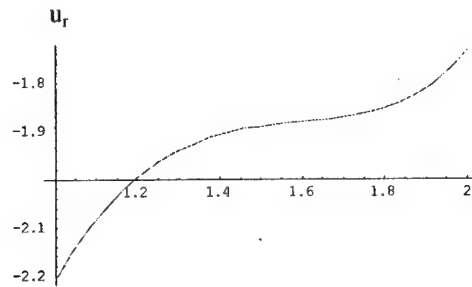


Fig. 7: Gradient radial displacement ($p_o > p_i$)

b. Case 2 : $p_o < p_i$

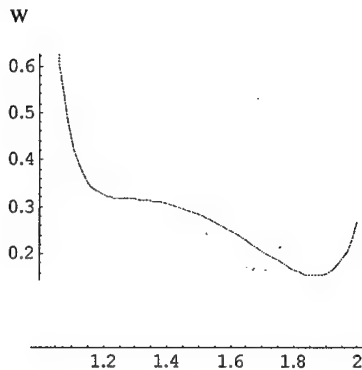


Fig. 8: Gradient strain energy density ($p_o < p_i$)

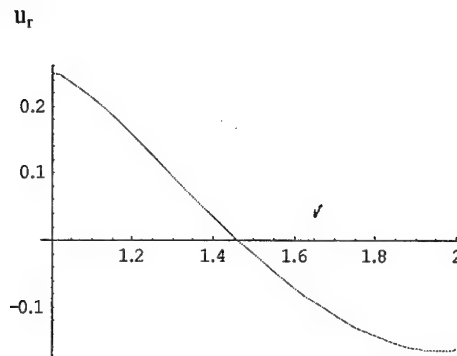


Fig. 9: Gradient radial displacement ($p_o < p_i$)

3. CONCLUSIONS

We have solved the spherical Lamé problem using the gradient elasticity model. One has to compare Figure 2 to Figure 6, Figure 3 to Figure 7 etc. It is apparent by inspection that gradient elasticity predicts different energy density distribution and different radial displacement distribution. Note particularly the difference between Figures 3 and 7. The different profiles of strain energy density and displacement will generally lead to different fracture behavior. We can suppose that an isotropic elastic material will be damaged when the strain energy density at some point exceeds a certain critical value. By simple inspection of Figures 2 and 6 we can see that, in case $p_i > p_o$, gradient elasticity predicts that fracture will probably occur at lower pressures than in the classical case. The opposite is true in the case $p_o < p_i$. This is a somewhat surprising preliminary result which should be further examined and verified. These different profiles may provide a potential way of experimentally testing gradient elasticity when realistic parameters of the respective coefficients are used.

4. REFERENCES

- [1] Mindlin R.D : Arch. Ration. Mech. Analysis **16**, 51-78, 1964
- [2] Mindlin R.D : Int J. Solids Structures **1**, 417-437, 1965
- [3] Ru C., Aifantis E.C. , A simple approach to solve boundary-value problems in gradient elasticity, Acta Mechanica **101**,59-68, 1993.
- [4] Ru C., Aifantis E.C, Some studies on boundary value problems in gradient elasticity, preprint (MTU Lecture Notes), 1993.
- [5] Morse -Feshbach, Methods of Theoretical Physics, Volume 1, 1959.
- [6] Kosmidis K., Master Thesis, AUT, 2001.

AUTHOR INDEX

Volume I

- Z. Agioutantis, 191
P. Anagnostopoulos, 39, 66
G. Anastassopoulos, 381
G. Arampatzis, 416
K. Arvanitis, 240
V. Assouti, 72
A. Avdelas, 228
B. Badalouka, 388
G. Badaloukas, 388
R. Barber, 52
A. Bekos, 381
D. Beskos, 210
V. Bontozoglou, 33
A. Boudouvis, 21
I. Chatjigeorgiou, 408
B. Coric, 282
H. Cramer, 298
I. Daniel, 320
J. Demetriou, 102, 108, 121
Y. Dimakopoulos, 84
D. Dimitriou, 102
C. Dimou, 275
A. Elenas, 254
R. Findei, 298
D. Fotiadis, 327
K. Gagas, 72
C. Galiotis, 401
C. Gantes, 261
E. Gdoutos, 320, 394
K. Giannakoglou, 72
P. Giokas, 333
T. Goudoulas, 27
S. Goutianos, 401
M. Hadjinicolaou, 59
N. Hajdin, 178, 282
D. Hatzichristou, 381
G. Hatzigeorgiou, 210
P. Kakavas, 375
N. Kalinderis, 381
A. Kaounis, 72
D. Karalekas, 394
E. Kastrinakis, 27, 96
J. Katsikadelis, 172, 204, 222
I. Kevrekidis, 21
S. Kobayashi, 290
C. Koimtzoglou, 401
P. Koliopoulos, 254
E. Koronaki, 21
V. Kostopoulos, 365
V. Koumoussis, 275
C. Kouris, 45
S. Kourkoulis, 339, 348
S. Kourtakis, 184
A. Koutras, 66
D. Krajcinovic, 155
J. Kratochvil, 14
V. Kytopoulos, 339
P. Ladeveze, 140
N. Lagaros, 246
J. Lemaitre, 163
A. Likas, 327
A. Liolios, 254
V. Loukopoulos, 90
D. Lucic, 282
J. Lytras, 381
I. Mademlis, 228
N. Malamataris, 33
R. Mandic, 178
D. Margaris, 114
Lj. Markovic, 146
N. Markovic, 282
S. Marnoutsidis, 228
G. Maugin, 1
S. Mavrakos, 408
G. Michaltsos, 234
V. Moulidianitis, 381
H. Mpimpas, 39
K. Nanou-Giannarou, 121
N. Ninis, 348
S. Nychas, 27, 96

- Th. Panidis, 127
 S. Panteliou, 381
 A. Papachristidis, 388
 M. Papadrakakis, 246
 Y. Pappas, 365
 G. Paschalis, 191
 N. Pelekasis, 78
 N. Pnevmatikos, 261
 C. Pourliotis, 108
 I. Prassianakis, 333
 C. Providakis, 184
 D. Ruzic, 146
 M. Sakellari, 254
 T. Salonikios, 267
 E. Sapountzakis, 222
 P. Sarantos, 108
 D. Saravanos, 357
 R. Schapery, 134
 C. Sciammarella, 314
 F. Sciammarella, 314
 S. Seitanis, 66
 M. Sfakianakis, 210
 W. Sharpe Jr., 306
 G. Sideridis, 96
 D. Smyrnaiois, 78
 K. Soldatos, 216
 A. Soldatos, 240
 D. Sophianopoulos, 234
 C. Sophocleous, 216
 K. Spiliopoulos, 198
 G. Stavroulakis, 240
 R. de Stefano, 365
 C. Stiakakis, 191
 M. Sunaric, 381
 D. Theodorakopoulos, 210
 C. Theodoropoulos, 21
 M. Titsias, 327
 J. Tsamopoulos, 45, 78, 84
 G. Tsiatas, 172
 Ch. Tzimopoulos, 416
 P. Vafeas, 59
 K. Valanis, 9
 D. Varelis, 357
 L. Vasiliadis, 254
 M. Vlachogiannis, 33
 D. Vlachos, 365
 N. Volakos, 52
 K.-A. Wang, 320
 W. Wunderlich, 298
 J. Yiotis, 204
 E. Zacharenakis, 240
 D. Zacharopoulos, 394
 T. Zervogiannis, 72

Volume II

- M. Abellan, 365
 E. Amanatidou, 149
 I. Andreadis, 177
 N. Anifantis, 52
 H. Antes, 28
 N. Aravas, 149
 Y. Bamnios, 342
 C. Baniotopoulos, 70, 78
 A. Bardzokas, 13
 D. Bardzokas, 22
 J. Bergheau, 365
 D. Beskos, 163, 328
 M. Betti, 78
 D. Bollas, 63
 C. Borri, 78
 D. Briassoulis, 57
 A. Carpinteri, 349
 N. Charalambakis, 276
 A. Charalambopoulos, 216
 C. Charitidis, 40
 B. Chiaia, 349
 K. Chong, 391
 P. Cornetti, 349
 C. Dascalu, 233, 239
 G. Dassios, 109
 D. Davis, 391
 R. de Borst, 365
 B. Demakos, 102
 R. Desmorat, 318
 A. Diamantopoulou, 46

- K. Dimitrakopoulou, 301
 R. Dorgan, 309
 E. Douka, 335
 E. Douka, 342
 P. Entchev, 120
 G. Exadaktylos, 140, 155, 189
 M. Filshtinsky, 22
 D. Fotiadis, 216
 G. Foutsitzi, 216
 G. Frantziskonis, 359
 C. Galiotis, 63
 H. Georgiadis, 289, 295
 D. Georgiou, 90
 E. Gerde, 1
 J. Gilarranz, 371
 P. Grammenoudis, 263
 P. Gupta, 33
 Y. Haddad, 245
 E. Hadjigeorgiou, 239
 D. Homentcovschi, 233, 239
 J. Huyghe, 365
 S. Ichtiaroglou, 379
 J. Jaric, 115
 X. Jiang, 170
 N. Kafoussias, 227
 V. Kalpakides, 126, 239
 T. Kalvouridis, 385
 G. Kamvyssas, 222
 T. Karakasidis, 177, 183
 C. Karakostas, 280
 F. Kariotou, 222
 D. Katsareas, 52
 A. Kekatou, 52
 K. Kishimoto, 115
 M. Kontoleon, 70, 78
 V. Koukouloyannis, 379
 S. Kourkoulis, 140
 D. Lagoudas, 120
 S. Logothetidis, 40
 G. Lykotrafitis, 295
 G. Manolis, 280
 M. Marder, 1
 R. Masiani, 257
 C. Massalas, 216
 A. Massih, 7
 G. Maugin, 126
 A. Mavraganis, 301
 E. Meletis, 33
 E. Mistakidis, 84, 90, 96
 X. Nie, 33
 M. Omiya, 115
 M. Pagitsas, 46
 O. Panagouli, 84
 D. Panayotounakos, 189, 196
 S. Papargyri-Beskou, 163, 328
 J. Parthenios, 63
 N. Politis, 90
 D. Polyzos, 163, 328
 B. Polyzos, 335
 G. Psarras, 63
 F. Psarros, 385
 O. Rediniotis, 371
 D. Sazou, 46
 E. Schettini, 57
 D. Schick, 269
 V. Sfakiotakis, 52
 V. Singh, 33
 P. Sofronis, 251
 K. Soldatos, 209
 J. Stabouloglou, 133
 G. Stavroulakis, 28
 S. Subramanian, 251
 D. Sumarac, 397
 E. Theotokoglou, 133
 A. Trochidis, 335, 342
 P. Trovalusci, 257
 G. Tsaklidis, 209
 Ch. Tsakmakis, 263, 269
 K. Tsepoura, 163, 328
 E. Tzirtzilakis, 227
 A. Vakakis, 170, 189
 I. Vardoulakis, 140, 289
 A. Varias, 7
 E. Velgaki, 289
 G. Voyiadjis, 309
 T. Wang, 115
 C. Younis, 196
 A. Zobnin, 13
 M. Zygomalas, 70

Volume III

- | | |
|--|------------------------|
| E. Aifantis, 29, 35, 67, 73, 102, 129, 136 | K. Kosmidis, 136 |
| H. Ait-Amokhtar, 22 | L. Kubin, 47 |
| F. Akintayo, 136 | D. Kugiumtzis, 29 |
| C. Anagnostopoulos, 116 | M. Latzel, 53 |
| H. Askes, 1 | S. Lisina, 90 |
| K. Chihab, 22 | S. Luding, 53 |
| A. Christou, 109 | G. Maugin, 67 |
| F. Chmelik, 16 | E. Meletlidou, 67 |
| A. Cornet, 109 | K. Moutsopoulos, 123 |
| R. de Borst, 1 | H. Neuhauser, 9, 16 |
| B. Devincre, 47 | A. Nortmann, 9 |
| H. Dierke, 9 | A. Potapov, 85, 90, 96 |
| G. Efremidis, 129 | J. Pouget, 61, 67, 73 |
| A. Fernandes, 61 | V. Rodyushkin, 85 |
| J. Grammatikopoulos, 116 | G. Stagika, 35 |
| I. Groma, 35 | P. Sutcliffe, 79 |
| S. Gromov, 96 | A. Tokiy, 40 |
| M. Gutierrez, 1 | N. Tokiy, 40 |
| S. Hadjispyrou, 116 | I. Tsagarakis, 129 |
| S. Ichtiaroglou, 35 | G. Utkin, 90 |
| T. Ioannidou, 73 | V. Varyukhin, 40 |
| V. Kazhaev, 96 | G. Wells, 1 |
| F. Klose, 9 | M. Zaiser, 102 |
| T. Konstantinova, 40 | A. Ziegenbein, 9, 16 |